UNIVERSITÀ DELLA CALABRIA

UNIVERSITA' DELLA CALABRIA

Dipartimento di Ingegneria Meccanica, Energetica e Gestionale

Dottorato di Ricerca in Ingegneria Industriale

CICLO XXXII

Toughening mechanisms and damage tolerance of bioinspired interfaces

Settore Scientifico Disciplinare ING-IND/14

Coordinatore: Ch.mo Prof. Franco Furgiuele

Firma ______________________________

Supervisore/Tutor: Prof. Marco Alfano

Firma Marco Alfano

Dottorando: Dott.ssa Chiara Morano

Firma

Chiara Morano

Abstract

Biologically inspired designs were deployed into selective laser sintering of polyamide substrates to study the mechanics of adhesion and debonding of adhesive bonded structural interfaces. In particular, through extensive series of experiments and simulations, the present study covers the effect of hollow channels, mimicking the base plate of the *Amphibalanus amphitrite*, and of sinusoidal interfaces, resembling those observed in sutures joints, on the mechanics of crack propagation in adhesive bonds. A model material system comprising adhesively bonded 3D printed substrates in the Double Cantilever Beam (DCB) configuration was selected for the analyses. Adhesive bonding and subsequent mechanical tests revealed the occurrence of a crack trapping effect, which hinders crack propagation and enhances energy dissipation with respect to the baseline interface. The use of bioinspired structures is shown to improve the performances of adhesive joints, enabling damage tolerance and, in the case of subsurface channels, also a weight reduction. Numerical simulations, carried out using finite element analysis (FEA) with interface elements, were also executed to gain a deep understanding of all mechanisms observed experimentally. The simulations were able to mimic the serrated behavior observed in experimental load-displacement responses, which was due to the snap-through interfacial cracking mechanism, i.e., a sudden and almost instantaneous growth of apparently stable cracks. Moreover, the mechanisms of fracture observed in the experiments (e.g., nucleation of a secondary crack at the interface) were reproduced with good accuracy in finite element simulations. The overall analysis demonstrates that is possible to improve joints effective fracture toughness by modifying joints architecture, even without any modification of adhesive type and/or interface properties (e.g., surface energy). This study further confirms that additive manufacturing represents a powerful platform for the experimental study of bio-inspired materials.

Sommario

Il presente lavoro di tesi analizza i meccanismi di adesione e cedimento nei giunti incollati con substrati realizzati mediante produzione additiva, le cui interfacce sono state modificate in modo da “mimare” strutture biologiche. In particolare, attraverso un’ampia campagna sperimentale e mediante simulazioni numeriche, è stato valutato l'effetto sul meccanismo di propagazione dei difetti in giunti incollati conseguente alla presenza di canali ispirati alla struttura della piastra di base del guscio dell’*Amphibalanus amphitrite*, e di interfacce sinusoidali simili a quelle osservabili nelle *suture*. Si è scelto di utilizzare un modello materiale comprendente substrati stampati in 3D incollati nella configurazione *Double Cantilever Beam* (DCB). I test meccanici hanno permesso di osservare il fenomeno del *“crack trapping”*, che ostacola la propagazione del difetto, incrementando la dissipazione di energia rispetto all'interfaccia di base. L'uso di strutture bio-ispirate si è dimostrato in grado di migliorare le prestazioni dei giunti incollati, consentendo una maggiore tolleranza al danno e, nel caso della presenza di canali, anche una riduzione del peso del giunto. Sono state dunque eseguite simulazioni numeriche, mediante analisi agli elementi finiti (FEA), utilizzando elementi coesivi; tali analisi hanno permesso di analizzare e comprendere in maniera più approfondita i meccanismi osservati sperimentalmente. Le simulazioni sono state in grado di riprodurre fedelmente il comportamento l’andamento “seghettato” delle curve carico-spostamento sperimentali, legato al meccanismo di *snap-through*, ovvero la propagazione improvvisa del difetto risultando essere apparentemente instabile. Inoltre, i meccanismi di frattura osservati negli esperimenti (e.g., nucleazione di un crack secondario) sono stati riprodotti con un’ottima affidabilità dalle simulazioni agli elementi finiti. Complessivamente è stato possibile dimostrare che si può migliorare l'effettiva resistenza alla frattura delle giunzioni incollate agendo sull'architettura del giunto, senza alcuna modifica del tipo di adesivo e/o delle proprietà dell'interfaccia (e.g., energia superficiale). Questo studio conferma inoltre che la produzione additiva rappresenta un potente strumento per la produzione di componenti caratterizzati da geometrie bio-inspirate.

Index

Introduction

Adhesive bonding is a suitable joining technique which is currently employed in many industrial fields, *e.g.*, automotive, aerospace, electronic. Structural bonding can increase the stiffness, fatigue life, and crash resistance of the built-up structures. However, the manufacturing process will inevitably introduce defects, such as entrapped air, lack of adhesion in areas with improper surface preparation, etc. Therefore, there has been a surge of interest around the development of strategies that can ensure toughening and damage tolerance in adhesive joints.

Previous works on adhesive bonding mostly targeted either the adhesive or the interfaces (or both). Concerning the works that target the adhesive, a vast variety of literature work has focused on the addition of nanofillers (Aradhana, Mohanty and Nayak, 2018; Jakubinek *et al.*, 2018; Khoramishad and Zarifpour, 2018), while more recently the effect of carrier clothes has been assessed (Heide-Jørgensen, Teixeira de Freitas and Budzik, 2018; Maloney and Fleck, 2019).

Regarding those that focused on the interface, various surface treatments have been proposed which allow controlling the *microscale* surface topography and surface chemistry. For example, classical sandblasting (Harris and Beevers, 1999; Rudawska, 2014), chemical and/or electrochemical pre-treatments (Lee and Qu, 2003; Lunder *et al.*, 2004; Goglio and Rezaei, 2013) and pulsed laser irradiation (Baburaj *et al.*, 2007; Alfano *et al.*, 2011; Langer *et al.*, 2012;

Rotella *et al.*, 2016; Tao, Alfano and Lubineau, 2018, 2019), have been used on a variety of materials, including steel, lightweight alloys and fiber-reinforced polymers. The use of surface pre-treatments enabled the improvement of the work of separation needed to sever the joints through enhanced chemical bonding and mechanical keying of the adhesive within the high-frequency micro-scale asperities. The effect of patterned interfaces, combining areas with distinct microscale topography, has also been the subject of a strong research effort (Chan, Ahn and Crosby, 2007; Malkin, Trask and Bond, 2013; Hernandez *et al.*, 2017; Heide-Jørgensen and Budzik, 2018). A common observation from previous works is that surface patterns induce crack arrest/re-initiation and have a leveraging effect on the overall work of separation and/or fracture toughness.

Increasing the surface area through *macroscale* roughness is another strategy that has beneficial effects on the fracture toughness with respect to a macroscopically flat interface. For example, the works from Zavattieri and co-workers focused on sinusoidal interfaces obtained using electrical discharge machining (Cordisco *et al.*, 2016), while that of Maloney and Fleck on square-wave interfaces obtained using water-jet cutting (Maloney and Fleck, 2018). In both cases, improved mode-I fracture properties of adhesive bonded Double Cantilever Beam (DCB) joints were reported. Still, in the same area, the effect of bio-inspired mechanical interlocking has been largely explored considering model material systems resembling the suture joints of shells and bones. The influence of fractal-like hierarchical sutures on the mechanical behavior was addressed by Lin et al. (Lin *et al.*, 2014), whilst Khoshhesab and Li analyzed the interlocking effect by using Koch's fractal geometry[1] (Khoshhesab and Li, 2018). It was shown that by changing the order of hierarchy in the sutures amplifies the stiffness, modifies favorably the normal to shear stress ratio, and changes the mechanism of failure. As a result, both strength and fracture toughness significantly increased.

An additional and interesting pathway to modify the interfacial response is based on the modification of the local stiffness at the interface, keeping the microscopic and/or the macroscopic surface topography unchanged. Earlier micro-scale experiments were carried out by Glassmaker et al. (Glassmaker *et al.*, 2007) and demonstrated that the modulation of local stiffness affects crack propagation and enables a *crack trapping* effect. The model material system was a structure with protruding fibrils topped by a thin plate, which was fabricated

---

[1] Fractal sutures are non-Euclidean geometry with a complex shape obtained with simple algorithms, which mimic many hierarchical structures observed in nature.

through molding into lithographically etched silicon. The flexibility of the thin plate was shown to play a major role on crack trapping. A similar trapping effect is exhibited by biological materials such as the base plate of the *Amphibalanus amphitrite*. Hui et al. (Hui *et al.*, 2011) developed an analytical model where the barnacle was considered as a shell capped with a thin base plate. Their model suggested that barnacles with calcareous base shells use a crack-trapping mechanism to enhance adhesion through the modulation of the driving force.

Leveraging on additive manufacturing and bio-inspiration, the present work aims to provide a contribution in the area of toughening strategies for interfaces in layered materials, with particular reference to adhesive joints. In particular, bio-inspired strategies that enable toughening and damage tolerance in adhesive joints and layered structures are herein pursued through an integrated experimental and numerical approach. Through finite element modeling and mechanical testing, the present work aims to reveal the effect of bio-inspired interfaces on the mechanisms of crack propagation and energy dissipation in layered materials. In particular, the work is focused on (i) sutures interfaces, such as those observed biological materials (e.g., bones, nacre or teeth), and (ii) subsurface bulk patterning, such as that reported in the base plate of the *Amphibalanus amphitrite*. Selective laser sintering was deployed to assist the fabrication of the model material system featuring these complex geometries. The overall work, including design and analysis stages, is developed with the aid of a significant modeling effort, carried out in the finite element framework using interface elements based on the Cohesive Zone Model of fracture.

The work and obtained results are discussed over five chapters which are organized as follows: the first chapter is a review of the main strategies reported in related works to improve damage tolerance, with particular emphasis on bio-inspiration. In the second chapter, the materials and methods employed in the experiments are described, with particular emphasis on model material systems employed for the analysis. The third chapter is focused on the obtained experimental results. In particular, attention is placed on the assessment of fracture toughness and overall energy dissipated during crack propagation in the proposed bio-inspired interfaces. In the fourth chapter, the finite element modeling approach is presented and a validated numerical model of the interfaces is obtained. This latter is then used in chapter five to perform a design exploration process and to carry out a parametric investigation. The tantalizing opportunity to tune energy dissipation by modifying the sub-surface architecture of the samples is presented and discussed in detail. Finally, a summary of the main conclusions of this work, and a number of directions in which this work could be extended, are presented in Chapter 6.

.

Chapter 1: Review of toughening strategies for adhesive joints.

Weight reduction in mechanical components represents one of the main goals of the transportation industry since it could play a significant role in the reduction of carbon dioxide emissions (CO_2). During the *Climate Change Conference* (COP21) held in Paris from 30 November to 12 December 2015, the United Nations agreed on a drastic reduction of CO_2 emissions to mitigate global warming. To tackle this challenge, both aerospace and automotive manufacturers are currently pursuing the use of lightweight materials to replace high strength steels and to enable the fabrication of more-efficient and lighter vehicles by reducing body weight. It was demonstrated (Hornung and Hajj, 2009) that, by reducing vehicle weight by 10% it is possible to increase fuel efficiency by up to 6%.

Currently, the main trend in the automotive field is to replace vehicle components previously made with steel by using lightweight alloys, polymers and fiber-reinforced composite materials (Avalle *et al.*, 2010; Mancini *et al.*, 2017). This approach requires finding new strategies to join materials with dissimilar properties such as polymers or composites. In this context, adhesive bonding emerges as a valid alternative to traditional techniques (e.g., fusion or spot welding, bolting, riveting) because it avoids common issues such as those associated with hole drilling, stress concentration, need for shimming. Structural adhesives, conversely, overcome these drawbacks, allows for more uniform stress distribution and the elimination of stress concentration, and improves corrosion resistance and allows for a weight reduction. Several studies demonstrated that joining with structural adhesives has the potential to replace traditional joining techniques in critical load-bearing applications (Barnes and Pashby, 2000; Avalle *et al.*, 2010; Loureiro *et al.*, 2010; He, 2011; Katsiropoulos *et al.*, 2012; Ocaña *et al.*, 2015). Actually, the structural adhesive industry for the automotive industry shows an annual increase rate higher than 7% (He, 2011).

However, adhesive bonding exhibits some disadvantages and, in particular, the main drawback is represented by the low resistance to crack propagation under the action of peel loading, which often results in catastrophic failure. For this reason, many studies in the last decade focused on the development of strategies that enable toughening and damage tolerance. In the following sections, a brief description of adhesive bonding will be presented followed by an extensive analysis of recent related works that report about interesting strategies that enable interfacial toughening and damage tolerance.

1.1. Fundamentals of adhesive bonding

Adhesive bonding consists of the union of two substrates employing an adhesive layer. The adhesive is a non-metallic substance that gives the possibility to joins different kinds of materials together that cannot be connected with the traditional techniques thanks to *adhesion forces* at the interfaces and *cohesive forces* characteristics of the adhesive. The stress components acting on the adhesive layer could be divided into (i) peel tension components on the direction parallel to the adhesive layer, and (ii) shear components on the perpendicular direction. It is clear that the first ones contribute to the development of adhesive-substrates detachment mechanism and, for this reason, the joint design should favor configuration that reduces these components.

For a given load condition, joint resistance depends on adhesive and substrates strength and, above all, by adhesive-substrates interaction. It is possible to identify three different zones that make up the adhesive joint, as shown in Fig. 1.1 and joint failure characteristics depend on the crack propagation zone:

- Cohesive zone: in this zone the adhesive is in his standard condition and exhibit his intrinsic strength;

- Adhesion zone: in this zone, adhesive properties are different due to his chemical interaction with substrates; his macroscopic characteristics are different from the nominal one;
- Transition zone: in this zone, the adhesive characteristics change along the section from the adhesion zone characteristic to the cohesive zone ones.

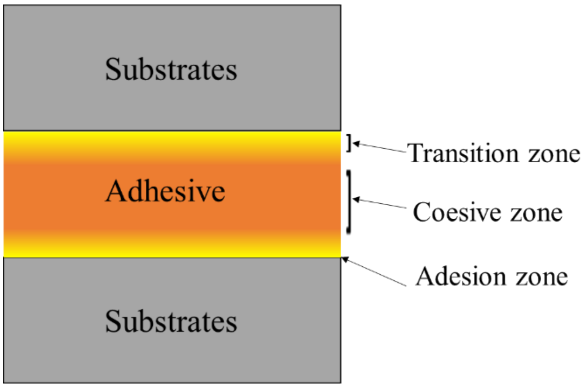

Fig. 1.1: Schematic of an adhesive joint section

When the crack propagates inside the cohesive zone, adhesive joint failure is called “cohesive failure”: this is the condition searched since, in that way, all the adhesive strength is exploited. When the defect propagates in the adhesion zone, it is possible to talk about “adhesive failure” and, finally, when the crack propagates in the transition zone, failure is defined as “near interface failure”.

As explained before, the best joint behavior is obtained when the joint fails in the cohesive zone. To reach this condition, it is necessary to help the interaction between adhesive and substrate that is based on chemical, micromechanics and intramolecular links. The first category of links, i.e., ionic, covalent or metallic bonds, is achieved only founding the right adhesive/substrate combination and is characterized by high strength even if it is sensible to humidity. The intramolecular link, i.e., hydrogen bonds and Van der Waals forces, is a weak connection but contribute significantly to adhesive strength. Finally, micromechanics links are mechanical anchoring system obtained when substrate surfaces are characterized by adequate characteristics. In particular, to exploit this latter mechanism, it is requiring the fulfillment of the following conditions:

- A good surface wettability that allows a satisfactory distribution of the adhesive on the surface;

- Good chemical interaction with adhesive to allow the creation of chemical and intermolecular links;
- High surface stability to ensure a satisfactory lifetime;
- Absence of superficial oxides or impurities that could detach from surfaces inducing adhesive bonding failure.

Very often, to ensure satisfactory surface quality, some treatments are needed before bonding. When the interaction between adhesive and substrate is good, it is possible to obtain adhesive failure that is the best condition.

As explained before, adhesive bonding exhibit some disadvantages such as:

- High values of time to market: adhesive need curing time that could imply more than 24 h;
- Need to adopt surface pre-treatments to guarantee a high quality of the joint;
- Low peel resistance;
- Sensitivity to environmental condition, e.g., temperature and humidity;
- Difficulty to control and eliminate defects into the adhesive bonding layer and low resistance to crack propagation;
- Permanent joint: it is not possible, to remove or repair an adhesive bonding joint.

Between all drawbacks described before, the lack of strength and low resistance to crack propagation are certainly among the major issues that prevent automotive and aerospace to use adhesives more broadly. The strategies that enable an increase of strength and fracture toughness can be classified in strategies that target (a) the adhesive, (b) the interface, or (c) the adjoining substrates. These strategies will be outlined in what follows by reporting on the most recent work published in the literature.

1.2. Toughening strategies that target the adhesive layer

Regarding the adhesive, different formulations are available on the market, optimized for different applications. Adhesives could be classified based on their chemical formulation, e.g., epoxides, acrylic, polyurethanic, on their appearance, e.g., liquid, high-density, film or tape, on their main characteristics, e.g., thermosetting, pressure sensible, and, above all, on their mechanical performances, i.e., structural, semi-structural or no-structural. Considering the circumstances in which there are going to be applied and to operate, it is possible to choose an adhesive that is most appropriate. It is well known that the strength of adhesive joints, provided there is an excellent degree of interfacial interaction, basically depends on the intrinsic cohesive strength of the adhesive. Consequently, it is possible to improve the mechanical behavior of the built-up joints by increasing the strength and fracture toughness of the adhesive layer. This goal can be achieved through the introduction of reinforcing particles, such as rubber particles or nano-particles (Akpinar *et al.*, 2017; Jojibabu *et al.*, 2017; Jakubinek *et al.*, 2018; Jia, Feng and Zou, 2018b, 2018a; Musiari *et al.*, 2018; Sadigh and Marami, 2018; Sánchez-Romate *et al.*, 2018; Brugo *et al.*, 2019). Jakubinek et al. (Jakubinek *et al.*, 2018) studied the effect of boron nitride nanotubes into epoxy adhesive joints. In particular, single-lap joints have been selected for tests, bonded with epoxy adhesive. Different nanotubes weigh percentages have been used, i.e., 0, 1, 2, 5 and 7 %. Adhesive joints fracture toughness increase with the introduction of nanotubes up to 15% more at 1 wt.% while failure surfaces roughness increase meaning that nanotubes inhibit facture. Similarly, Korayem et al (Korayem *et al.*, 2015) evaluate CFRP-to-steel joint resistance with the introduction of carbon nanotube into an epoxy adhesive. Double strap joints have been fabricated with both pure and modified adhesive. SEM analysis of fracture surfaces reveals that the introduction of nanotubes modify the type of interfacial failure for which failure at the adhesive-CFRP interface is more pronounced probably due to higher Young’s modulus on the modified adhesive. Moreover, the ultimate axial strain along with laminates in samples with modified epoxy adhesive is higher than the same value obtained for samples with pure epoxy meaning that nanotubes can transfer more load to substrates. Musiari et al. (Musiari *et al.*, 2018) evaluated fracture toughness improvement using an electrospun polymeric nanomat as a reinforcing network into the adhesive layer through DCB joints tests. Substrates have been realized using 2024-T3 aluminum alloy, bonded with bi-component epoxy adhesive. Two different configurations have been considered: “virgin samples”, i.e., DCB with unchanged adhesive structure and nano-modified sample, i.e., a nanofibrous mat was inserted into the adhesive layer. In particular, the nanofibrous web was pre-impregnated with the adhesive and, after that, it was placed between two metal substrates. Even if crack propagation was at resin-adherent interfaces, the introduction of the nanofibrous mat into the adhesive layer allows improving fracture toughness. Moreover, SEM analysis permits the observation of nanofibers attachment to adherent surfaces and, consequently stretched during crack propagation. This occurrence could be associated with a bridging mechanism that induces crack path deviation, i.e., increase of joint fracture toughness. Jia et al. (Jia, Feng and Zou, 2018b) evaluated the influence of graphene reinforced epoxy adhesive on fracture resistance. Double Cantilever Beam samples have been fabricated with fiber-reinforced polymer (FRP) substrate and using pure epoxy adhesive and modifying it with the addition of graphene nanoplatelets (GNPs). Experimental results demonstrate that Mode-I fracture toughness increase with the addition of nanoplatelets into the epoxy adhesive. In particular, Mode-I fracture toughness modified adhesive with a graphene content equal to 0.25 wt% exhibits an enhancement up to 5 times compared with pure epoxy adhesive. Increasing the graphene content, Mode-I fracture toughness of adhesive decreases due to the aggregation of graphene in adhesive. The mechanical behavior of the DCB joints obtained modifying adhesive was also analyzed using finite element analysis showing a good agreement between experimental and numerical results. Zhu et al. (Zhu *et al.*, 2016) evaluated the effect of the introduction of solder balls into the adhesive layer. Cross-tension samples have been realized with steel substrates and an epoxy-based adhesive. Balls of 0.3 mm diameter have been added into the adhesive layer: Bi-Sn solder was chosen since it melts at a temperature lower than the adhesive cure one. Results demonstrate an increase of strength between 17.5 and 40% with solder addition. Even if the adhesive modification could help to improve joint resistance, acting on substrates allow major flexibility together with the possibility to increase significantly joints resistance. Some strategies available in literature will be discussed below.

1.3. Toughening strategies that target the interfaces

1.3.1. Planar interfaces

Interface modification is referred to as chemical, mechanical and electromechanical actions operate at the microscale with the aim to modify surface characteristics of materials to improve and preserve the bonding strength (i.e., adhesion). Surface treatments range from simple cleaning to chemical attack, mechanical actions such as sandblasting, lapping, since surface micropatterning and micro structuring.

The effectiveness of one treatment over another is not absolute but everything depends on the constituent material of the substrates and the characteristics of the applied adhesive. Numerous studies have turned their attention to surface treatments concerning the type of material and adhesive. Actually, chemical and mechanical treatments are really diffused in many industrial fields to improve adhesive joints fracture toughness and many studies demonstrates the effectiveness of these strategies (A. F. Harris and Beevers, 1999; Sancaktar and Gomatam, 2001; Borsellino, Di Bella and Ruisi, 2009; Goglio and Rezaei, 2013; Rudawska, 2014; Boutar *et al.*, 2016). *Chemical treatments* are widespread since they help the creation of a chemical bond between substrates and adhesive enabled the improvement of the work of separation needed to sever the joints (Lee and Qu, 2003; Lunder *et al.*, 2004). This kind of surface treatment shows a good influence on adhesive joints strength subjected to a moist environment (Goglio and Rezaei, 2013). However, in the last years, because of their impact on the environment, a significant research effort has been carried out to replace traditional chemical treatments with cleaner alternatives. *Mechanical treatment*s, such as the classical sandblasting helps to enhance joint fracture toughness thanks to high-frequency micro-scale asperities (A. F. Harris and Beevers, 1999; Sancaktar and Gomatam, 2001; Rudawska, 2014; Boutar *et al.*, 2016). Increase surface roughness could help the interaction between adhesive and surfaces thanks to micromechanical interaction. However, this improvement is not a direct consequence since it depends also by the ability of the adhesive to penetrate surface asperities. In particular, Boutar et al. (Boutar *et al.*, 2016), studied the surface characteristics and, in particular, surface roughness in relation with adhesive joints strength using Single Lap Joints (SLJ). Samples have been realized with different materials, i.e., aluminum and copper, and one adhesive type, mono-component polyurethanic adhesive. The surfaces have been treated using different abrasive papers. It was found that an increase in surface roughness improves joint strength, in particular, the strength increases up to a point where a further increase in roughness causes the strength to decrease. This result suggests that there is not a direct correspondence between micro-scale asperities and joints resistance as demonstrates in other studies (A. F. Harris and Beevers, 1999; Sancaktar and Gomatam, 2001; Rudawska, 2014). A method that is used as a valid strategy to improve adhesive joints strength is pulsed laser irradiation (Baburaj *et al.*, 2007; Alfano *et al.*, 2011; Rotella *et al.*, 2015; Moroni *et al.*, 2018; Musiari *et al.*, 2019; Tao, Alfano and Lubineau, 2019). Pulsed lasers represent a useful tool for surface cleaning since it is able to eliminate all contaminants from the surface without adversely affect the base material. Moreover, it could be used to modify surface topography improving roughness, wettability, and hardness (Rotella, Alfano and Candamano, 2015). Rotella et al. (Rotella *et al.*, 2016) evaluated the influence of laser ablation on T-peel and SLJ joints with quasi-static tests. Samples substrates have been realized with DP600 steel bonded with two different epoxy adhesives. Laser treatment was compared with sandblasting and ultrasonic bath cleaning. Results demonstrate an increment of shear strength up to 15% for SLJ joint with ablated surfaces and up to 100% for T-peel joints with the same surface treatment. The same study demonstrates also a higher resistance of these joints to accelerated aging.

Laser ablation could also be used to locally modify surface characteristics to create micropatterns (Tao, Alfano and Lubineau, 2018). In particular, the authors analyzed the effect of laser irradiation on the mechanical behavior of DCB joints. Joints have been fabricated using carbon fiber reinforced polymer (CFRP) substrates that were irradiated using a pulsed CO_2 laser system. Untreated surfaces and classical peel-ply have been used as a reference. Mechanical test results allowed to identify the impact of laser pre-treatments on the Mode-I fracture toughness of DCB joints. A library of surface pre-treatments suitable for the CFRPs was identified. Subsequently, the individual surface pre-treatments were properly combined to generate patterned interfaces with spatially varying fracture toughness, as shown in Fig. 1.3(a). The proposed patterning strategy enabled the generation of multiple adhesive ligaments in the wake of the growing crack, with a consequent increase in strength and fracture toughness of the DCB adhesive joints. In particular, the toughness was even higher than that predicted by combining the toughness of the individual treatments with the classical rule of mixtures.

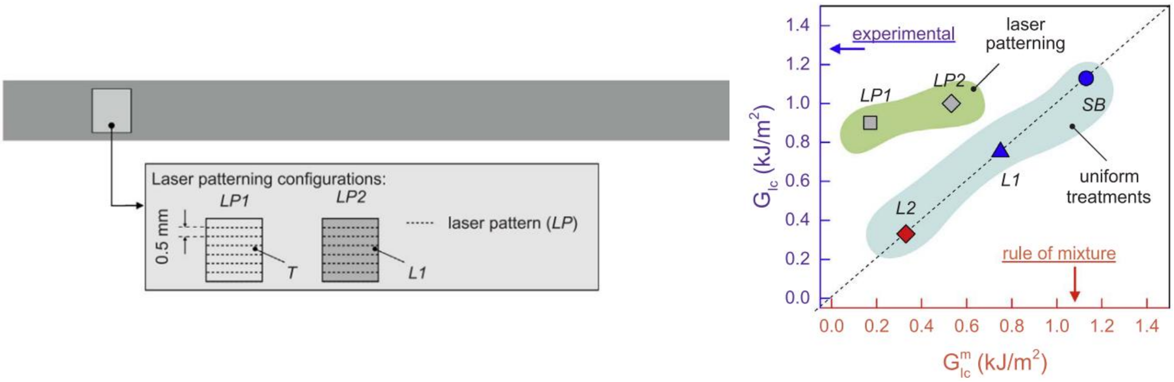

(a) (b)

Fig. 1.2: (a) Schematic of two laser patterned surface and (b) comparison between fracture toughness value obtained experimentally (y-axis) and using the rule of mixtures. L2: fully exposed fibers; L1: laser cleaning; SB: sand-blasting (Tao, Alfano and Lubineau, 2018).

A similar approach is to create interfacial patterns by using mechanical or chemical treatments as suggested in other works (Chan, Ahn and Crosby, 2007; Budzik, Jumel and Shanahan, 2012; Malkin, Trask and Bond, 2013; Ranade *et al.*, 2018). Chan et al. (Chan, Ahn and Crosby, 2007) demonstrate the influence of surface patterning in order to evaluate the role of a periodic variation of adhesive strength of the interface. Tests have been conducted on 90-degree peel adhesive joints with soft elastomers substrates bonded on a glass substrate. The pattern was created by chemical treatments with a strong phase obtained with reactive silane coating, i.e., r-SAM, and a weak phase obtained with passive silane coating, i.e., i-SAM. Three different types of pattern shapes have been chosen, i.e., circular, triangular and lines and all of them have been realized with r-SAM regions on i-SAM surfaces and vice versa. Some tests have been conducted on unpattern samples and results have been then compared with data obtained for patterned substrates. Results have been evaluated considering the average peel force surface density of r-SAM zones, i.e., independently by channel shape or dimensions. It was found that with a well-defined pattern, it is possible to increase adhesion strength and it was also observed a dependence by pattern shape meaning that the other mechanisms occur during tests, i.e., the density of r-SAM zone is not significant to describe joints behavior. In particular, the best results have been obtained with a circular reactive pattern with an increase of 115% if compared with unpattern reactive surfaces. This phenomenon is due to a change in the contact line, as demonstrated in Fig. 1.3 that increases the resistance for the crack to propagate and, for that, additional energy is required to allow crack propagation. This mechanism is common for all pattern shapes but, for the circular ones, the contact line is blunt more than for the other geometries and, for that, this configuration seems to be more efficient.

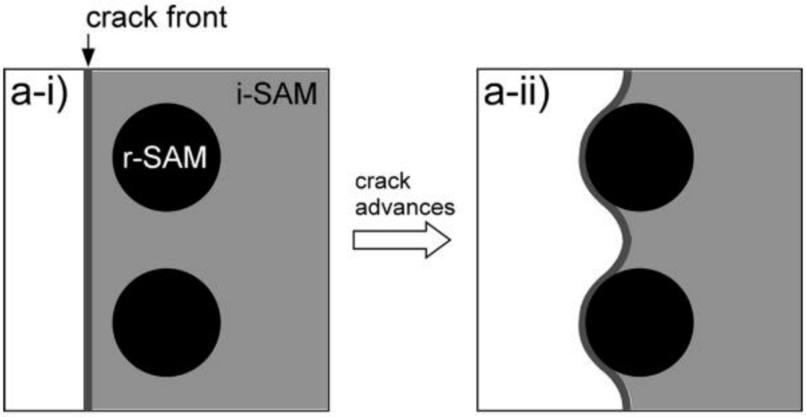

Fig. 1.3: Crack front deflection due to reactive pattern on bonded surfaces as observed by Chan et al. (Chan, Ahn and Crosby, 2007).

1.3.2. Non-planar interfaces

Results obtained by changing surface characteristics demonstrate that variation of adhesive strength along interfaces could improve significantly the joint strength. This objective could be also obtained creating surface micropatterns featuring protruding structures that favor mechanical interlocking (Sitti and Fearing, 2003; Reddy, Arzt and Del Campo, 2007; Kim *et al.*, 2010; Suzuki *et al.*, 2013; Wang *et al.*, 2015; Yukimoto, Matsuzaki and Todoroki, 2015; Matsuzaki, Tsukamoto and Taniguchi, 2016). Several strategies were inspired by the excellent adhesion properties shown by biological materials such as insects, spiders, and geckos (Packham, 2010; Jagota and Hui, 2011). Several works addressed dry adhesion (Sitti and Fearing, 2003; Reddy, Arzt and Del Campo, 2007). However, surface micropatterns could also facilitate the interaction between an adhesive and the substrates. Kim et al (Kim *et al.*, 2010), studied the effect of surface micropatterning on the polymer-steel interface. A microline-patterns perpendicular to crack propagation direction was created on the steel surface by chemical acting material with Nital, i.e., a solution obtained with a mixture of nitric acid and ethanol. Two different samples geometries have been selected: a bi-material end-notched flexure (ENF) test was used for mode-II and a single-leg bend (SLB) test for was chosen for mixed-mode. Results demonstrate that the adhesion strength increase with increasing surface roughness obtained with surface patterning. This increment was related to a mechanical interlock mechanism that involves also plastic deformation. Suzuki et al. (Suzuki *et al.*, 2013) demonstrate the improvement in fracture toughness of adhesive joints by imprinting microstructures on the composite surface. The final target is to modify the loading mode without changes in loading condition but just acting on defect path at crack tip moving from Mode-I to Mode-II since in the last condition crack needs an increment of the energy to propagates. This was obtained by imprinting a square-wave microstructure on silicon mold that was then used to transfer the pattern to composite. The influence of pattern size and shape on joint behavior was evaluated thanks to finite element simulations and results have been compared in terms of apparent fracture toughness, i.e., the average energy consumption per unit crack growth. In particular, it was found an increase in his value by increasing both pattern height and pattern width even if, this latter seems to have a higher influence on joint behavior. Overall, fracture toughness increases by a local modification of loading condition reaching a value more than five times higher than the reference one, i.e., no modifications. A similar result was also obtained by applying mixed-mode loading conditions (Yukimoto, Matsuzaki and

Todoroki, 2015). Surface micropatterning has been used also to create mechanical interlocking as in Matsuzaki et al. work (Matsuzaki, Tsukamoto and Taniguchi, 2016) as shown in Fig. 1.4. In particular, undercut micropattern have been created on PP parts: PP was heated until the crystalline melting point, inserted between a sliding table with a micropattern and, then, cooled and separated from the mold. Different micropattern shapes have been chosen by varying the undercut angle and the effect was evaluated by butt-joints tensile tests. Results, as shown in Fig. 1.4, exhibit an increase of adhesive strength with the increase of undercut angle. In particular, the best result was obtained for a 25° undercut angle with a 1.7 times higher value for the average strength. This result verified that the surface modification by imprinting interlocking micropattern is a valid strategy in improving adhesive joint strength at low production cost.

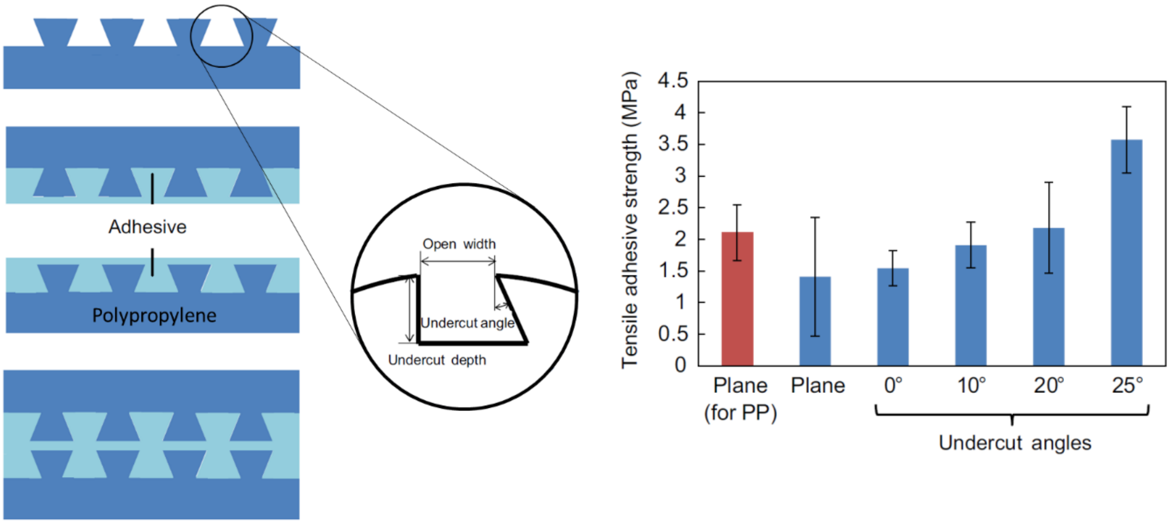

(a) (b)

Fig. 1.4: (a) Interlocking mechanism and (b) tensile adhesive strength values in function of undercut angle variation (Matsuzaki, Tsukamoto and Taniguchi, 2016)

These studies demonstrate that interface modification is a useful instrument for improving the interaction between adhesive and substrates and, for that, joints fracture toughness. By changing the dimension of surface modification, we move from micro to macro scale. In addition, in this approach, natural materials inspired several works that used biomimetic structures. The main idea is to modify the crack propagation mechanism by tailoring the crack path. Interfaces in natural materials are characterized by complex structures, as observed in bones, teeth or shells, e.g., ammonoid, turtle or (Saunders, Work and Nikolaeva, 1999; Jaslow, 2000; Shahar *et al.*, 2009; Li, Ortiz and Boyce, 2011; Porter *et al.*, 2017). These kinds of structures are commonly called *sutures* and they are useful for many mechanical functions. Some examples of this kind of structure available in natural materials are visible in Fig. 1.5. Suture complexity helps to improve its efficiency introducing also an interlocking mechanism, and improving the stress transfer, that varies from a peel-dominated to shear-dominated one.

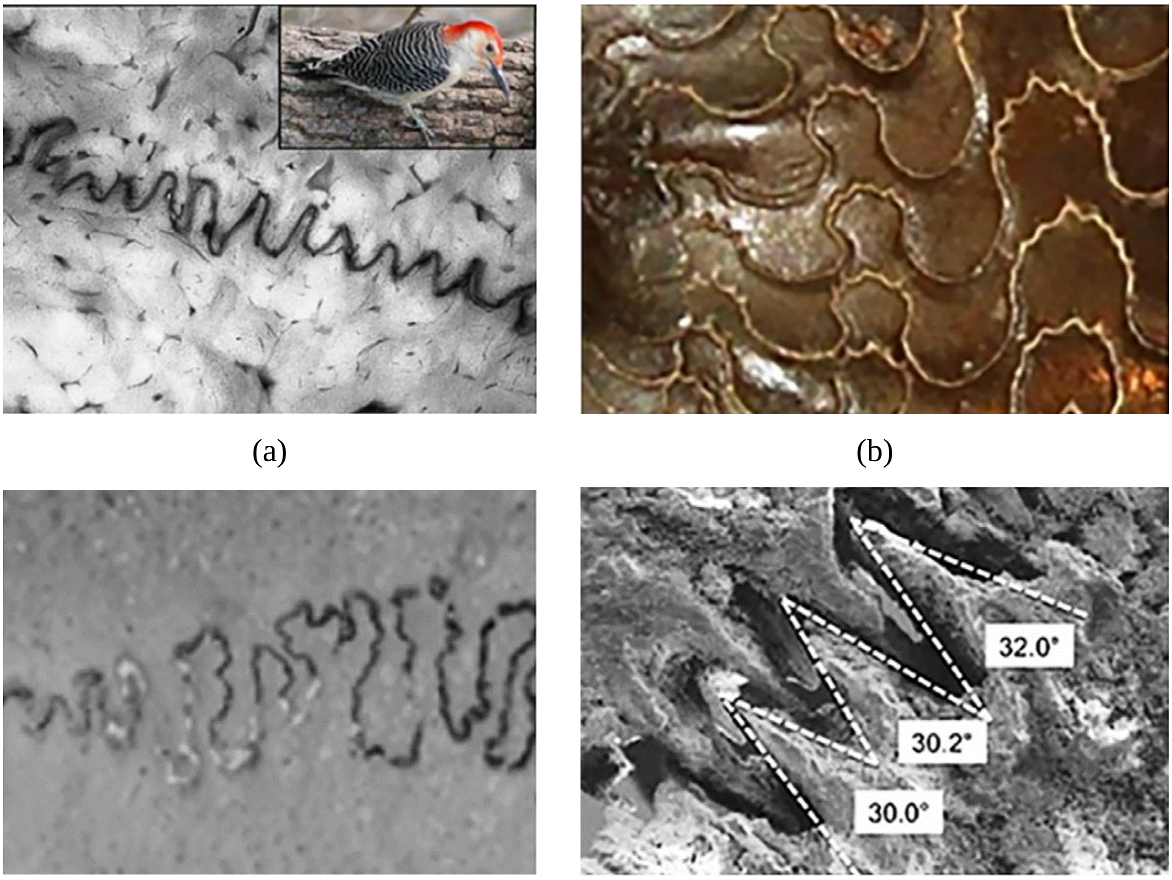

(a) (b)

(c) (d)

Fig. 1.5: Example of suture that could be observed in nature: (a) red-bellied woodpecker beak, (b) Ammonite shell, (c) Pan troglodytes' cranium and (d) sea-turtle shell. All images have been adapted from (Malik, Mirkhalaf and Barthelat, 2017)

In the last years, a lot of works have focused their attention on the possibility to adopt architected interfaces to improve joints performances (Erica Lin *et al.*, 2014; Ghazlan, Ngo and Tran, 2015; Cordisco *et al.*, 2016; Liu *et al.*, 2017; Malik, Mirkhalaf and Barthelat, 2017; Khoshhesab and Li, 2018; Maloney and Fleck, 2018). Maloney and Fleck (Maloney and Fleck, 2018) designed a square-wave architecture interface and studied his influence with butt-joints. In particular, it was studied tensile traction-displacement response by varying adhesive layer thickness and square-wave amplitude. It was also chosen to carry on tests on benchmark butt joints samples, i.e., with flat interfaces, and single lap joints since square-wave joints response could be obtained as a combination of these two geometries. Results demonstrate that the peak load depends on joints amplitude: as this parameter increase, the peak load value grows even if, stress concentration at square-wave corners increases too. It was also observed a change into failure mechanism: after an initial linear response, defects start growing in correspondence of square wave corner making response became non–linear. These defects, characterized by a cylindrical shape, propagates into the shear zone and, after that, their coalescence induces joints failure. These mechanisms produce an increase in overall energy request for failure. Cordisco et al. studied fracture along sinusoidal interfaces (Cordisco *et al.*, 2016). Double Cantilever Beam specimens have been realized using aluminum substrates where the sinusoidal interface was obtained by wire EDM. Different sinusoidal shapes have been used in order to evaluate the effect of wavelength variation on joints fracture toughness also in comparison with flat DCB joints. Results demonstrate a translation towards higher load values with wavelength reduction accompanied by a delay in crack propagation mechanism. It is important to consider also that interfaces shape modify loading conditions at the crack tip introducing Mode II contribution. Numerical simulations have also confirmed results.

Natural sutures are characterized by high irregularity and their effect was studied by Liu et al. (Liu *et al.*, 2017). In particular, the authors studied the influence of suture complexity on mechanical properties. They formulate an analytical model to represent irregular morphology of suture with a random wavelength and amplitude. Models prediction was also confirmed by numerical simulation. A schematic of suture geometry adopted for the analytical model is represented in Fig. 1.6. Eleven different models have been designed with different levels of irregularity, i.e., no irregularity or irregularities percentage between 10-50%. Results demonstrate that, by increasing irregularities percentage, the strain to failure increases significantly while the tensile stiffness is constant. Furthermore, morphological irregularities provide an increase in damage tolerance by increase ductility with a bare reduction in strength. This latter reduction could be overcome by decrease the tooth tip angle. These results demonstrate the efficiency of irregularities in sutures in nature explained why this kind of interface is so widely diffuse in nature.

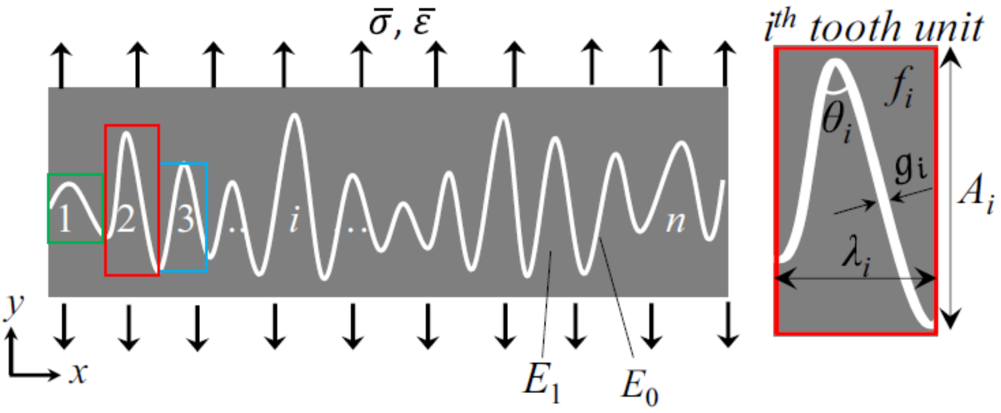

Fig. 1.6: A schematic of suture and their complexity (Liu et al., 2017)

Suture complexity is also due to the presence of hierarchical structures as could be observed in Fig. 1.5 (b) and (c). This approach helps to obtain also an interlocking effect that allows achieving high mechanical performance such as a high toughening effect. A lot of studies design hierarchical structures such as structure proposed by Khoshhesab end Li (Khoshhesab and Li, 2018). The authors studied the interlocking phenomena in biological sutures by using Koch fractal geometry. Fractal sutures are non-Euclidean geometry with complex shapes obtained with simple algorithms and, in particular, the Koch curve was proposed by Helge von Koch by an iterated function system. The structure of the Koch curve was described by friction coefficient μ and four different geometry parameters as shown in Fig. 1.7: (i) N, i.e., the number hierarchy; (ii) r_n, i.e., the radius used to avoid stress concentration, needed to take into account imperfection due to fabrication process; (iii) a_0, i.e., the dimension of the Koch curve when N=0, that allow to identify the total length of each Koch fractal arc for different value of N as $L_N = a_0 (4/3)^N$; (iv) g, i.e., a small gap between two edges of top and bottom parts.

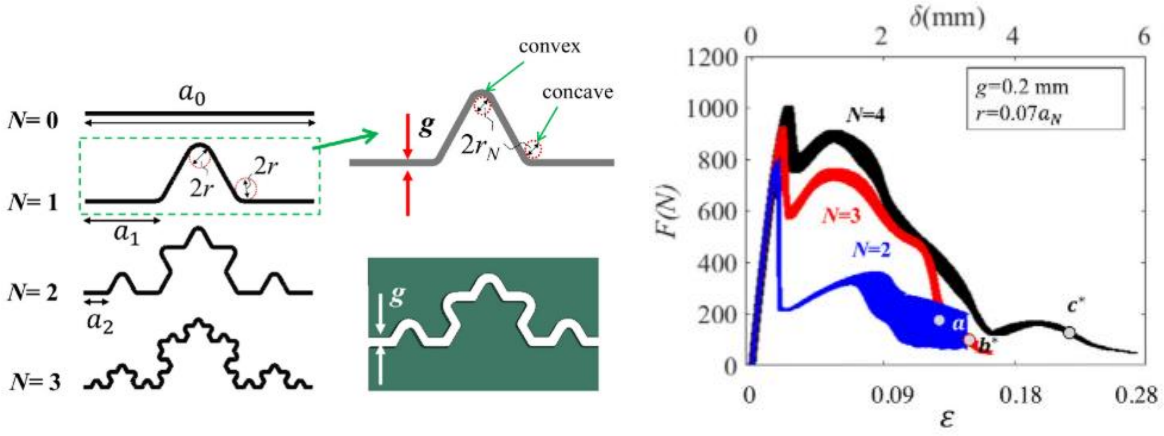

(a) (b)

Fig. 1.7: (a)Koch fractal geometry used to create 3D printing sample and (b) Load-displacement curves obtained during experimental tests (Khoshhesab and Li, 2018).

Both numerical simulation and experimental tests on 3D printed samples were carried out in order to analyze the mechanical performances of the fractal suture. As it was found that increasing the number of iteration allows increasing the fracture toughness by orders of magnitude, three different values of N have been chosen, i.e., N= 2,3 and 4. Load-displacement curves obtained with both experimental tests and numerical simulation show how increasing curve hierarchy enhances the load peak even if the difference between the peaks obtained with N=2 and N=3 is more significant than between N=3 and N=4 (Fig. 1.7). This improvement depends on the increase in the contact area and on the interlocking effect.

In order to deeply understand the influence of each geometry parameter on the fractal interlocking, an analytical model was built based on experimental and numerical results. The perfect model obtained choosing $g=r_n=\mu=0$ to demonstrate that theoretically is always possible to enhance the load peak by increasing N value. However, it is impossible to assess the perfect condition and, introducing non zero value for the above variables, the initial slope of the load-displacement curve increase until N=4 and, after that, it decreases and, eventually becomes zero. This result demonstrates that the mechanical response of Koch fractal geometry is strictly dependent on design imperfection and their influence could become dominant for the high value of N. Therefore, considering the imperfection, it is possible to identify the optimum value for the number of hierarchy that allows maximizing the load peak value.

Lin et al. (Erica Lin *et al.*, 2014) evaluate experimentally influence of hierarchical suture interface on mechanical performance using 3D printing ability to create complex structures.

Samples have been realized using acrylic-based polymer for substrates and a rubber-like material for the interfacial layer. Sutures have been designed with four geometries, i.e., anti-trapezoidal, rectangular, trapezoidal and triangular, and three orders of hierarchy, i.e., N=1, 2 and 3. Results have been compared in terms of stiffness, strength and fracture toughness. Stiffness grows by increasing order of hierarchy reaching the maximum value for triangular geometry, i.e., one order of magnitude, even if all interfaces allow improving stiffness if compared with a flat interface. Tensile strength increase for triangular and trapezoidal for N=2 and decrease for the other two geometries. Instead from N=2 to N=3 all samples exhibit an increase of tensile strength. This enhancement was attributed to changes in the fracture mechanism. In fact, the failure mechanism occurred by interfacial failure, minor tooth failure, and major tooth failure. A combination of these three mechanisms that was observed into N=3 sutures, contribute to an overall increase of the tensile strength of the interfaces. Finally, tensile toughness differs for each geometry reaching the maximum values at a different hierarchical level, i.e., at N=3 for triangular and trapezoidal shape, at N=2 for rectangular shape and at N=1 for anti-trapezoidal ones. Overall, the authors found that increasing suture complexity by less than six times, stiffness increases by 50 times while strength and toughness by 5 times. The best solution was found using triangular suture interfaces. Malik et al. (Malik, Mirkhalaf and Barthelat, 2017) designed bio-inspired "jigsaw"-like suture and analyzed their pullout response. This suture geometry was evaluated analytically, numerically and experimentally varying the pull-out angle and, in particular, evaluating energy dissipation, tensile stress, and stiffness. Results demonstrate that resistance to pull-out is enhanced by increasing pull-out angles and friction coefficient; the highest tensile stress is due to frictional traction that occurs due to contact between tabs. Optimization procedure reveals that maximization of stiffness, strength and energy absorption could be obtained reducing the friction coefficient and increasing interlocking, i.e., higher pull-out angles. Furthermore, toughness increases 45 times if compared with plain samples.

1.4. Toughening strategies that target the bulk substrates

Natural composites are characterized by multilayer structures obtained by the alternation of stiff and strength materials alternated by soft layers. The same materials are very often characterized by high resistance and/or extraordinary mechanical properties, e.g., bones, teeth or nacres

(Dunlop and Fratzl, 2010, 2013; Wegst *et al.*, 2015; Zhang, Heyne and To, 2015). The high toughness of thus biological materials is interesting and inspired the design of artificial composites with these characteristics (Smith *et al.*, 1999; Evans *et al.*, 2001; Okumura, 2005; Libonati *et al.*, 2016). The reason for the toughness increase in these composites was found in the deflection of the crack path at weak interfaces as observed in the previous section for surface micropatterning. A valid approach to obtain this goal is to obtained composites by overlapping layers with different stiffness (Fratzl *et al.*, 2007; Launey and Ritchie, 2009; Kolednik *et al.*, 2011, 2014; Beese *et al.*, 2014). Launey et al. (Launey and Ritchie, 2009) analyzed the principal features of different kinds of materials, i.e., metals, polymers composites and ceramic, in comparison with biological materials, i.e., bone, nacre, and wood that exhibit higher mechanical characteristics thanks to hierarchical and/or complex structures. The key to obtaining artificially behavior similar to biological materials is to control composite structure to create complex structures also able to adapt themselves to different environmental conditions. Valid progress made in that direction is the creation of a nacre-like or bone-like structure by overlapping stiff ceramic layers with very thin layers of soft lubricant polymeric layers and, in that way, it was found a tougher effect. Kolednik et al. (Kolednik *et al.*, 2011) compared, by finite elements simulations, driving force, i.e., J_{tip}, obtained for crack growth into homogeneous material with the same value obtained for defect propagation into composite obtained by overlapping two different layers obtaining a periodic variation of Young's modulus. Results demonstrate that the driven force of homogeneous material is characterized by a linear increase with the crack dimension growth; moreover, the parameter evolution into composite shows sudden drops when the crack reaches the middle of the softer layer and, after that, it starts to grow again as shown in Fig. 1.8 (b). The authors created an analytical model to design this kind of material and, in particular, they found that, if the low value of Young's modulus is equal to zero, the crack is unable to propagate, i.e., crack goes into a void. It is clear that this effect could be exploited when the crack propagates along the direction perpendicular to Young's modulus variation.

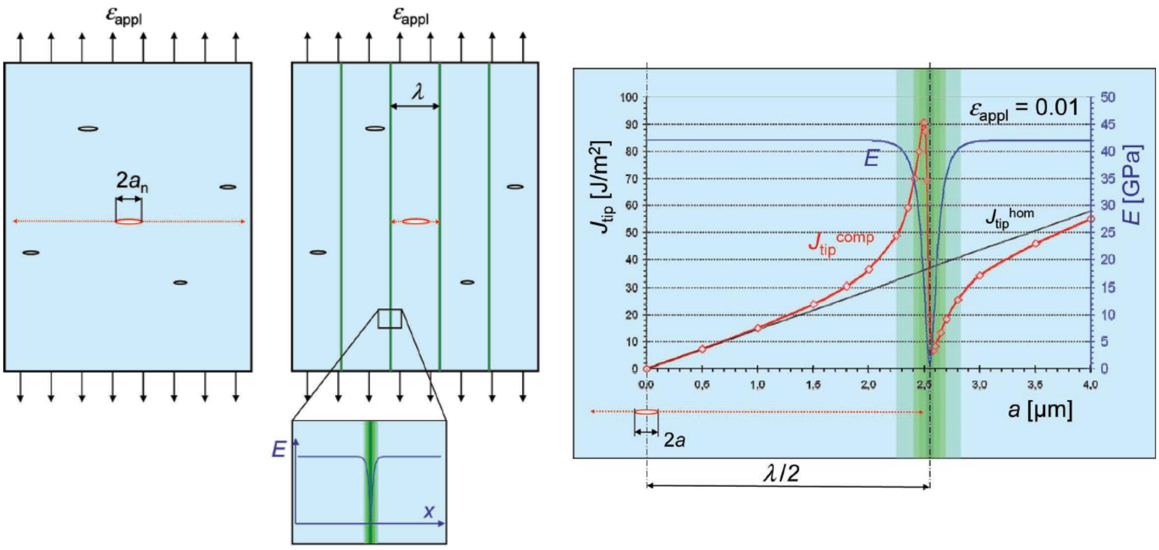

(a)

(b)

Fig. 1.8: (a) A schematic of composite material realized with periodic variation of the Young modulus and (b) comparison of driving force evolution obtained on homogenous material (black curve) and composite material (red curve) (Kolednik et al., 2011).

The same authors studied also other types of materials with E variation (Kolednik *et al.*, 2014). In particular, fracture toughness gets for composite materials obtained with the periodical variation was compared with a sinusoidal variation of Young modulus and with a discontinuous variation for the same parameters. Results demonstrate that composite with discontinuous E variation exhibit higher fracture toughness values if compared with the same composite obtained with a periodical variation. However, in all configuration, the improvement is more significant as smaller is the soft layer thickness since his presence must not affect the global resistance of the composite. Beese et al. (Beese *et al.*, 2014) followed the same approach with composite realized by the alternation of the graphene oxide layer and polymethyl methacrylate layers, i.e., GO and PMMA respectively. GO layer thickness was kept constant while PMMA was varied in order to evaluate his influence. Different composite performances have been evaluated by comparing driving force at crack tip obtained with finite element simulations. Crack propagation into materials shows an irregular mechanism due to the arrest of its growth at PMMA/GO interfaces as observed previously. This improvement becomes more significant with PMMA thickness reduction as observed above by Kolednik et al (Kolednik *et al.*, 2014).

Stiffness modulation could be obtained not only by the design of composite materials with the overlap of different compliance materials; another valid way is to achieve the same results is removing or adding material in some specific areas. For example, Xia et al. (Xia *et al.*, 2013) studied the adhesion of a thin substrate with stiffness heterogeneities, i.e., adhesive tape, on rigid substrates, i.e., plastic substrates.

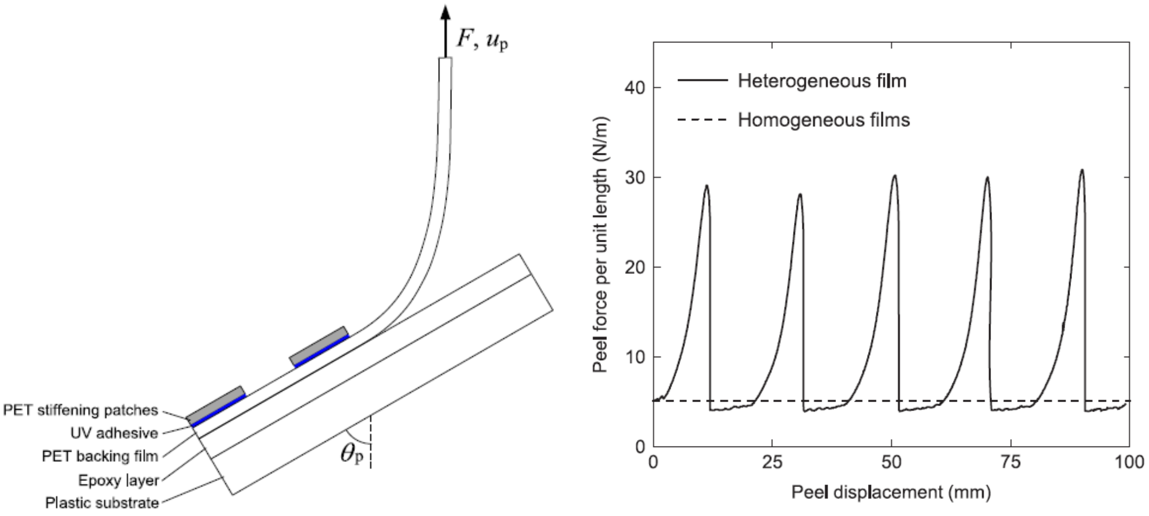

(a) (b)

Fig. 1.9: (a) Peel test configuration conducted on heterogeneous thin film and (b) load-displacement fluctuation related to stiffness variation (Xia et al., 2013).

In particular, they compared experimental results with theoretical prediction work out for different joints conditions, i.e., homogeneous film, two segments heterogeneous film and periodically heterogeneous film with a large or small period. Tests allow the evaluation of peeling force by considering different peeling angle as shown in Fig. 1.9. Results demonstrate that the introduction of heterogeneities into sample stiffness produces load fluctuation. Specifically, when the crack tip is approaching the stiff region, load increases reaching a peak at compliant/stiff region interface and, after that, when the crack tip is inside the stiff region, load drops off suddenly. After that, the cycle is repeated (see Fig. 1.9). Overall, stiffness modulation creates an increase of the peel force due to rapid variation in the elastic energy stored when crack tip approaches stiff regions since a significant aliquot of work done is spent for bending these regions. Best enhancement is obtained with a periodically heterogeneous film with the largest period.

Similar behavior was also observed by removing material from substrates. A lot a studies demonstrates as this approach could increase adhesion strength of this structures obtained with driving force modulation(Glassmaker *et al.*, 2007; Majumder, Ghatak and Sharma, 2007; Shen, Hui and Jagota, 2008; Vajpayee *et al.*, 2009; Afferrante, Carbone and Demelio, 2012; Arul and

Ghatak, 2012). For example, Afferrante et al. (Afferrante, Carbone and Demelio, 2012), studied the energy release rate variation, i.e., G, into a structure obtained by removing material from substrates creating parallel channels as reported in Fig. 1.10. In particular, they focused their attention on the modification of channels' geometrical parameters and how that could change driving force evolution. The problem was studied using numerical simulation. It is important to notice that this value was normalized respect value obtained for a flat surface, i.e., no channels. It was obtained a periodical variation of this parameter during crack propagation (Fig. 1.10). Its fluctuation means it could be possible reaching a condition in which the driving force is lower than the adhesive energy and, consequently, defect growth will be arrested. This effect occurs when the structure is deformable enough, i.e., the G function has a minimum. On the other hand, when G increase, the crack propagates very fast, i.e., the driving force is higher than the adhesive energy. Geometrical features influence compliance and, for that, will influence the minimum value of G. Best results have been obtained by extending the distance between channels and reducing the thickness of the base plate. Overall, the increase of compliance of the structure allows the transfer of energy from crack tip to outlying areas, delayed crack propagation. This mechanism of arrest and then fast propagation of crack related to driving force fluctuation is defined as "crack trapping".

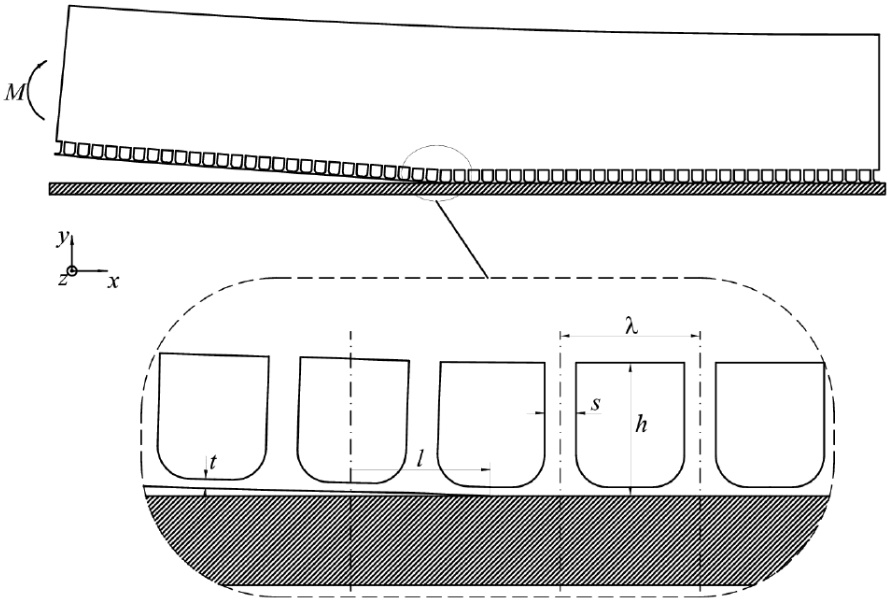

(a)

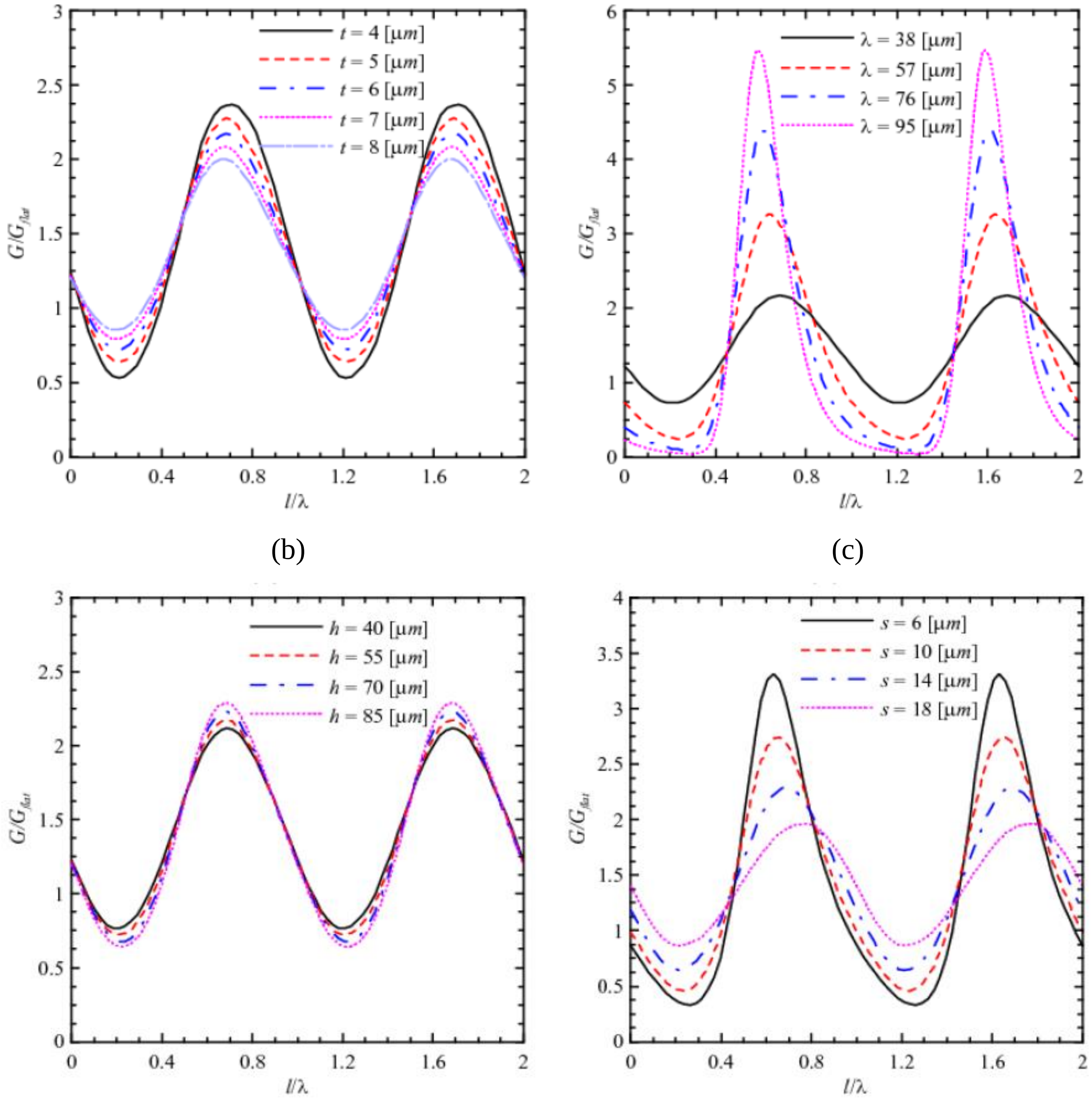

(b) (c)

(d) (e)

Fig. 1.10: Schematic of geometry used during the numerical simulation and driving force evolution obtained modifying geometrical features: (b) thickness of the base plate (c) channels period (d) channels height (e) distance between channels (Afferrante, Carbone and Demelio, 2012).

Similar geometry has also been studied by Glassmaker at al. (Glassmaker *et al.*, 2007). The authors created a fibrillary sample, similar to the structure described above, molding polydimethylsiloxane into lithographically etched silicon. Samples have been characterized using both DCB tests and indentation with a spherical indenter pressed into contact with a constant displacement rate. Also, in this case, driving force evolution shows some fluctuation as a function of crack tip position allowing to reach adhesion energy release rate values up to nine times higher than the reference samples. Indentation tests show changes into residual indent and an increase in hysteresis area meaning a higher request of energy to deform sample. As for the other toughening method, also in this case nature offers an example of the efficiency of this kind of structure such as Barnacles (Hui *et al.*, 2011; Raman and Kumar, 2011; Burden *et al.*, 2012; Wang *et al.*, 2017).

(a) (b)

Fig. 1.11: Group of barnacles and their ability to attach on rocks (Acorn Barnacle, no date) and (b) Barnacle’s picture (Kamino, 2013).

Barnacles are small crustaceans that live in shallow and tidal waters Fig. 1.11. These animals are able to attach themselves to submerged surfaces by secreting proteins that cure into a thin layer similar to cement. His ability to attach itself to different kinds of surfaces into an “unfriendly” environment is very interesting. The barnacle *Amphibalanus Amphitrite* shell structure was analyzed using an X-ray radiograph and tomograms by Hui et al. (Hui *et al.*, 2011). These images reveal the presence of radial channels into the base plate of the animal, as shown in Fig. 1.12 (Hui *et al.*, 2011). Their detachment mechanism was studied through analytical modeling. Results demonstrated that barnacles resist crack propagation through a crack trapping mechanism. The driving force is characterized by fluctuation that allows crack propagation arrest.

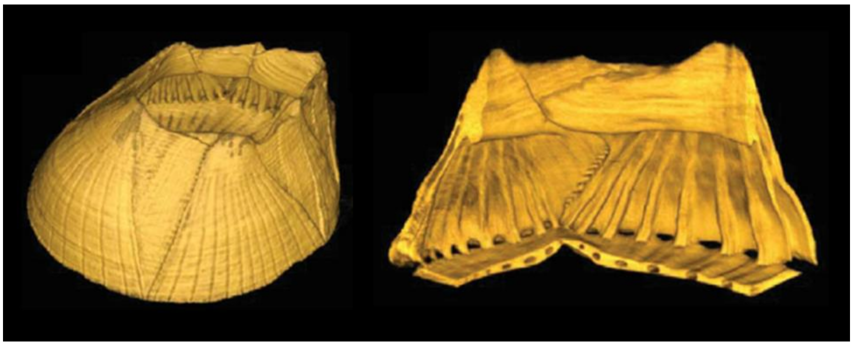

(a)

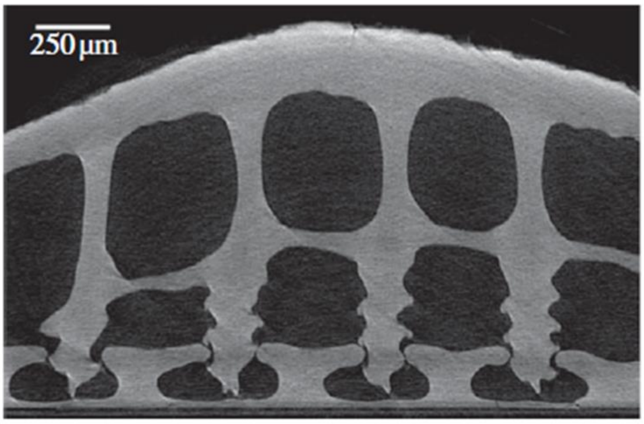

(b)

Fig. 1.12: Volume-rendering tomograms of *Amphibalanus* Amphitrite and (b) 2D tomogram of barnacle shell section showing longitudinal channels in the base plate. All images have been adapted from (Hui et al., 2011).

1.5. Thesis scope and organization

The recent literature works discussed above indicate that a valid approach to improve strength and fracture toughness of adhesive joints is to modify the mating substrates by introducing a local variation of stiffness, or elastic heterogeneities, or the global shape of the mating surfaces. Biomaterials provide a multitude of examples that can inspire actual engineering applications. In this work, the attention was mostly focused on two fundamentals bio-inspired strategies that can potentially enhance toughness and damage tolerance in adhesive joints. That is the use of patterned interfaces resembling the suture observed in ammonite shell, and the use of sub-surface bulk patterns, such as those observed in the base plate of the *Amphibalanus Amphitrite*. Both strategies have been fairly overlooked, especially from the experimental point of view. The actual geometries of the structures analyzed in this work have been extracted from the experimental data presented earlier in this Chapter. In particular, to assess the effect of sutures on crack propagation, it was chosen a model material system consisting of a sinusoidal interface in which the main dimensions, i.e., amplitude and wavelength, have been determined to reproduce the actual amplitude/wavelength ratio observed in the above biomaterials. Similarly, the effect of subsurface channels inspired by the barnacles' base plate has been analyzed. For sample fabrication, the aspect ratio of the channels with respect to the base plate thickness has been chosen in a way that it matches the experimentally observed one.

To probe the response of these bio-inspired interfaces, DCB adhesive joints have been fabricated with the aid of additive manufacturing (i.e., 3D printing). Thanks to the ability to build complex geometries, 3D printing represents a suitable platform for the experimental analysis of bio-inspired materials. Experimental tests on DCB joints have been conducted to understand the role of channels and sinusoidal interfaces during crack propagation. The experimental work comprises mechanical testing, and high-resolution imaging carried out in-situ to resolve the mechanics of crack growth. The experimental effort is augmented with an extended computational analysis that relies on the use of cohesive zone modeling in the finite element framework. On the one hand, the numerical modeling approach undertaken aims to support a critical appraisal of the mechanisms of failure observed experimentally. On the other hand, the physically validated model will be used to perform a parametric investigation that aims to fill the dearth of knowledge in this field and bring forward alternative solutions that can improve even further the damage tolerance capabilities of the proposed interfaces.

The results of such a research effort could facilitate the transferability of these strategies to actual adhesive joints used in high-end products in automotive and aerospace. At the same time, developing suitable bonding strategies for 3D printed components is interesting of its own. Reliable adhesive bonding can help in overcoming the issues associated with the limited build volumes of current 3D printers. The work is organized in chapters as follows: in the next chapter, i.e., the second chapter, the materials, and methods employed in the experiments are described, with particular emphasis to model material systems employed for the analysis. The third chapter is focused on the obtained experimental results. In particular, attention is placed on the assessment of fracture toughness and overall energy dissipated during crack propagation in the proposed bio-inspired interfaces. In the fourth chapter, the finite element modeling approach is presented and a validated numerical model of the interfaces is obtained. This latter is then used in chapter five to perform a design exploration process and to carry out a parametric investigation. A tantalizing opportunity to tune energy dissipation my modifying the sub-surface architecture of the samples is presented and discussed in detail. Finally, a summary of the main conclusions of this work, and a number of directions in which this work could be extended is presented in Chapter 6

Chapter 2: Materials and methods

2.1. Materials

In order to study crack trapping effect at the macro-scale, bio-inspired structures have been introduced in adhesive bonded Double Cantilever Beam (DCB) obtained using Selective Laser Sintering (SLS).

The Selective Laser Sintering technique allows the fabrication of a 3D part by an overlay of 2D profile layers: a high power laser melts a powdered material, e.g., metals, polymers, that is placed up a printing plate. The laser scans the powder layer and selectively fuses the material following a specific path described by the 3D model of the final part, e.g., CAD model. After that each powder layers have been scanned, the printing plate is lowered by one-layer thickness and a new powder layer is applied for a new scan step: the process is repeated until the part is completed.

DCBs substrates have been fabricated using the EOS Forminga P110 3D printer (Eos, Germany) with a commercial nylon powder (EOSITIN P/PA2200). The effective building volume of the 3D printer is equal to 200 mm x 250 mm x 330 mm while the building speed is 20 mm^3/h. The laser type used for sintering is CO_2, 30W. The working layer thickness is dependent on the material type and it could vary between 0.06 mm and 0.12 mm.

PA2200 is a fine-powder with a polyamide 12 with an average grain size equal to 56 µm. The materials properties are reported in Tab. 2.1(referred to the sintered parts).

Substrates have been bonded with a bi-component epoxy adhesive, Loctite Hysol 9466 (Henkel, Germany). The mechanical properties of the adhesive are reported in Tab. 2.2.

Tab. 2.1: Mechanical and thermal properties of sintered parts obtained from PA2200 powder

	Value	*Unit*
Melting Temperature	184	°C
Density	0.90-0.95	g/cm^3
Tensile modulus	1700±150	MPa
Tensile strength	45±3	MPa
Elongation at break	20±5	%
Flexural modulus	1240±130	MPa
Ball indentation Hardness	77.6±2	MPa
Glass transition temperature	23.5-50	°C
(Van Hooreweder *et al.*, 2010)		

Tab. 2.2: Hysol 9466 properties (Loctite-Henkel, 2014)

	Value	*Unit*
Appearance (Mixture)	Off-white opaque paste	-
Mix ratio by volume - Resin: Hardener	2:1	-
Glass transition temperature	62	°C
Tensile modulus	1718	MPa
Tensile strength	32	MPa
Elongation at break	3	%
Shore Hardness (ISO 868)	60	Durometer D

2.2. Samples description

Mechanical properties of sintered parts have been studied through the fabrication of dogbone samples according to ASTM-D 638-14 (ASTM Standard D638-14, 2004). The standard suggests different geometry and testing speed as a function of material dimensions and characteristics, i.e., rigid, semi-rigid or non-rigid plastics. As the samples were 3D printed rather than obtained from a plate, there were no technological limitations. For this reason, it was chosen the smallest sample size, i.e., type IV, to facilitate more repetitions given the limitations of the build volume. Specimen dimensions are reported in Fig. 2.1.

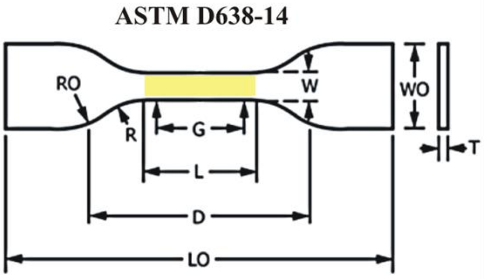

W = 6 mm L = 33 mm R0 = 25 mm
T = 4 mm D = 65 mm L0 = 115 mm
G = 25 mm R = 14 mm W0 = 19 mm

Fig. 2.1: Dogbone geometric characteristics according to *(ASTM Standard D638-14, 2004)*.

Adhesive properties have been evaluated using Double Cantilever Beam (DCB) and, in order to cross-check the obtained results, Tapered Double Cantilever Beam (TDCB) samples were also prepared. The corresponding geometry and dimensions are shown in Fig. 2.2. The total length (L) of the substrate is equal to 150 mm and the width (B) is 15 mm. Two different values for the substrate thickness were chosen for DCB samples, i.e., 6 mm and 8 mm. The loading blocks, required to coupling the samples to the testing machine, have been added to the 3D CAD model employed for SLS. For both geometries, the total length of the bonding area is equal to 120 mm while the adhesive thickness, t_a, is 0.2 mm for DCB samples while it was changed for TDCB, i.e., t_a=0.5 and t_a=0.6 mm. In particular, it was chosen to increase adhesive thickness for the TDCB sample to promote stable propagation, i.e., prevent crack path deflection during propagation. In fact, some preliminary tests demonstrate that small adhesive thickness, i.e., t_a <0.5 mm, does not allow to obtain a steady-state load-displacement response, as it will be discussed later. Notice that, given the expected brittle response of the PA/epoxy joint, increasing the thickness of the adhesive layer should have a minor effect on the fracture toughness (Kinloch, 1987). Thus, it is surmised that the contribution arising from adhesive bulk dissipation should feature limited variations with the thickness of the adhesive layer.

DCB and TDCB samples allow the determination of the Mode-I critical strain energy release rate (the tensile opening mode), i.e., G_{IC}. DCB specimens assembly is simpler with respect to the TDCB specimens, that are more complex and expensive. However, TDCB samples have the advantage that the height taper is built to obtain a linear change in compliance with crack length, which simplifies the determination of critical strain energy since it is not necessary to measure the crack length during the test.

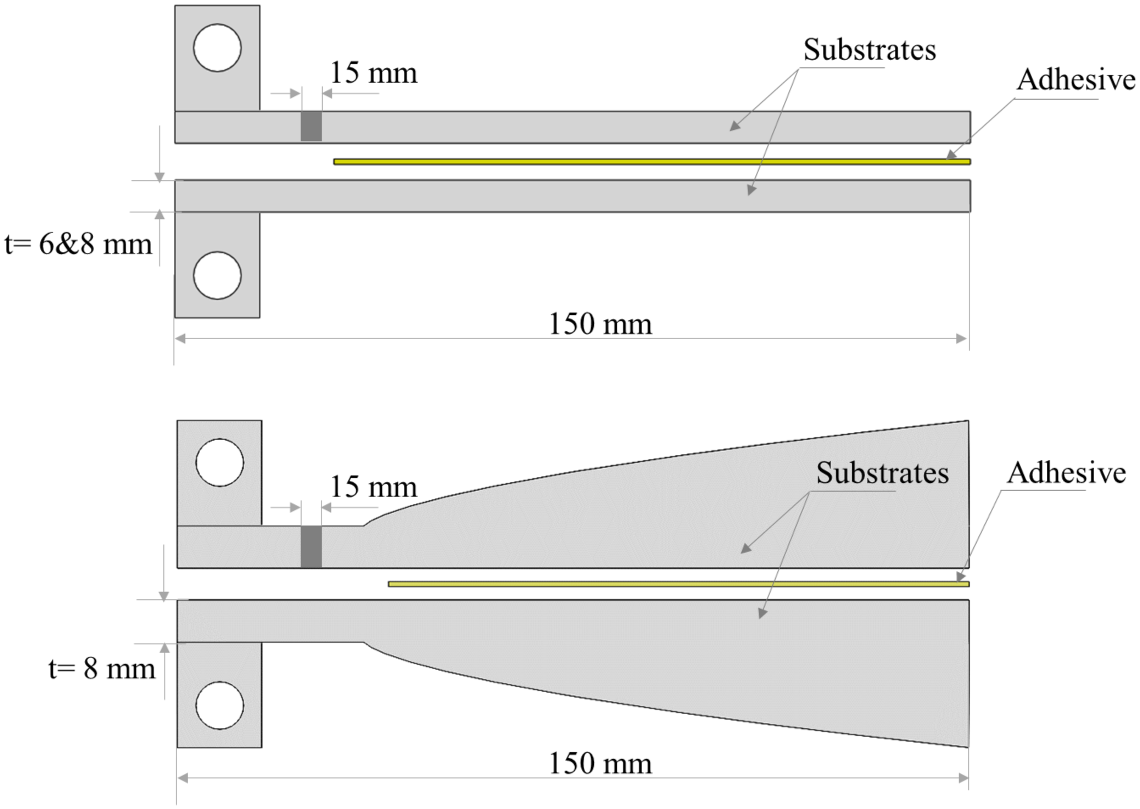

Fig. 2.2: Schematic of the Double Cantilever Beam and Tapered Double Cantilever Beam fabricated in this work.

Tests require that LEFM conditions are met and, for that reason, it is important to choose the right dimensions for the substrates as suggested by ASTM D3433 Standard. DCB adherents dimensions have been chosen to secure conditions described in the ASTM standard and to fit the building volume.

2.3. Joints fabrication

DCB and TDCB substrates were bonded using the epoxy bi-component adhesive described above. Before bonding, substrates have been ultrasonic cleaned in an acetone bath for 5 minutes to eliminate all dust and contaminants from the surfaces. After that, samples have been subjected to a drying procedure at 30 °C for 2 minutes. An anti-sticking tape was used to prevent bonding and create a pre-crack, as shown in Fig. 2.3 (a). Nylon wires have been employed during bonding procedure (Fig. 2.3 (b)) in the direction perpendicular to crack propagation to ensure the consistency of the adhesive thickness. Samples were clamped to facilitate removal of the adhesive in excess and to prevent unwanted substrate misplacement during curing (Fig. 2.3 (c) and (d)). The rate of adhesive cure changes in function of ambient temperature and, in particular, the elevated temperature may be used to accelerate the process. For example, the adhesive produced to suggest a time of 24 h at room temperature, of 4-6 hours at 40 °C and of 1,5 h at 80-100°C. To avoid mismatches in mechanical properties due to differences in curing temperature, the adhesive curing was carried out at 40 °C for five hours in an MTS 651 climatic chamber (MTS Systems Corporation, USA).

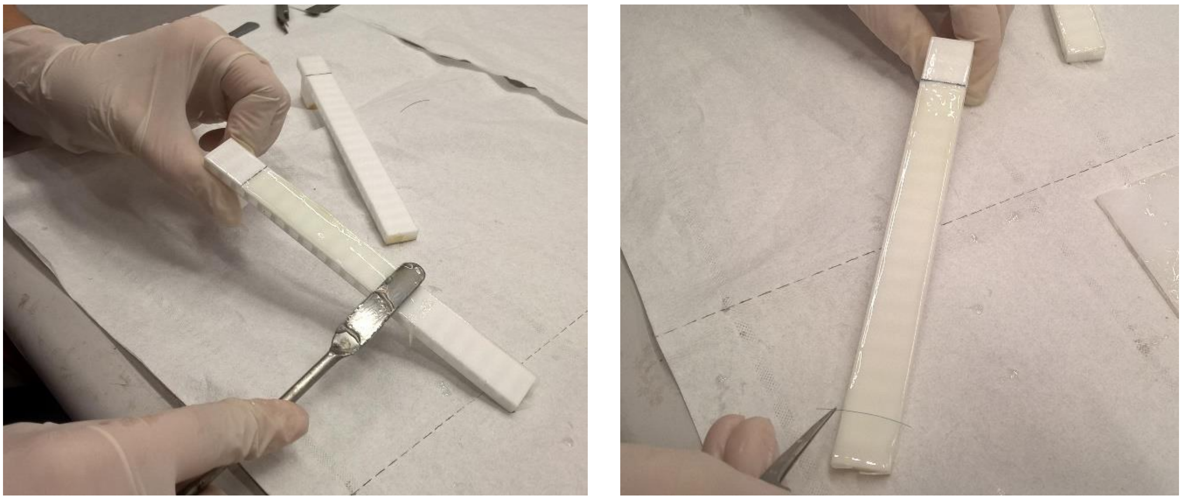

(a) (b)

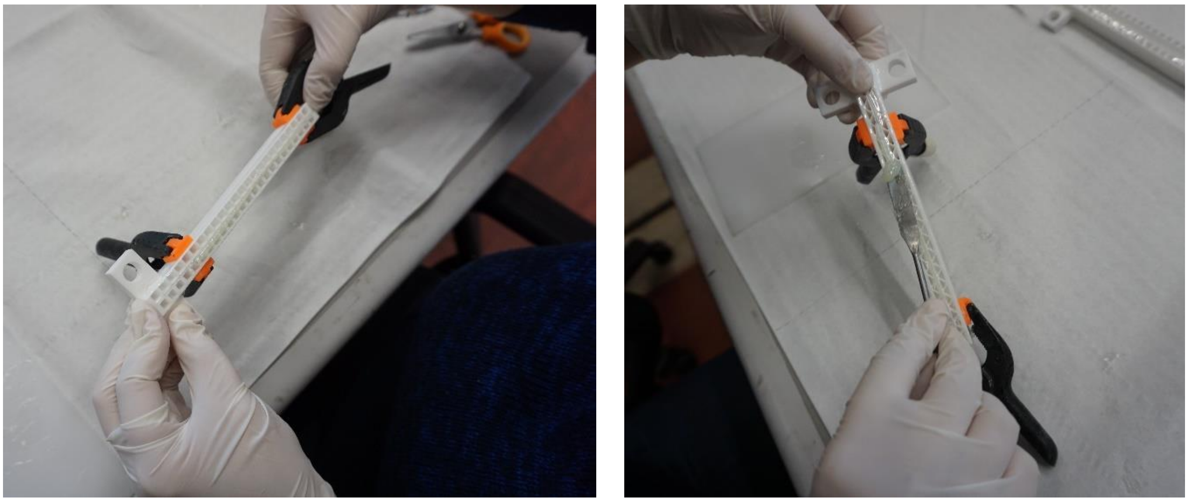

(c) (d)

Fig. 2.3: Bonding procedure (a) application of the adhesive on substrates, (b) insert of nylon wires employed during bonding procedure, (c) Samples clamping and (d) removal of the adhesive in excess.

At the end of the curing process, the surface quality and the adhesive thickness were verified using stereoscope S6D (Leica, Wetzlar, Germany). Images have been acquired using DFC 320 camera (Leica, Wetzlar, Germany). A workstation with the *Leica Application Suite* software package (Leica, Wetzlar, Germany) was used to analyze the images.

Regarding TDCB samples, because of the shape of the substrate, a different strategy was used to clamp the samples during curing. The first solution adopted to solve the problem was adding a template to the cad model as reported in Fig. 2.4. Adding these parts to joints assembly, it was possible to use clamps to fix samples. Nevertheless, this configuration did not provide satisfactory results. Indeed, it was not possible to fully avoid substrates sliding during curing. For this reason, a new solution was elaborated and it is shown in Fig. 2.5: extra protruding features, namely clamping blocks, have been added to TDCB samples to simplify the application of the clamping force and to guarantee proper alignment of the specimens.

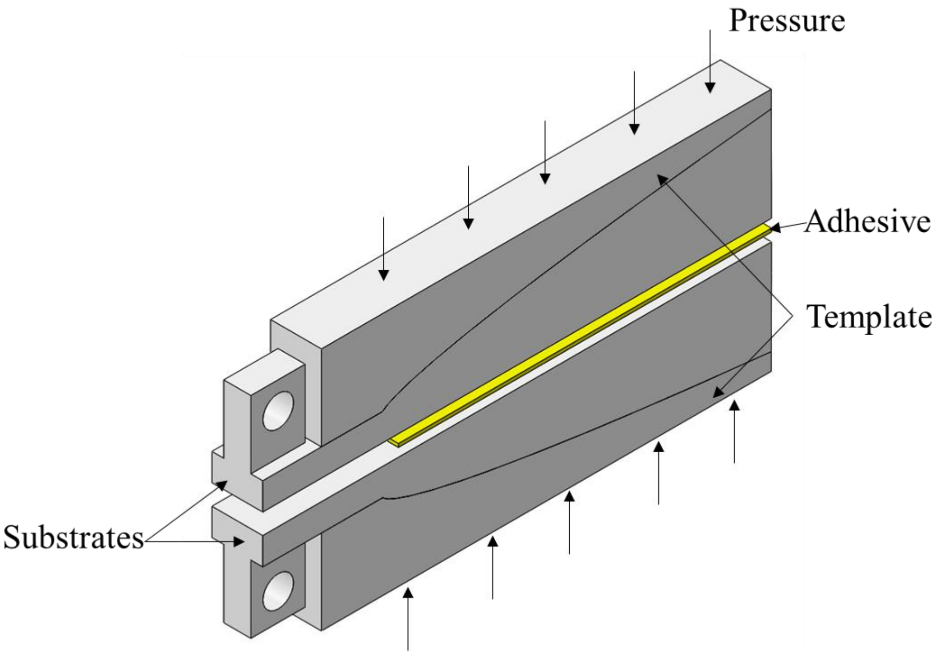

Fig. 2.4: CAD model of the Tapered Double Cantilever Beam and initial clamping strategy employed for fabrication including a template

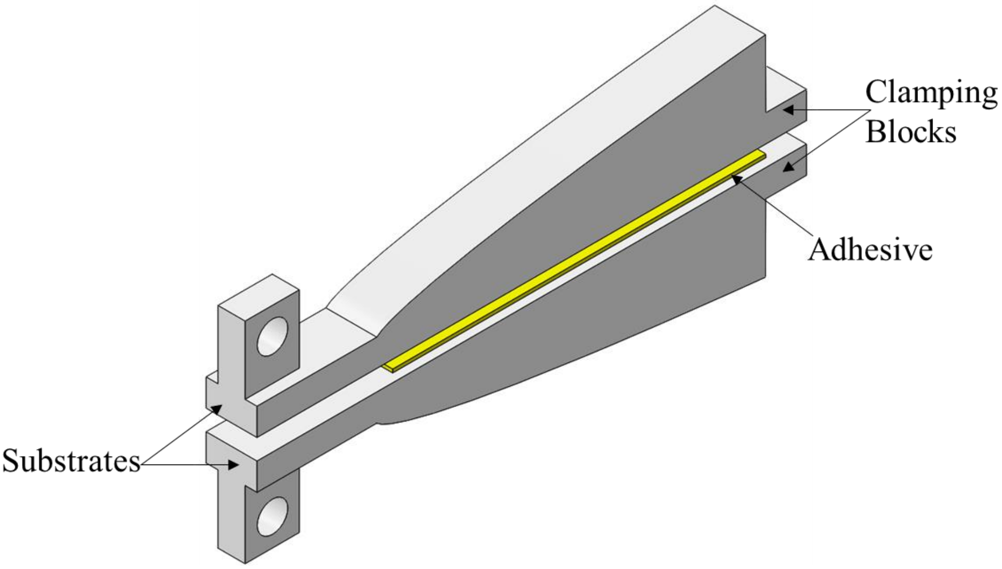

Fig. 2.5: CAD model of the Tapered Double Cantilever Beam and final clamping strategy employed for joint fabrication with fixing blocks.

2.4. Mechanical testing and data reduction

Mechanical tensile tests have been carried out using an electromechanical testing machine, i.e., MTS Criterion Model 42 (MTS Systems Corporation, USA) with a 5 kN loading cell. From each test, true stress-true strain curves were obtained. Digital Image Correlation technique was employed to determine the values of Young’s modulus and Poisson’s ratio. The images were acquired by a GigE camera (Prosilica GT) with a maximum resolution of 2448x2050 pixels with a pixel dimension equal to 3.45 µm x 3.45 µm, a maximum frame rate of 15 fps, and a 2/3’’ CCD sensor (Sony ICX625). The camera was interfaced with commercial software (Vic-Snap, Correlated Solutions) to acquire images through an acquisition board (DAQ-STD-8D, National Instruments), i.e., a voltage proportional to the crosshead displacement was used to acquire an image every 0.5 mm.

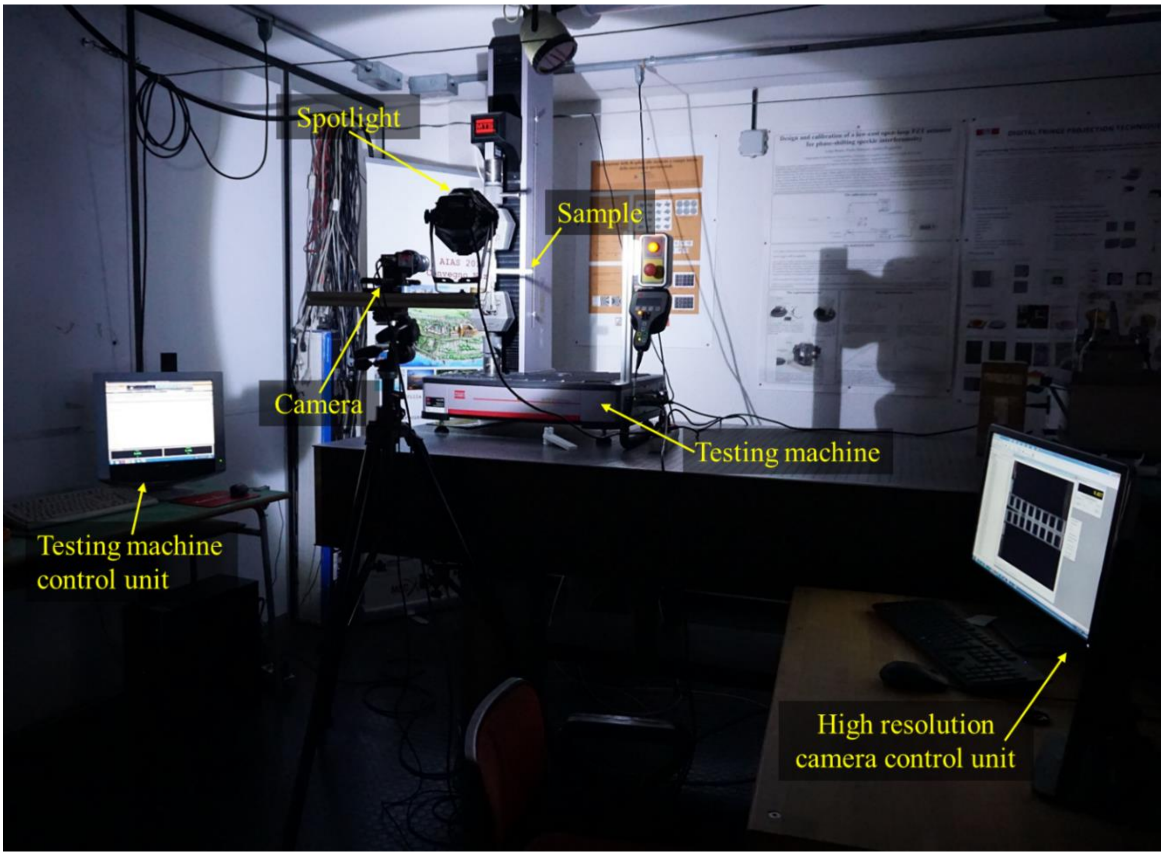

Fig. 2.6: Experimental setup used for the Digital Image Correlation technique available at DIMEG-UNICAL building 46D.

A workstation with a VIC-2D software package (Correlation Solution Inc., version 2009.2.0) was used to analyze the speckle images. The same setup was also used during mechanical tests conducted on DCB samples and to monitor crack propagation. The experimental setup used during all tests is reported in Fig. 2.6. Tensile tests have been carried out at different displacement rates, selected according to ASTM D638 (ASTM Standard D638-14, 2004), i.e., 0.5 mm/min 5 mm/min, 50 mm/min. A similar analysis has been carried out on the adhesive joints, as described later in the dissertation. Moreover, since the rate of adhesive hardening and its mechanical strength depends on the curing temperature, the response of the thermoplastic 3D printed material to high temperature has been scrutinized. The objective is to ascertain its capability to resist high temperature heating without detrimental effects on its mechanical properties and eventually, use high temperature curing for the adhesive joints. To this aim, bulk specimens were heated up to 100 °C for 1 hour using an MTS 651 climatic chamber (MTS Systems Corporation, USA). The samples were put into the preheated climatic chamber and, after the heat treatment, they have been slowly cooled down to room temperature.

DCB and TDCB tests were carried out using the electromechanical testing machine mentioned above with different crosshead displacement, i.e., 0.5 mm/min and 5 mm/min. Some preliminary tests were performed to identify the influence of the displacement rate on the sample's behavior.

For the DCB samples, the fracture energy, i.e., G_{IC}, could be determined using the equation suggested by ASTM D3433-99 (ASTM Standard D3433-99, 2012) (Eq.2.1), which is dependent on crack length. However, since it is difficult to evaluate the crack dimension with good accuracy, it is also possible to obtain an expression that is independent of this parameter. According to LEFM, the fracture energy could be obtained by the following expression.

$$G_C = \frac{P_c^2}{2W}\left(\frac{dC}{da}\right)\bigg|_{a=a_c} \tag{2.1}$$

Where:

- a is the crack length;
- W is the substrate width;
- P_C is the critical load that is obtained at the critical crack length a_c;
- $C = \delta/P$ is compliance, where δ is crosshead displacement.

The Euler-Bernoulli beam theory allows expressing compliance as:

$$C = \frac{\delta}{P} = \frac{2a^3}{3EI} \tag{2.2}$$

Where:

- I is the moment of inertia of the substrate section;

It is possible to get the following expression for the fracture energy by substituting the compliance in Eq. 2.2:

$$G_{IC} = \frac{P_c^2}{W}\frac{a^2}{EI} \tag{2.3}$$

Finally, eliminating a from Eq. 2.3 and substituting it in Eq. 2.4, it is possible to obtain the following expression, which does not depend on crack length:

$$G_{IC} = \frac{P_c^2}{WE\mathrm{I}}\left(\frac{3EI\delta}{2P_c}\right)^{\frac{2}{3}} \tag{2.4}$$

As will be explained later, this equation was used to determine the critical fracture energy from experimental data. The equation was obtained by assuming a perfect encastred cantilever. However, this model does not take into account rotation and deformation that occur at the crack tip. For this reason, to take account of that, other models have been proposed, e.g., corrected beam theory. Nevertheless, since the final purpose only to estimate the fracture toughness that will be afterward validated with finite element simulation, the above-mentioned equation provides an adequate appreciation.

TDCB samples, as stated earlier, have the advantage that the height taper, i.e., *H*, is built to obtain a linear change in compliance with crack length. For this reason, height could be obtained by keeping constant a geometry factor, i.e., m, described by the following expression:

$$m = \frac{3a^2}{H^3} + \frac{1}{H} = cost \tag{2.5}$$

Therefore, the fracture energy could be obtained using the later expression:

$$G_{IC} = \frac{4P^2m}{EW^2} \tag{2.6}$$

As suggested by ASTM D3433-99 (ASTM Standard D3433-99, 2012), m value was fixed equal to 3. The other dimensions were chosen to fit the printing building volume and, for this reason, these were chosen equal DCB dimensions, as reported in Fig. 2.2.

2.5. Damage tolerant bio-inspired subsurface channels

2.5.1. Details of the proposed geometries for the sub-surface channels

In this work, the attention has been mostly focused on two fundamentals bio-inspired strategies that enable toughening and damage tolerance in adhesive joints: the use of patterned interface resembling the suture observed in ammonite shell, and the use of sub-surface bulk patterns, such as those observed in the base plate of the *Amphibalanus Amphitrite* (Hui *et al.*, 2011). The radial channels of barnacles' base plate have been analyzed and, in particular, their aspect ratio with respect to the base plate thickness has been maintained. Circular and square cross-section, represented in Fig. 2.7 (a) and (b), have been deployed into DCB adhesive joints. The dimensions and spacing are inspired to that of the actual barnacle, with reference to the leading edge of the base plate.

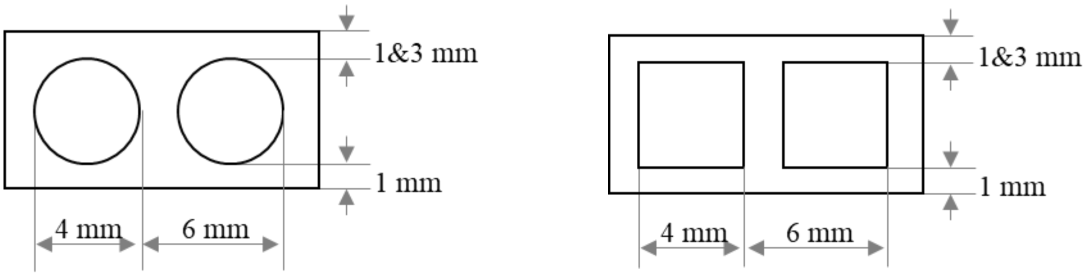

(a) (b)

Fig. 2.7: Schematic representation of the subsurface channels deployed into selective laser sintering of the DCB adhesive joints.

2.5.2. Evaluation of the driving force

It is expected that the subsurface channels will provide a significant crack-trapping effect, which arises because of the modulation of the driving force at the interface. The fact that for a growing crack between the mating substrates, the presence of subsurface channels can significantly modify the available driving force, was demonstrated on the numerical ground, and experimentally by resorting to standard micro-lithography (Glassmaker *et al.*, 2007; Afferrante, Carbone and Demelio, 2012).

In order to ensure that a similar effect holds for the particular model material system selected in this work, finite element simulations were carried out to extract the energy release rate using a *boundary layer* approach (Kalamkarov, Kudriavtsev and Parton, 1990; Zavattieri, Hector and Bower, 2008). The numerical model is described in Appendix A.

The obtained driving force for the selected channel geometries is shown in Fig. 2.7. Results are given in non-dimensional fashion, by dividing the obtained energy release rate, i.e., the *J*-integral of the bio-inspired interface, by the value obtained for the corresponding flat interface. The results are reported in Fig. 2.8.

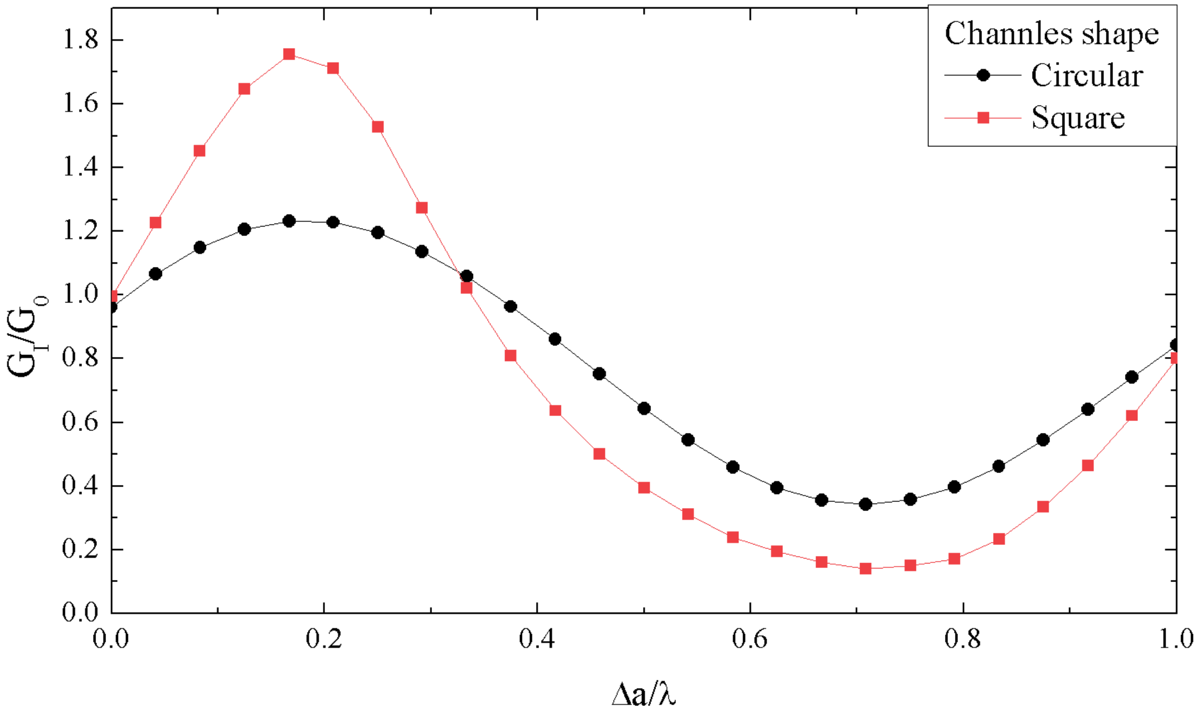

Fig. 2.8: Normalized energy release rate for circular (black curve) and square channels (red curve).

The bio-inspired channels locally modify the stiffness and, for this reason, the normalized *J*-integral changes as a function of crack tip position. In particular, when the normalized energy ratio is < 1, the energy available at the crack tip is less than that supplied at the remote boundary.

Therefore, in actual tests, for a given supplied external energy the crack will slow down and eventually will be arrested, requiring an increase of external load for re-initiation. Similarly, there are locations where the ratio is >1, in this case, the energy available at the crack tip will be larger than that supplied by the external loading, which will lead to unstable crack propagation. The same behavior was observed in other works with similar geometries (Glassmaker *et al.*, 2007; Afferrante, Carbone and Demelio, 2012). It is possible to conclude that both channels' geometries are expected to trigger a modulation of the energy release rate, although the exact details regarding the variation of the driving force may slightly differ from that of the actual DCB adhesive joints.

2.6. Architected sinusoidal interfaces

As described in the previous chapter, damage tolerance could be improved by modifying the adhesive layer, the interface, or the bulk substrate (e.g., subsurface channels). An interesting strategy employed in recent works (Cordisco *et al.*, 2016; Liu *et al.*, 2017; Khoshhesab and Li, 2018) is based on the variation of substrate macroscopic morphology in order to reach a twofold objective: (i) generate mechanical interlocking that aids adhesive bonding; (ii) increase the bonding area and induce mixed-mode opening. In this work, these aims have been pursued through DCB adhesive joints with a sinusoidal interface inspired by sutures interfaces (Li, Ortiz and Boyce, 2011; Malik, Mirkhalaf and Barthelat, 2017). The sinusoidal interface could be described using the following equation (2.7):

$$y(x) = A \sin\left[\left(\frac{2\pi}{\lambda}\right) x\right] \tag{2.7}$$

Where λ is the sinusoidal wavelength and $2A$ is the amplitude of the sinusoid as reported in Fig. 2.9.

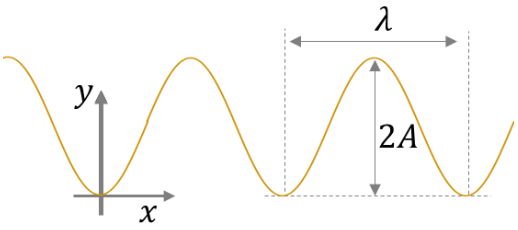

Fig. 2.9: Details of sinusoidal interfaces.

Three values of λ have been chosen, i.e., 4, 6 and 8 mm while A value was fixed equal to 2 mm. Sinusoidal interface aspect ratios $(A/\lambda,)$ were chosen to reproduce the characteristic dimensions of the suture of the Ammonite shell (Erica Lin *et al.*, 2014; Paul, 2015). As for subsurface channels, it is expected that the variation of interfacial shape plays an important role in the modulation of the driving force.

This effect can be studied by evaluating J-integral using the approach described in Appendix A.

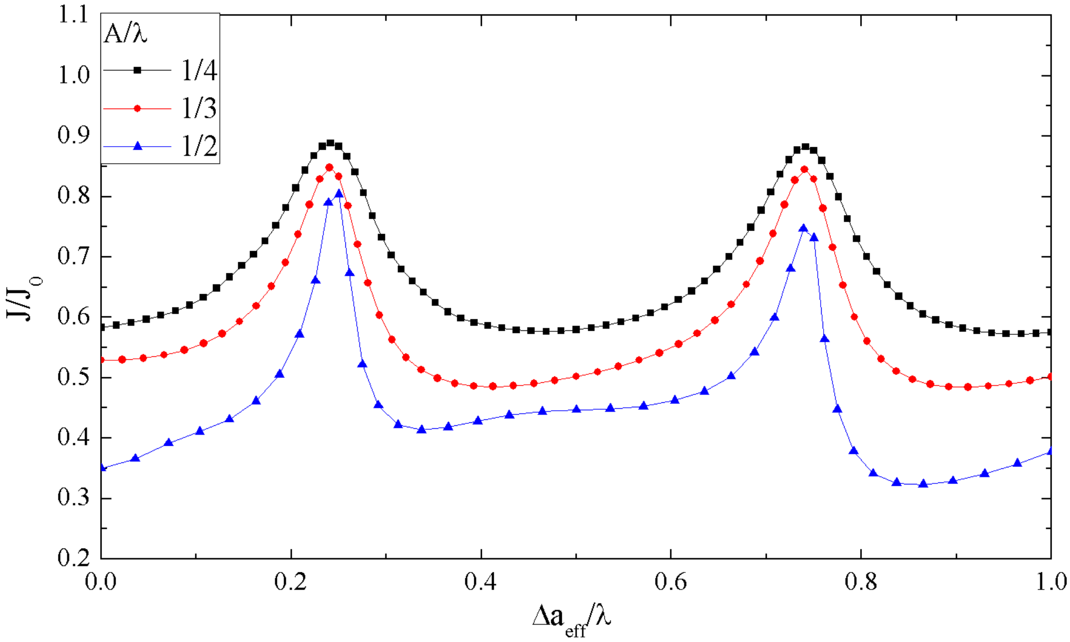

Fig. 2.10: Normalized energy release rate of sinusoidal interface with A/λ ratio equal to 1/4 (black curve), 1/3 (red curve), and 1/2 (blue curve).

Results have been compared in terms of normalized energy release rate, i.e., the J-integral of the sinusoidal interface was divided by J_0, which is the reference value obtained on a flat interface and equal to the stress intensity factor applied on the remote boundary. The results are reported in Fig. 2.10. The lower is the J/J_0 ratio, the smaller is the crack tip driving force with respect to the remote applied one, which implies that a higher load will be required to advance the crack in actual mechanical tests (assuming a constant value for the critical fracture energy). The results demonstrate that a sinusoidal interface is endowed with a modulation of the energy requested for crack propagation similar to that observed for the subsurface channels. As such it can hinder crack propagation, and the most effective geometry should be the one for which A/λ = 1/2. This point will be later assessed in the experiments.

2.7. Summary of fabricated samples

In order to simplify the discussion of the results, it was chosen to identify the sample with a code that contains information about sample type and the corresponding fabrication batch. The overall sets of samples that have been fabricated and tested are summarized in Tab. 2.3.

Tab. 2.3: Summary of samples realized with a 3D printer

#batch	***Sample type***	***Number of samples***	***thickness [mm]***	***sample code***
1	Dogbones	5	-	DB#1
	DCB Benchmark	3	6	BM6#1
		3	8	BM8#1
	DCB Square channels	3	6	S6#1
		3	8	S8#1
	DCB Circular channels	3	6	C6#1
		3	8	C8#1
2	Dogbones	10	-	DB#2
	TDCB Benchmark	5	-	TBM#2
3	TDCB Benchmark	15	-	TBM#3
4	Dogbones	5	-	DB#4
	DCB Benchmark	5	6	BM6#4
5	DCB Benchmark	5	6	BM6#5
	DCB Square channels	5	6	S6#5
6	Dogbones	5	-	DB#6
	DCB Benchmark	5	6	BM6#6
	DCB Square channels	5	6	S6#6
7	DCB Sinusoidal wave λ=8	4	6	W6_λ8#7
		4	8	W8_λ8#7
	DCB Sinusoidal wave λ=6	4	6	W6_λ6#7
	DCB Sinusoidal wave λ=4	4	6	W6_λ4#7

In particular, the first part is referred to sample’s type, e.g., DB means dogbone, while the second part is referred to belonging batch e.g., #01 means that the samples were printed in the first batch.

For biomimetic joints with architected sinusoidal interfaces, the code includes only information about the sinusoidal period since amplitude does not change, i.e., *2A* is equal to 4mm. Images of the 3D printed biomimetic joints are reported in Fig. 2.11 and in Fig. 2.12. Images of the adhesive bonded joints have been acquired with the high-resolution camera described before.

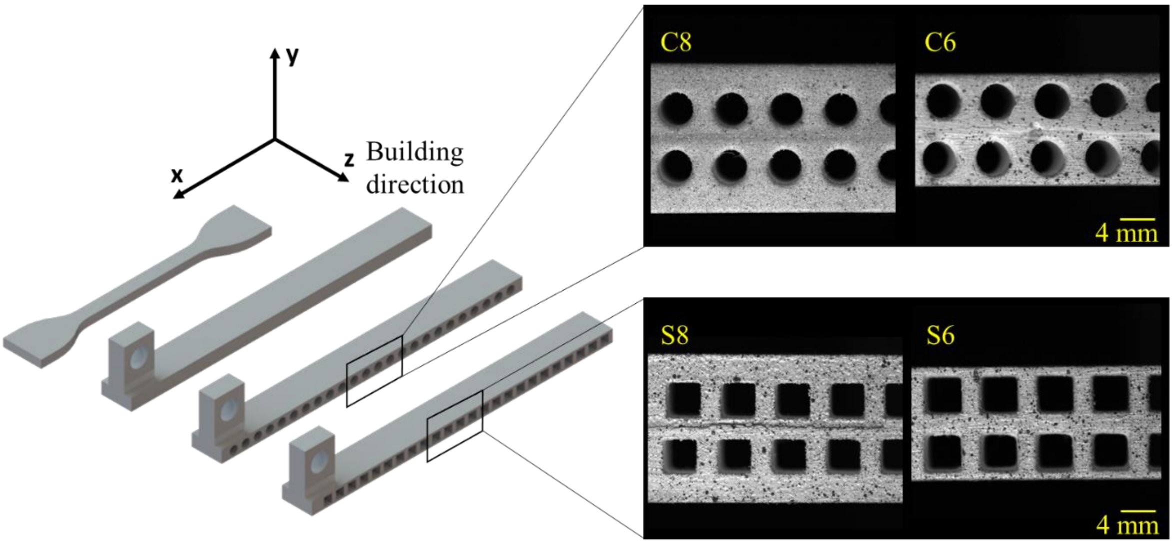

Fig. 2.11: Schematic of samples, including dogbone and DCB adhesive joints with and without subsurface channels

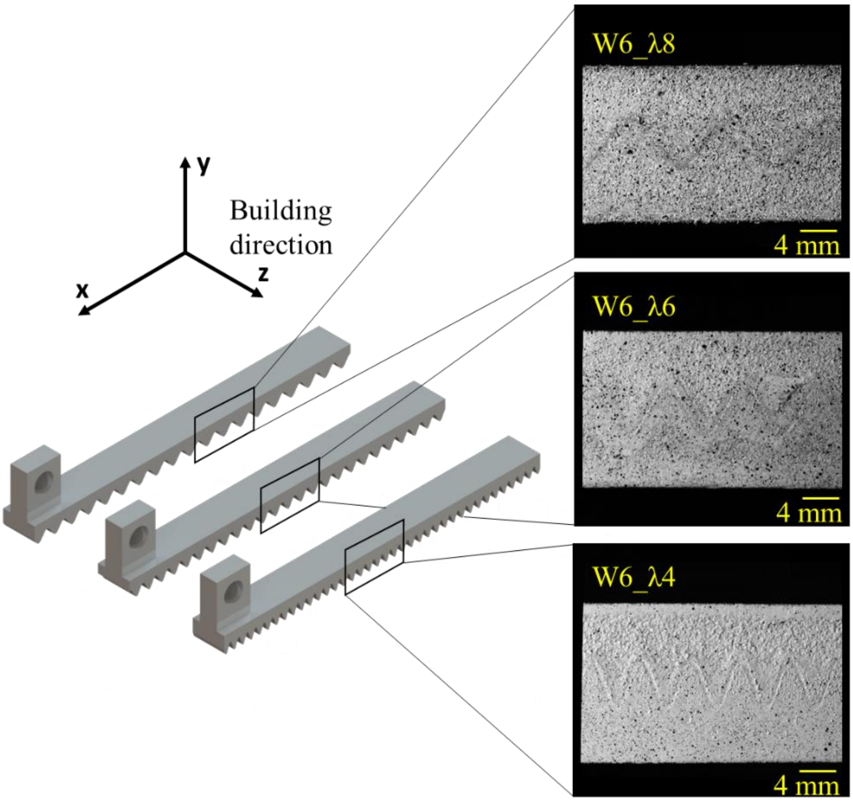

Fig. 2.12: Schematic of biomimetic architected joints with sinusoidal interfaces realized by 3D printing

2.8. 3D printing: limitations

Selective Laser Sintering technique is one of the most reliable 3D printing techniques as regards product quality. Nevertheless, few fabrication defects and inaccuracies have been recorded, and are discussed in this section. The main issues are associated with the obtained dimensional accuracy and surface quality. Dimensional measurements, such as those given in Fig. 2.13, have been carried out to make a posteriori estimation of the obtained printing accuracy. The schematics highlight the main deviations observed between the CAD model and the actual part. In particular, it is observed the square channels feature rounded edges, thinner “base” plate, and larger channel size and pillar thickness. However, it is also noted that the dimensional inaccuracies had a somewhat random nature, given that in other batches the above-mentioned issues were sometimes negligible. As the sintering process leads to the melting of the thermoplastic particles, it is also very hard to guarantee sharp edges, as shown in Fig. 2.13.

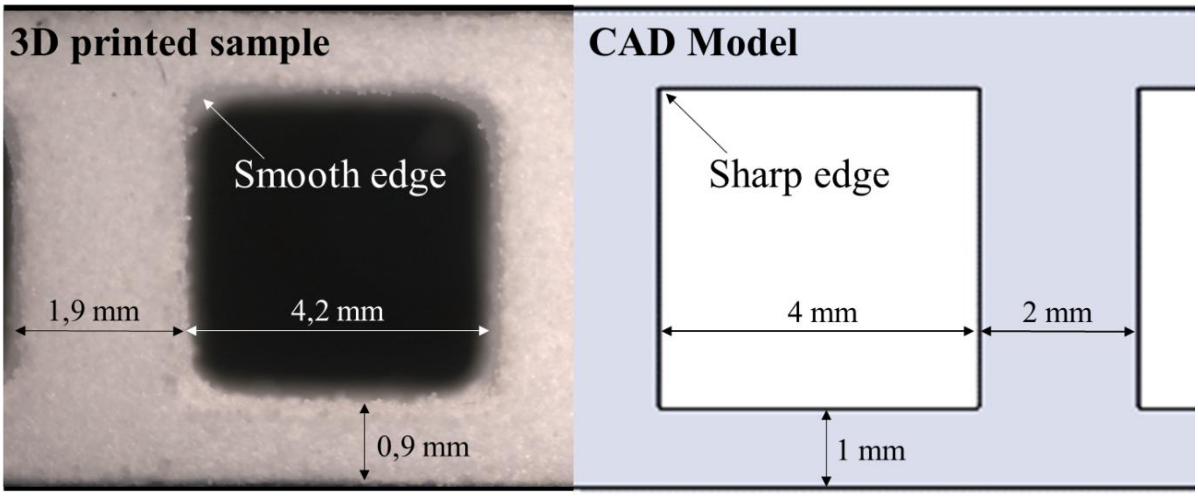

Fig. 2.13: Dimensional accuracy in 3D printing.

On another note, batch-to-batch variations of surface quality were also observed. This difference is strictly related to SLS technology: nylon powder that is not melted during the print process is reused for several printing cycles, as suggested by 3D printer producer and that made some variation in final surface characteristics. For this reason, surface roughness has been evaluated using a profilometer as shown in Fig. 2.14.

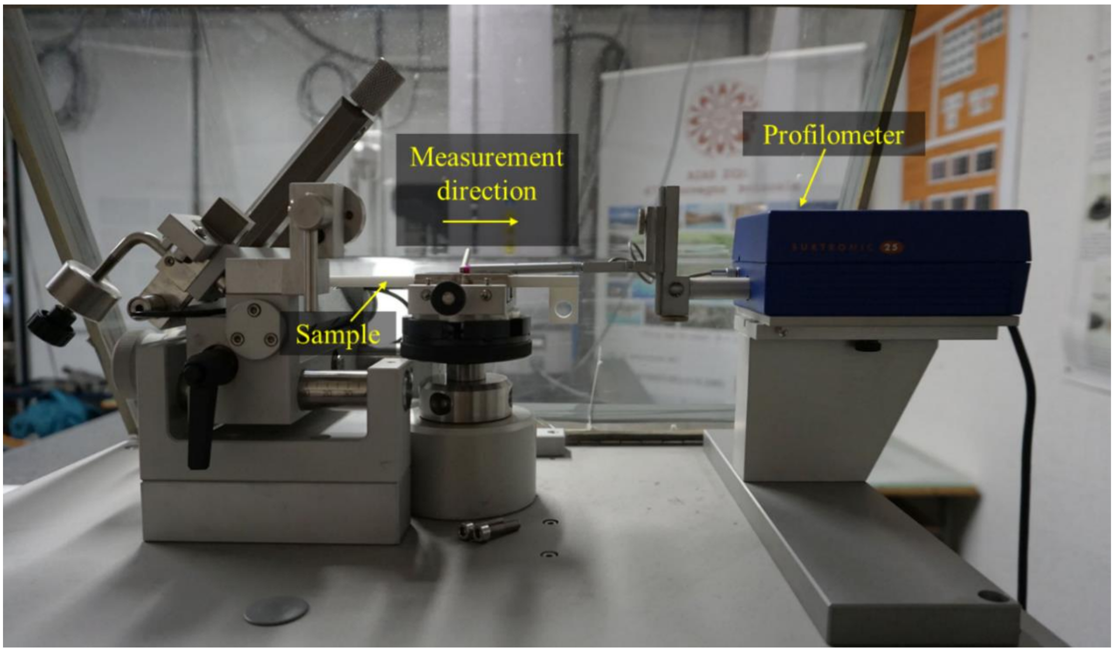

Fig. 2.14: Experimental setup used for roughness measurement.

Results have been compared in terms of R_z since a preliminary analysis demonstrates that joint response is more affected by R_z rather than by the others, e.g., R_a. This value has been detected in the longitudinal direction. R_z is the average absolute value of the five highest peaks and the five lowest valleys over the evaluation length, i.e., N=5.

$$R_z = \left|\min_{1 \leq j \leq N} r_j\right| + \left|\max_{1 \leq j \leq N} r_j\right| \tag{2.13}$$

Roughness profiles have been measured in six different zones on the surface of each sample. Roughness measurements have been done on three different samples of each batch, i.e. 18 values. Surface roughness was obtained as the average between these 18 values. Inconsistent data points were excluded from the analysis using the Chauvenet criterion (Dally, 1987). In particular, it was chosen to exclude all values that lie outside a probability band corresponding to 90% of reliability (using a Gaussian distribution). The results will be explained in the next chapter to evaluate the effect of surface roughness of joints behavior.

Chapter3: Experimental results

3.1. Material properties

Polymeric materials, due to their structure, exhibit a viscoelastic behavior and, for that, their properties could change a lot as a function of environmental conditions, temperature or strain rate. Moreover, the 3D printing process may introduce anisotropy due to residual stress related to heat shrinkage or building direction. All these factors need to be evaluated and accounted for in subsequent fracture tests.

3.1.1. Effect of crosshead displacement rate

As explained before, polymer characteristics are strictly dependent on crosshead displacement speed due to potential viscoelastic effects and, for this reason, tensile tests have been carried out at different displacement rates. An initial cross-head displacement equal to 5 mm/min was chosen according to ASTM D638 (ASTM Standard D638-14, 2004). Starting from this value, two other velocities have been considered in the analysis: the first one is one order of magnitude higher and the second is one order of magnitude lower, i.e., 0.5 mm/min and 50 mm/min.

The stress-strain curves, obtained using these displacement rates are reported in Fig. 3.1. Results demonstrate that, as for all polymers, nylon is sensible to displacement rate: with the increase of displacement rate, the elongation at break decrease while the yield strength increases. However, differences become more notable modifying displacement rate from 5 to 50 mm/min, while they are mostly negligible raising the rate from 0.5 to 5 mm/min. Therefore, for low displacement rates, i.e., quasi-static loading, viscoelastic effects do not heavily affect the material behavior. For this reason, it was chosen to use 0.5 mm/min. displacement rate for all tests, such that potential rate-dependent effect due to the viscoelastic response of the nylon substrates is minimized as much as possible.

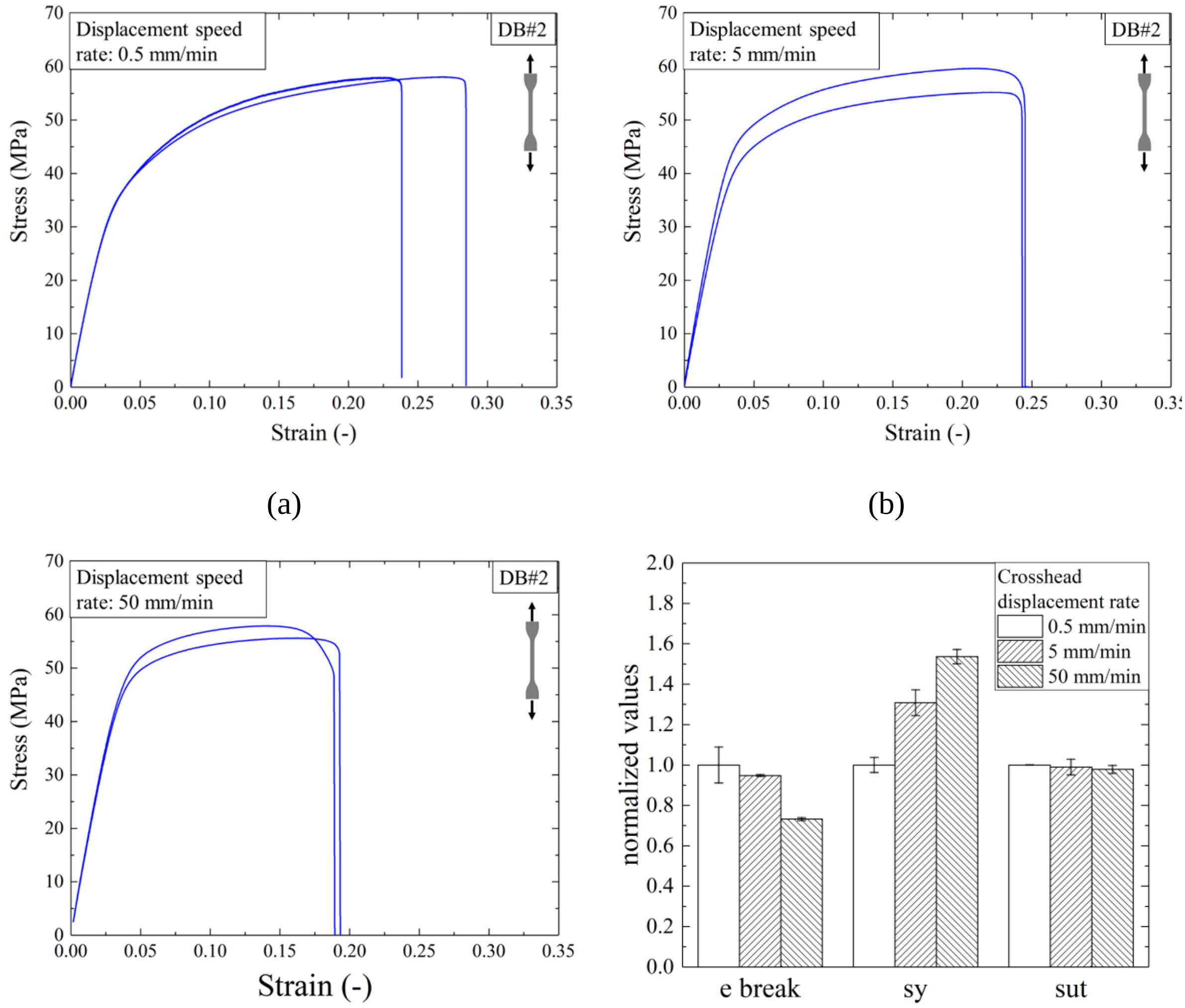

(a) (b)

(c) (d)

Fig. 3.1: Stress-strain curves obtained on dogbone samples using speed rate equal to (a) 0.5 mm/min (b) 5 mm/min and (c) 50 mm/min.

3.1.2. Effect of build-direction and post-curing by thermal heating on the mechanical properties of 3D printed nylon

The mechanical properties of 3D printed parts may be affected by anisotropic effects due to the specific building direction selected for printing. This point was assessed by printing dogbone samples in the x- and z- directions of the building volume (see chapter 2). The results, not reported herein for brevity, allowed to conclude that the material response was essentially unaffected by the build direction. It is also important to consider that printing slender structures in the out-of-plane z-direction of the building plate is more expensive and time-consuming if compared to printing with laser scans in the in-plane directions. Moreover, it can adversely affect the structure of the material. Therefore, this building option is normally not pursued.

High temperature curing of the selected epoxy adhesive can improve the mechanical properties. However, as discussed in the previous chapter, it is important to ascertain whether high temperature curing may affect the properties of the 3D printed material. In particular, selected dogbones (DB#2) samples have been heated up to 100 °C for 1 hour by using a climatic chamber [MTS 651 MTS Systems Corporation, USA]. After that, samples have been gradually cooled down until they reached room temperature. The results of tensile tests are reported in Fig. 3.2. It is possible to notice that heat treatment seems to reduce experimental variability as it is clearly noticeable in both stress-strain behavior (Fig. 3.2 (a)) and dispersion of elongation at break, yield and ultimate stress average values (Fig. 3.2 (b)). The dogbones that were not subjected to heating are characterized by some difference in the post-yielding of the stress-strain curve, even if the elastic behavior is almost the same in all cases, i.e., no changes in the yield stress. Moreover, differences in stress-strain curves between samples with difference thermic treatment are not so significant, demonstrating that printed nylon is less affected to residual stress compared to 3D printed metallic samples (Buchanan and Gardner, 2019; Qianru Wu *et al.*, 2019) were thermal treatment is necessary before the employment of printed parts.

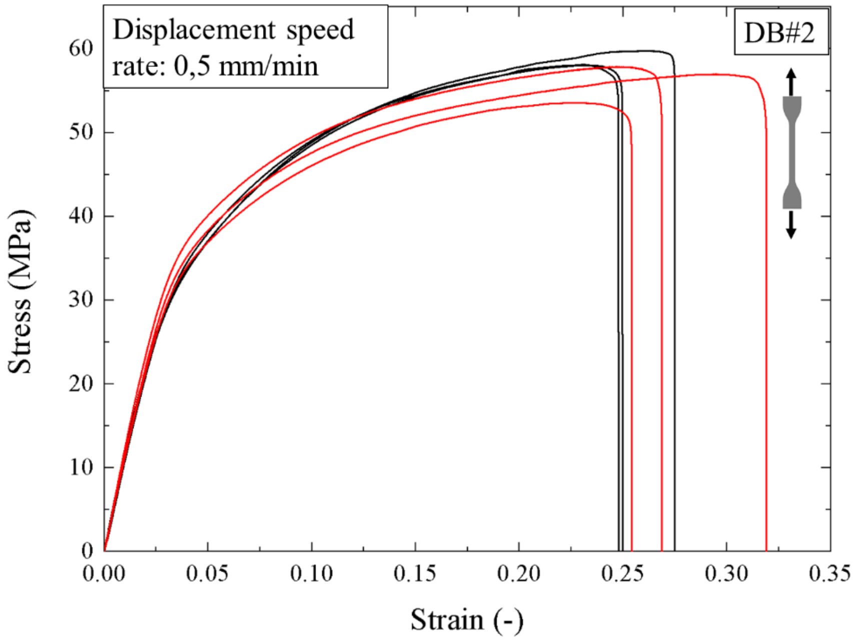

(a)

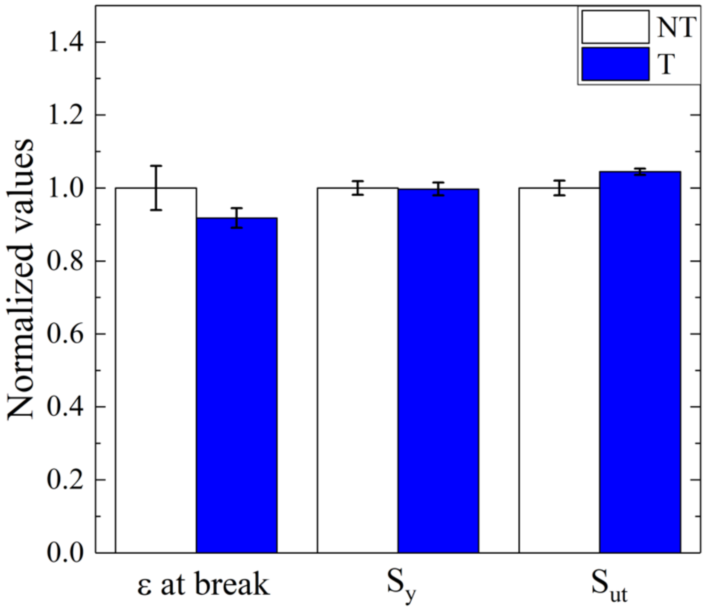

(b)

Fig. 3.2: (a) Stress-strain curves obtained on dogbone samples with (black curves) and without (red curves) thermal treatment and (b) comparison of elongation at break, yield and ultimate stress average values among samples with (blue) and without (white) heat treatment.

3.1.3. Determination of the mechanical properties

In order to evaluate the mechanical properties of 3D printed nylon, tensile tests on dogbone specimens have been conducted according to ASTM-D 638-14 (ASTM Standard D638-14, 2004) using a 0.5 mm/min displacement speed rate. Tensile tests allow obtaining the true stress-true strain curve. The Young's modulus and the Poisson's ratio have been determined with the aid of the displacement maps, obtained from Digital Image Correlation, as shown in Fig. 3.3. The method works as a virtual extensometer: it is possible to measure full-field displacement by tracking a random texture on the sample's surface. The first image, used as reference (i.e., ε=0), is dived in a small portion, called subsets and characterized by a grayscale intensity value. By comparing high-resolution images of the deformed sample, one can evaluate surface deformation by maximizing a similarity function of the grayscale intensity values inside each subset. This technique is valid until the surface is characterized by a non-repetitive and high contrast pattern. For this reason, a random grayscale speckle was created by using acrylic paint as reported in Fig. 3.3. The camera was interfaced with commercial software (Vic-Snap, Correlated Solutions) in order to use an analogic acquisition through an acquisition board (DAQ-STD-8D, National Instruments), i.e. a voltage proportional to the crosshead displacement was used to acquire an image every 0.1 mm. Finally, the DIC software package (Correlation Solution Inc., version 2009.2.0) was used to analyze the speckle images to obtain strain values in both transversal and longitudinal directions. Stress values have been obtained from the electromechanical testing machine by dividing load values for the specimen area.

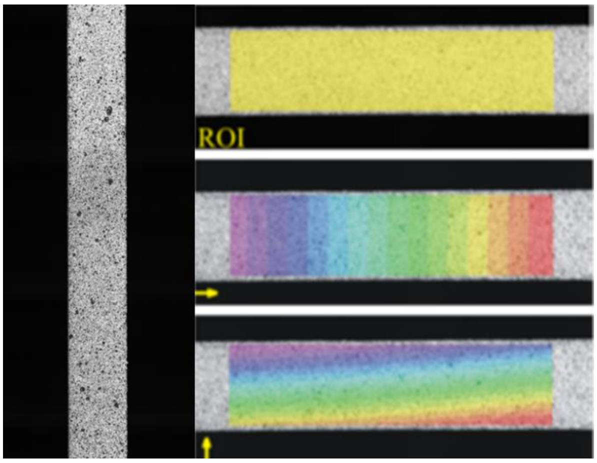

Fig. 3.3: Displacement field obtained using the Digital Image Correlation technique.

The ratio between the applied stress and the strain, obtained from the digital image correlation, is equal to Young's modulus. Similarly, Poisson's ratio was obtained by dividing transversal strain by the longitudinal one. The yield stress was obtained by the intersection between the stress-strain curve and a straight line parallel to the elastic line, with an offset along *x*-axis equal to ε=0.002 as suggested by ASTM D638 (ASTM Standard D638-14, 2004). A typical example of the stress-strain curve obtained after the tensile test is reported in Fig. 3.4.

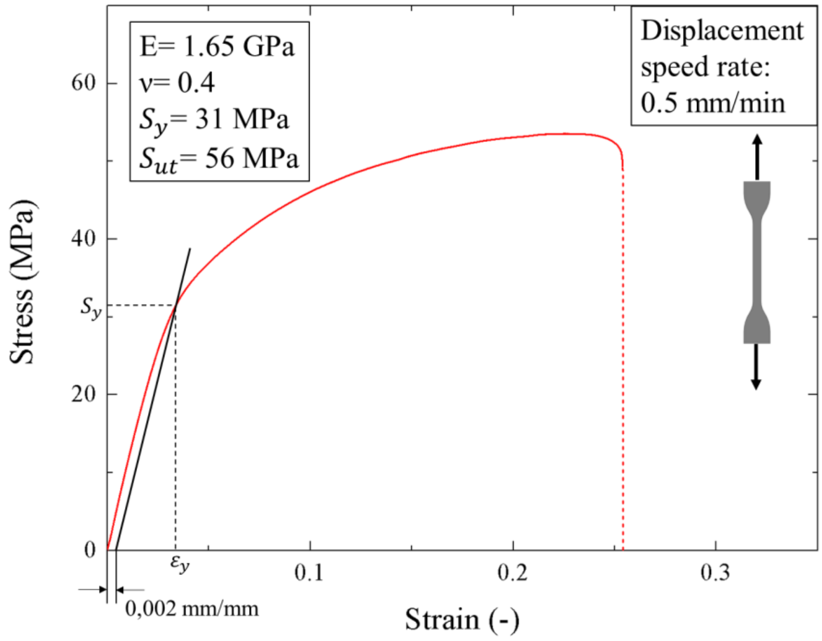

Fig. 3.4: Tensile test results as stress-strain response obtained on 3D printed dogbone samples.

Tab. 3.1: Mechanical property average values of sintered parts obtained from experimental tests

	Value	*Unit*
Tensile modulus	1650	MPa
Elongation at break	26	%
Yield strength	30	MPa
Ultimate strength	57	MPa
Poisson's ratio	0.4	-

The results indicated a non-linear elastic behavior for the 3D printed material, while the corresponding mechanical properties are summarized in Tab. 3.1. It should be noted that the yield strength is lower than that reported by the manufacturer (EOS GmbH, no date). This difference could be attributed to a mismatch in the displacement rate used to extract the data, though the rate used by the manufacturer is not known at this point. In fact, it is clearly known that polymeric material characteristics are strictly dependent on cross-head displacement speed due to viscoelastic behavior. Moreover, Young's modulus and Poisson's ratio obtained with the DIC technique are in agreement with data provided by the nylon powder producer.

3.1.4. Assessment around the robustness of identified properties due to 3D printing batch-to-batch to variations

Tensile specimens from different printed batches have been tested in order to identify eventual batch-to-batch variations of material properties. Tests have been carried out on three different samples for each batch. However, in the fourth batch, one curve was excluded from the analysis due to an anomalous response of the sample, i.e., collapse at low displacement value probably due to the presence of fabrication defects. Each sample was marked by a progressive code consisting of two parts, as explained in the previous chapter: the first is referred to the sample type, e.g., DB means dogbone while the second part indicates the belonging batch, e.g., #01 represents the batch number. Fig. 3.5 shows tensile test results obtained for different batches.

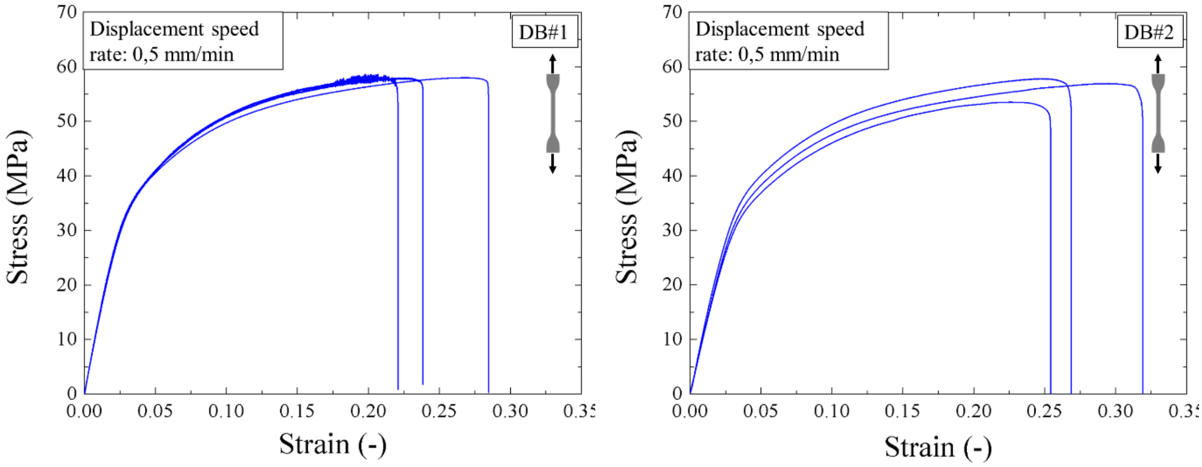

(a) (b)

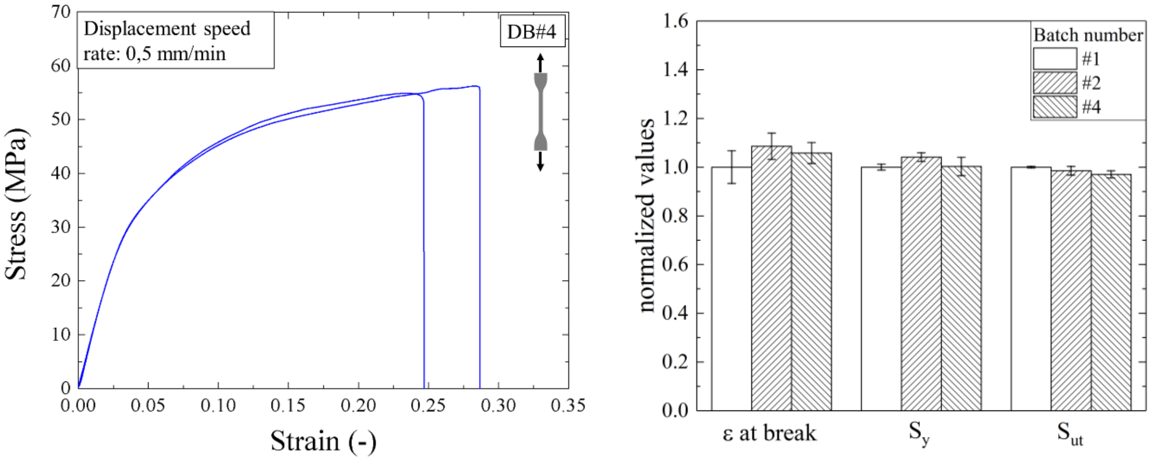

(c) (d)

Fig. 3.5: Stress-strain curves obtained on dogbone samples belonging to (a) first (b) second and (c) fourth production batch and (d) comparison of elongation at break, yield, and ultimate stress average values among samples belonging to different batches

Stress-strain curves exhibit some variations especially regarding the elongation at break. However, the variation range of each group seems to intersect the other ones and, for this reason, it is not possible to attribute these changes to the variations in the batch of fabrication. The observed batch-to-batch variations, as supported by Fig. 3.3(d), look to be negligible and allow us to conclude that the properties of the 3D printed dogbones obtained through SLS are relatively stable and do not vary from batch to batch.

3.2. Double Cantilever Beam and Tapered Double Cantilever Beam

3.2.1. Results of mechanical tests on Double Cantilever Beam adhesive joints

The load-displacement curves obtained during DCB tests on bulk samples of batch#1 with a thickness equal to 8 mm and 6 mm are shown in Fig. 3.6 and Fig. 3.7. Results obtained for both sets of samples exhibit the typical mechanical response of DCB joints: after an initial peak associated with fracture initiation, the applied peel load decrease gradually, i.e., softening zone. However, the experimental curves are characterized by some degree of scattering in the softening region that can be attributed to the observed crack path deflection from the upper to the lower interface (see Fig. 3.8), as well as to potential slight variations of adhesion across the interface.

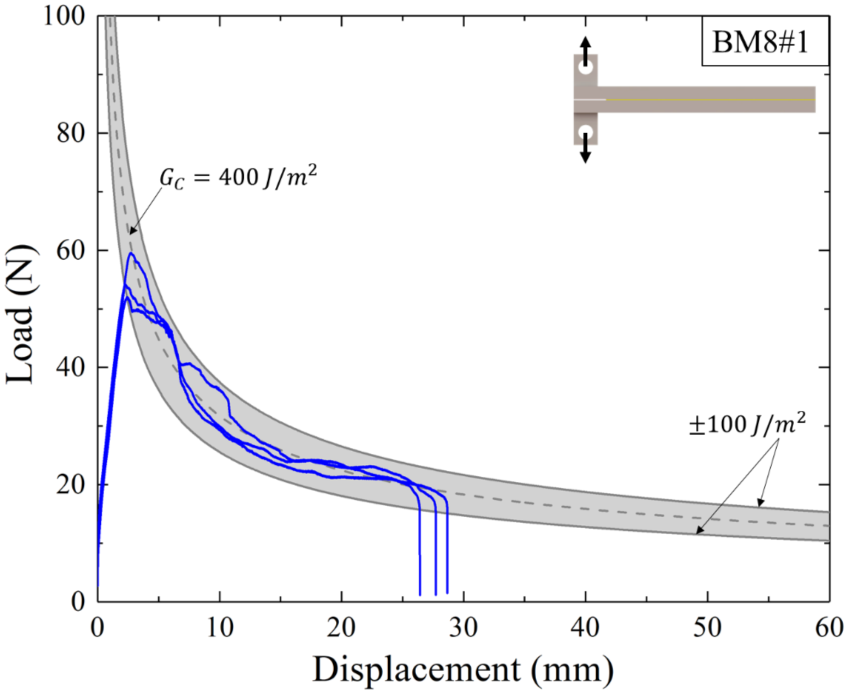

Fig. 3.6: Load displacement curves obtained on DCB samples realized in the first batch with 8mm substrate thickness.

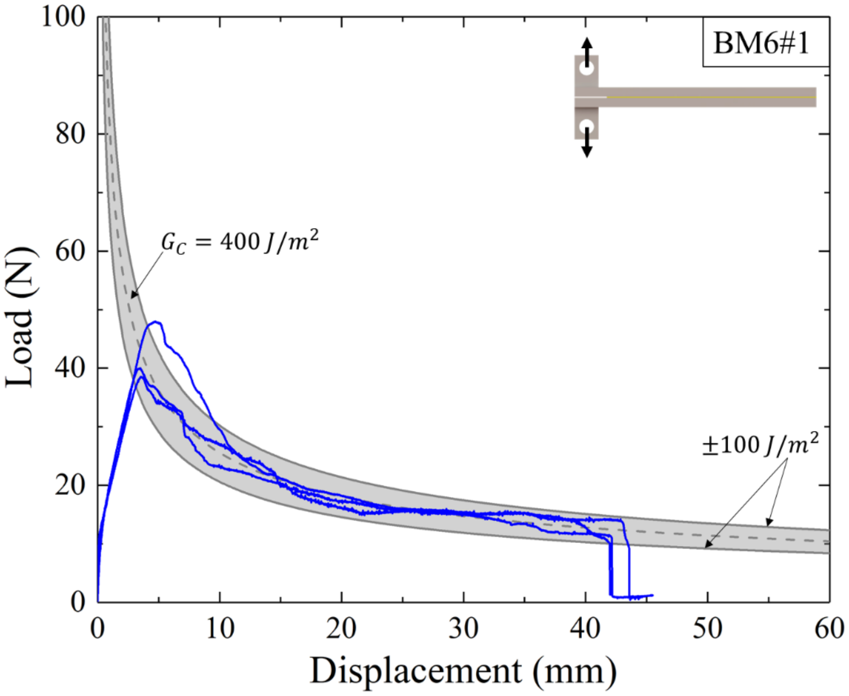

Fig. 3.7: Load displacement curves obtained on DCB samples realized in the first batch with 6mm substrate thickness.

Results have also been compared in terms of fracture energy. Equation 3.1, from Linear Elastic Fracture Mechanics (Anderson, 2005), was employed to identify the fracture energy in the post-peak region since substrate geometry and experimental load-displacement data are known:

$$\delta = \frac{2(b\ G_{Ic})^{\frac{3}{2}}\sqrt{EI}}{3\ F^2} \tag{3.1}$$

where:

- δ is the crosshead displacement;
- b is the sample width;
- G_{Ic} is the fracture toughness of the joint;
- E is Young's modulus;
- I is the moment of inertia;
- F is the applied peel load.

To identify the value of the joint fracture toughness, G_{Ic} was varied until the analytical curve could fit, with a good approximation, the experimental data. The average value for the fracture toughness for this batch was found to be equal to 400 J/m^2 for both values of t as reported in Fig. 3.6 and Fig. 3.7. It is worth noting that the present value is somewhat different from that obtained in previous works (Alfano *et al.*, 2011; Chiodo *et al.*, 2015). where the fracture toughness was determined considering samples with metal substrates and was equal to 2700 J/m^2. However, the difference can be addressed to the peculiar mechanism of failure observed in the experiments, i.e., whereas in previous works failure was cohesive within the adhesive layer, herein interfacial failure was observed in all tests as can be observed from fracture surfaces shown in Fig. 3.8. It is certainly possible to promote adhesion by performing any of the available surface preparation techniques or using a primer. However, it was beyond the scope of current work.

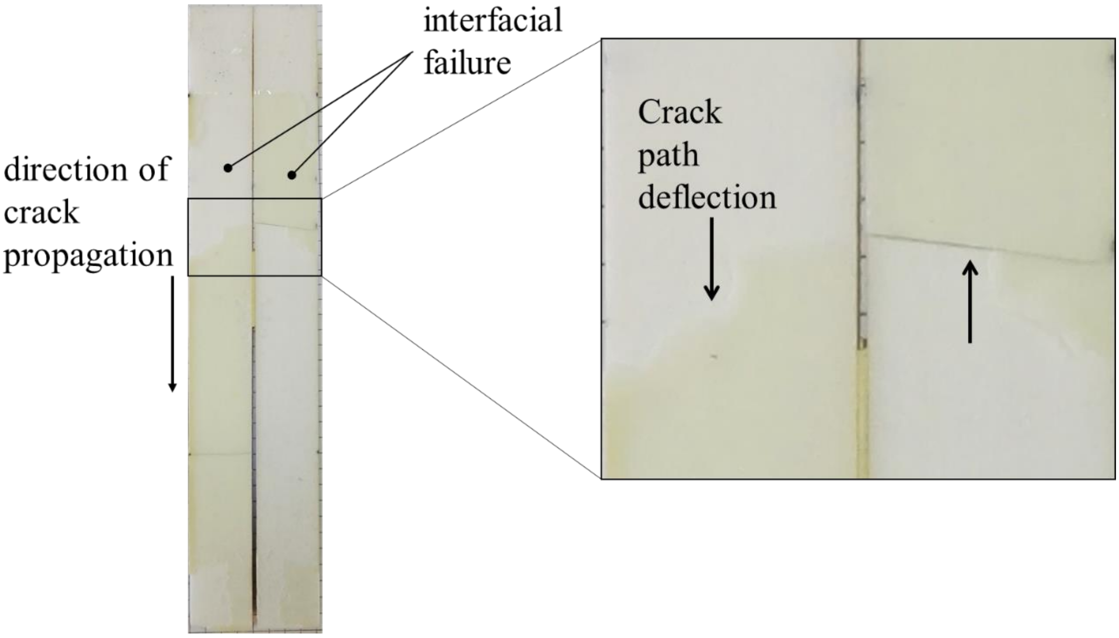

Fig. 3.8: Typical fracture surface of the DCB joint.

3.2.2. Analysis of the obtained values of fracture toughness

Fracture toughness depends not only on the characteristics of the adhesive but also on the properties of the mating surfaces, especially when failure is dominated by interfacial fracture. As shown in the previous chapter, additive manufacturing may lead to changes of surface roughness of the final parts because of variations in the powders employed for printing and for this reason, it is important to maintain strict control on this factor to make sure that eventual variations in fracture behavior are not coming from processing factors. This is an important point for the outcome of current research, because the selected model material system, comprising epoxy-bonded nylon substrates, should be able to display a consistent interfacial mechanical response from batch to batch. It is only through the fulfillment of this condition that the subsequent mechanical responses of bio-inspired samples can be truly associated with the proposed interfacial designs, rather than to variations in interfacial response due to scattering in surface morphology.

Load-displacement curves obtained during DCB tests on bulk samples of batch#4, #5 and #6 with $t =$ 6 mm are reported in Fig. 3.9 (a), (b) and (c). Batches production parameters have been maintained constant except for batch#4 where samples have been realized using only new powder (i.e. no addition of recycled one, as it is commonly done in SLS). Using Eq. 3.1, different values for average fracture toughness have been found, i.e., 350 J/m^2 for BM6_#2, 450 J/m^2 for BM6_#3 and 425 J/m^2 for BM6_#4. These values have been obtained by interpolating experimental data with an analytical curve following the same method described before. These differences in fracture toughness value have been compared with differences in surface roughness, and results are reported in Fig. 3.10 together with a typical roughness profile recorded in the experiments. A very good correlation between the average roughness and the average fracture toughness is observed. Notice that the lowest roughness value was achieved for samples realized without recycled powder. However, this condition corresponds to the lowest fracture toughness. Therefore, it is apparent that the considered model material system displays some degree of sensitivity to surface roughness, similarly to what has been observed in previous works (A. F. Harris and Beevers, 1999; Boutar *et al.*, 2016; Rotella *et al.*, 2016). However, it should be also recognized that the fracture toughness is characterized by a relatively high scatter and, also, that the dispersion bands are partially overlapped. Consequently, even if the average values of fracture toughness show a comparable trend with average roughness, the observed scatter also suggests that the differences in the obtained fracture toughness may have low significance from a statistical viewpoint. However, these results represent a useful basis for the analysis and evaluation of the mechanical response of the bio-inspired samples associated with the different fabrication batches.

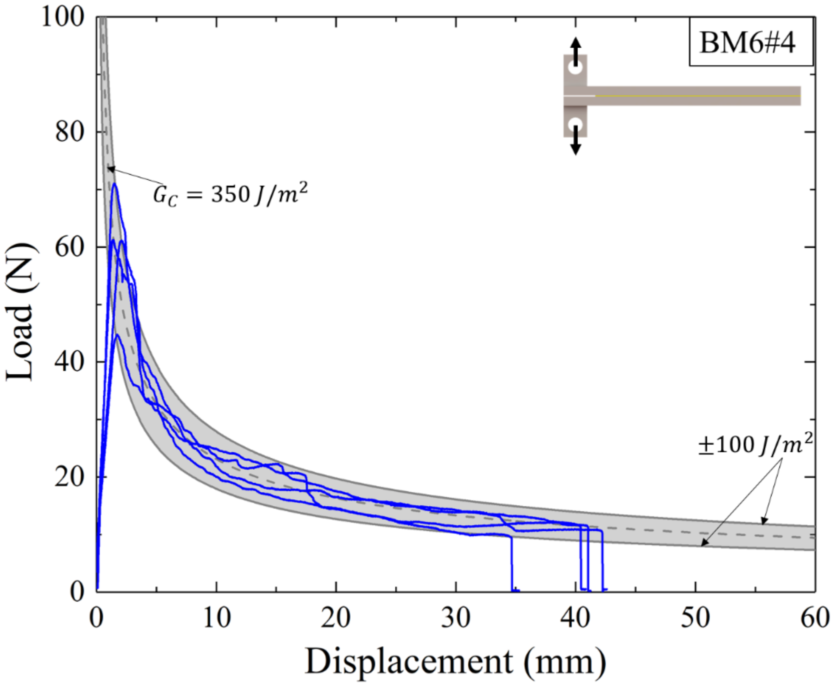

(a)

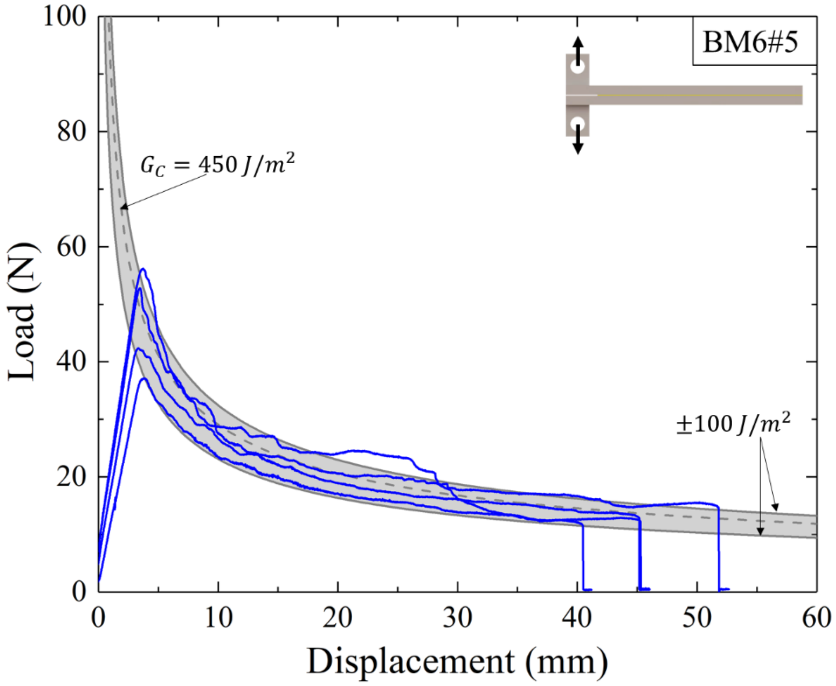

(b)

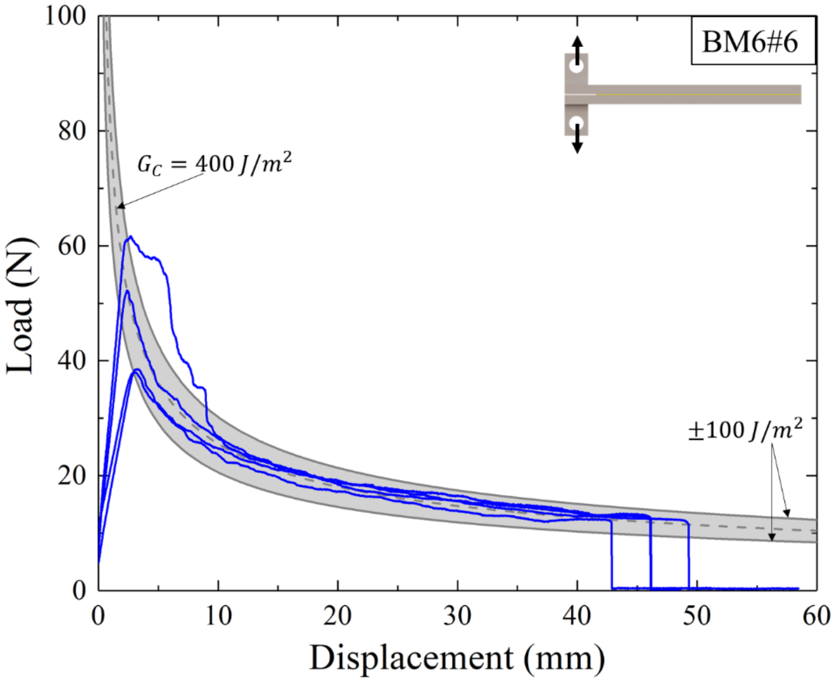

(c)

Fig. 3.9: Load displacement curves obtained on DCB samples and fracture toughness of batch (a) #4 (b) #5 and (c) #6.

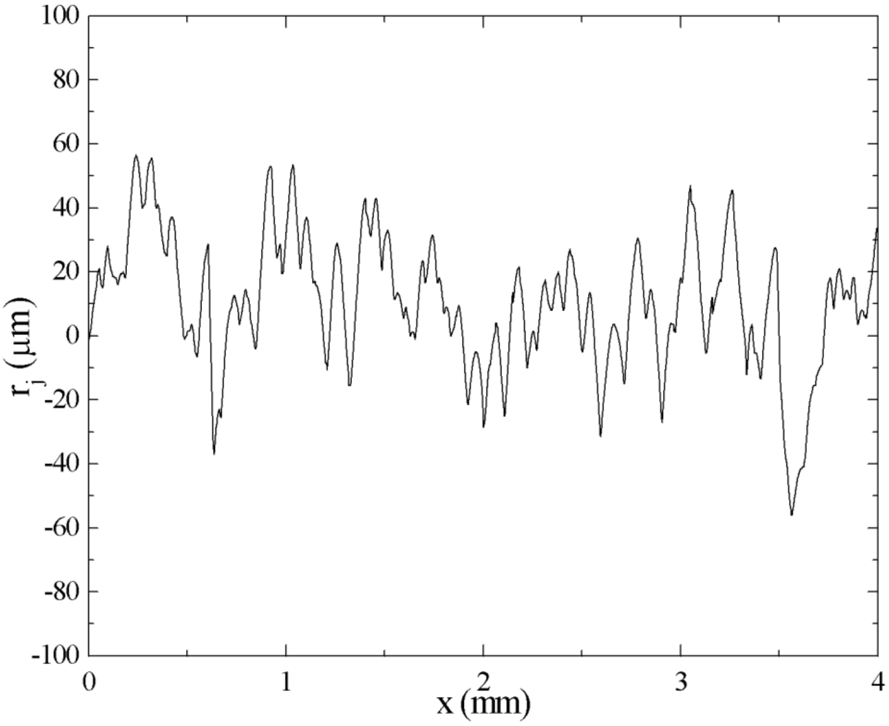

(a)

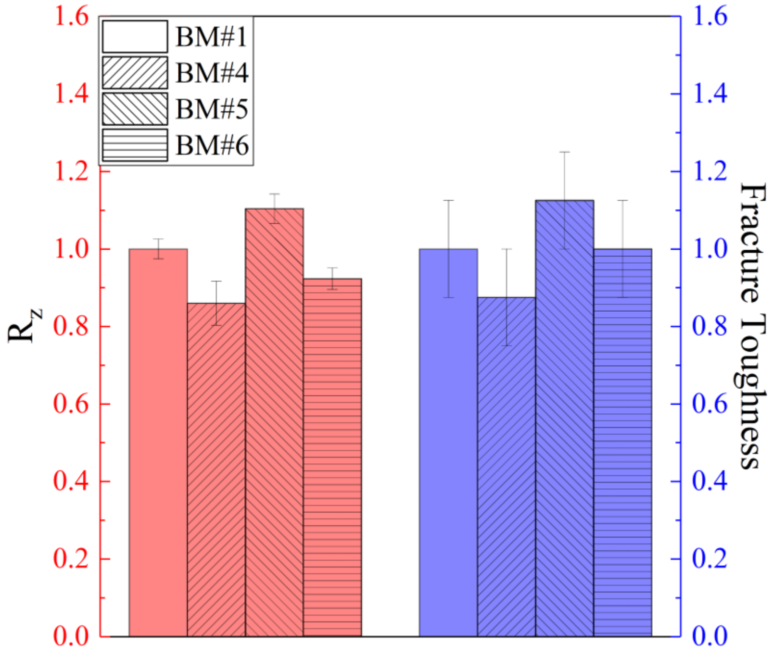

(b)

Fig. 3.10: a) Example of roughness profile obtained with a profilometer and (b) comparison between fracture toughness (blue) and roughness values on the longitudinal direction (red) of different batches normalized respect to data from the first batch, i.e., R_z.

3.2.3. Tapered Double Cantilever Beam

The load-displacement curves obtained in TDCB tests on TBM_#2 have been excluded from the analysis due to issues occurred during fabrication, i.e., misaligned joints and variability of the adhesive layer thickness. Load displacement curves obtained from TDCB tests on TBM_#3 are reported in Fig. 3.11 and Fig. 3.12 and these results are referred to samples realized with two different adhesive thickness, i.e., t_a equal to 0.6 mm and t_a equal to 0.5 mm. Both results are characterized by a high dispersion for both ultimate displacement and load average value. As explained in the previous chapter, TDCB joints potentially allow us to achieve a steady-state crack propagation accompanied by a load plateau in the load-displacement curves. However, it is apparent that the mechanical tests did not allow us to achieve a clear plateau in the mechanical response, as shown in Fig. 3.12 and 3.13. To this aim, it should be noted that because of manufacturing constraint the actual TDCB joints were resized compared to the dimension suggested by ASTM D3433-99 (ASTM Standard D3433-99, 2012). This might be a potential reason for the discrepancy between the expected and the obtained experimental response. The results of mechanical tests have been compared in terms of fracture toughness.

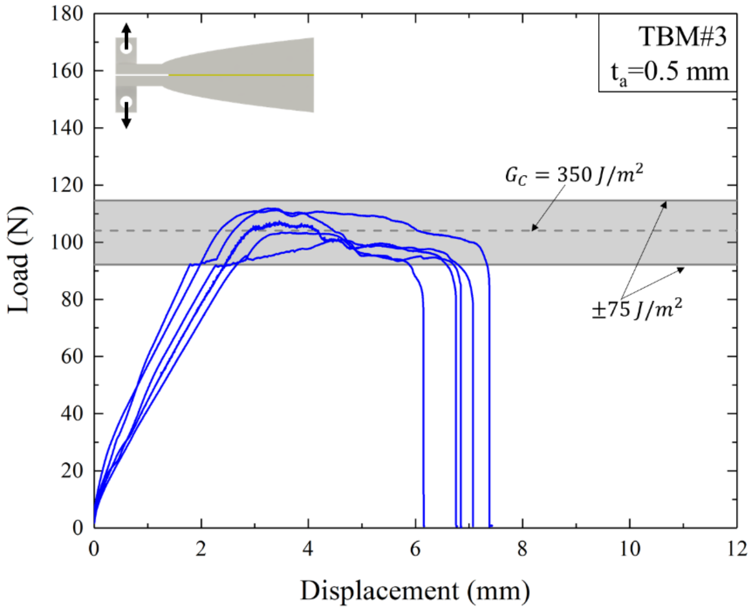

Fig. 3.11: Load displacement curves obtained on TDCB samples with t_a equal to 0.5 mm.

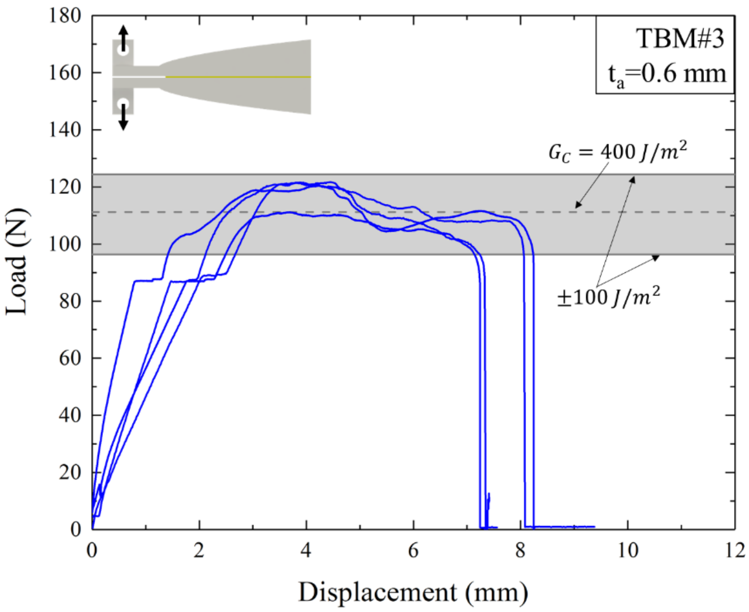

Fig. 3.12: Load displacement curves obtained on TDCB samples with t_a equal to 0.6 mm.

After calculating the average value of load for each test, equation 2.6 in the previous chapter from (Anderson, 2005), was employed to identify the fracture toughness G_{Ic} since substrate geometry data are known. The value for the fracture toughness for t_a=0.5mm was found to be equal to 350±75 J/m^2 and 400±100 J/m^2 for t_a=0.6mm as reported in Fig. 3.11 and Fig. 3.12. These values are in good agreement with results obtained on DCB samples.

Even then, fracture toughness values have been related to surface roughness and compared with DCB data. In particular, it was calculated the average value among data described above, neglecting in this phase, differences in adhesive thickness since the final objective is to relate fracture toughness to surface roughness. The results are shown in Fig. 3.13. Global results seem to be at odds with results obtained for DCB samples: it was found that, even if the average surface roughness is high, the average fracture toughness decreases compared with DCB results. However, it should be recognized that the range of variation of the roughness of TDCB substrates is quite large, and does not allow to draw reliable conclusions on this point. Moreover, the subsequent mechanical tests are only based on the DCB configuration. Therefore, this point will be explored in future works.

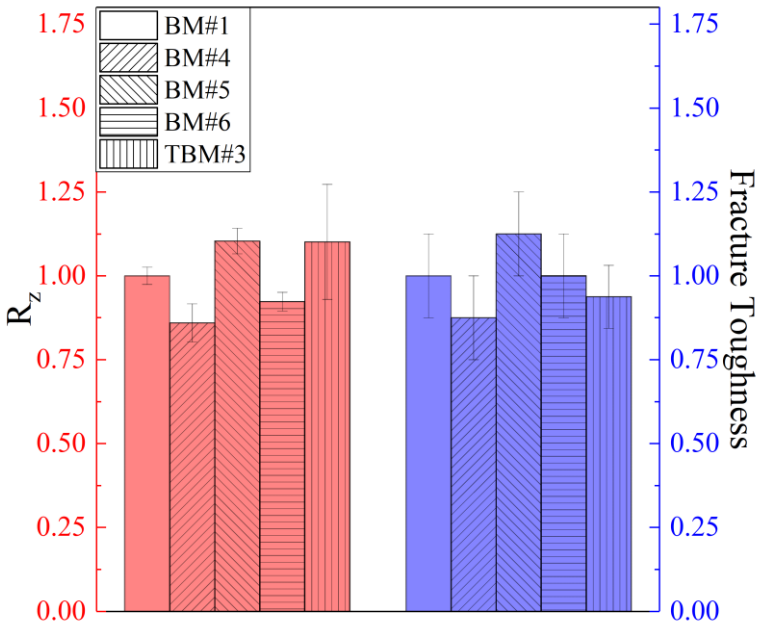

Fig. 3.13: Roughness values on the longitudinal direction (red) and fracture toughness values (blue) of different batches for DCB and TDCB samples normalized with respect to data from the first batch.

3.3. Bioinspired double cantilever beam adhesive joints

The load-displacement curves of DCB tests carried on samples with circular and square subsurface channels with two different substrate thicknesses are reported in Fig. 3.14. DCB samples without modification, i.e., benchmark samples, have been used as a reference in order to evaluate improvement in joint behavior with the addition of subsurface channels. The load-displacement curve related to bio-inspired samples exhibits a shift toward higher loads that becomes more significant with square subsurface channels. In all tests, it was also observed an increment of the displacement at failure that became more significant for the substrate with square subsurface channels. This increment of applied displacement occurs in conjunction with the hindering of crack propagation, along with an increment of the energy requested for crack propagation.

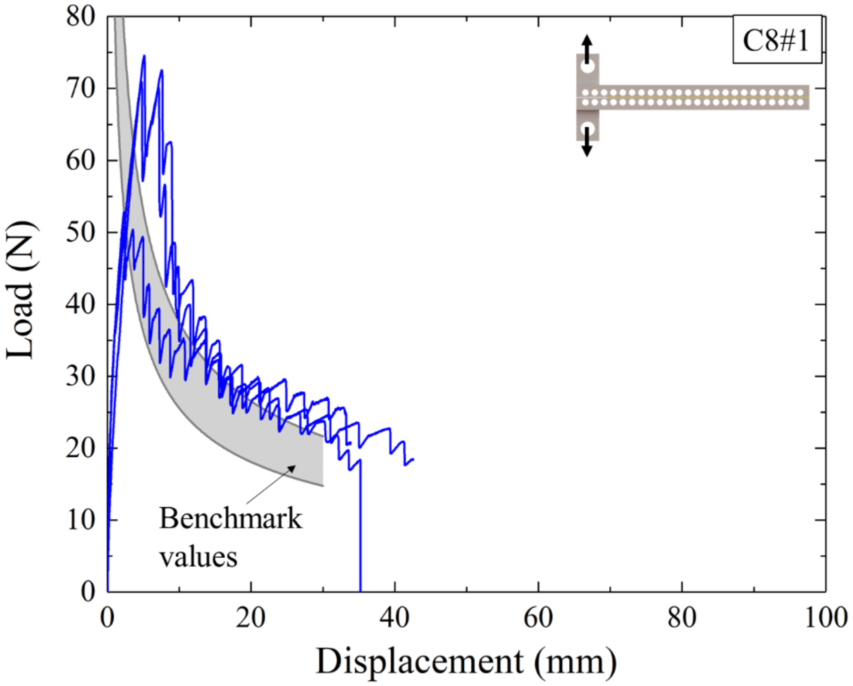
C8#1
Load (N)
Displacement (mm)
0
10
20
30
40
50
60
70
80
0
20
40
60
80
100
Benchmark values

(a)

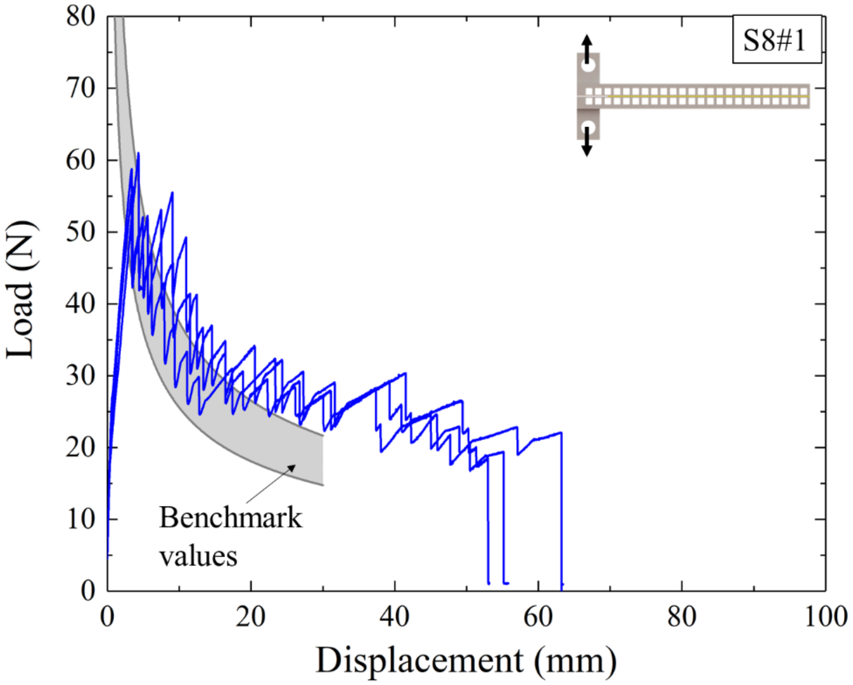
S8#1
Load (N)
Displacement (mm)
0
10
20
30
40
50
60
70
80
0
20
40
60
80
100
Benchmark values

(b)

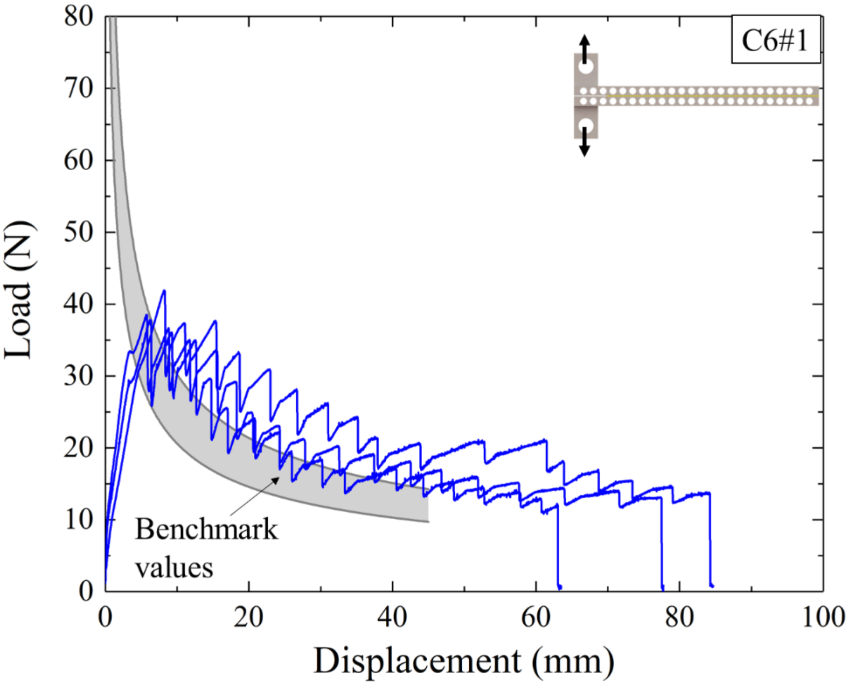

(c)

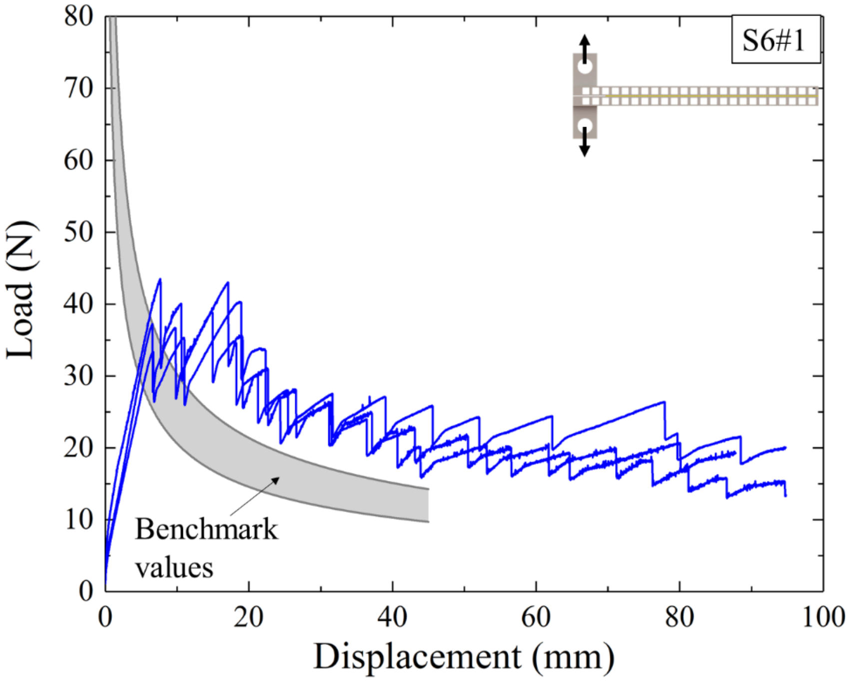

(d)

Fig. 3.14: Load displacement curves obtained on DCB samples with subsurface channels related to a) C8_#1, b) S8_#1, c) C6_#1 and d) S6_#1.

Global responses are characterized by load fluctuations for all channels shape and substrate thickness due to a crack trapping effect, i.e., a periodic alternation between crack hindering/arrest and sudden propagation, as observed by FE analysis by Afferrate et al. (Afferrante, Carbone and Demelio, 2012). It is important to notice that no differences were observed in the mechanisms of failure (interfacial) and the appearance of fracture surfaces, which further confirms that the observed variations in the mechanical response are due to the channels.

Load fluctuations occurring during crack propagation do not allow the crack to propagate smoothly, but rather with intermittent arrests and initiations at the location of the channels. High-resolution images of the crack tip region have been recorded in order to investigate the crack propagation behavior. Since joints with thinner substrates have shown a larger increase of dissipated energy, the analysis has been restricted to this case. The acquisition of high-resolution images was synchronized with the crosshead displacement, thereby allowing to easily associate the locations where the images were taken on the load-displacement curve. The snapshots, as shown in Fig. 3.15 and Fig. 3.16, correspond to points that lie around a load fluctuation and permit to identify the crack tip position where the load peak is reached. That condition is achieved when the crack front is approaching the pillar. In this phase, until the load reaches the peak, the crack grows very slowly meaning that most of the supplied energy is stored in the material rather than contributing to crack propagation. After that, the crack snaps through and the load drops, and a portion of the stored elastic energy in the beam is suddenly lost in the process, and released as kinetic energy. This gives rise to oscillatory waves, which dissipate the released energy, for instance, in the form of heat. Similar behavior was obtained for composite materials comprising an alternation of stiff and compliant layers perpendicular to the crack growth direction (Kolednik *et al.*, 2011).

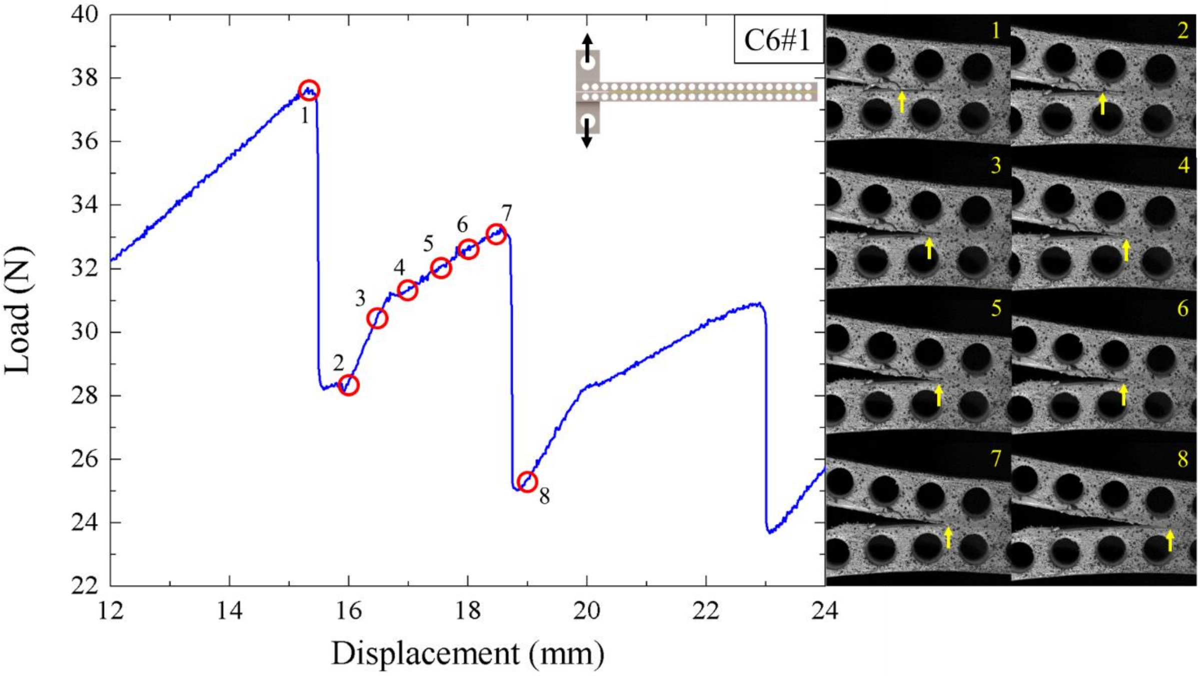

Fig. 3.15: Comparison between the load-displacement curve and high-resolution snapshot on DCB joint with circular bioinspired channels and substrates thickness equal to 6 mm.

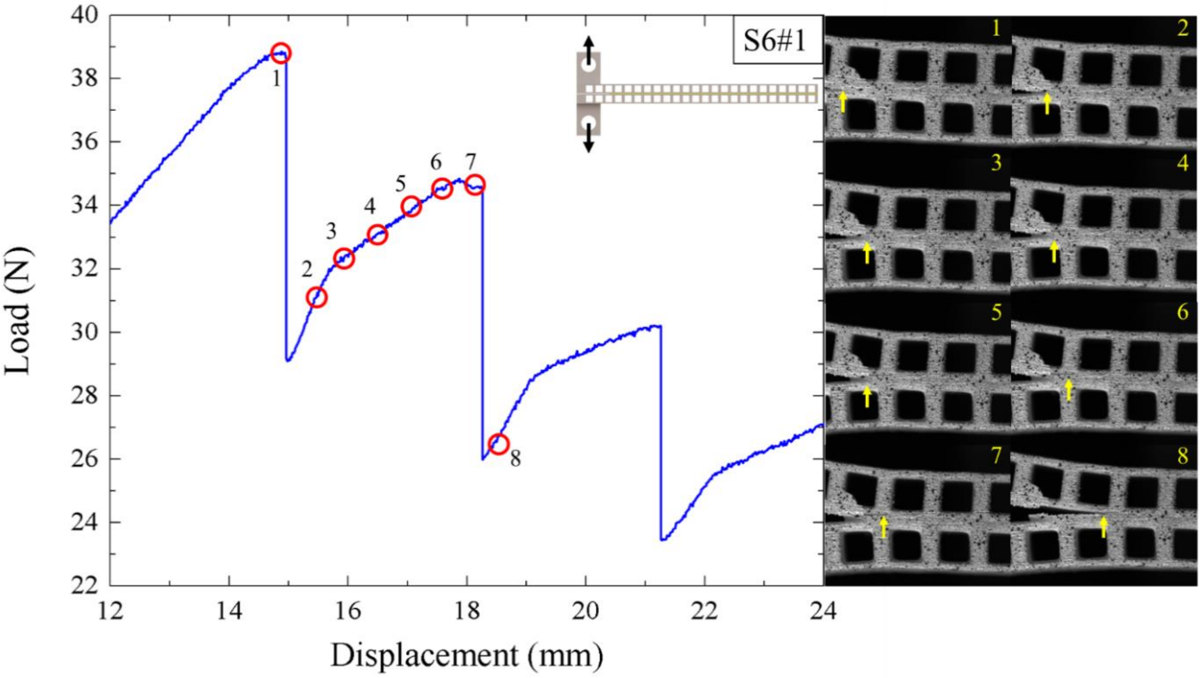

Fig. 3.16: Comparison between the load-displacement curve and high-resolution snapshot on DCB joint with square bioinspired channels and substrates thickness equal to 6 mm.

Load fluctuations are also characterized by a change in slope and this modification was studied in relation to crack propagation as shown in Fig. 3.17. The global response confirms what observed using high-resolution images: when the load increase, the crack grows very slow and, after that, when the load drops off, the crack jumps. It is also possible to notice that crack growth rate changes in correspondence of slope discontinuity. However, because the accuracy in the determination of the crack tip position from high-resolution images can be fairly low, additional experimental work should be done to further assess this point.

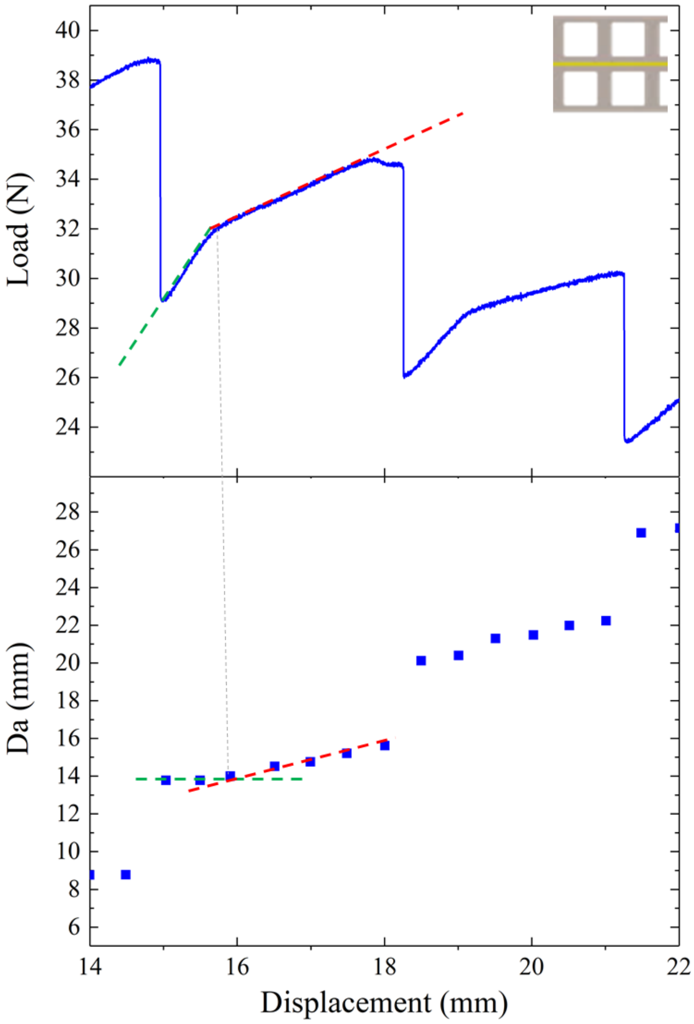

Fig. 3.17: Crack propagation mechanism on DCB joints with bioinspired interfaces

Global results have been compared evaluating the energy requested for crack propagation as shown in Fig. 3.18. As explained before, the energy was obtained by calculating the area below load-displacement curves. These values have been then divided by crack area, i.e., crack length multiplied by sample width and then normalized respect to values obtained for benchmark samples. Results demonstrate that, even if the crack trapping reproduction is independent by channel shape, the latter strongly influences the energy requested for crack propagation. In particular, the best results have been obtained with a thinner substrate with square channels. This result allows assuming that plastic energy plays a significant role in this mechanism. In fact, residual plastic deformation has been observed in correspondence of sharp edges, i.e., square, and thin parts that work as beam subjected to bending, i.e., the upper part of square channels.

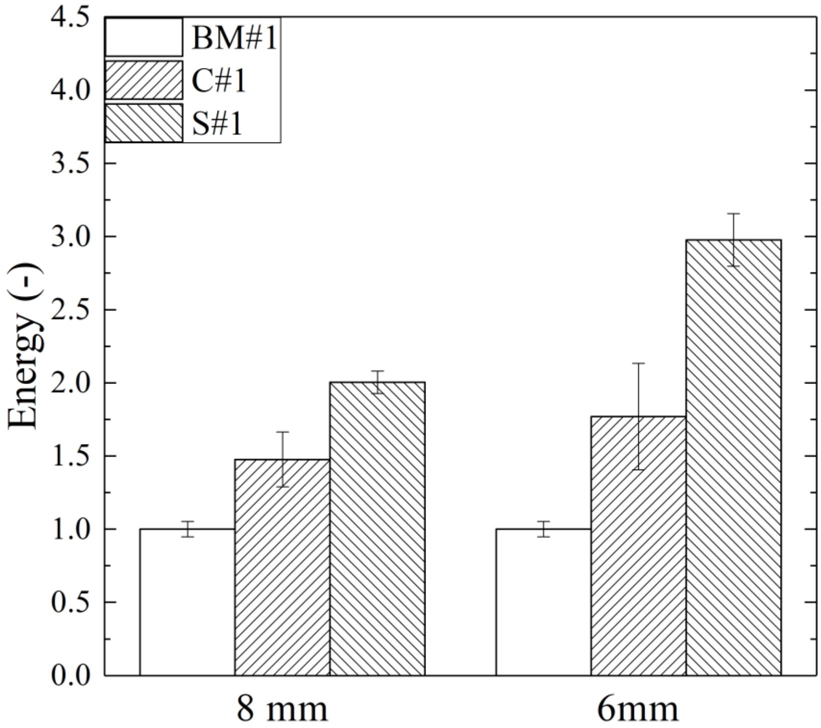

Fig. 3.18: Energy requested for crack propagation obtained experimentally on DCB joints with bioinspired channels

3.4. Toughening using non-planar interfaces

As in the previous chapter, the results obtained on DCB samples with a flat interface have been used as a reference for a comparative analysis with samples with substrate modification, i.e.; sinusoidal interface. The load-displacement curves of DCB tests carried on samples with the sinusoidal interface are reported in Fig. 3.19. Substrates with A/λ equal 1/4 were realized using two different thicknesses, i.e., 6 mm and 8mm. All curves exhibit a shift toward higher loads corresponding to an increment of the energy requested for crack propagation and an increment of the displacement at failure value also due to an increment of the bonded area. Load-displacement curves are characterized by load fluctuations for all sinusoid used to modify the joint interface and for both substrates thickness. These fluctuations, together with the curves shift, increases the energy requested for the crack propagation and it could be noted that this increment became more significant with A/λ equal 1/2. A similar behavior was also observed by Cordisco et al. (Cordisco *et al.*, 2016) for test carried out on aluminum DCB joint with sinusoidal interfaces; However, the authors did not observe load fluctuations in all tests and that could be attributed to difference in sinusoidal length scale compared with sample dimension: with low values of sinusoid wavelength, interface modification seems to acts more as "high roughness" than as architected interface. The adhesive failure occurred in all tests as observed from fracture surfaces on benchmark samples. Unlike DCB joints with the flat interface, in these tests, the crack path changes from one substrate to the other during each sinusoidal period producing bridging ligaments and plasticization and fracture of the adhesive. Furthermore, substrates exhibit plastic deformation at the end of all tests that became more noticeable with the increment of the A/λ ratio.

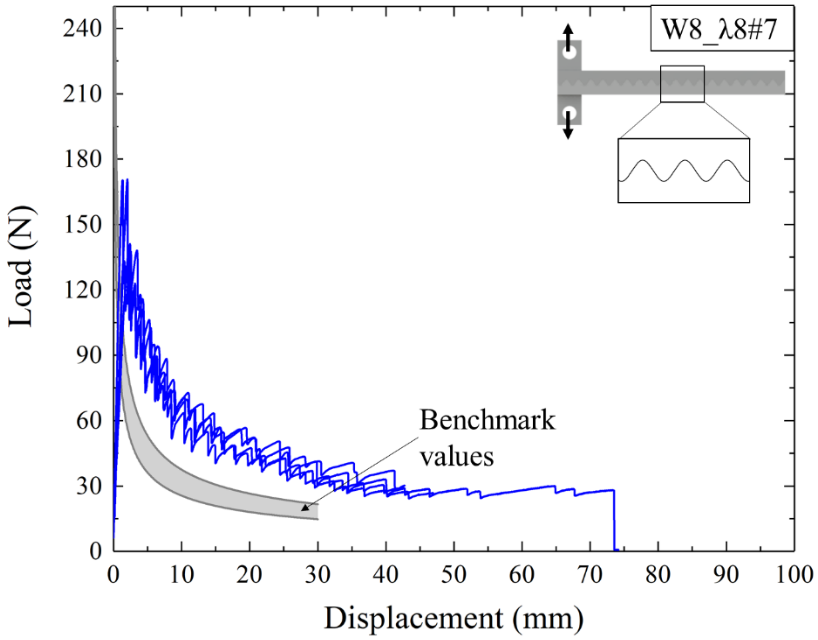

(a)

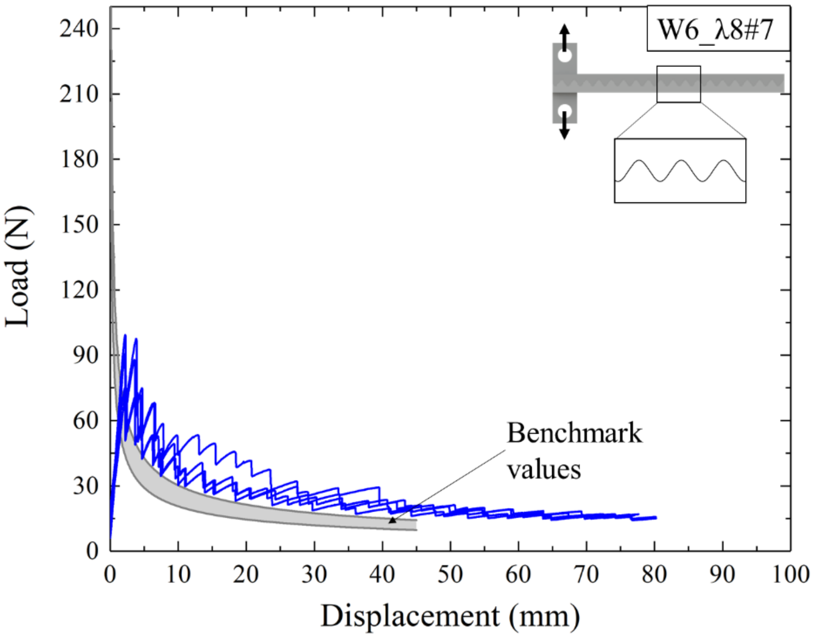
W6_λ8#7
Load (N)
Displacement (mm)
Benchmark values
0
30
60
90
120
150
180
210
240
0
10
20
30
40
50
60
70
80
90
100

(b)

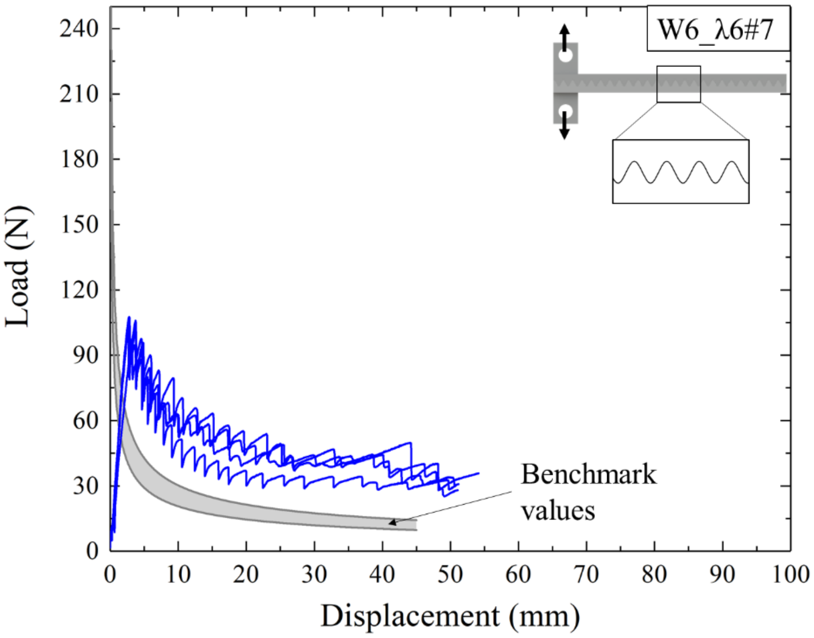
W6_λ6#7
Load (N)
Displacement (mm)
Benchmark values
0
30
60
90
120
150
180
210
240
0
10
20
30
40
50
60
70
80
90
100

(c)

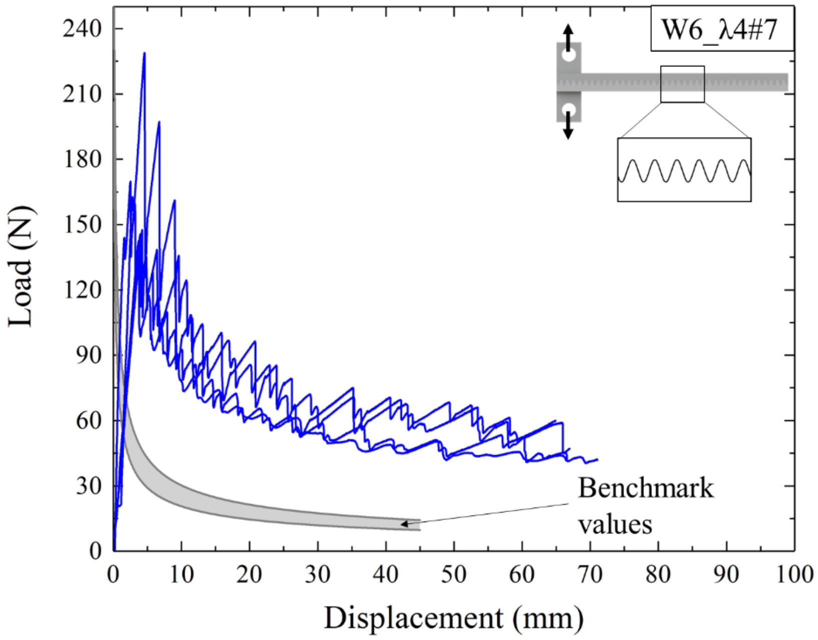

(d)

Fig. 3.19: Load displacement curves obtained on DCB samples with sinusoidal interface related to a) SIN8_1/4_#7, b) SIN6_1/4_#7, c) SIN6_1/3_#7 and d) SIN6_1/2_#7

The modification of DCB joints introduces a local mixed mode in crack propagation mechanism and that helps to arrest crack propagation since it is well known that propagation in Mode-II needs more energy if compared with pure Mode-I (Anderson, 2005). Results have been also compared in terms of the energy requested for crack propagation. This value was calculated as the area below the load-displacement curves. As explained in the previous chapter, the increment of the energy requested for crack propagation with the sinusoidal interface is also due to an increment of the bonded area. For this reason, all energy values have been divided by the effective crack area calculated multiplying the sinusoidal interface length with substrate width. All values have been normalized respect values obtained on benchmark samples. Results, shown in Fig. 3.20, demonstrate that the modification of the interface allows increasing the energy requested for crack propagation. In particular, since energy values have been dived by the propagation area, the increase is just related with the introduction of Mixed-Mode in the crack propagation mechanism and, for that reason, the best result was obtained with A/λ equal to 1/2 with a value four times higher than reference one.

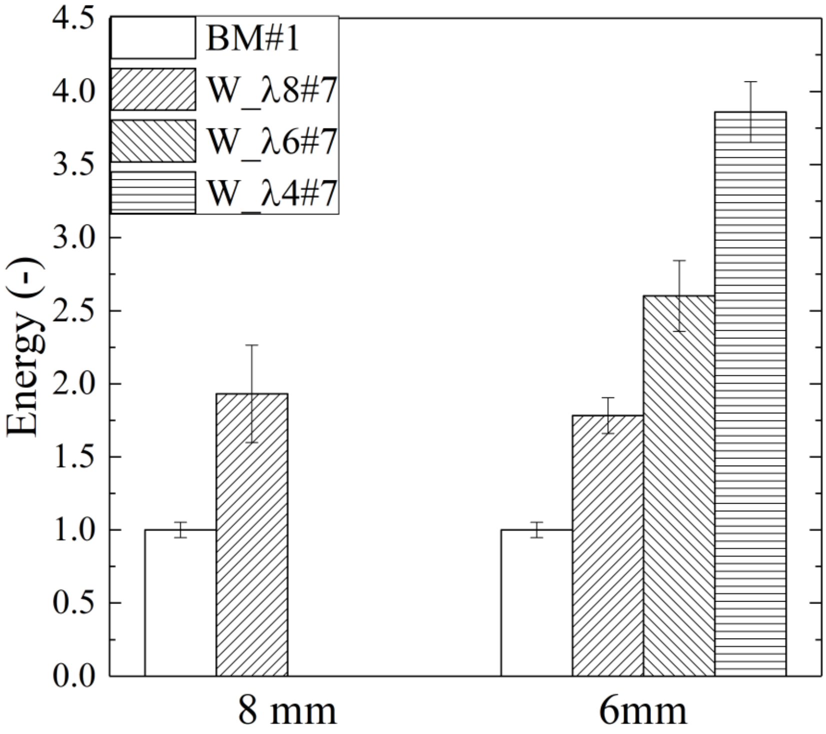

Fig. 3.20: Energy requested for crack propagation obtained experimentally on DCB joints with bioinspired sinusoidal interfaces

The crack trapping mechanism was analyzed using high-resolution images. It was chosen to acquire images of the crack tip region to analyze the crack trapping mechanism deeply and whole sample images to evaluate crack length. The images acquisition was done by correlating the analogic acquisition with crosshead displacement in order to identify the location on load-displacement curves where the images have been captured. Fig. 3.21 shown high-resolution images analysis of crack trapping mechanism of W_λ4#7 samples. The snapshots corresponding to points located around a load fluctuation allow identifying the crack tip position where the load peaks or minimums are reached. When the crack tip is located on the sinusoid peak (point 2), the crack grows very slowly until it is arrested when it is located on the sinusoid side (point 5). In this phase, the crack grows very slowly and the load reaches the peak meaning that the corresponding portion of the supplied energy is employed to advance the crack in mixed-mode conditions. After that, the load drops off and the crack propagates very fast reaching the next sinusoid peak (from point 5 to point 6). That is related to unstable crack propagation. The crack propagates along with the substrate-adhesive interface and, when it is located on the sinusoid side, the crack path is deflected to the other interface allowing the development of an adhesive ligament (Fig. 3.21 (b)). During crack growth, ligament deformation requires supplementary energy that causes an increase in load that reaches a local peak (points 1 and 7). After that, the ligament fails and the load drops off and the energy stored into the adhesive layer is released (point 2 and point 8). Overall, both mechanism contributes to crack trapping phenomena even if the load fluctuation related to ligament development and failure is smaller than fluctuation related to changes in the propagation mechanism.

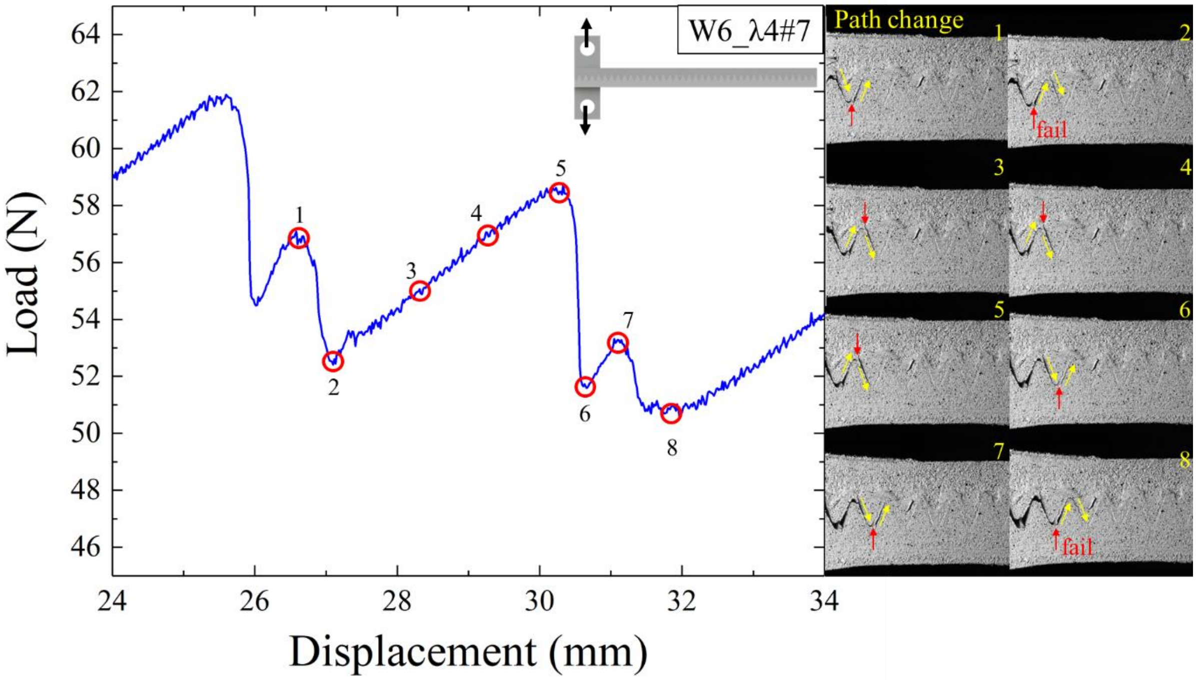

(a)

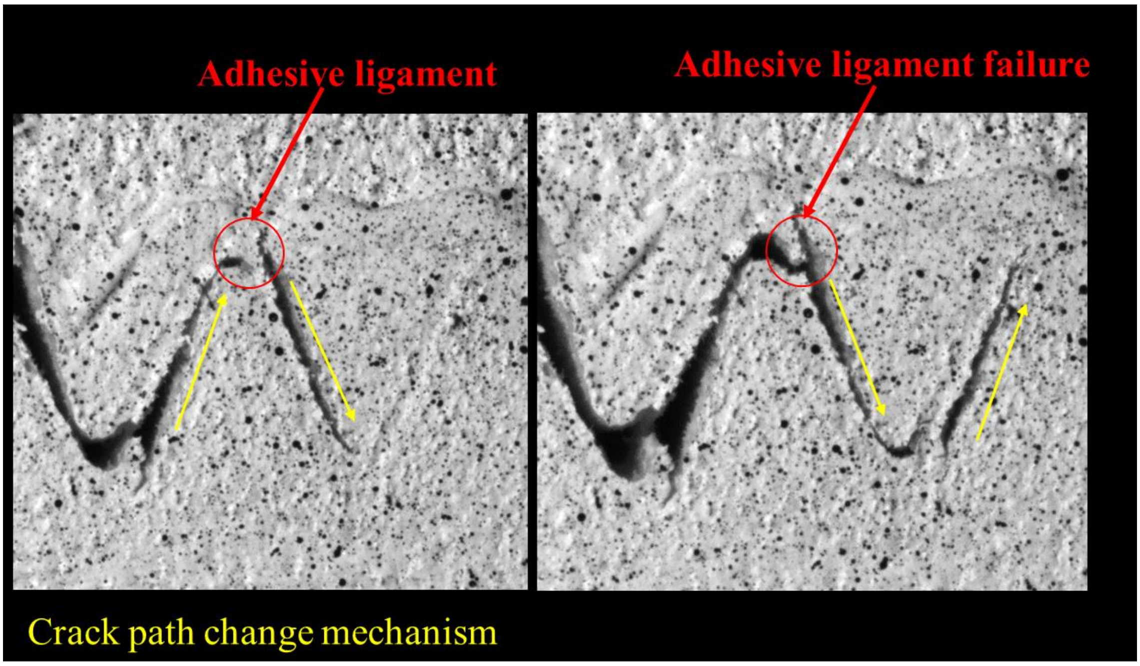

(b)

Fig. 3.21: (a) Comparison between the load-displacement curve and high-resolution snapshot on DCB joint with sinusoidal bioinspired interface and substrates thickness equal to 6 mm and (b) images of crack propagation mechanism.

Chapter 4: Finite element modeling

A frequently used modeling approach to assess crack propagation in engineering materials, including adhesive bonded interfaces, is the cohesive zone model (CZM) of fracture (Hillerborg, Modéer and Petersson, 1976; Jin, Paulino and Dodds, 2003; Li *et al.*, 2005; Alfano *et al.*, 2009; Park and Paulino, 2011). The CZM assumes that cohesive tractions hold paired cohesive surfaces together. The separation of cohesive surfaces is then dictated by the cohesive law, which is a traction-separation relation, such that final failure is obtained when the opening displacement reaches a critical value. The area under the cohesive model is defined as *cohesive energy*. Increasing the opening displacement, the traction increases until it reaches a maximum (i.e., cohesive strength) and then, following a softening curve, it decreases to zero when the displacement is equal to the critical value. When the traction is zero, a new crack surface is created.

The cohesive zone model is a powerful tool to analyze crack propagation in adhesive joints. The application of the cohesive zone model to crack propagation problems requires the determination of the traction-separation law and, in particular, the determination of: (i) the initial stiffness of the model, (ii) the cohesive strength, (iii) the cohesive energy (or the critical displacement), (iv) the shape of the curve. Although cohesive strength and energy have been shown to be more important than the specific shape chosen for the cohesive(Park and Paulino, 2011; Alfano, Lubineau and Paulino, 2015), several shapes for the traction-separation laws have been proposed in the published literature, e.g, bilinear model (Hillerborg, Modéer and Petersson, 1976), trilinear model (Yang, Thouless and Ward, 1999), exponential model (Xu and Needleman, 1994) to list a few.

In this chapter, we discuss the results of FE simulations carried out to analyze the mechanics of debonding along bioinspired interfaces.

4.1. Determination of cohesive fracture parameters

Finite element simulations of crack propagation were performed using cohesive elements available in an FE commercial code (Abaqus Standard 14.1, Simulia Corporation). The cohesive model chosen for this purpose is the bilinear one and the determination of the cohesive properties was carried out using experimental data obtained from mechanical testing of benchmark Double Cantilever Beam (DCB) adhesive joints, as described in the previous Chapter. Cohesive parameters have been then validated by comparing actual experimental results obtained for bio-inspired joints with the corresponding FE predictions. The calibration procedure was carried out using experimental data obtained for the first production batch. Notice that potential differences between finite element simulations and experimental results from other batches will be addressed to the variations highlighted previously concerning material fabrication.

4.1.1. Mechanical properties of the substrates

The material characteristics employed in the numerical simulations were determined in tensile tests of *dogbone* samples under quasi-static loading (i.e., 0.5 mm/min), as described in the previous chapter. The material was assumed to be linear-elastic and isotropic. The elastoplastic properties used as input variables in Abaqus/Standard are reported in Tab. 4.1, while a typical σ-ε curve is shown in Fig. 4.1.

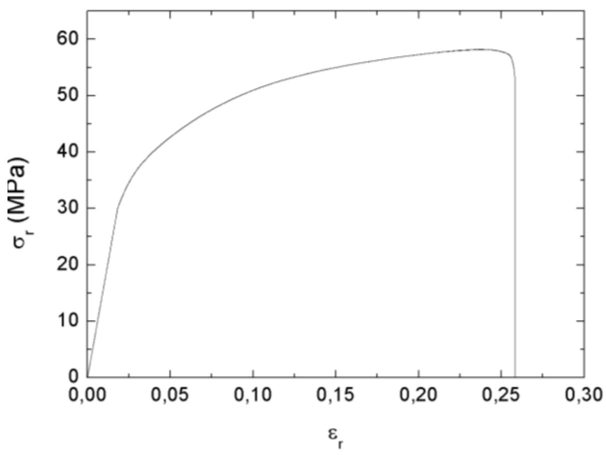

Fig. 4.1: Stress-strain response of nylon dogbone samples

Tab. 4.1: Mechanical properties of nylon substrates

Young's modulus	E	1650 MPa
Poisson's ratio	ν	0.4
Yield Strength	S_y	30 MPa
Plastic Strain	ε_r	0.018
Ultimate Strength	S_{ut}	60 MPa

4.1.2. Cohesive model

The adhesive thickness was replaced by a single row of cohesive elements and, therefore, the adhesive layer was not explicitly accounted for in the simulations. Although the selected approach assumes constant peel stresses through the thickness of the adhesive layer and does not account for the local constraint in the stress field, it can still provide accurate results (Yang, Thouless and Ward, 1999; Zavattieri, Hector and Bower, 2008). A bilinear law, provided by the following equations, could describe the cohesive element response, employed in the simulations (Fig. 4.2):

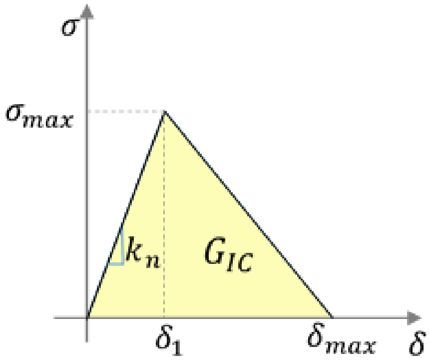

Fig. 4.2: Fracture separation law of cohesive elements

$$\sigma = \begin{cases} k_n\delta & 0 \le \delta \le k_n \cdot \sigma_{max} = \delta_1 \\ \sigma_{max}\dfrac{(\delta_{max}-\delta)}{(\delta_{max}-\delta_1)} & \delta_1 \le \delta \le \delta_{max} \\ 0 & \delta \ge \delta_{max} \end{cases} \quad (4.1)$$

Where k_n is the initial stiffness, σ_{max} is the cohesive strength, δ_{max} is the maximum displacement at failure and δ_1 is the crack opening at maximum strength. The cohesive energy is given by the area below the $\sigma - \delta$ curve:

$$G_{IC} = \frac{\sigma_{max}\delta_{max}}{2} \quad (4.2)$$

Therefore, to characterize the fracture behavior using cohesive elements, three distinct properties must be identified: k_n, σ_{max} and G_{IC}. As suggested by Högberg (Högberg, 2006), the initial stiffness could be calculated as:

$$k_n = \frac{\bar{E}}{t} \quad (4.3)$$

Where t is the adhesive layer thickness and $\bar{E}$ is effective Young's modulus of the adhesive layer, obtained by:

$$\bar{E} = \frac{E(1-\nu)}{[(1-2\nu)(1+\nu)]} \quad (4.4)$$

where ν and E are the Poisson's ratio and Young's modulus of the adhesive. Using the adhesive Young's modulus and its thickness, the cohesive zone stiffness was found to be equal to 8500 MPa/mm.

As said before, an energetic linear model was employed for the damage evolution criteria. The energy criterion defines damage evolution in terms of the energy required for failure (cohesive energy) after the initiation of damage. The value of this energy, G_{IC}, was set equal to the value obtained from experimental results, i.e., 0.4 kJ/m^2.

4.1.3. Mesh generation

In this work, two different kinds of elements have been used: CPE4 and COH2D4. The first is a four-node two-dimensional plane strain element used for the substrates modeling. The second one, i.e., COH2D4, is four-node two-dimensional cohesive elements and it was used for the adhesive layer. Two different models have been created, one for DCB samples with substrate thickness equal to 8 mm and a second one for the thinner substrates, i.e., 6mm. The number of elements employed for the thicker model is 43262 of which 42252 liner quadrilateral elements of type CPE4 and 1010 linear quadrilateral elements of type COH2D4 whereas the number of nodes is 43778. Similarly, the number of elements employed in the second model is 23223 of which 22203 linear quadrilateral elements of type CPE4 and 1020 linear quadrilateral elements of type COH2D4. The total number of nodes is equal to 23711. A single layer of cohesive elements was used and element size was gradually reduced to obtain numerical convergence and to ensure that the cohesive zone was resolved with a sufficient number of interface elements. For this reason, the cohesive element size was set equal to 0.1mm. The details of the FE mesh are provided in Fig. 4.3 for the 8mm-thick substrates DCB adhesive joints.

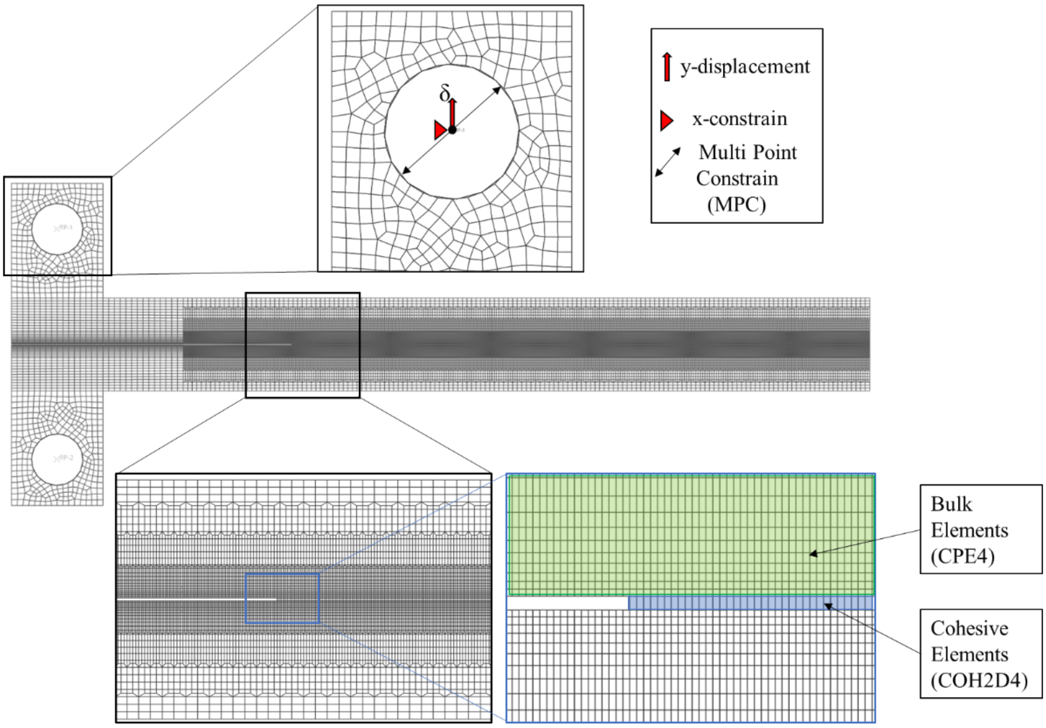

Fig. 4.3: Details of the mesh

4.1.4. Boundary conditions

The applied load was imposed under displacement control. The displacement was applied as shown in Fig. 4.3. The connection between the load application point and the loading blocks has been done using a multi-point constrain (MPC).

Boundary conditions are described in Fig. 4.3. Displacement in the *x*-direction at the load application point was equal to zero. Similarly, the *y*-displacement at the loading blocks was set equal to 30 mm to resemble the opening condition imposed by the testing machine.

Non-linear static analyses with large displacement and small strain were performed. The outputs requested are the load-displacement curves and a complete breakdown of dissipated energy, i.e., cohesive energy, elastic energy, plastic energy, and total energy.

4.1.5. Analysis setting parameters and requested output variables

The following settings were employed to facilitate the convergence of finite element simulations:

- *Time incrementation type* can be automatic or fixed time incrementation. In the first case, the software starts the incrementation using the value chosen for the initial increment size and the size of subsequent time increments are adjusted based on how quickly the solution converges. Using the fixed time incrementation, the value entered for the initial increment size is used throughout the step. In this work, it was chosen to use the automatic time incrementations, because it guarantees the best results in terms of computational costs.
- *The Maximum number of increments*: Abaqus restricts the maximum number of increments in each step. If the step exceeds this number of increments, the analysis ends. The default value, that is equal to 100, was increased up to 10^6.
- *Initial increment size*: Is the initial value of the increment size used by Abaqus. In this case, this parameter was fixed equal to 0.001
- *Minimum and maximum increment size*: These two parameters are involved only for automatic time incrementation. These parameters are referred to the maximum and minimum values of the increments. If the problem solution needs a smaller time increment than the chosen one to reach a convergent solution, it terminates the analysis,

and for this reason, the choice of this parameter is important. The maximum and maximum values of the increment size were set equal to 0.02 and 10^{-20} respectively.

It is also possible to customize all variables that control the algorithms convergence and time integration accuracy. The default variables usually work well, but customizing them may help to solve for particularly difficult analyses. In this case, it was also chosen to increase the number of maximum attempts needed to reach increment convergence up to 20.
Simulation outputs have been modified to include some variables required for our analyses. In particular, in addition to default variables (e.g., deformation, stress, etc.), it was included also: (i) energy variables, in order to evaluate different amounts of energy requested for crack propagation; (ii) SDEG parameter that evaluate the cohesive element damage (i.e., SDEG= 0 means no damage, SDEG=1 means the element is fully damaged and does not bear any traction).

4.1.6. Determination of initial crack length

During the experiments, a pre-crack procedure was carried out, therefore the actual value of the initial crack length (a_0) at the beginning of mechanical tests was not known with good accuracy. To account for the increment in crack length due to the pre-crack procedure, a correction was made in FE models adding a new term, i.e., Δa. To find the optimum value for Δa, numerical simulations were performed and, in each analysis, the value of Δa has been modified. The initial trial value for numerical simulation was chosen as follows. The initial slope of the load-displacement response obtained in the experimental tests depends on the initial crack length and could be obtained by the following equation stemming from beam theory:

$$\frac{\Delta P}{\Delta \delta} = \frac{3EI}{2(\Delta a)^3} \tag{4.5}$$

$\Delta P/\Delta\delta$ versus Δa plots were built using experimental and analytical data, as shown in Fig. 4.4. The horizontal curves are referred to experimental tests, and represent the experimental range of variation of the initial slope. The analytical values of the slope as a function of the initial crack length, as obtained using the above Eq. 4.5, are also reported, and the intersection between experimental and analytical curves provides an estimate of the actual initial crack length, i.e., “a_0+Δa”, where a_0 is equal to 32 mm.

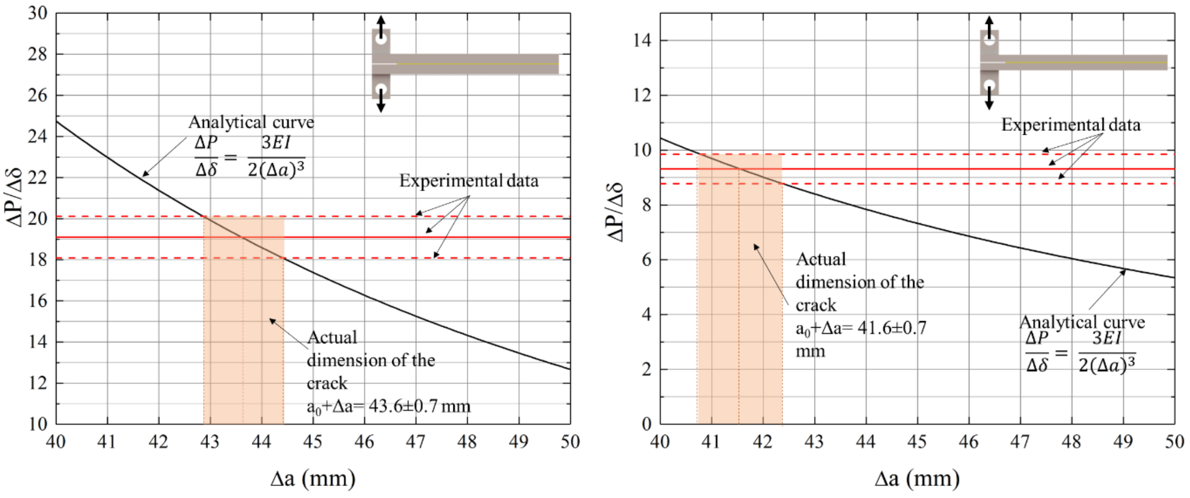

(a) (b)

Fig. 4.4: Comparison between analytical and experimental results to evaluate Δa for: (a) t=8 mm, (b) t=6mm, with a_0= 32mm.

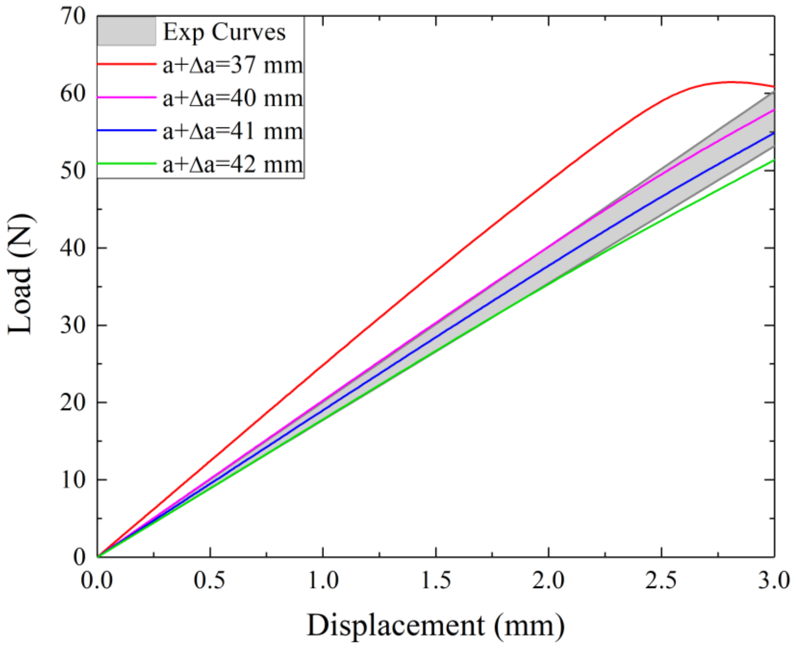

Fig. 4.5: Comparison between numerical and experimental results to evaluate Δa value for t=8 mm with a_0= 32mm.

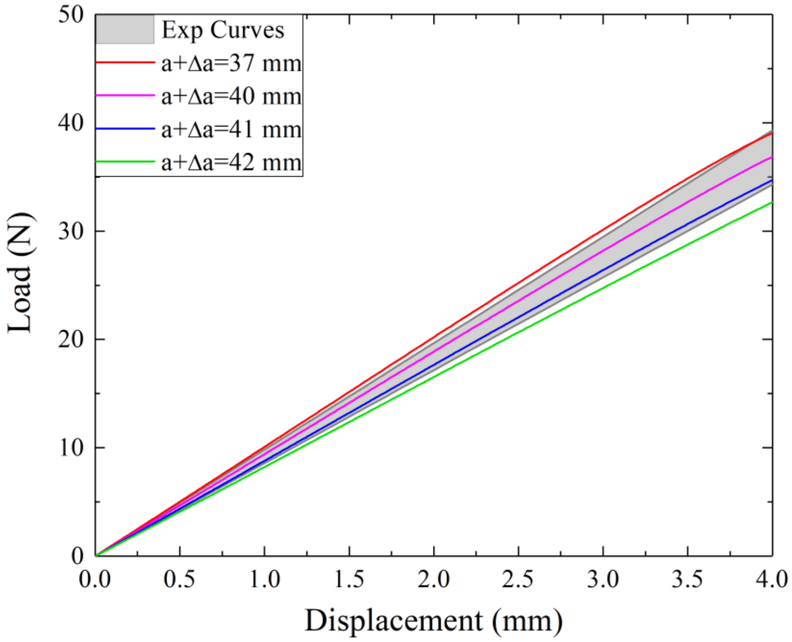

Fig. 4.6: Comparison between numerical and experimental results to evaluate Δa value for t=6 mm with a0= 32mm.

Since the analytic model considers a clamped configuration and neglects the root rotation associated with the adhesive layer, the corresponding response is much stiffer and then may lead to an overestimate of initial crack length. For that reason, an additional comparison between numerical and experimental results was carried out to refine the value of Δa. The results are shown in

Fig. 4.5 and Fig. 4.6.

For both cases, the initial value of Δa which provided the best fit was approximately equal to 10 mm, according to the results obtained from the comparison between the analytical model and experimental results. This value was tuned in FE simulations to fit the experimental results. The outcome of the procedure provided a_0+Δa= (41±1)mm for the DCBs with 8mm-thick substrates, and (40±1)mm for the DCBs with 6mm-thick substrates. In both cases, the average value was used in the subsequent numerical simulations.

4.1.7. Determination of cohesive energy

The first parameter considered for the calibration of the cohesive model was the cohesive energy. The variation of the cohesive energy affects the area under the load-displacement curves: increasing G_{IC}, the area below the load-displacement curve increases. The first trial value was obtained by comparing the experimental results with the analytical predictions from linear elastic fracture mechanics, as described earlier. The results provided fracture energy in the range 400±100 J/m^2 for both sets of benchmark DCB adhesive joints. The obtained fracture toughness was used as the initial guess for the cohesive fracture energy, and then it has been tuned until a match between experimental and numerical load-displacement curves was achieved. The so obtained FE results and the corresponding experimental curves are reported in Fig. 4.7 and Fig. 4.8.

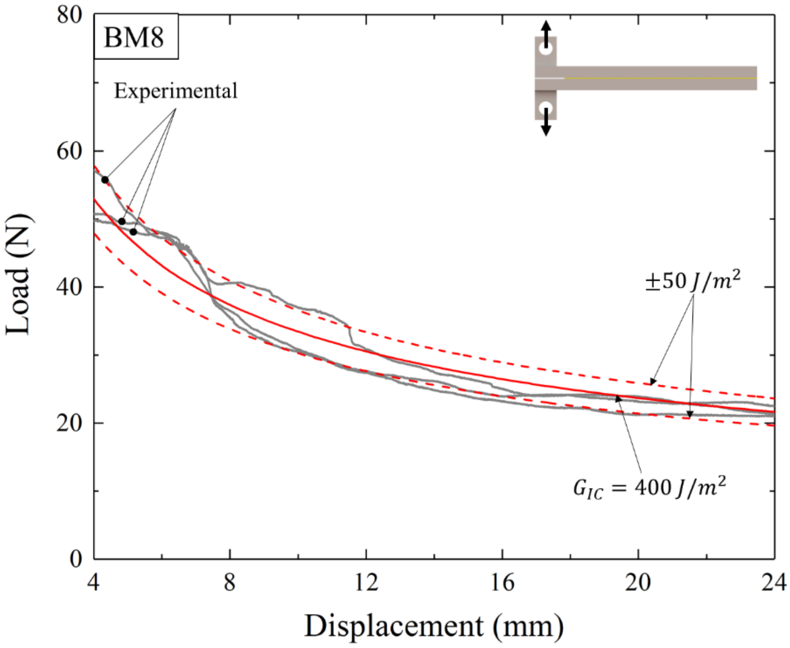

Fig. 4.7: Comparison between numerical and experimental results in the softening region and determination of cohesive fracture energy (t=8mm).

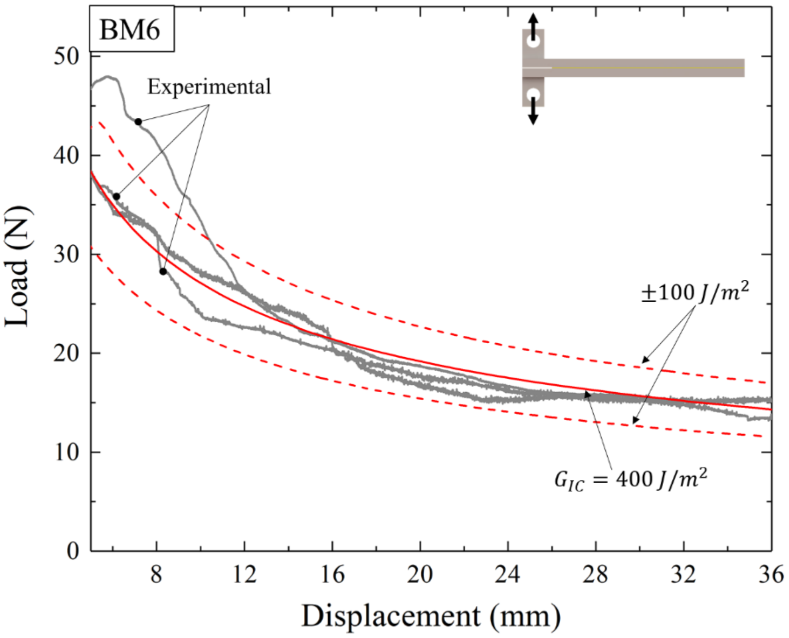

Fig. 4.8: Comparison between numerical and experimental results in the softening region and determination of cohesive fracture energy (t=6mm).

The variation range of the cohesive energy as found is equal to 400 ± 50 J/m^2 for both sets of samples. Notice that the obtained fracture energy is well below the value recorded in other works (Alfano *et al.*, 2011; Chiodo *et al.*, 2015) where the same adhesive was used to bond metallic substrates. This discrepancy, as explained in the previous chapter, could be readily explained considering the difference occurred in the crack propagation process: in fact, the fracture was adhesive (at the adhesive/substrate interface) instead of cohesive (inside the adhesive layer).

4.1.8. Determination of cohesive strength

The variation of the cohesive strength affects the peak load in the load-displacement curves, while the area is almost unchanged. It is noted that the available experimental results could not provide direct information regarding σ_{max}. Therefore, it is often estimated by curve fitting the peak region of the global response of DCB adhesive joints (Alfano *et al.*, 2009). Here, an initial guess was initially chosen equal to 10 MPa based on the results of a previous work where the same adhesive was deployed (Alfano *et al.*, 2011). The first trial value has been varied until a reasonable match between experiments and simulations was achieved. The simulation load-displacement curves were obtained by held constant fracture toughness value while cohesive strength has been tuned. Results, shown in Fig. 4.9 and in Fig. 4.10, compared FE curves with experimental ones. For 6 mm substrate thickness, one of the experimental curves was eliminated from the calibration procedure for anomalous behavior in the peak region (Fig. 4.10) - as explained in the experimental section.

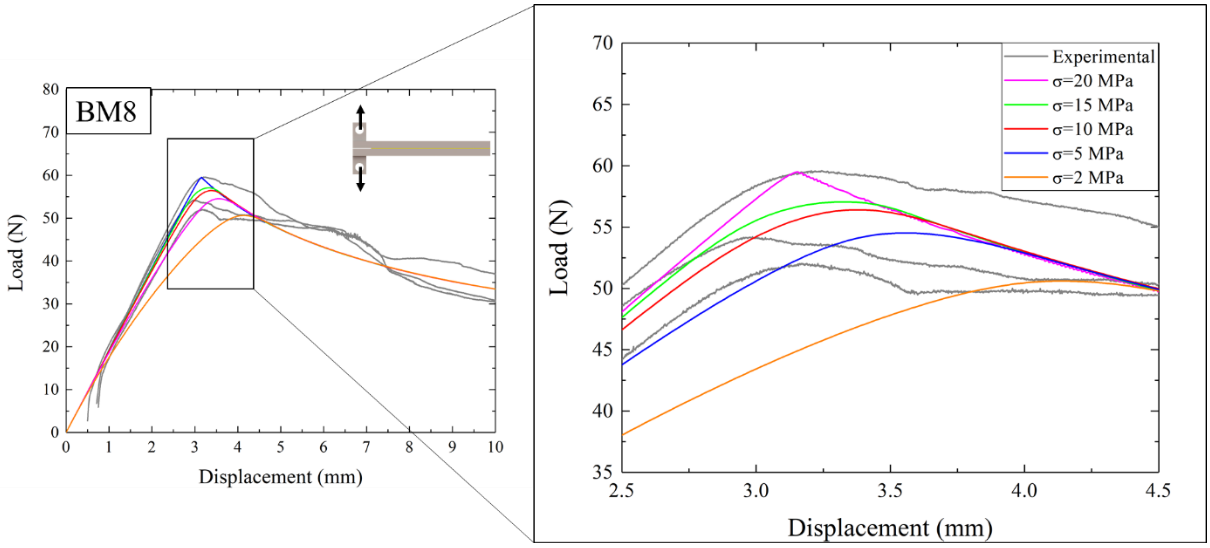

Fig. 4.9: Comparison between numerical and experimental results in the peak region and determination of cohesive strength (t=8mm).

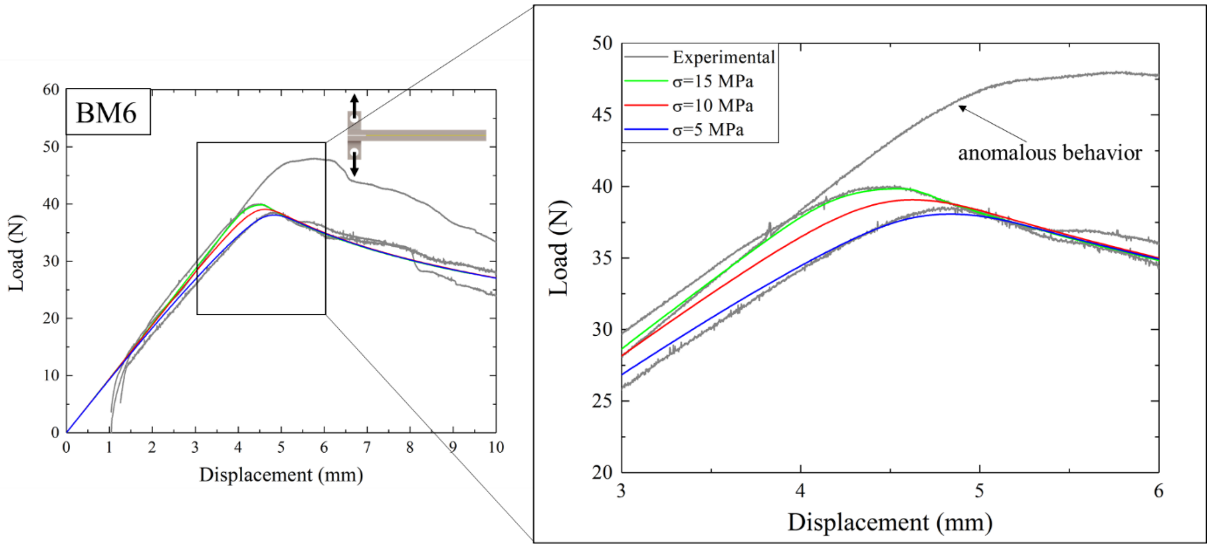

Fig. 4.10: Comparison between numerical and experimental results in the peak region and determination of cohesive strength (t=6mm).

The variation range of the cohesive strength has been found to be equal to 11MPa ± 9 MPa for 8mm substrate thickness and 10MPa ±5MPa for 6 mm substrate thickness. The obtained range of cohesive strength should be addressed to the high scatter of the experimental data in the region where the maximum load is attained. Moreover, potential blunted crack tips, or the formation of adhesive pockets, can largely affect the initial load-displacement response in DCB tests.

4.2. Finite element simulations of bio-inspired DCB adhesive joints

The cohesive properties determined in the previous section were deployed to assess the experimental data obtained in fracture tests of DCB with subsurface patterns. The specimen geometric characteristics were described in the previous chapter, and are recalled in Fig. 4.11.

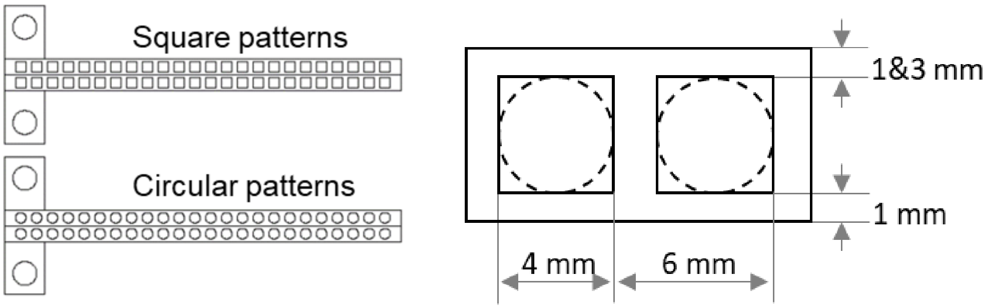

Fig. 4.11: Geometry and dimensions of the subsurface channels of bio-inspired DCB samples.

4.2.1. Viscous stabilization

The introduction of the channels in the substrates causes a variation in the crack propagation mechanism: the crack grows very slowly until the load reaches a maximum, after which there is a sudden load decrease and the crack “jumps” in a mechanism similar to stick-slip behavior. This crack propagation behavior, which resembles the *crack trapping* mechanism observed in some biomaterials, and which has been described earlier, introduces instability that needs to addressed in finite element simulations. For this reason, a viscous stabilization was employed to prevent numerical issues. The formulation proposed in ABAQUS was employed, where a very small fictitious viscosity is introduced in the cohesive zone law to regularize unstable behavior, and aid convergence (Dávila, Camanho and Turon, 2008; Ranatunga, 2011). In the regularization process, the damage variable is replaced by a viscous damage variable, which, in turn, is defined through an evolution equation involving a small viscous coefficient. Ancillary finite element simulations were executed to identify a viscosity coefficient small enough to lead to stable propagation with negligible viscous dissipation. The results are given in Fig. 4.12 and show that the introduction of increasing viscosity into the simulations can largely affect the shape of the load-displacement curve. With a viscosity factor equal to 10^{-2} s^{-1}, the numerical model is not able to reproduce the softening curve; with a viscosity factor between (10^{-3}÷10^{-5}) s^{-1}, the numerical model is able to reproduce the softening curve but the shape is very different from the shape obtained without the introduction of the viscosity stabilization; with a viscosity factor between to (10^{-5}÷10^{-6}) s^{-1}, the results are comparable to the results obtained without viscosity coefficient, therefore, the effect can be considered negligible. A value smaller than 10^{-6} s^{-1} could not allow achieving convergence during the simulations with patterned substrates. Therefore the viscosity was set equal to 10^{-6} s^{-1} was then selected for subsequent analyses.

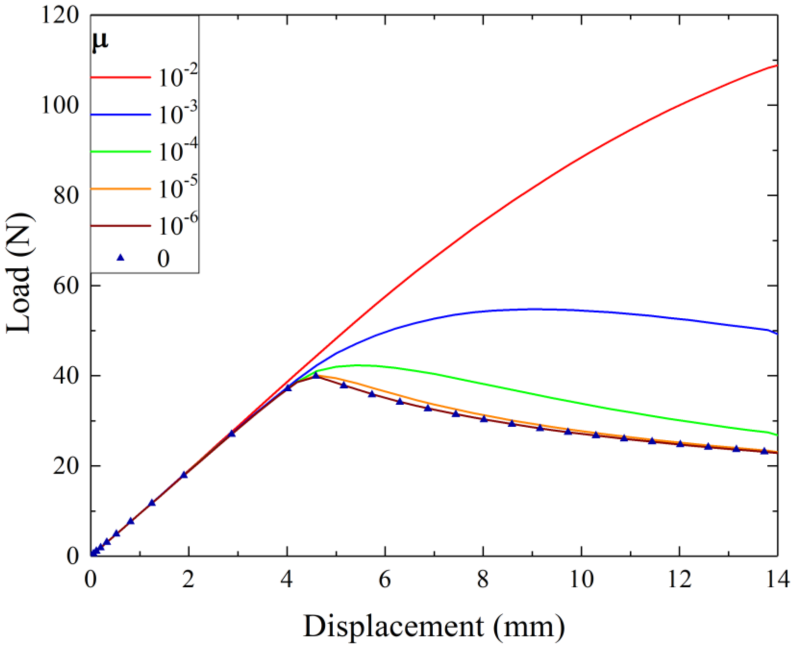

Fig. 4.12: Effect of viscous dissipation on the load-displacement response of DCB adhesive joints.

4.2.2. Accounting for substrate plasticity

The presence of subsurface channels modifies the bending stiffness of the beam; therefore, during mechanical tests, the stresses could exceed the yield stress. The effect of plasticity could be non-negligible for thin substrates (h=6mm) and long cracks. For this reason, the introduction of plasticity in the material model is necessary to ascertain the experimental results. A comparison among FEA results obtained using an elastic model and an elastoplastic model is shown in Fig. 4.13 and Fig. 4.14. The introduction of plasticity in the model induces a variation in the global response, which suggests an increase in energy dissipation because of plastic work carried out in deforming the arms of the sample. Therefore, plastic energy can contribute to the overall work of fracture, and therefore needs to be accounted for. For this reason, the σ-ε curve obtained from experimental tests was used as an input value for the definition of the material's property. It is also important to notice that the difference between elastic and elasto-plastic models became more noticeable for higher values of the crack length and square subsurface channels. This effect is due to the approach of the crack tip to the end of sample interfaces, i.e., high crack values, even if this effect is more noticeable for square subsurface channels. In particular, the introduction of plasticity in the material models produces a shift toward higher load value and toward the right of the load peaks, as shown in Fig. 4.13 and Fig. 4.14, i.e., crack propagation is slower.

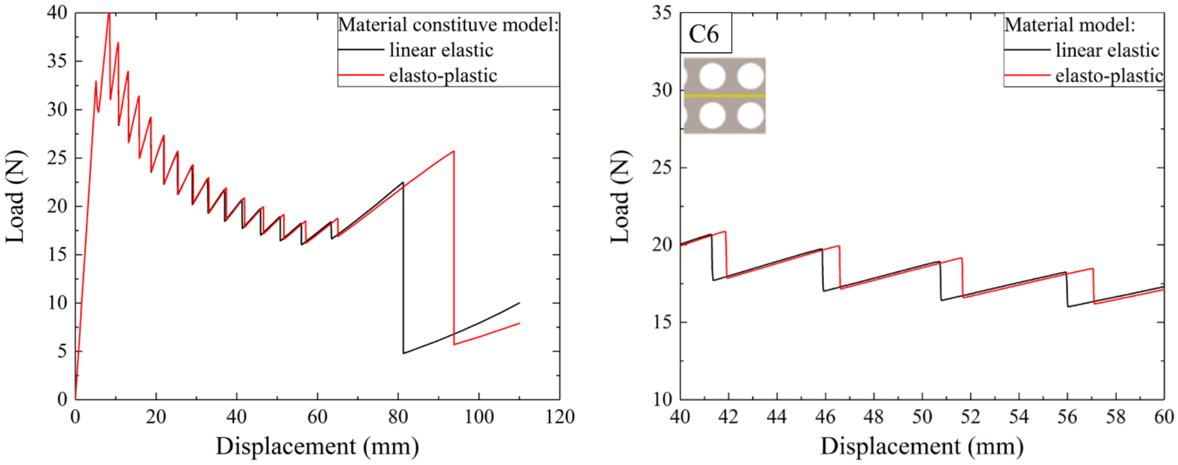

(a) (b)

Fig. 4.13: Effect of substrates plasticity on the load-displacement response for DCB samples with circular channels and t=6mm.

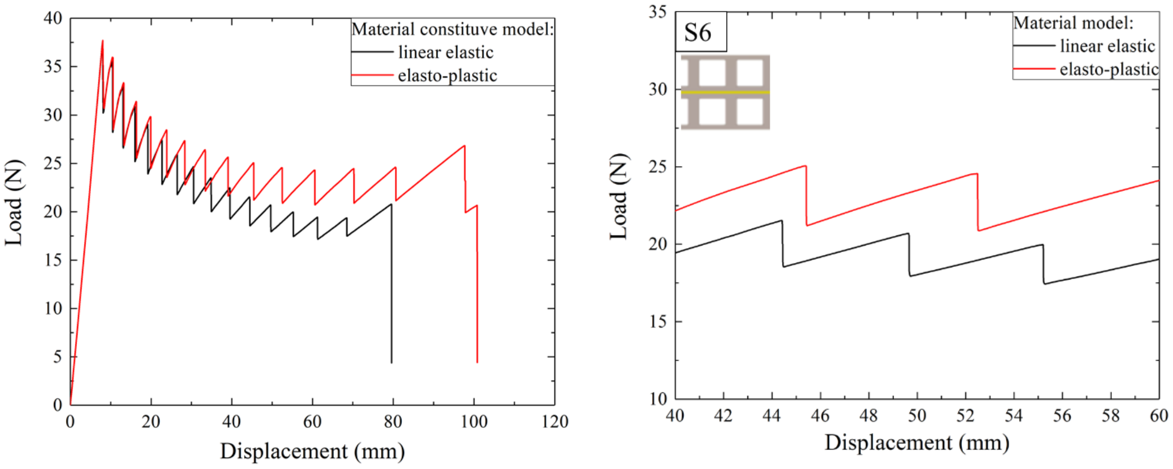

(a) (b)

Fig. 4.14: Effect of substrates plasticity on the load-displacement response for DCB samples with square channels and t=6mm.

4.2.3. Determination of crack length for patterned substrates

As already stated, the initial crack length (a_0) at the beginning of the mechanical tests was not known with good accuracy. For that reason, a comparison between numerical and experimental curves is fundamental to find a better estimate of Δa, and the results are shown in Fig. 4.15 and Fig. 4.16. For all cases, the initial value of Δa for the numerical simulation was chosen according to the results obtained for bulk: the $a_0+\Delta a$ value has been set approximately equal to 40 mm.

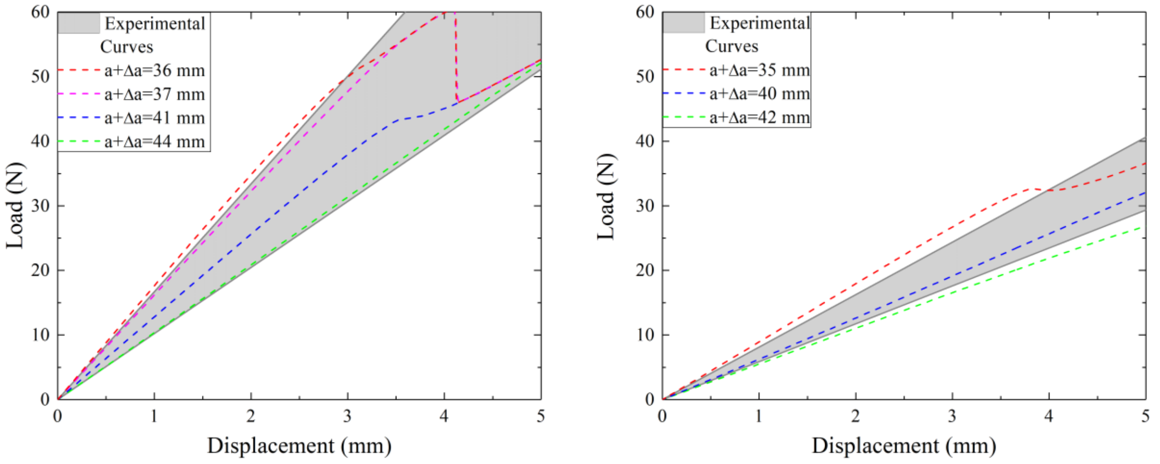

(a) (b)

Fig. 4.15: Comparison between numerical and experimental results to evaluate Δa for a) t=8 mm and b) t=6 mm for the substrate with circular channels (a_0= 32mm).

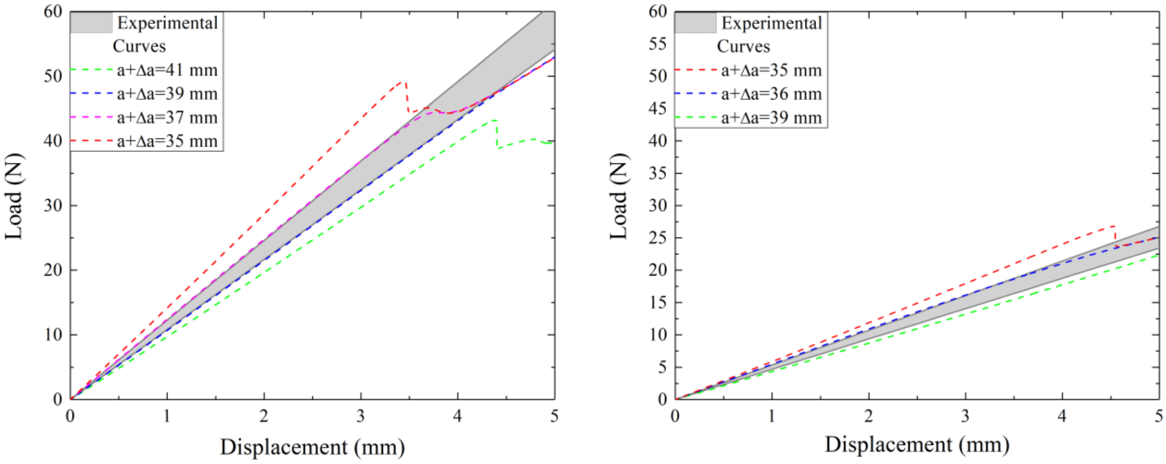

(a) (b)

Fig. 4.16: Comparison between numerical and experimental results to evaluate Δa for a) t=8 mm and b) t=6 mm for the substrate with square channels (a_0= 32mm).

In the end, the a_0+Δa value has been estimated to be equal to (40±3) mm for 8mm substrate thickness, and (38.5±3.5) mm for 6mm substrate thickness for the circular pattern. For the substrates with the square pattern, the values of (38±1) mm and (37.5±1.5) mm have been found for 8 mm and 6mm thickness respectively. In both cases, the average value was used for the FE simulations.

4.2.4. Comparison between finite element and experimental results

Numerical simulations with the subsurface pattern samples were carried out using the cohesive parameters found using bulk samples. A comparison between numerical and experimental results is shown in Fig. 4.17-Fig. 4.20. The results demonstrate that when using the cohesive parameters determined from the analysis of benchmark DCB adhesive joints to simulate the response of bioinspired DCBs, an excellent fit with experiments could be obtained. Furthermore, the numerical model can reproduce the serration of the global response observed in the experiments described earlier. Moreover, it is interesting to note that similar serrated behavior was also reported by Maloney and Fleck (Maloney and Fleck, 2019b) in testing aluminum/epoxy joints featuring stop-holes within the adhesive layer. In our approach, the adhesive layer is virtually unaffected, thereby avoiding the complexity associated with drilling stop-holes (in relatively thick adhesive layers).

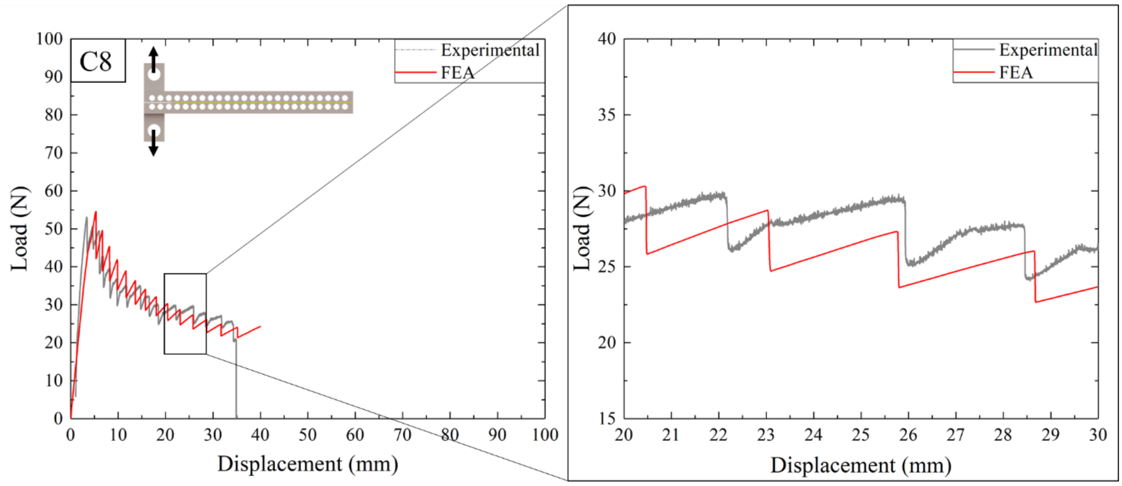

Fig. 4.17: Comparison between numerical and experimental results for the substrates with circular channels with t=8mm.

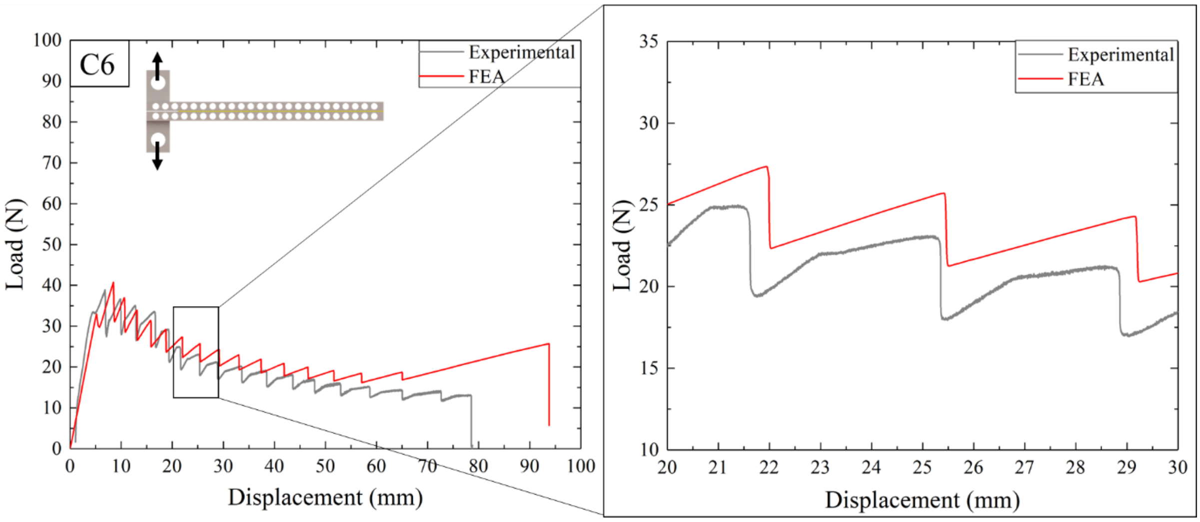

Fig. 4.18: Comparison between numerical and experimental results for the substrates with circular channels with t=6mm.

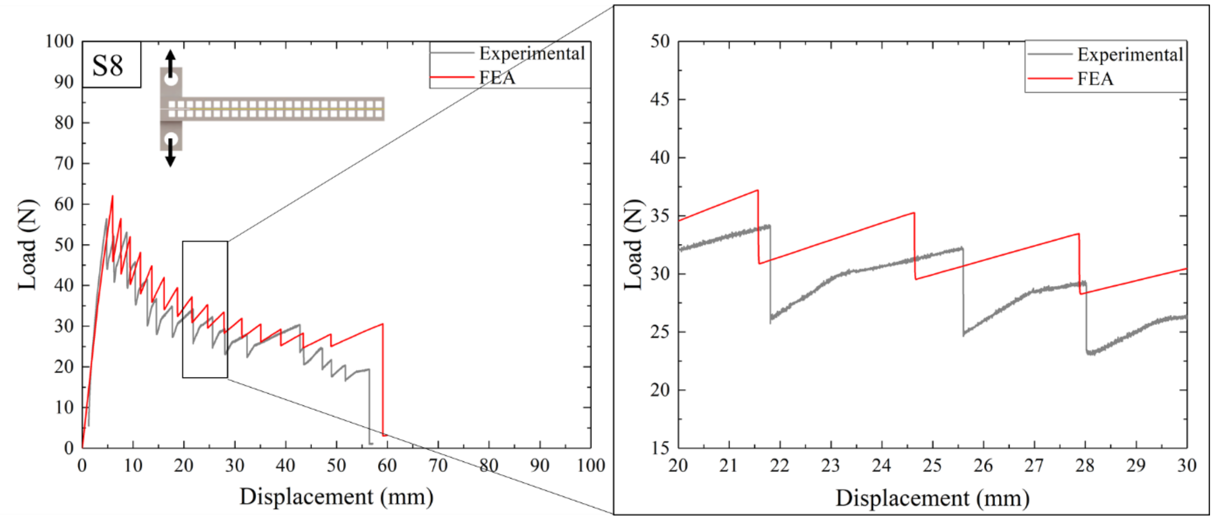

Fig. 4.19: Comparison between numerical and experimental results for the substrates with square channels with t=8mm.

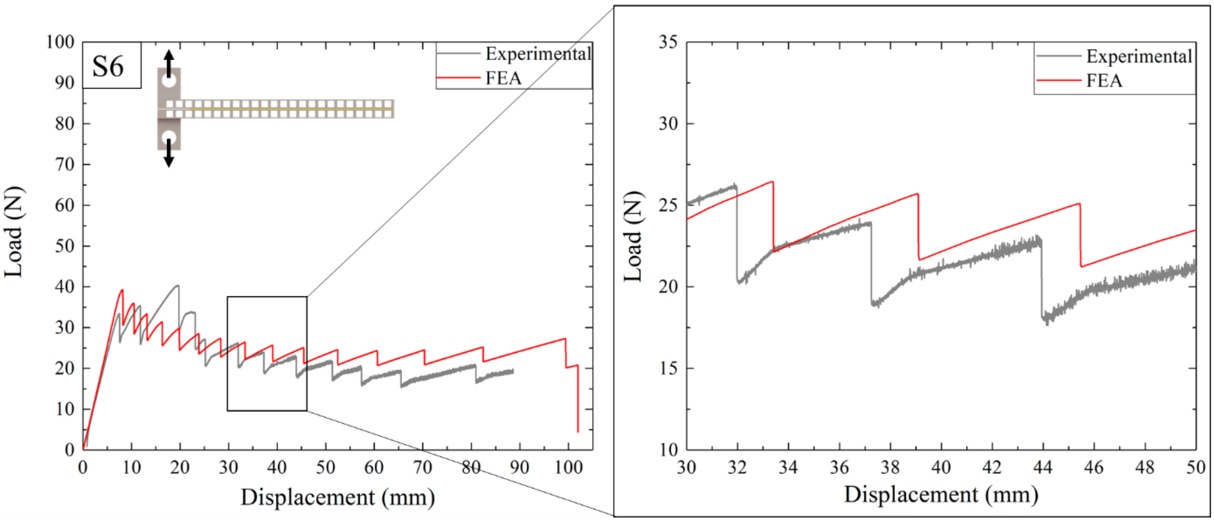

Fig. 4.20: Comparison between numerical and experimental results for the substrates with square channels with t=6mm.

The model is also able to reproduce the same period seen in the experimental curves, i.e., the distance between two load peaks in numerical and experimental results are comparable. FE curves mimic the nuance of the responses recorded in the experiments, i.e., the difference between peak and minimum loads for each period are comparable. The main differences between experiments and simulations are observed for relatively short cracks, i.e., $a_0+\Delta a$ equal to 50 mm, as shown in Fig. 4.21. This variability is mainly due to experimental factors that cannot be captured by the present simulations, such as potential adhesive pockets, nucleation of interfacial damage and crack path kinking. Overall, the total energy dissipation, i.e. the area under the load-displacement curve, is comparable in both simulations and experiments.

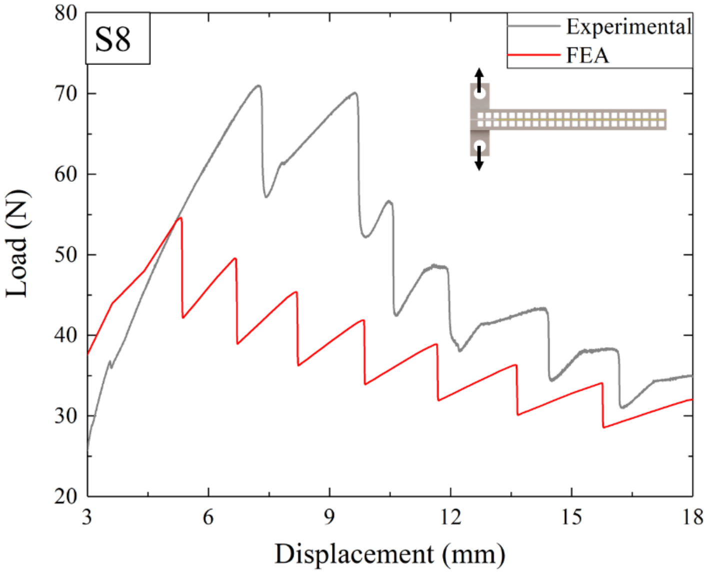

Fig. 4.21: Difference between experimental and numerical load-displacement curves due to the variability of the adhesive fillet.

The crack propagation mechanism was also analyzed by evaluating the damage variable (SDEG), which indicates the position and extension of the fracture process zone concerning the position of the channels. Interestingly, it was observed that cohesive damage nucleates also in front of the main growing crack, although the simulations did not reveal the formation of an actual secondary crack. Referring to Fig. 4.22 it is possible to observe the increase of stiffness degradation parameter (SDEG) of cohesive elements in correspondence of some characteristics points of load fluctuation. It was found that the crack tip position in all characteristic points is similar to the crack position observed experimentally by high-resolution imaging. Furthermore, for square channels, when the crack tip is located below channels, a secondary damage zone nucleates below the pillar (Point 1). After that, the length of this zone increases (Point 2) until the two damage zone coalesce because of the failure of the residual adhesive ligament which is associated with a sudden load drop (Point 3). After that, the mechanism restart in the next load fluctuation.

As observed also during experimental tests, the FE responses are characterized by slight variations in the slope during the rising portion of the load-displacement trace. However, in FE simulations, that happens only for short crack lengths. A further assessment of this point was made by looking at the values of the SDEG parameter in correspondence of the slope changes. The results are shown in Fig. 4.23. Apparently, the slight variation of the slope observed in the simulations is concurrent with damage nucleation in front of the primary crack front. The main conclusion that can be drawn is that the slope variation is associated with the crack propagation process, whose rate of growth seems to increase at point 2. Interestingly, it seems that a connection also exists with the nucleation of damage ahead of the main crack. However, it is difficult to conclude in a reliable fashion that it had a significant effect on the slope variation discussed here, while it is also true that the secondary damage, if any, could not be observed in the corresponding experimental results.

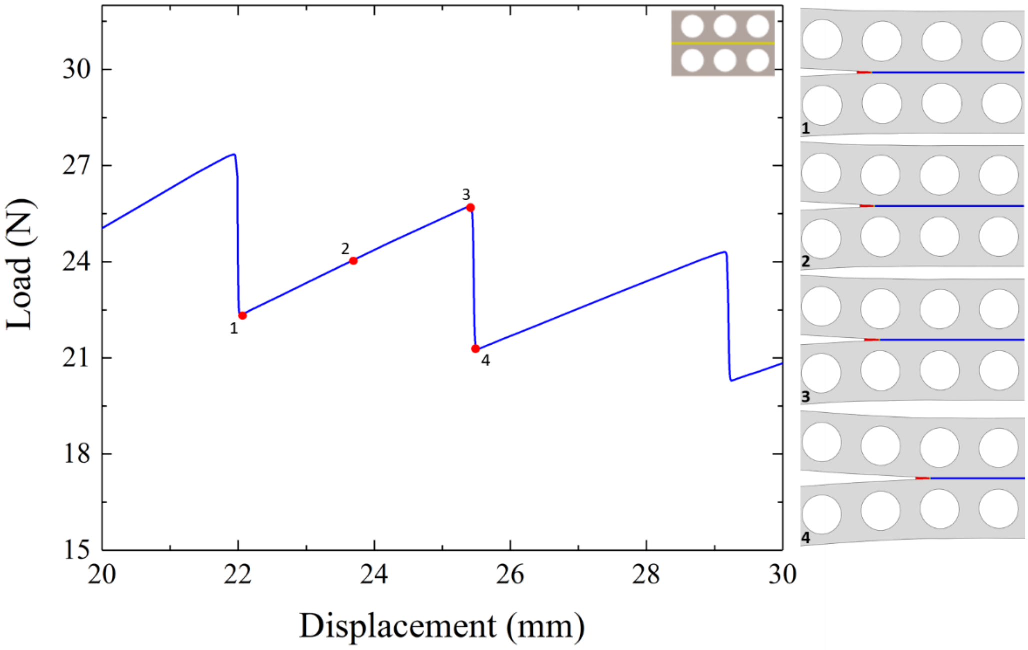

(a)

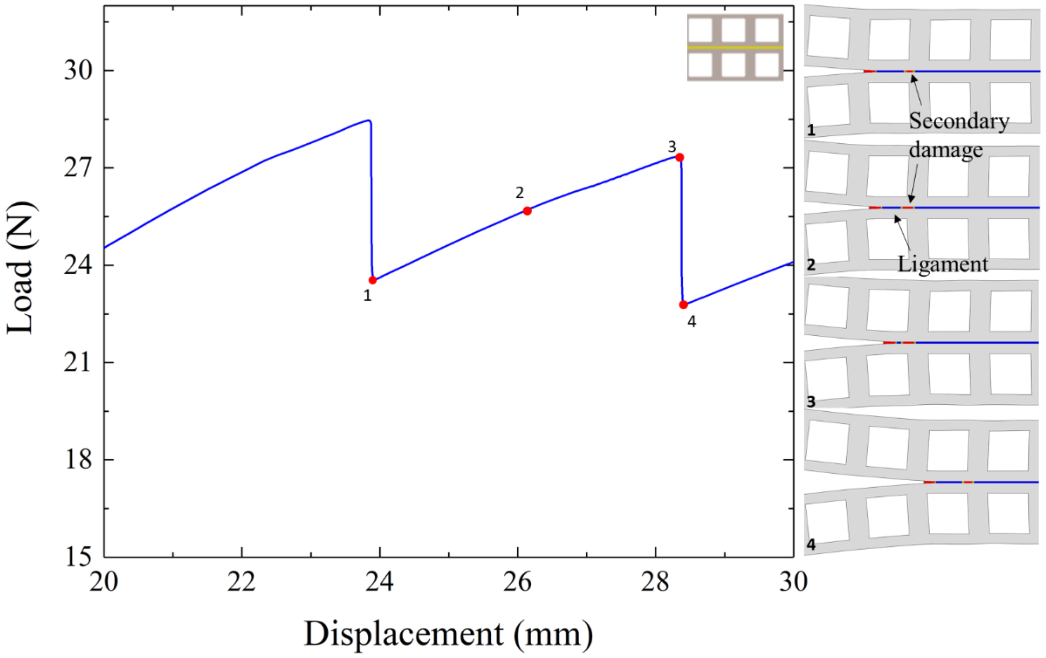

(b)

Fig. 4.22: Crack trapping mechanism observed in FE simulations of fracture in DCB adhesive joints: (a) circular channels and (b) square channels.

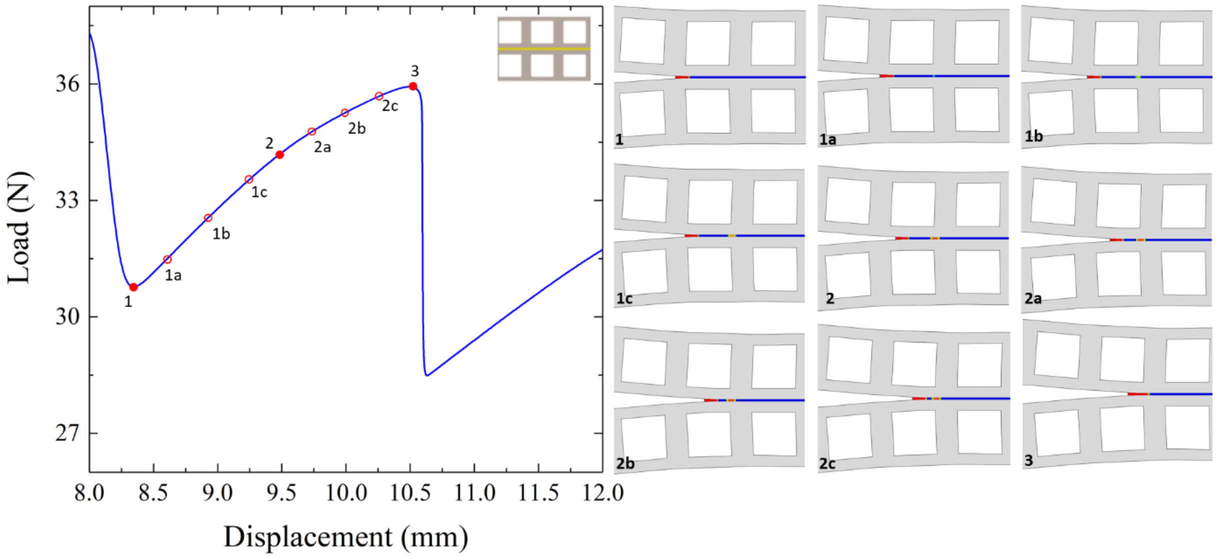

Fig. 4.23: Cohesive elements damage evolution in relation to slope change on load-displacement curve

4.3.Energy Analysis

Results have been compared in terms of the energy supplied for crack propagation. In particular, the FE simulations allow segregating the following energy contributions, i.e., the energy dissipated by fracture (*ALLDMD*), the energy dissipated by rate-independent plastic deformations (*ALLPD*), and the recoverable strain energy (*ALLSE*). The total strain energy is obtained as a sum of all the previous contributions (*ALLIE*).

The energy supplied during crack propagation has been given as a function of the applied displacement in Fig. 4.24 to Fig. 4.27. As expected, the energy contributions exhibit an upward trend with the displacement increment. The elastic energies, Fig. 4.24, increase significantly with the introduction of the subsurface channels for both substrates thicknesses and the displacement at failure increase considerably, i.e., more than two times higher than the value obtained for the benchmark. This is due to the increased compliance that also enables the crack trapping mechanisms discussed earlier, which results in the serrated behavior observed in the data.

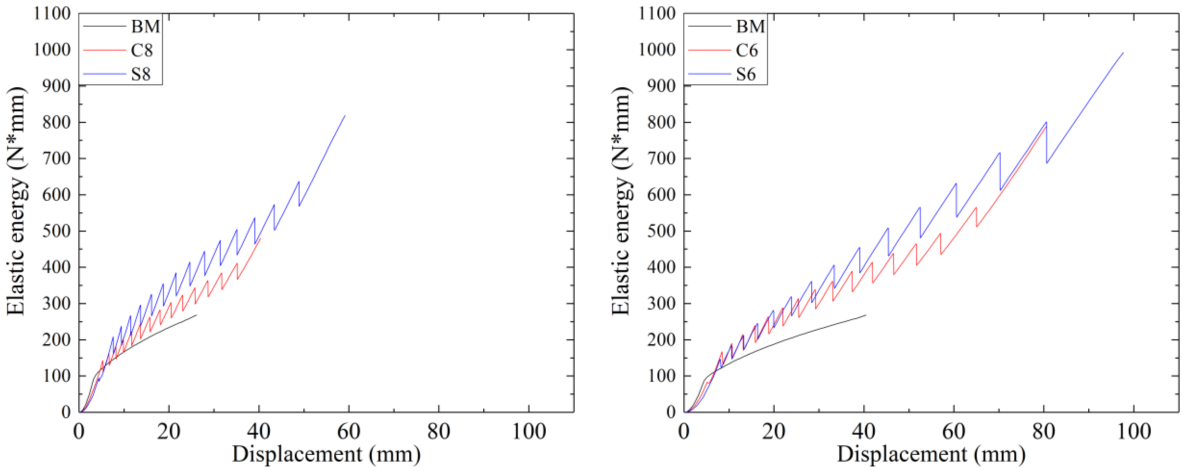

(a) (b)

Fig. 4.24: Elastic energy evolution during crack propagation for DCB adhesive joints with substrates thickness equal to (a) 8mm and (b) 6mm.

Concerning the energy dissipated by fracture, the results are reported in Fig. 4.25. For a given opening displacement, it is clear that the introduction of the subsurface channels modifies the rate of crack propagation since less fracture energy is supplied, for a given applied opening displacement, with respect to the benchmark. The variation in the crack propagation rate as a function of the applied displacement appears to be dependent on both substrate thickness and geometry of the channels. Notice that the slight discrepancies among the obtained fracture energies (total values) may be due to small differences in crack length and/or numerical errors.

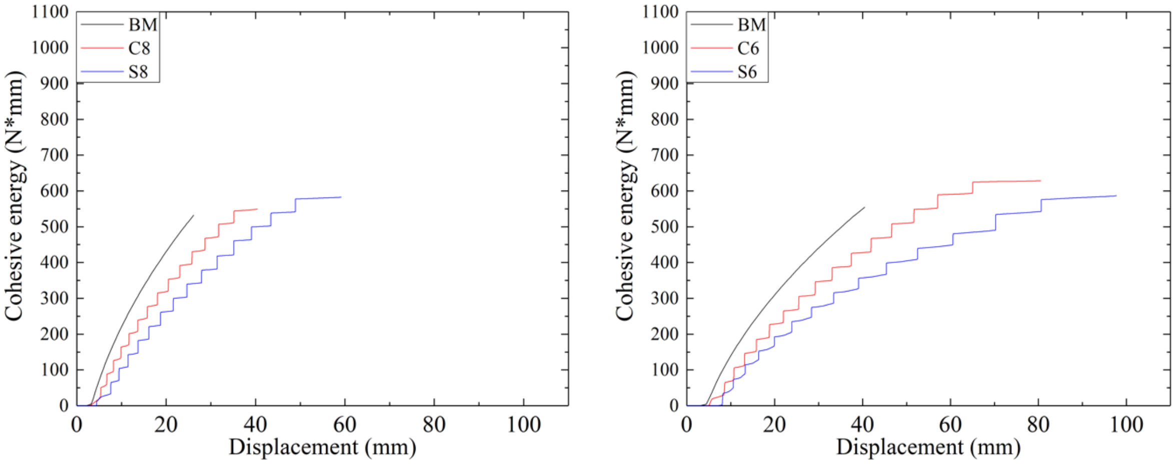

(a) (b)

Fig. 4.25: Cohesive energy evolution during crack propagation for DCB joints with substrates thickness equal to (a) 8mm and (b) 6mm.

The energy input dissipated in the form of plasticity within the substrates is given in Fig. 4.26. It is clear that there is no plastic deformation of the adherents for the benchmark DCB adhesive joints. For the bio-inspired samples, plasticity is more significant only for the samples featuring square channels and, obviously, it increases as the thickness decreases. FE simulations indicated that most of the plastic deformation is occurring around the sharp corners of the square channels. The overall contribution of plasticity to the dissipated energy becomes relevant only for long cracks and thin substrates, and this is due to the particular model material system selected for the analysis, i.e., the DCB joint. Finally, the total energy is given in Fig. 4.27. It is shown that because of the subsurface channels the total energy dissipated in the process increase largely, although there is no actual variation in neither the fracture energy nor the cohesive strength of the interface.

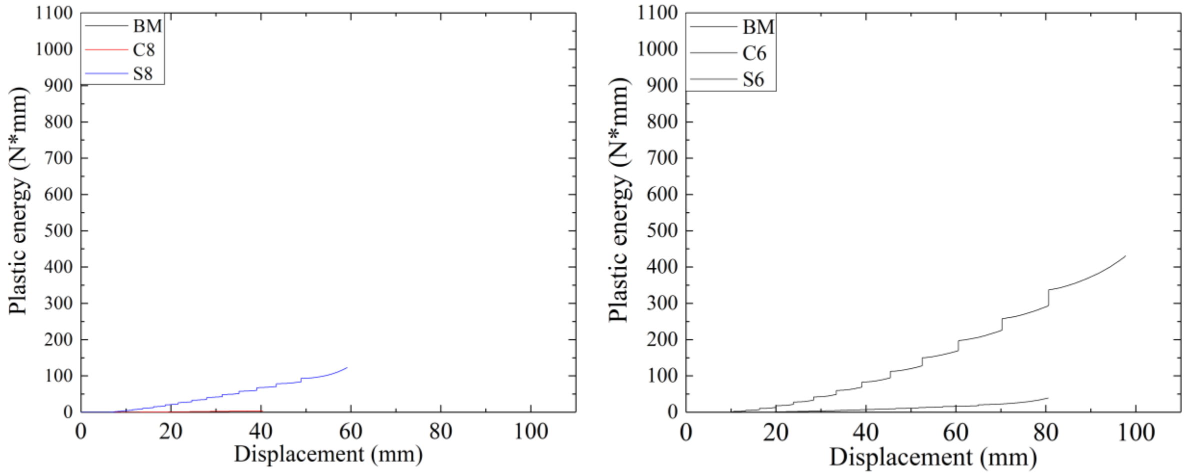

(a) (b)

Fig. 4.26: Plastic energy evolution during crack propagation for DCB joints with substrates thickness equal to (a) 8mm and (b) 6mm.

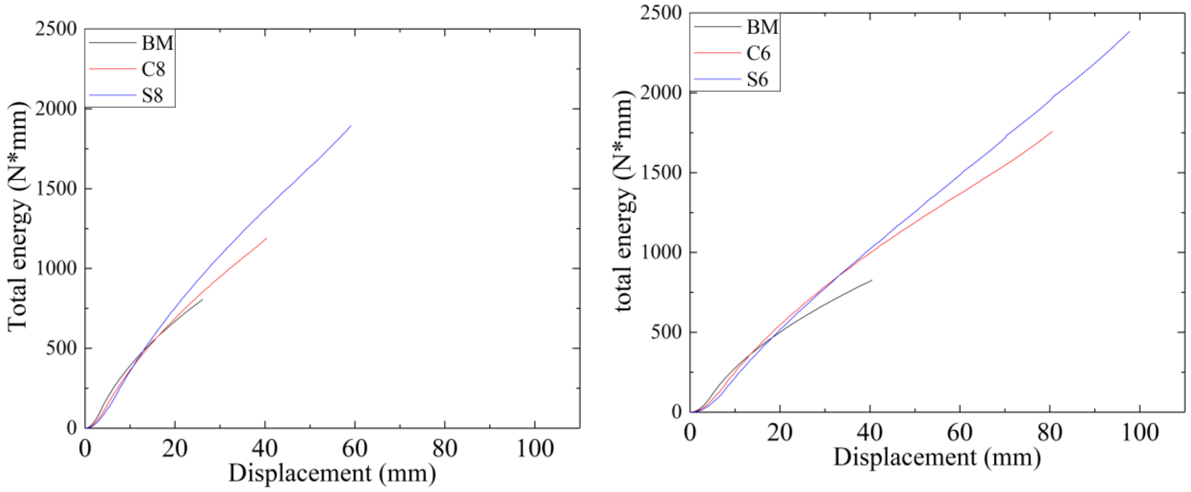

(a) (b)

Fig. 4.27: Total energy evolution during crack propagation for DCB joints with substrates thickness equal to (a) 8mm and (b) 6mm.

The serrated behavior observed in all contributions to the dissipated energy was analyzed in more detail in Fig. 4.28. In each period, the elastic energy increases with the applied displacement until it reaches a maximum (from point 1 to point 2) meanwhile, both cohesive and plastic energies are almost constant. After that, the elastic energy is released suddenly while both cohesive and plastic energies increase (from point 2 to point 3): this variation corresponds to unstable crack propagation. Finally, the cycle repeats itself for the next channel. This periodical storage and sudden release of elastic energy increase, along with the plastic contribution, the total energy requested for crack propagation. These confirm of experimental results: the available energy exceeds the energy requested for crack growth producing the unstable crack propagation. In the end, the overall energy dissipated during crack propagation is increased thanks to channel presence.

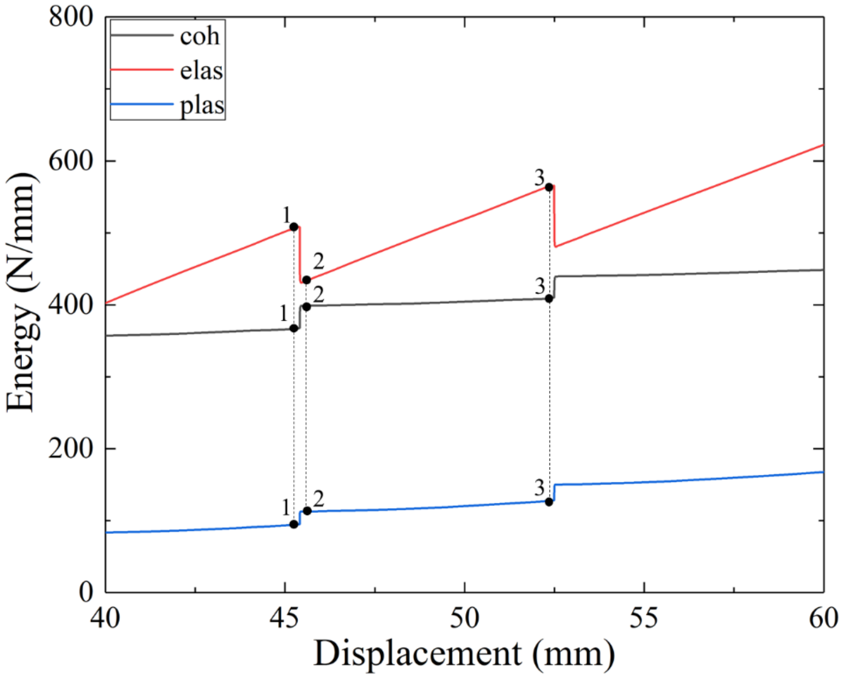

Fig. 4.28: Comparison between fracture (coh), elastic and plastic energy for one period of crack propagation as obtained for DCB joint with square channels (t= 6 mm).

The previous energy contributions are now summarized in the form of bar diagrams in order to draw some additional observations. The energies were divided by the crack area and the results are reported in Fig. 4.29-Fig. 4.31. In order to highlight the differences associated with the introduction of subsurface channels, the energy per unit area was divided by the energy obtained in the case of bulk samples.

All the energy contributions achieving separation increase with the introduction of subsurface channels, independently of channel shape. Furthermore, as discussed above, the degree of plasticity depends on substrate thickness and channel shape. With circular channels, the plastic energy is still very low while it reaches more significant values with the introduction of the square shape. This depends on local plasticization in the channel corners as shown in Fig. 4.32. However, it should be noted that the actual square channels in 3D printed samples feature somewhat rounded corners. Therefore, the actual degree of stress concentration and dissipated plasticity might be lower than that estimated from FE simulations. This is confirmed by the bar plots reported in Fig. 4.31 which shows that the energy estimated in FE simulations is always larger than that observed in the experiments. However, it is also recognized that a certain degree of uncertainty is also associated with the cohesive properties employed in the simulations. This point will be explored further in Chapter 5.

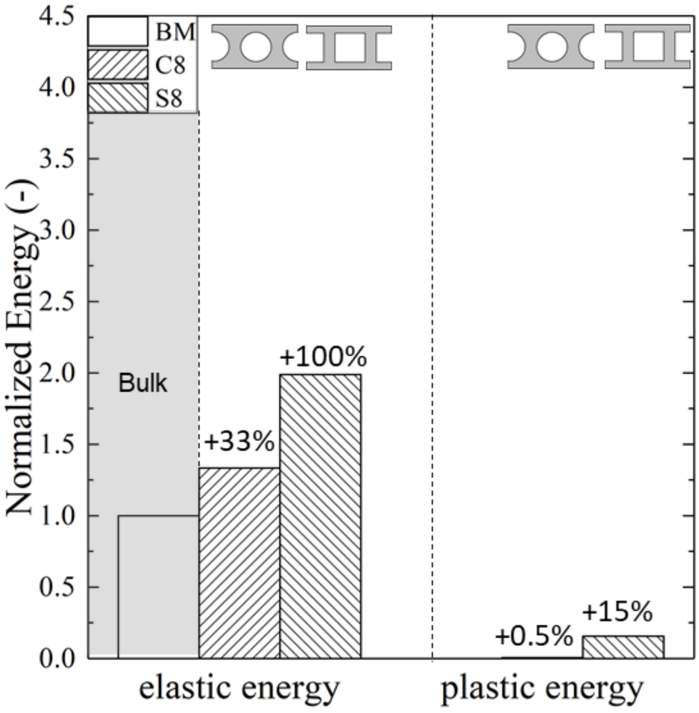

Fig. 4.29: Plastic and elastic energy dissipation as a function of different sample's geometry for t=8mm.

Moreover, for the square channels, it is interesting to observe that a significant portion of plastic energy was also observed in the thin plate in the upper part of the substrates (Fig. 4.32). In fact, the bending of the DCB arms eventually leads to inelastic deformation, thereby increasing the amount of energy dissipated in the process. Similar deformations were observed also experimentally, but only for relatively large crack length, as reported in Fig. 4.32.

The maximum value of dissipated energy (total) requested for crack propagation was obtained using thin substrates (6 mm) and square channels subsurface pattern (Fig. 4.31). In particular, the total energy is three times higher than that obtained for benchmark samples.

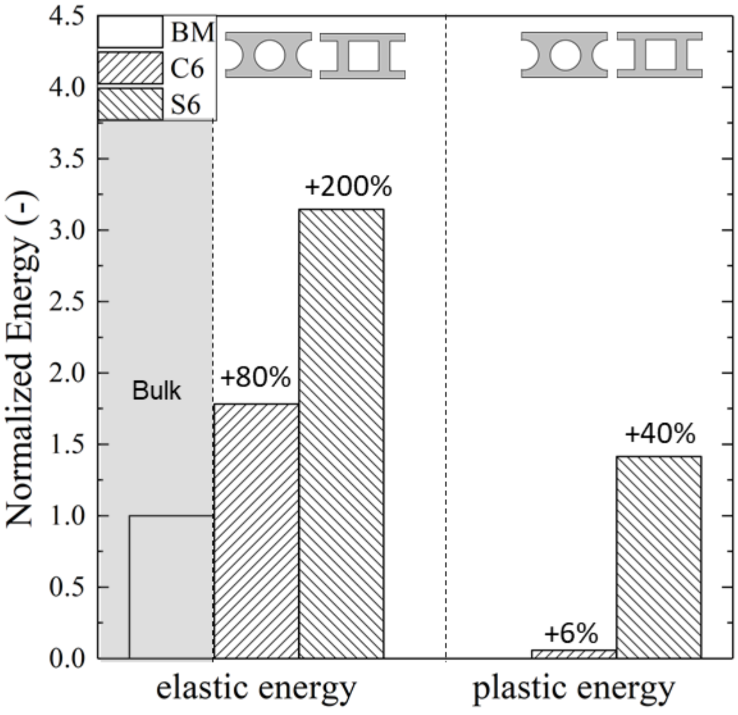

Fig. 4.30: Plastic and elastic energy dissipation as a function of different sample's geometry for t=6mm.

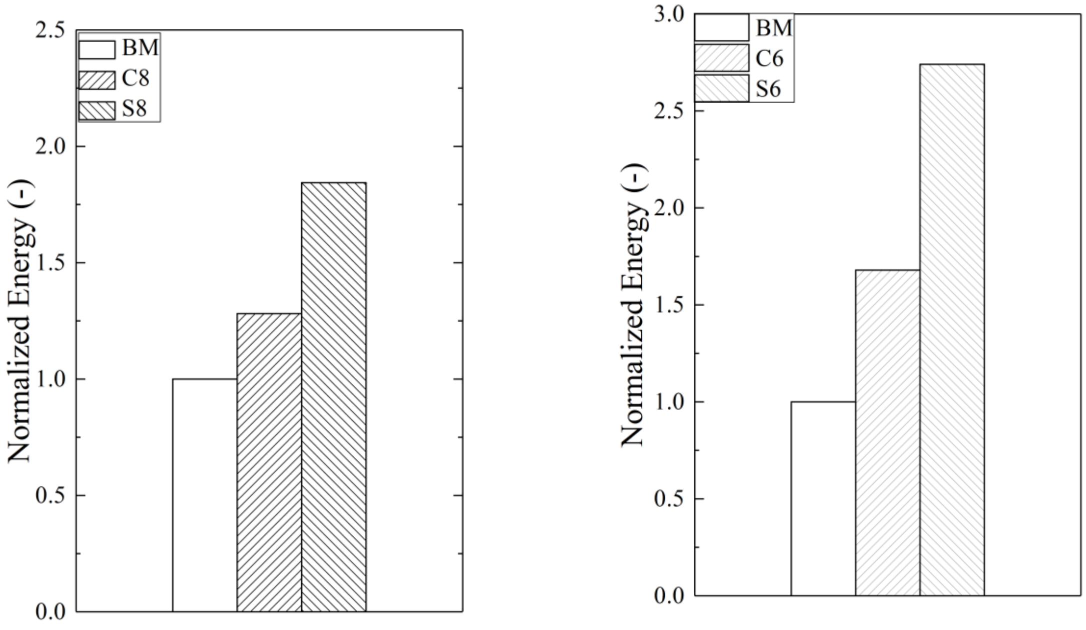

(a)

(b)

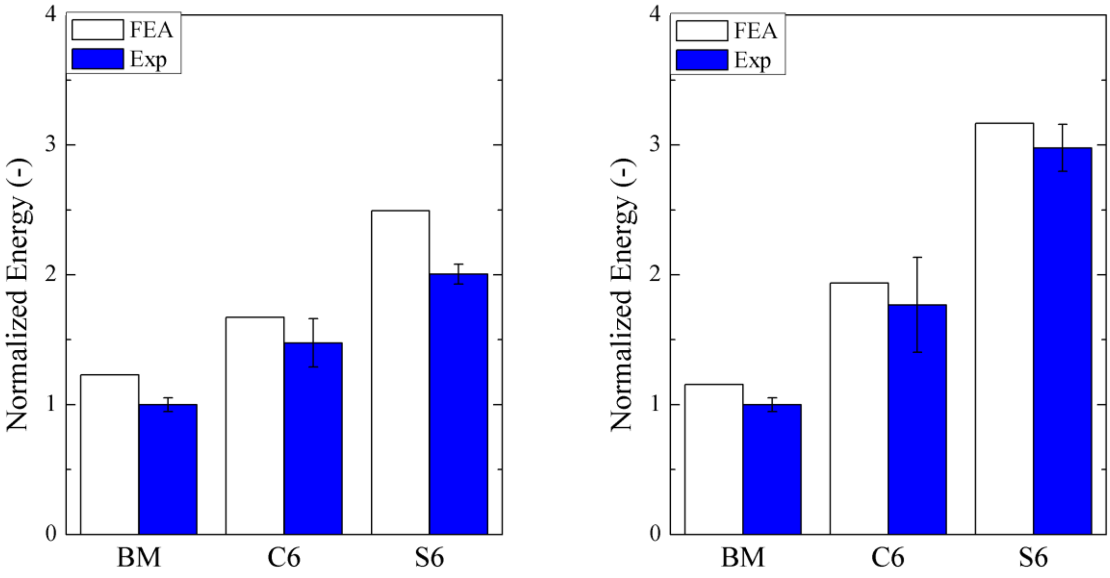

(c) (d)

Fig. 4.31: Total energy dissipated numerically during crack propagation for a) t=8 mm b) t=6mm and comparison between total energy dissipated numerically and experimentally for (c) t=8 mm (d) t=6mm.

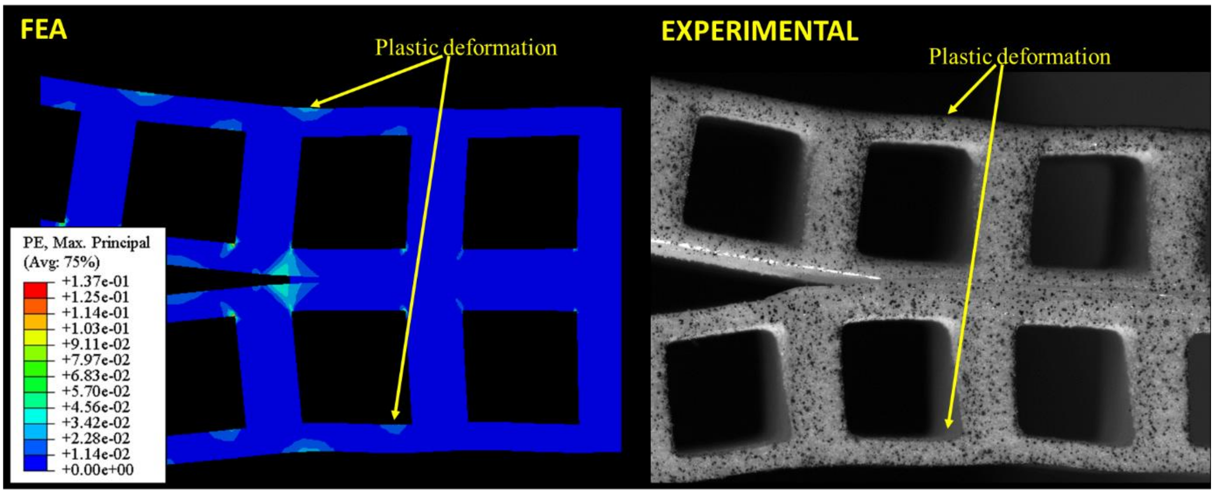

Fig. 4.32: Plastic deformation occurred experimental and numerical on the upper thin plate of DCB joint with square channels

It should be also noted that the introduction of the channels also reduces the weight of the substrates. The bio-inspired DCB adhesive joints with square channels and thinner substrates were endowed with 37% weight reduction while increasing largely the dissipated energy. The assessment of the numerical results further confirms the beneficial effect of the proposed bio-inspired design, which largely improves dissipated energy and damage tolerance in adhesive bonded DCB adhesive joints. The energy dissipated during crack propagation had a strong dependence on the channels' shape, thus highlighting potential tunability with channel geometry. The validated numerical model employed herein will be deployed in Chapter 5 to deepen this point.

4.4. Effect on channel misalignment

Since the final goal of this study is the possibility to apply this technology to adhesive joints used in many industrial fields, it is clear that the effect of potential misalignment generated during assembly should be accounted for. An FE study has been then performed and, for simplicity, this effect was evaluated only considering thin substrates with square channels. A new variable was introduced, i.e., w, to quantify the degree of misalignment and it is defined as shown in Fig. 4.33. It was chosen to modify this parameter with 0.5 mm increments between 0, i.e., symmetrical joints, and 3 mm, i.e., the channel periods are in the opposite phase.

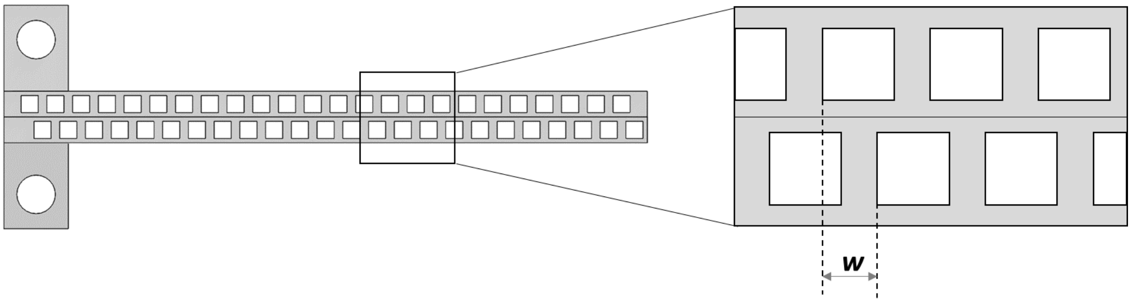

Fig. 4.33: Geometrical model of non-symmetrical joints

It is clear that channels misalignment produces an unsymmetric loading condition and, for that, mixed-mode loading conditions are introduced. However, it was chosen to use a mode-independent model for the cohesive model as done in recent works (Jain, Liechti and Bonnecaze, 2019). It is supposed that the degree of mode mixity does not largely modify the work of separation even if some experimental tests could be necessary to confirm this assumption. The load-displacement curves of these DCB joints are reported in Fig. 4.34. For simplicity, it was chosen to report as a percentage of the channel period in order to obtain immediate information about channel misalignment. It is possible to see that increasing distance between channels period, load-displacement curves are closer to the benchmark curve.

However, for small misalignment that could be attributed to difficulties during joints fabrication, this reduction is very small and does not invalidate mechanism efficiency. Furthermore, the crack trapping mechanism is still visible in all joints.

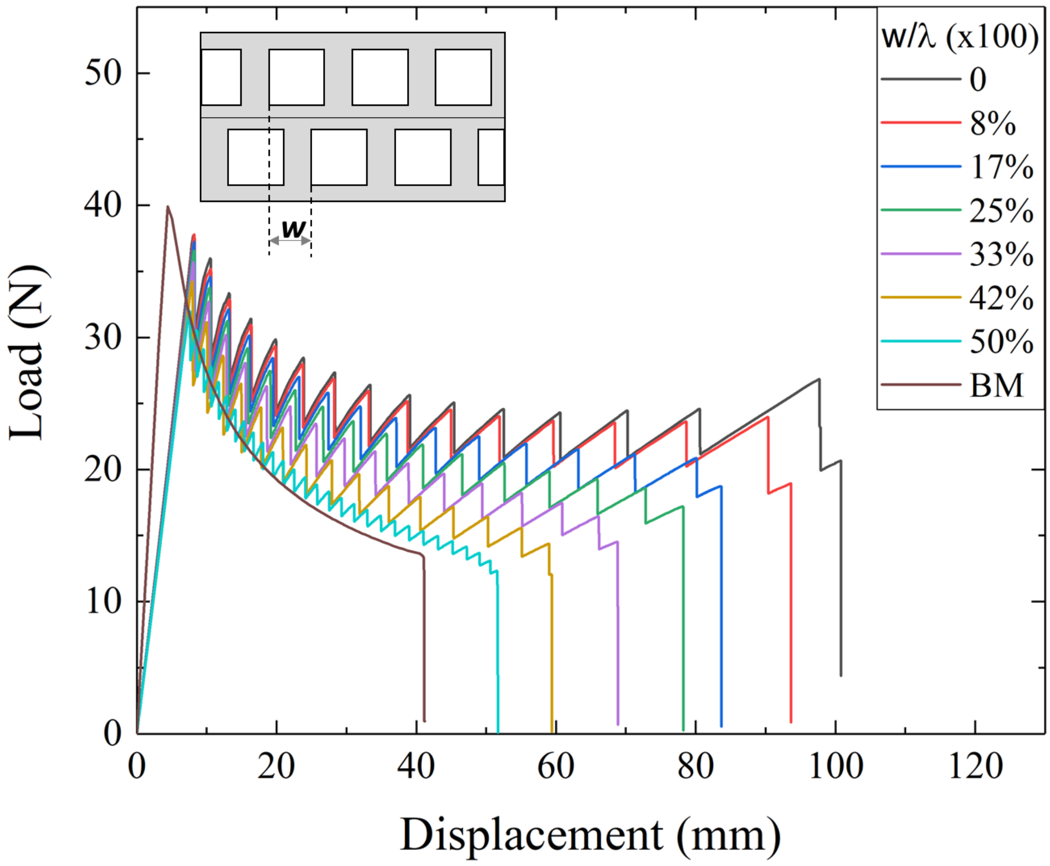

Fig. 4.34: Load-displacement curves obtained for non-symmetrical joints by increasing misalignment.

This result is very interesting because it demonstrates that crack trapping phenomenon reproduction does not require high precision in joints fabrication, establishing the applicability of that solution on large-scale, e.g., industrial fields.

4.5. Analysis of cohesive parameters on crack trapping effect

The influence of Traction-Separation Law (TSL) parameters on the load-displacement curve was analyzed. It is worth pointing out that for a benchmark DCB sample, the cohesive parameters are related to the fracture process zone by the following equation:

$$l_{fpz} = \alpha \frac{EG_c}{\sigma^2} \tag{4.6}$$

Where:

- l_{fpz} is the fracture process zone length;
- α is a constant the depends by joint geometry
- E is the adhesive Young's modulus;
- G_c and σ are the TSL parameters, i.e., adhesive fracture toughness and critical strength;

In order to assess the effect of the fracture process zone on the numerical simulations, the above equation was used as a first-order approximation to estimate the variation of the process zone with cohesive fracture properties.

It was chosen to modify the two main TSL parameters, i.e., G_c and σ keeping constant the Young modulus of the adhesive and therefore k_n, and substrate characteristics. The two parameters have been varied separately from the reference ones, among reasonable limits for the considered configuration. It was chosen to carry out simulations on DCB joints with the thinner substrate and both channels geometries and substrate material was assumed to be linear-elastic and isotropic removing plasticity from the model in order to simplify it. The maximum values for G_c and σ were fixed equal to 0.8 N/mm and 10 MPa respectively. Starting from the reference values, i.e., $G_c = 0{,}4\ N/mm$ and $\sigma = 10\ MPa$, it was chosen to modify each parameter by keeping the other constant. Both values have been increased and decreased and the l_{fpz} value was evaluated for each parameter combination (unless α value). Even if the fracture process zone could vary during crack propagation, it was chosen to carry out a comparative analysis in order to evaluate cohesive parameters influence and, for this reason, Eq. 4.6 could be used. The whole simulation plan that has been carried out is summarized in Tab. 4.2 and Fig. 4.35 are reported, by the way of example, two different TSL shapes obtained using some of the cohesive parameters reported in Tab. 4.2. For each configuration, it is also reported the l_{fpz} value. In particular, given that the equation used is developed for the standard DCB samples, it implies that we can only have a rough estimate of the process zone size through a coefficient that multiplies an unknown constant that has been named as alpha in the Tab. 4.2. Although the precise dimensions of the process zone could be estimated from FEA, here we just want to give, in a semi-quantitative fashion, an idea of the variation (increase or decrease) of the process zone size when comparing the various cases.

Tab. 4.2: Cohesive parameters variation plan

ID	Cohesive energy (N/mm)	Cohesive strength (MPa)	δ_{max} (mm)	δ_1 (mm)	l_{fpz} (mm)	l_{fpz}/R (l_{fpz}/B)
#1	0.1	10	0.02	0.001212	2 α	0.5 α
#2	0.2		0.04		3 α	1 α
#3	0.4		0.08		7 α	2 α
#4	0.8		0.16		14 α	3 α
#5	0.4	2	0.4	0.000242	170 α	43 α
#6		6	0.13	0.000727	19 α	5 α

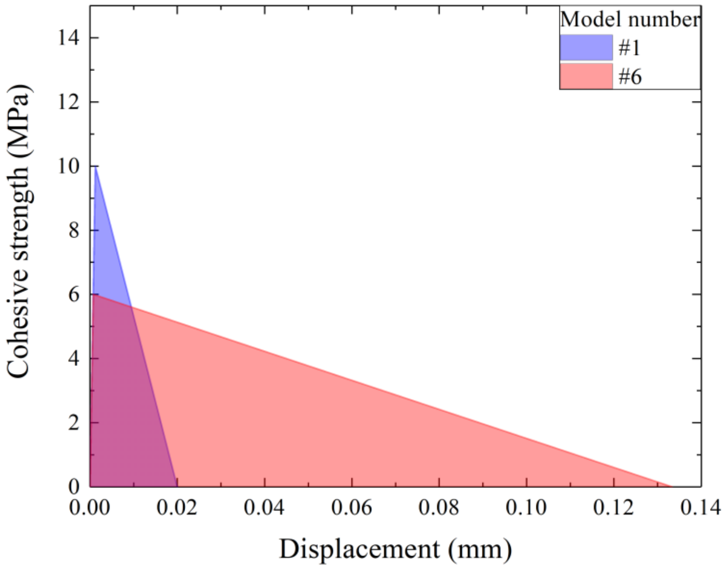

Fig. 4.35: Example of cohesive laws employed in the simulations

Load-displacement curves obtained varying σ for both subsurface channels are reported in Fig. 4.36 (a) and (b). It is possible to notice that reducing the σ value, peak load are lower meaning that the energy requested for crack propagation is lower for both channel geometries. Therefore, by increasing σ value, the influence on joint behavior seems to be negligible and load-displacement curves are similar. This result could be related to the fracture process zone dimension: when its dimension increases if compared with the initial dimension, it was found a weakening effect since load starts to decrease. Similar behavior was also observed by Sills and Thouless (Sills and Thouless, 2015) since they found that increasing the cohesive strength without modifying the fracture toughness produces a weakening effect.

TSL parameters influence has been evaluated also by comparing results in terms of ΔP, $\Delta\lambda$ and $\frac{l_{fpz}}{R}$. ΔP was calculated as the difference between the peak load and peak minimum during load fluctuation, $\Delta\lambda$ was obtained as the distance between two peak load. The results are reported in Fig. 4.36 (c) and (d). Both parameters increase by increase the cohesive strength. Results allow assuming that for $\sigma < 10\ MPa$, channels presence appears to be less effective to improve the effective fracture toughness of the joint suggesting that it is required interaction between l_{fpz} and channels dimensions, i.e., the $\frac{l_{fpz}}{R}$ ratio should be small. In fact, increasing $\frac{l_{fpz}}{R}$ ratio, load fluctuation is diminished and the load-displacement curve is closer to benchmark behavior.

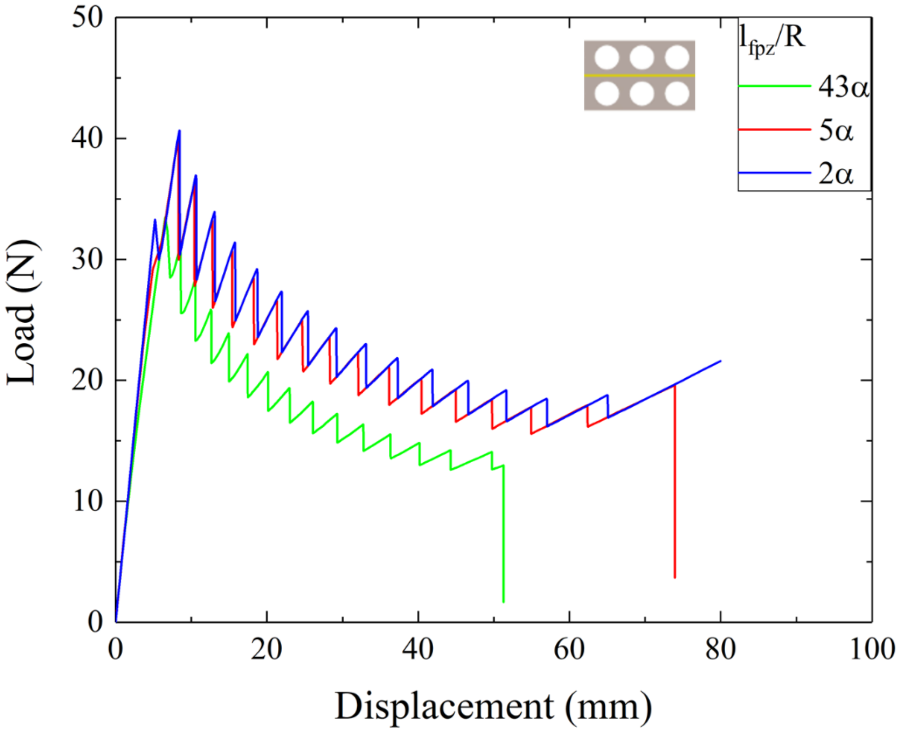

(a)

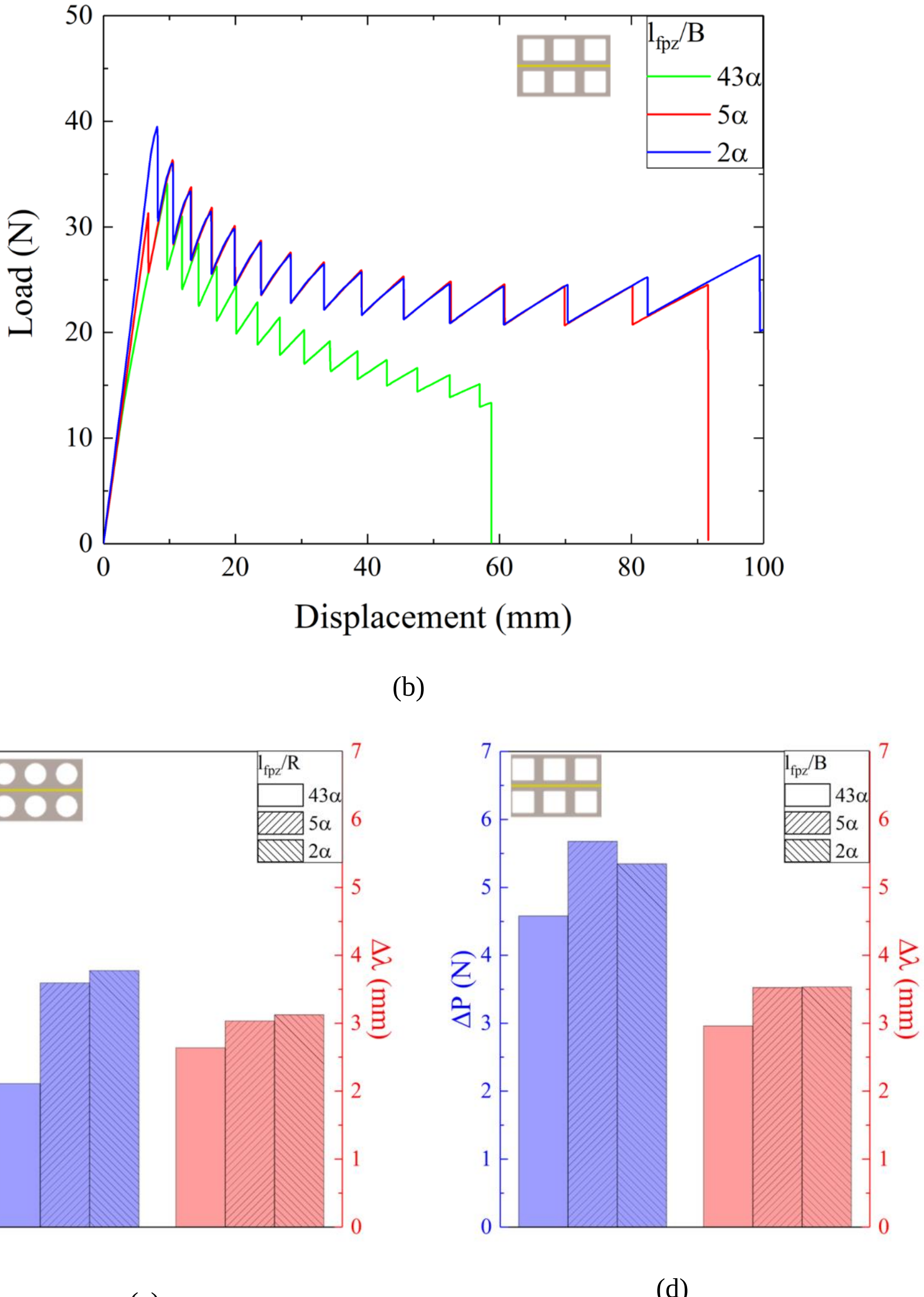

(b)

(c)

(d)

Fig. 4.36: Load displacement curves modification of (a) circular channels and (b) square channels and ΔP, $\Delta\lambda$ variation on (c) circular channels and (d) square channels obtained varying cohesive strength.

Load-displacement curves obtained varying G_c for both subsurface channel shape are reported in Fig. 4.37 (a) and (b).

It is possible to notice that increasing G_c value, load increase, meaning that the energy requested for crack propagation is higher for both channel geometries and vice versa. This result is not in agreement with what obtained for the fracture process zone. It was previously observed that when l_{fpz} value increase, the energy requested for crack propagation decrease. In this case, it seems that with an increase in the fracture process zone, the energy requested for crack propagation grows. Moreover, it is important to notice that l_{fpz} is increased by increasing fracture toughness of the joint and that is, of course, related to an increase of the energy requested to allow the propagation of the defect. Considering that, it could be necessary to compare the improvement in joint behavior with a benchmark with the same cohesive parameters.

TSL parameters influence has been evaluated also by comparing results in terms of $\varDelta P$, $\varDelta\lambda$ and results are reported in Fig. 4.37 (c) and (d). Both parameters increase by increase the cohesive fracture toughness up to $G_c = 0.8\, N/mm$ even if, $\varDelta P$ seems to be more affected by this variation for both channel shapes, reaching a value more than 3 times higher than the initial one for circular channels and more than 2 times higher for square channels. This difference is probably related to change into the material model, i.e., linear-elastic instead of elasto-plastic. In fact, it was observed previously that the increase of the energy requested for crack propagation for subsurface square channels is strictly related to plastic deformation around sharp edges and on the thin upper plate. The load fluctuation mechanism was analyzed on DCB joint with square subsurface channels in order to evaluate how fracture process zone changes during propagation for different TSL. As described above, it was used the SDEG parameter from the FE analysis.

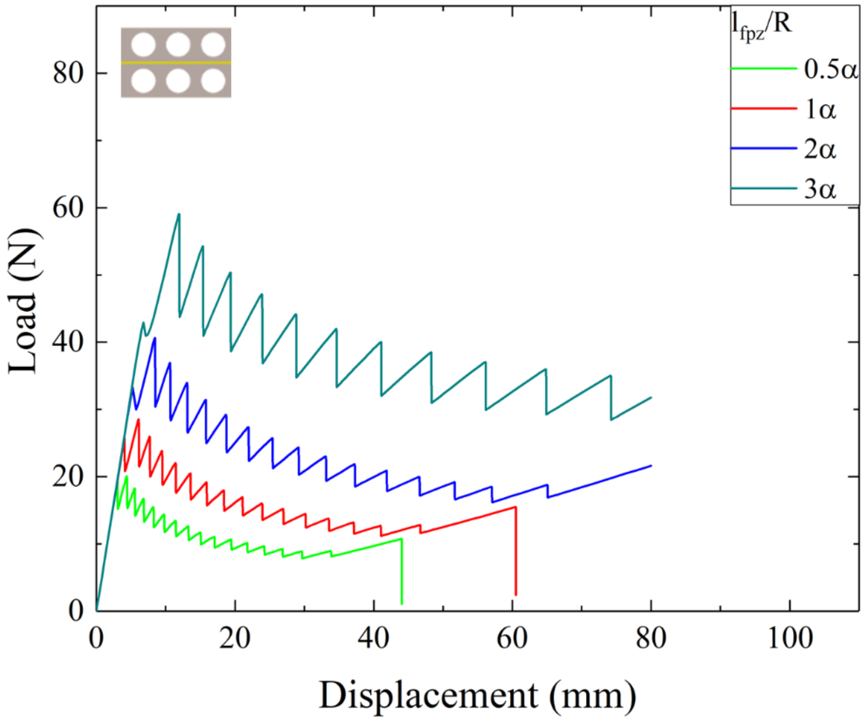
l_{fpz}/R
0.5α
1α
2α
3α
Load (N)
Displacement (mm)
0
20
40
60
80
100

(a)

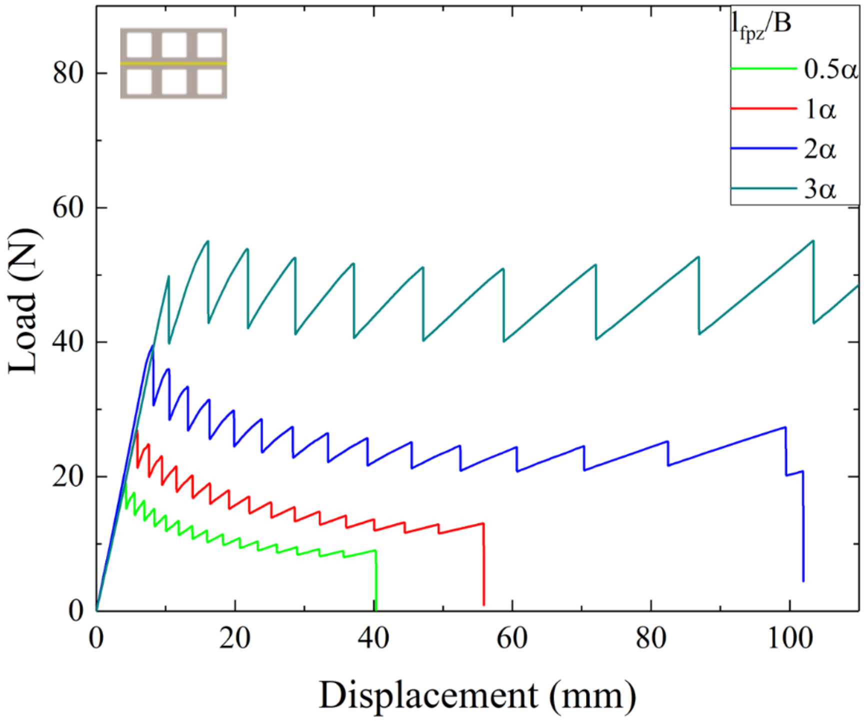
l_{fpz}/B
0.5α
1α
2α
3α
Load (N)
Displacement (mm)
0
20
40
60
80
100

(b)

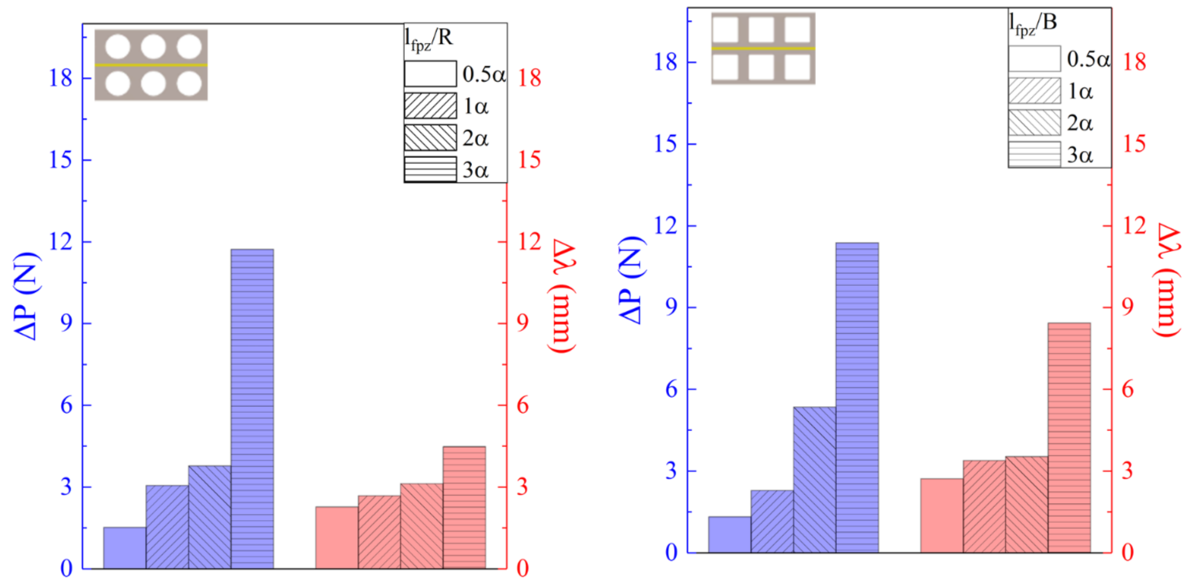

(c)

(d)

Fig. 4.37: Load displacement curves modification of (a) circular channels and (b) square channels and ΔP, $\Delta\lambda$ variation on (c) circular channels and (d) square channels obtained varying cohesive energy.

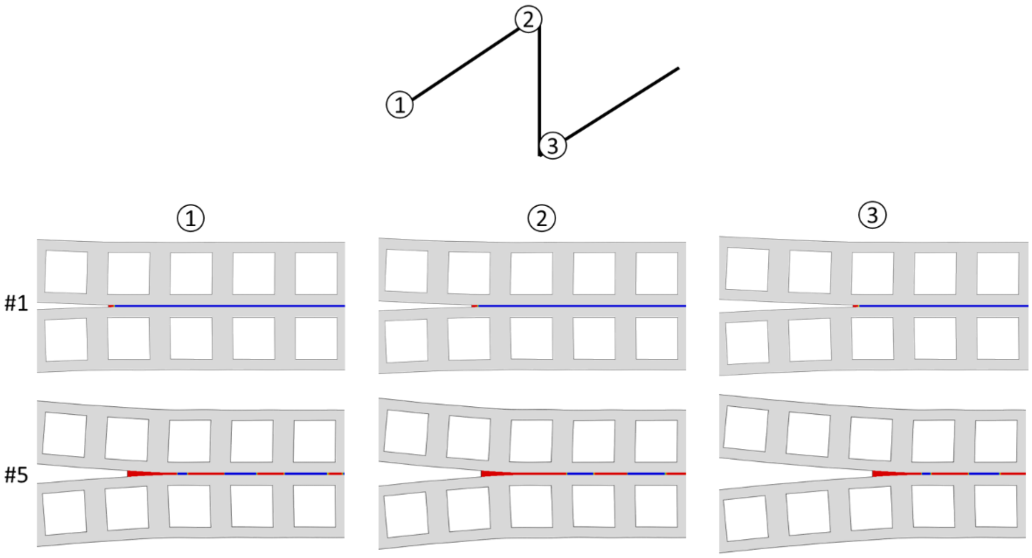

Fig. 4.38: Fracture process zone evolution for point 1, 2 and 3 for different cohesive parameters: #1 G_c=0.1 and σ= 10 and #5 G_c=0.4 and σ= 2.

Results of the analysis on model #1 and model#5, which are characterized by the lowest and the highest fracture process zone length respectively, are reported in Fig. 4.38. The crack propagation mechanism is the same observed during experimental tests and numerical simulation in the previous section. Crack propagation is stable (from point 1 to point 2 in Fig. 4.38) when the crack tip is located below the channels and it became unstable (from point 2 to point 3 in Fig. 4.38) when the crack tip is below the pillar with an instantaneous release on elastic energy. It is also noticeable that the length of the fracture process zone change in function of cohesive parameters in accordance with what obtained with Eq. 4.6. In particular, it was found that model #5 is characterized by the development of damage behind the main growing crack front as described before. It is possible to observe the increase of stiffness degradation parameter (SDEG) of cohesive elements below pillars ahead of the main crack front.

4.6. Application to DCB with sinusoidal interfaces

As explained before, the initial crack dimension (a_0) at the beginning of the mechanical tests was unknown. In addition, in this case, the numerical model was modified in order to reproduce the initial slope of experimental curves and the results are shown in Fig. 4.39-Fig. 4.42. For all cases the initial value of Δa for the numerical simulation was chosen according to the results obtained for bulk: the $a_0+\Delta a$ value has been settled equal 40 mm for both substrate thickness. At the end, the $a_0+\Delta a$ value has been estimated to be equal to (19±3) mm for 8mm substrate thickness with a/λ ratio equal to 1/4, (21±3) mm for 6 mm substrate thickness with a/λ ratio equal to 1/4, (18.5±1.5) mm for substrates with a/λ ratio equal to 1/3 and (19±1) mm for sinusoidal interface with a/λ ratio equal to 1/2. In all cases, the average value was used for the FE simulations.

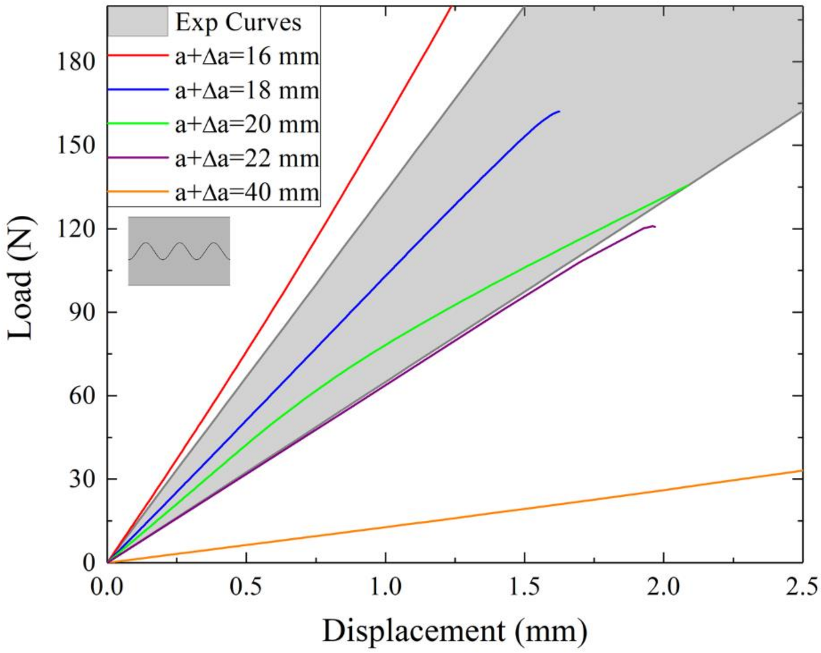

Fig. 4.39: Comparison between numerical and experimental results to evaluate Δa value for DCB joints with sinusoidal interfaces characterized by A/λ ratio equal to 1/4 and substrates thickness equal to 8 mm.

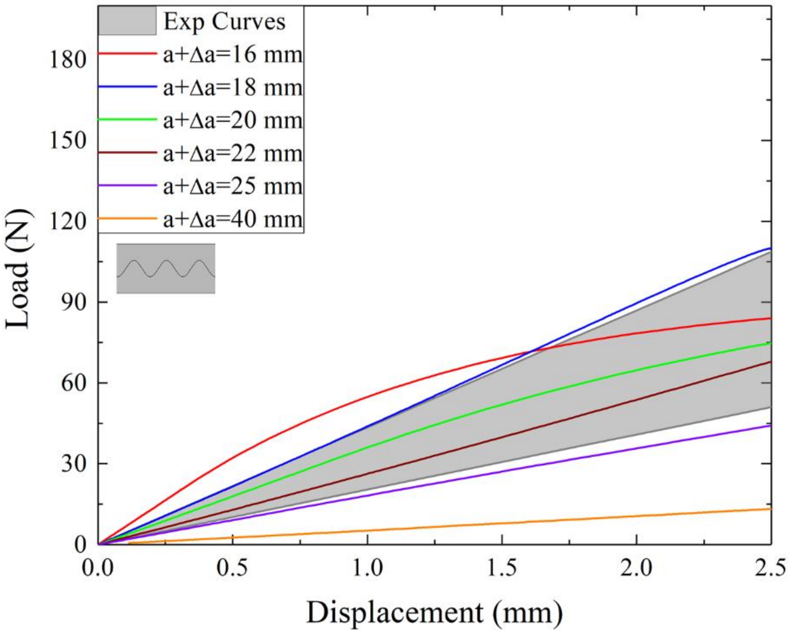

Fig. 4.40: Comparison between numerical and experimental results to evaluate Δa value for DCB joints with sinusoidal interfaces characterized by A/λ ratio equal to 1/4 and substrates thickness equal to 6 mm.

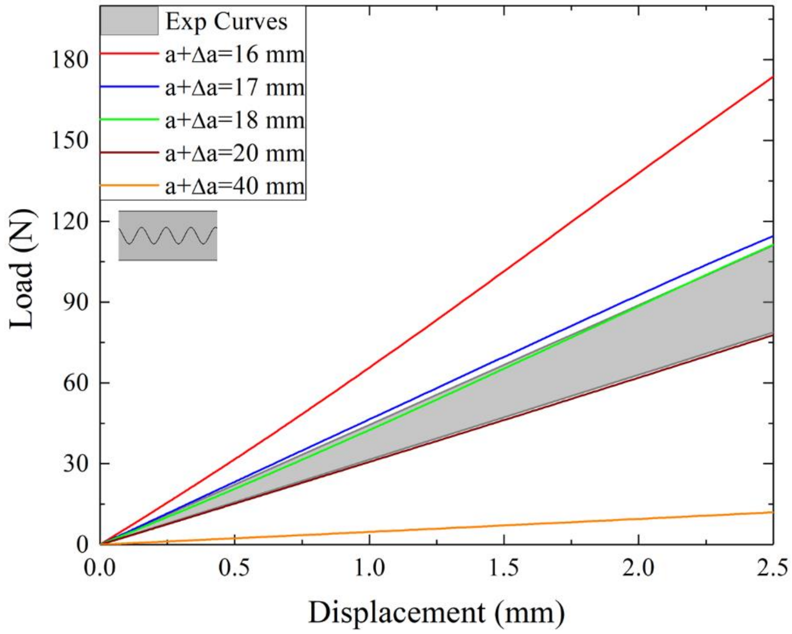

Fig. 4.41: Comparison between numerical and experimental results to evaluate Δa value for DCB joints with sinusoidal interfaces characterized by A/λ ratio equal to 1/3 and substrates thickness equal to 6 mm.

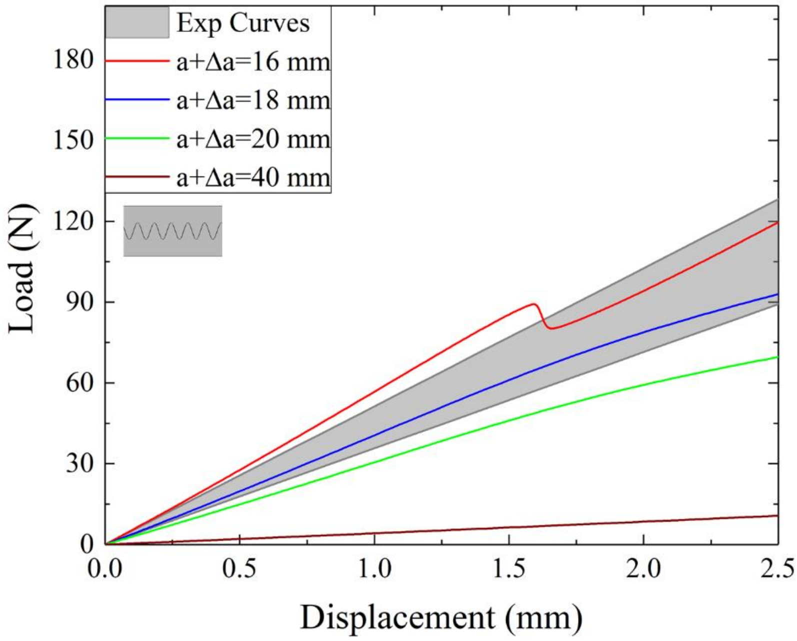

Fig. 4.42: Comparison between numerical and experimental results to evaluate Δa value for DCB joints with sinusoidal interfaces characterized by A/λ ratio equal to 1/2 and substrates thickness equal to 6 mm.

4.6.1. Comparison between numerical and experimental results

Numerical simulations with the sinusoidal interfaces were carried out using the cohesive parameters found using bulk samples and validated during simulation with subsurface channels. As explained in the previous chapter, the sinusoidal interfaces fail under mixed-mode conditions. Nevertheless, it was chosen to use a mode-independent model for the cohesive model as done in recent related works (Jain, Liechti and Bonnecaze, 2019). It is surmised that the degree of mode mixity does not largely modify the work of separation needed to sever the brittle epoxy/PA interface. A comparison between numerical and experimental results is shown in Fig. 4.43-Fig. 4.46.

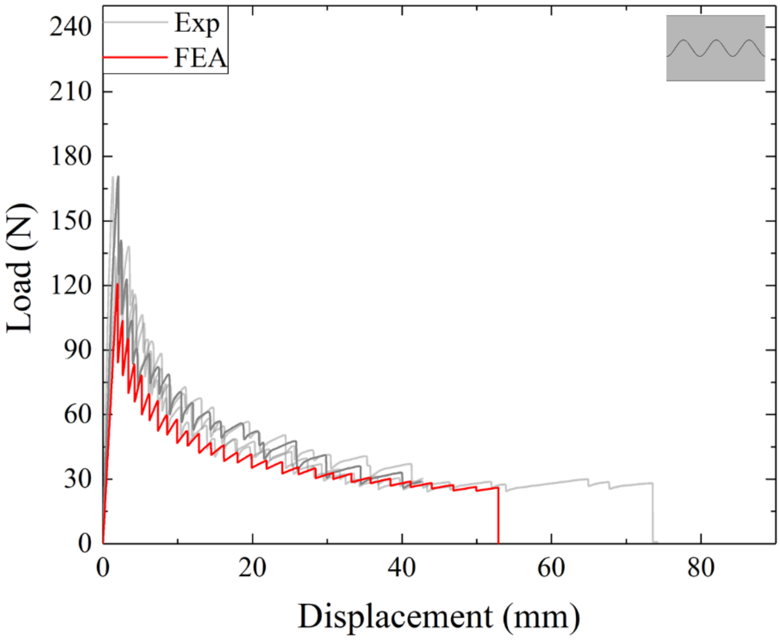

Fig. 4.43: Comparison between numerical and experimental results DCB joints with sinusoidal interfaces characterized by A/λ ratio equal to 1/4 and substrates thickness equal to 8 mm.

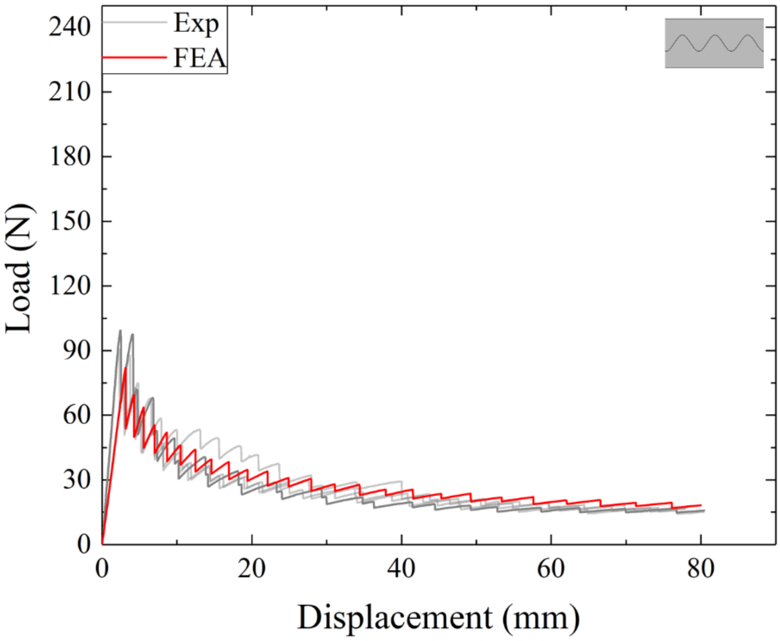

Fig. 4.44: Comparison between numerical and experimental results DCB joints with sinusoidal interfaces characterized by A/λ ratio equal to 1/4 and substrates thickness equal to 6 mm.

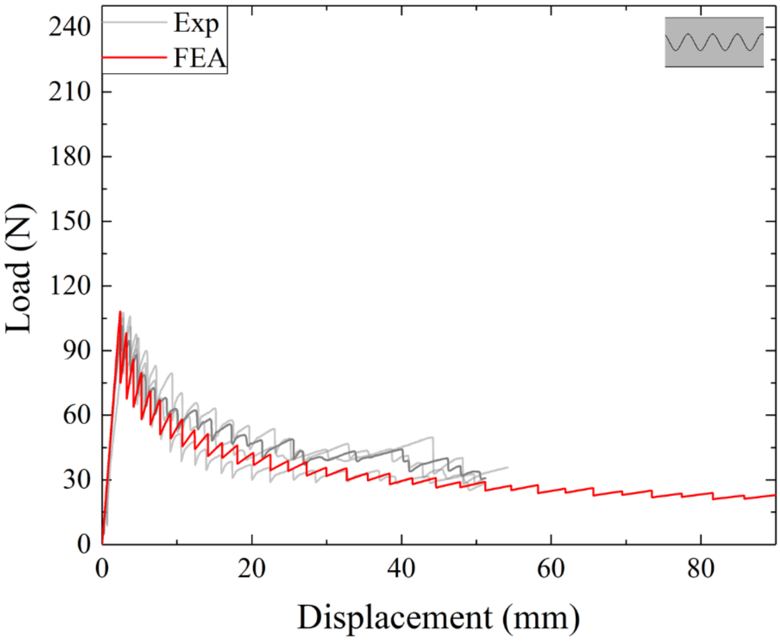

Fig. 4.45: Comparison between numerical and experimental results DCB joints with sinusoidal interfaces characterized by A/λ ratio equal to 1/3 and substrates thickness equal to 6 mm.

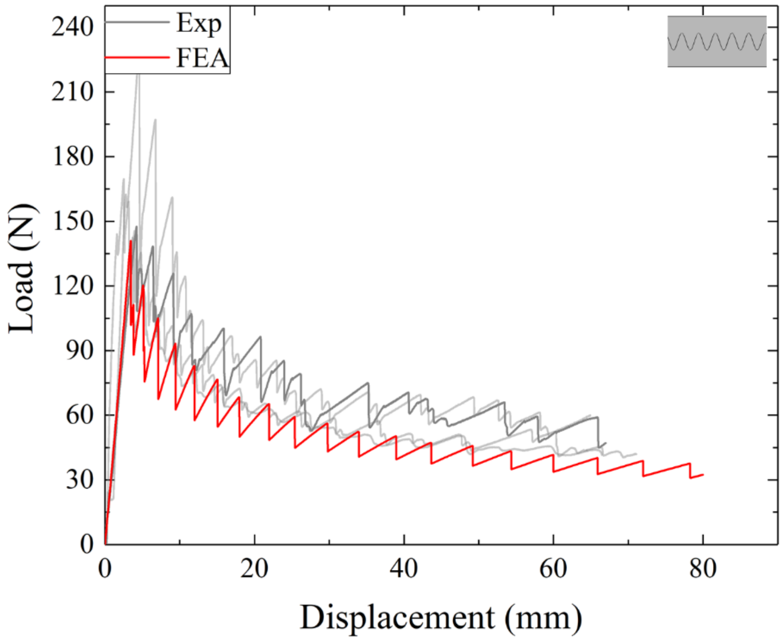

Fig. 4.46: Comparison between numerical and experimental results DCB joints with sinusoidal interfaces characterized by A/λ ratio equal to 1/2 and substrates thickness equal to 6 mm.

The results demonstrated that the numerical model underestimates joints behavior even if the cohesive parameters chosen for the cohesive law allow fitting the experimental curves with a good approximation. Neglecting the mode II that occur when defect growth along sinusoidal side, produce differences between numerical and experimental results and these difference became more evident for DCB joints with sinusoidal interfaces characterized by A/λ ratio equal to 1/2, where the mode II component is indeed higher. However, the numerical model is able to follow the same period seen in the experimental curves: the distance between two load peaks in numerical and experimental results are comparable. Load peaks and load minimums in each period of FE curves and experimental curves are fairly comparable. Moreover, the changes in the crack propagation path, that was observed experimentally, cannot be reproduced numerically since the adhesive layer was replaced with a single row of cohesive elements. This could justify the additional differences between experiments and simulations.

The total amount of each energetic contribution at the end of each simulation carried out on thinner substrates were compared in order to analyze the increase of the energy requested for crack propagation. As explained in the previous section, all values were divided by the crack area, i.e., crack length multiplied by substrate width, in order to obtain energy per unit area.

Then, all the values were compared with and the results are reported in Fig. 4.47-Fig. 4.48. In order to consider the improvement in energy dissipation obtained with the introduction of sinusoidal interfaces, the energy per unit area values were divided by the energy dissipated by bulk samples. In particular, attention was focused on the elastic energy, and on the effect of plasticity.

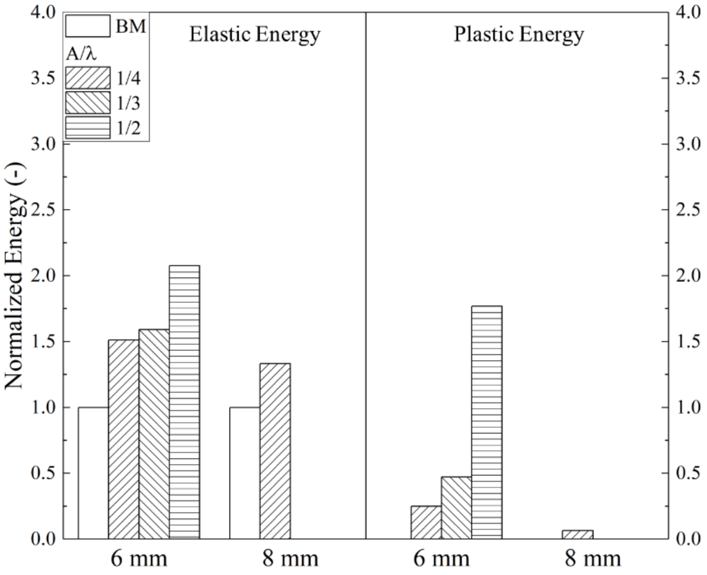

Fig. 4.47: Plastic and elastic energy dissipation as a function of different sinusoidal interfaces for both substrates thickness.

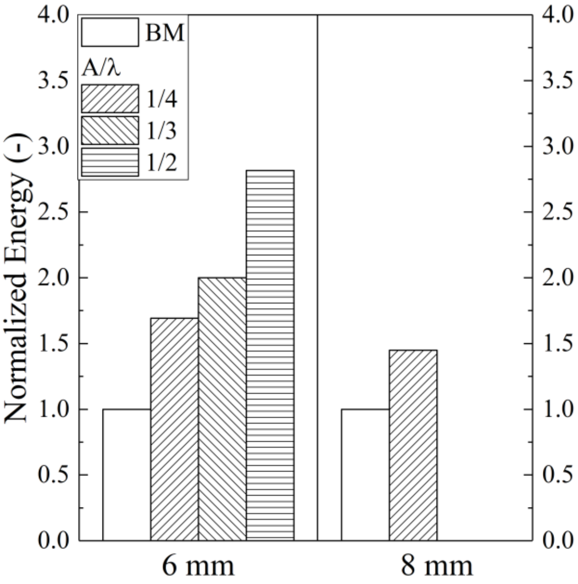

Fig. 4.48: Total energy dissipated numerically during crack propagation for sinusoidal adhesive joints with (a) t=8 mm and (b) t=6mm.

All the energy values increase modifying interfaces shape independently of sinusoid characteristics. Furthermore, results demonstrate that plastic energy is still necessary to exploit the increase of joint damage tolerance obtained with plastic energy dissipation, i.e., the best behaviors were obtained for joints with high plastic deformation. Plastic energy increase by increasing the A/λ ratio reaching the highest value for A/λ equal to 1/2. As for the other energy aliquot, the maximum value of the total energy requested for crack propagation was obtained using thin substrates (6 mm) and A/λ ratio equal to 1/2 for which total energy is four times higher than that obtained for benchmark samples. These values have also been compared with experimental results and it was found a good agreement between two results even if, as observed from load-displacement curves, experimental values are higher than the same values obtained experimentally as shown in Fig. 4.49.

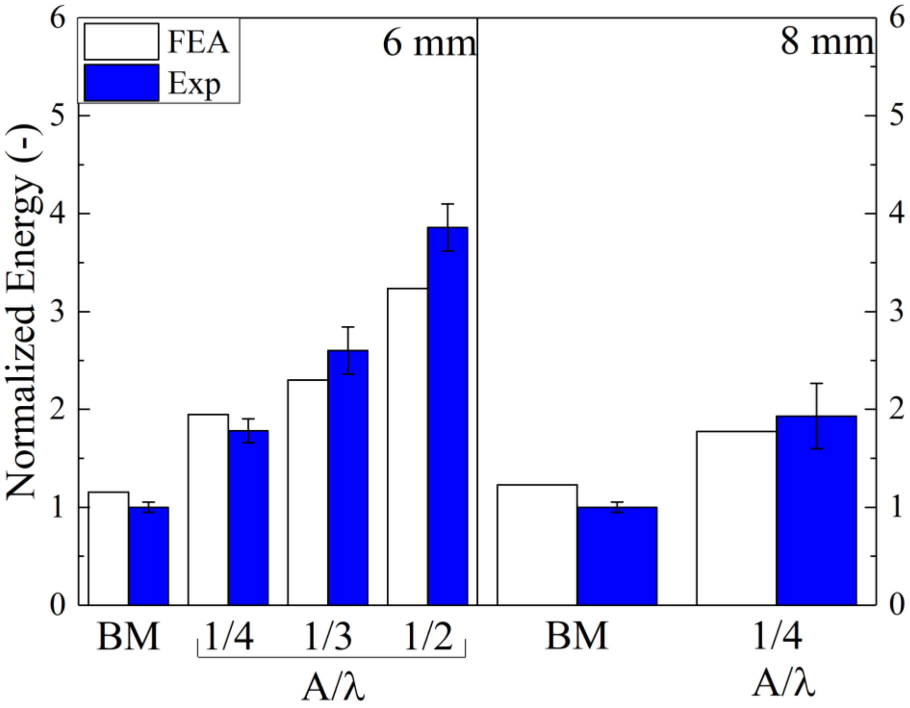

Fig. 4.49: Comparison between total energy dissipated numerically and experimentally for sinusoidal DCB joints with t=8 mm and t=6mm.

Even if sinusoidal interfaces allow reaching similar improvement in damage tolerance, subsurface channels introduce also a weight reduction and, for this reason, the analysis of this type of adhesive joints has been further assessed in the subsequent part of this work.

Chapter 5: Improved design choices based on FEA

Experimental and numerical results reported in the previous chapters indicated that the energy requested for crack propagation depends on the shape and size of the channels, and the overall variation of compliance. This suggests that it is potentially possible to tune energy dissipation by varying the selected variables, such as the shape, the period, the size of the channels. This goal has been pursued using two different approaches. In the first one, a simple design exploration strategy has been used to assess the response of DCB adhesive joints for varying channels architecture. In the second part of the chapter, an additional approach is described, whereby an "optimal" design is sought by using a parametric analysis based on the definition of a set of non-dimensional geometrical variables.

5.1 Design exploration

The results reported in the previous chapters have shown that for thin substrates the energy dissipated was largely increased through the "dissipation" of elastic energy sudden released during crack growth as well as through plastic deformations within the adherents. The plastic deformations were mainly due to the presence of regions of stress concentrations, as well as the strain energy stored within the bent arms, such as the upper plate of the pillar between the channels. In order to explore alternative geometries that could provide an enhancement in the total work of fracture, it was chosen to explore triangular subsurface channels with different orientations and with different angles and side lengths. A schematic of all geometries considered is reported in Fig. 5.1. Different models have been classified with a progressive code: T6#"n" where T means triangular channels, 6 indicate substrates thickness, i.e., 6mm, and “n” is a progressive number that identifies the model. Geometries haven been developed also taking into account 3D printing limits, i.e., small admissible dimension and sharp edges reproduction.

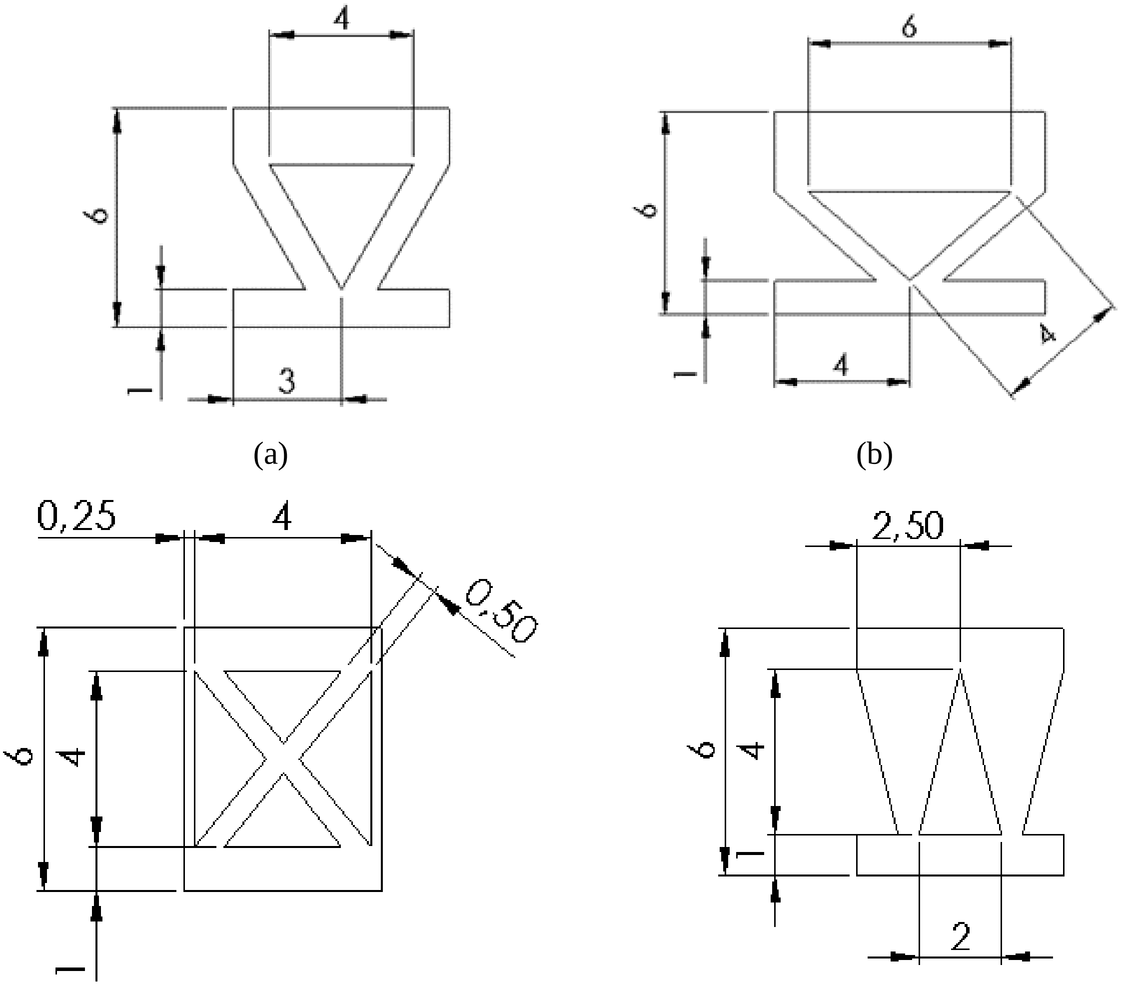

(a) (b)

(c) (d)

Fig. 5.1: Geometric features of triangular channels chosen for new DCB joints: (a) T6#1, (b)T6#2, (c)T6#3 and (d)T6#4.

In addition to the geometries described above, it was also chosen to analyze the effect of a combination of previous channels shape, i.e., circular and square channels. New geometry obtained is shown in Fig. 5.2 and it will be called “Buttonhole”. The details of the geometry and corresponding dimensions are also given in the same schematic.

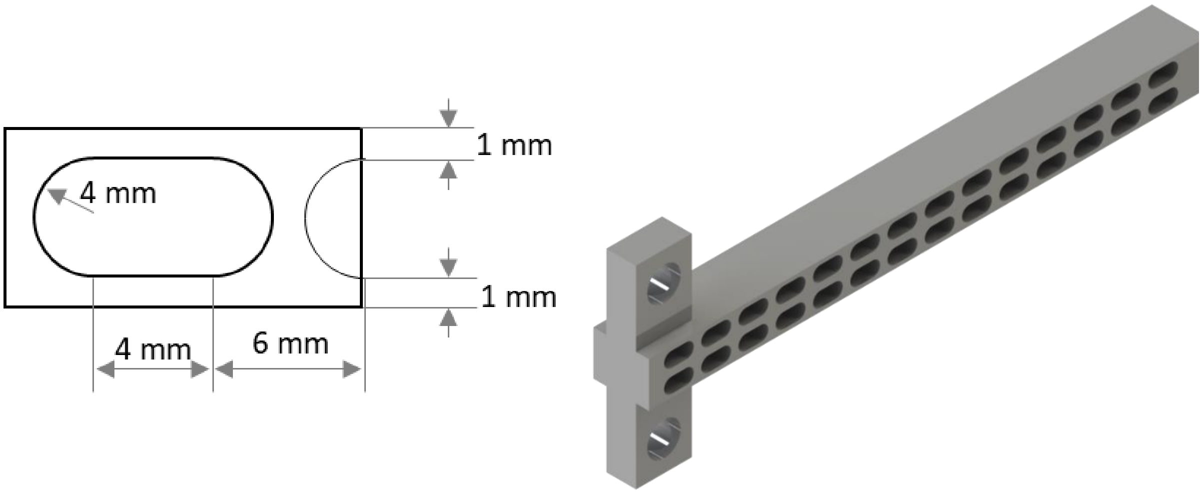

Fig. 5.2: Buttonhole channels geometry and 3D model of DCB joint with buttonhole bioinspired channels

A finite element model for each of the above geometries was created and crack propagation was assessed using the cohesive zone approach. As explained in the previous chapter, the law chosen for this purpose is the bilinear one and the cohesive parameters are those obtained previously by comparing experiments and simulations. Substrate behavior was assumed to be elasto-plastic since it was shown to have a relevant role in the overall work of separation. Load-displacement curves obtained for all samples are reported in Fig. 5.3. All geometries still allow achieving a serrated behavior in the load-displacement curves because of the crack-trapping effect discussed earlier. The displacement at failure and the amplitude of load fluctuations vary as a function of channel shape, thus demonstrating that the ability to delay crack propagation depends on the geometry of the channels.

The load-displacement curve obtained on DCB joint with buttonhole channels is reported in Fig. 5.3 (a). Notice that the simulations predicted a plastic collapse of the thin upper part of the joint for larger values of crack length. This phenomenon is shown in Fig. 5.4. Even if plastic deformations are large, the substrates do not reach fracture since the maximum stress was lower than the ultimate stress evaluated experimentally. However, the observed large increase in the applied load prompted the evaluation of this sample geometry in subsequent experimental tests. The crack propagation mechanism is similar to that observed previously: propagation is hindered when the crack tip is located around the pillar while it propagates very fast when it is located below the channels. For triangular channels, it is still possible to achieve a crack propagation mechanism that closely follows that observed in other geometries since this geometry still induces compliance variation as for the other geometries.

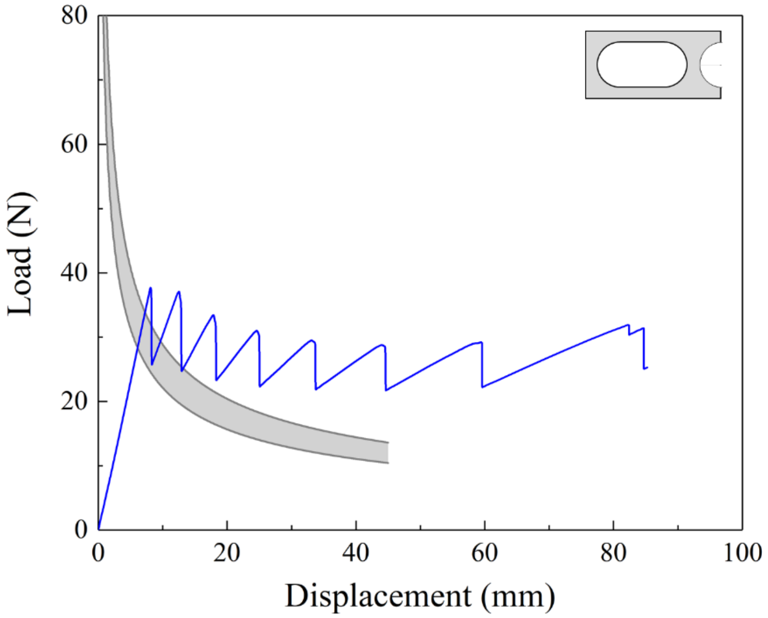

(a)

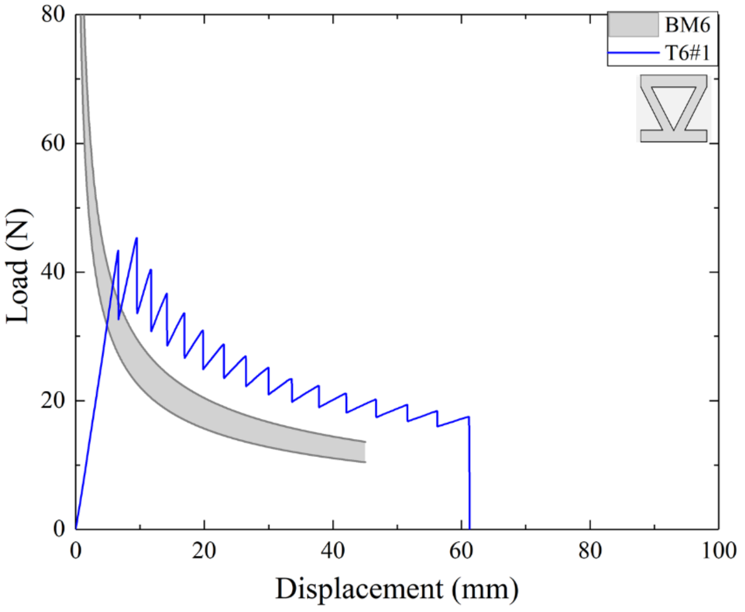

(b)

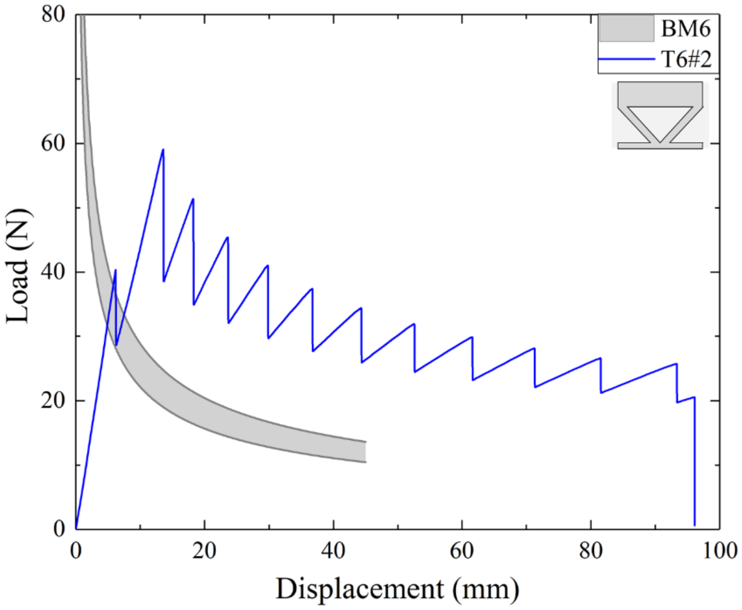
80
60
40
20
0
Load (N)
0
20
40
60
80
100
Displacement (mm)
BM6
T6#2

(c)

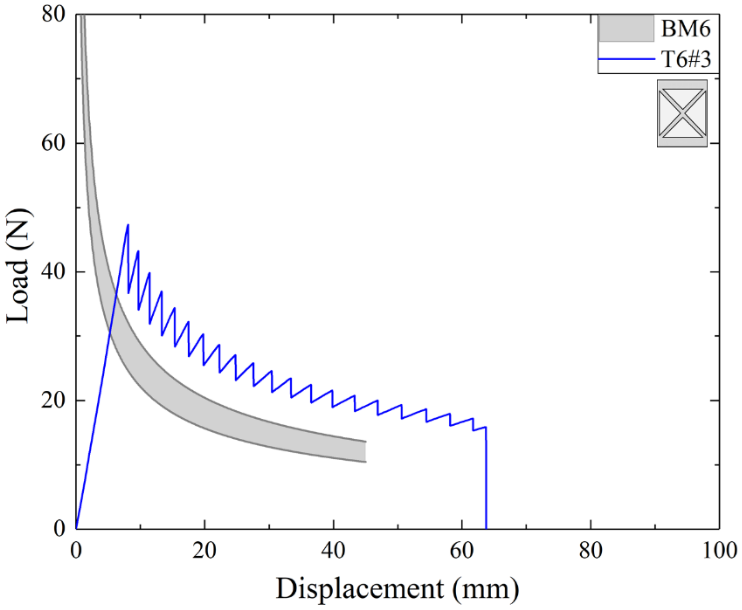
80
60
40
20
0
Load (N)
0
20
40
60
80
100
Displacement (mm)
BM6
T6#3

(d)

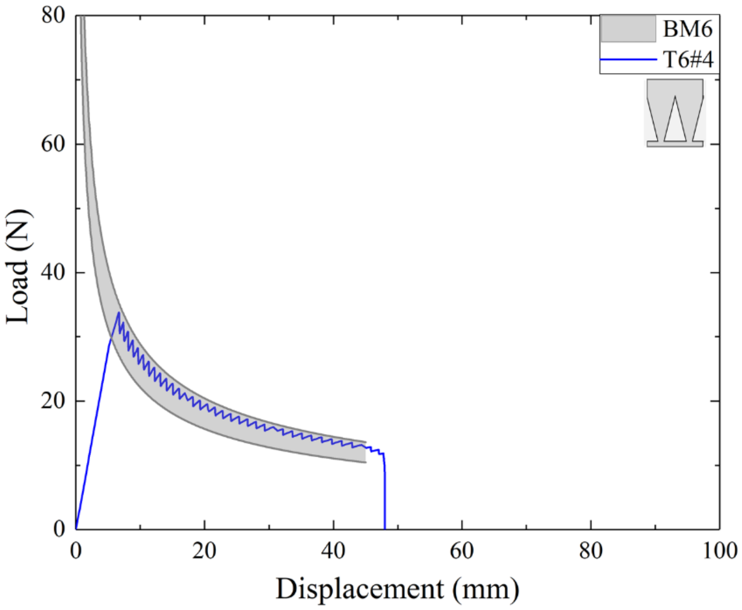

(e)

Fig. 5.3: Load displacement curves obtained numerically on bioinspired DCB joints with (a) buttonhole channels and triangular channels: (b) T6#1 (c) T6#2 (d) T6#3 (e) T6#4

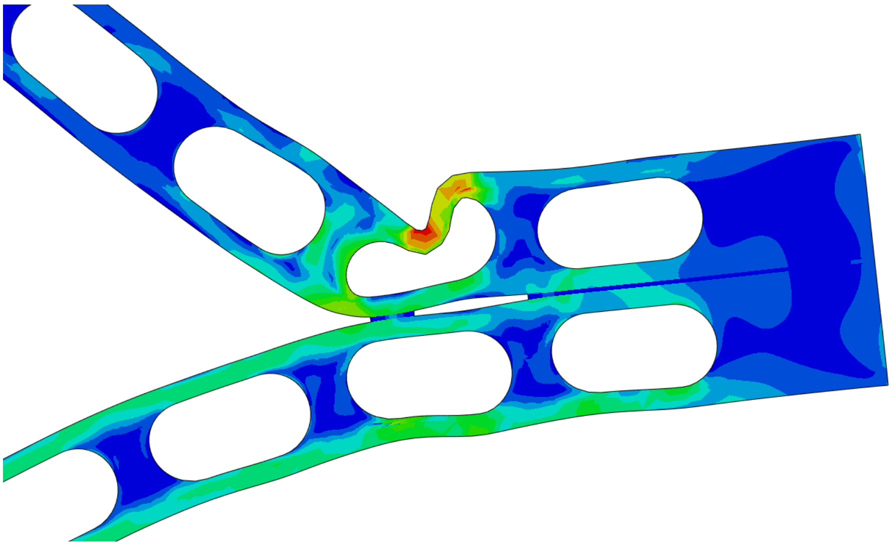

Fig. 5.4: High plastic deformation occurred during crack propagation on DCB joint with buttonhole channels

Subsurface channels efficiency has been also compared in terms of energy requested for crack propagation and, in particular, plastic and elastic energy components have been evaluated individually. As explained in the previous chapter, all values were divided by the crack area, i.e., crack length multiplied by substrate width, in order to obtain energy per unit area. All energy values were divided by reference value obtained on benchmark samples and, in addition, they were compared with previous results. The results are shown in Fig. 5.5. Except for one case, i.e. T6#4, the dissipated energy increase irrespective of channel shape. Depending on the shape of the channels, there is also a variable contribution associated with plasticity that contributes to the overall work. Plastic energy increase with the introduction of the channels in the substrates reaching higher values with T6#2, while for T6#4 there is basically no effect of the channels and the response is indeed fully within the bounds of the benchmark samples.

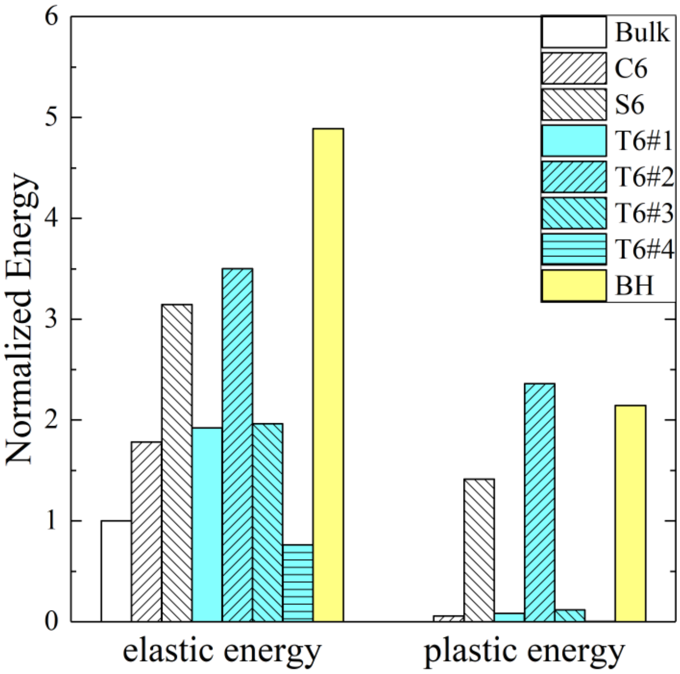

(a)

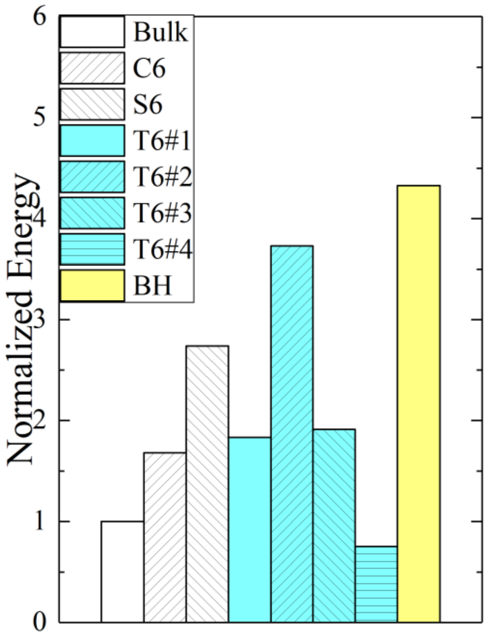

(b)

Fig. 5.5: Energy values for different geometries: (a) elastic and plastic contributions and (b) total energy requested for crack propagation

Moreover, in T6#1 and T6#3, plastic energy is very low as observed previously for circular channels. Instead, T6#2 and the buttonhole geometry discussed earlier, show plastic dissipation comparable if not higher than that of the samples with square channels. This is due to the considerable plastic dissipation occurring because of the geometrical details of the substrates, see Fig. 5.6.

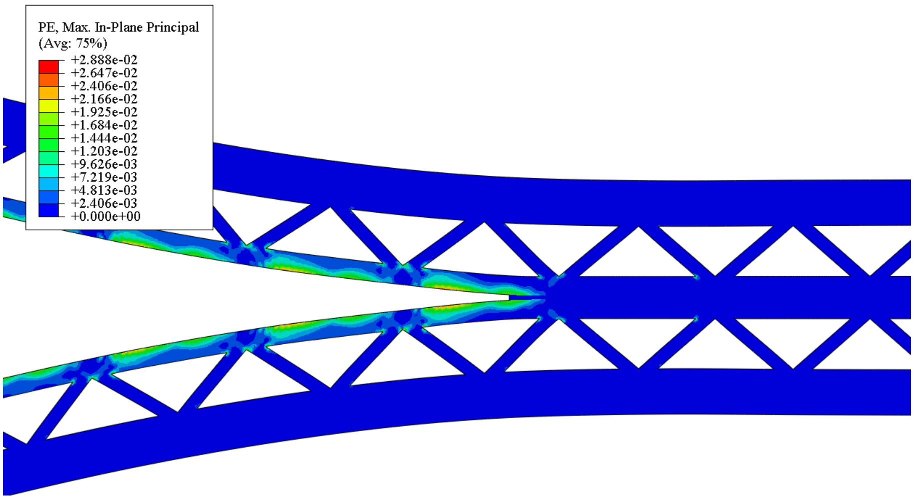

(a)

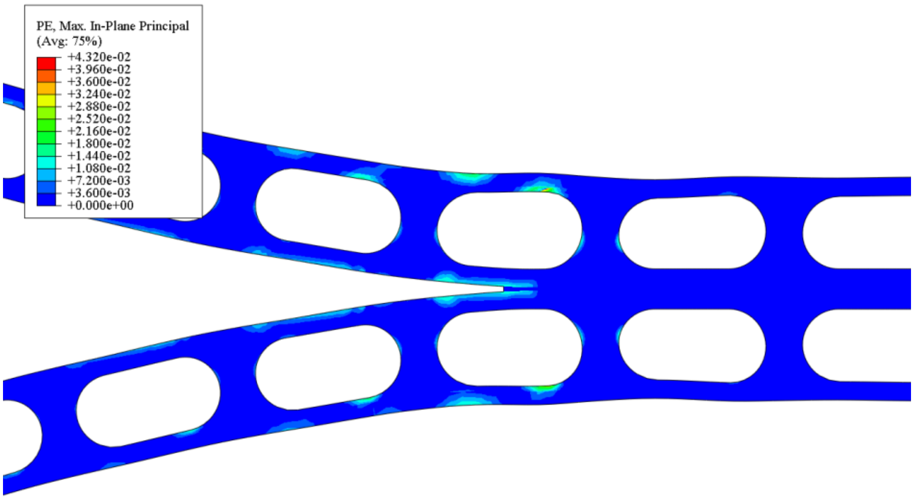

(b)

Fig. 5.6: Plastic deformation occurred during crack propagation for (a) T6#2 channels and (b) buttonhole channels

Localized plastic deformations occur at the corners for T6#2 and at the extended top plate for the sample named buttonhole. The results show that it is possible to increase the energy requested for crack propagation and, for this reason, it was chosen to reproduce experimentally these samples by 3D printing and adhesive bonding. The results will be discussed in the next section.

5.2 Experimental validation

Numerical results highlighted in previous sections demonstrate that it is possible to improve the energy requested for crack propagation and to hinder crack propagation by modifying channel shape. In particular, triangular and buttonhole channels have been chosen from the numerical study for subsequent 3D printing. 3D printed DCB joints with bioinspired channels have been realized as described before. Benchmark samples and target bioinspired joint with square cross-section channels have been added to the printing batch to verify the cohesive properties of the interface of the new batch. The load-displacement curves of DCB tests carried on samples with triangular and buttonhole subsurface channels with substrate thickness equal to 6 mm are reported in Fig. 5.7.

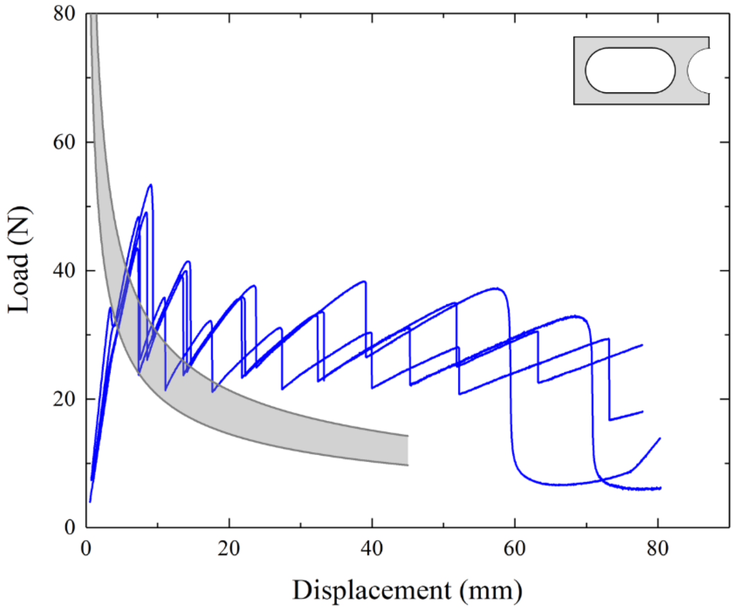

(a)

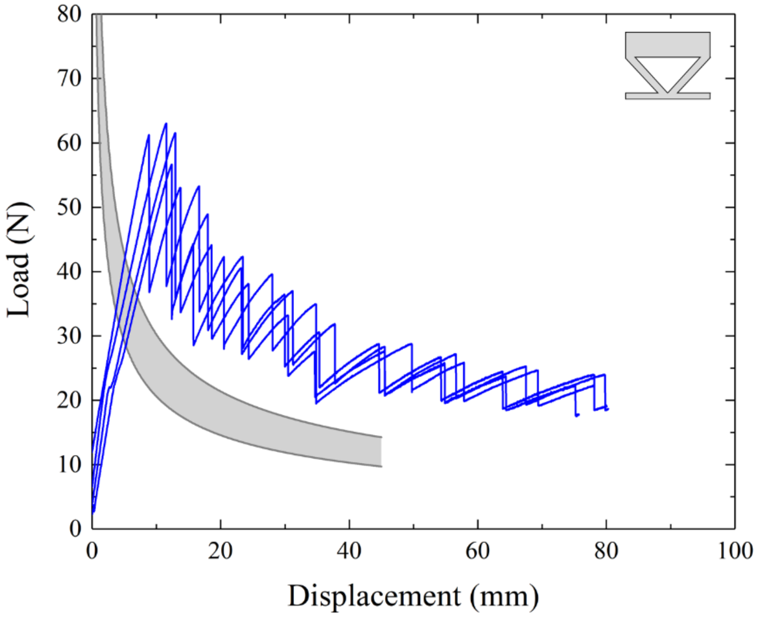

(b)

Fig. 5.7: Load displacement curves obtained on DCB samples with subsurface channels related to a) buttonhole b) T6#2.

It can be observed that also with these two different geometries, global responses are shifted towards higher load values and are characterized by strong load fluctuations. This result demonstrates that the introduction of subsurface channels allows reproducing crack trapping effect, independently by channel shape. Regarding buttonholes channels, Fig. 5.7 (a), two experimental curves showed changes in their shape for high displacement values. This behavior is related to the collapse of the thin plate in the upper part of the joint that was also observed numerically, as shown in Fig. 5.8. High compressive stresses induce buckling instabilities of the top plate, even if this effect was obtained for smaller displacement during experimental tests compared to FE simulations. It is interesting to notice that this condition did not involve substrate fracture as predicted by numerical simulations demonstrating that this structure is able to store high values of elastic energy and plastic deformations. Moreover, crack propagation was arrested.

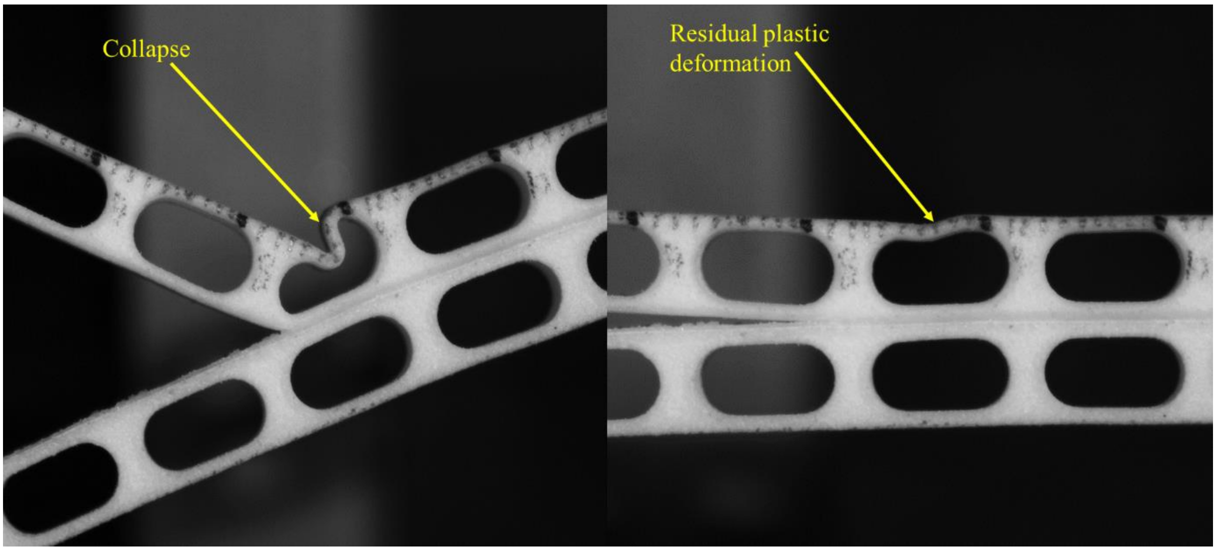

Fig. 5.8: Collapse of the thin structure on DCB joints with buttonhole channels observed experimentally under loading (left) and afterload removal (right).

Experimental results have been also compared with FE simulations in Fig. 5.9. It is possible to notice that for both channels geometry, the two curves obtained, i.e., numerical and experimental, are characterized by very similar behavior: it was found similar load fluctuation period and amplitude. Some differences have been observed for triangular channels where experimental curves suggest that the absorbed energy was higher than that predicted by the FE simulations. This difference was attributed to variation in nominal fracture toughness since, during experimental tests, some variations in fracture toughness have been obtained for different production batches. In fact, these samples (T6#2 and buttonhole) have been realized in two different batches. Nevertheless, the global response obtained for both channels shape with the two methods, i.e., experimental and numerical, are similar and comparable.

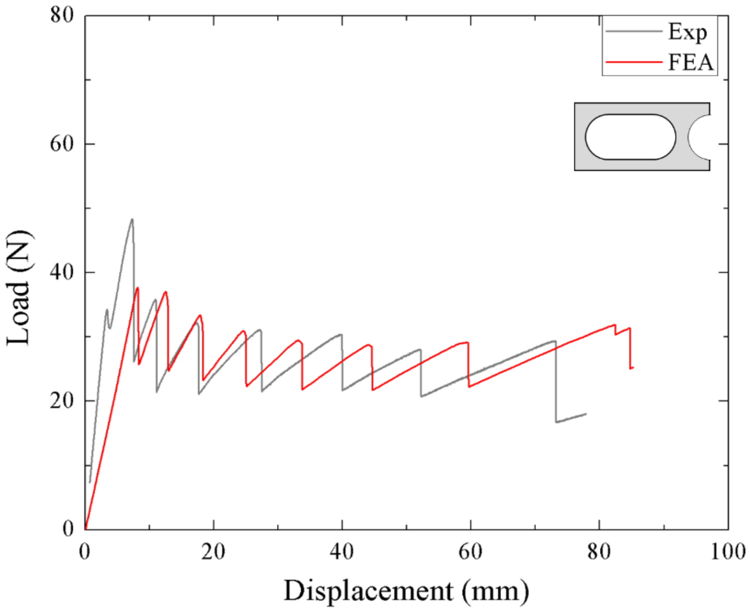

(a)

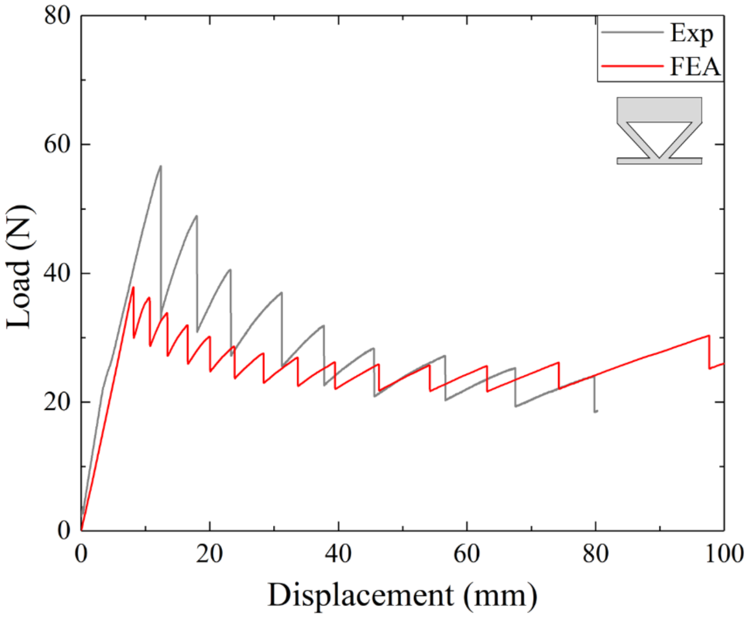

(b)

Fig. 5.9: Comparison between numerical and experimental results on DCB joints with (a) buttonhole channels and (b) triangular channels

The crack trapping mechanism was again assessed by using high-resolution images as reported in Fig. 5.10 and these results have been compared with snapshots from FE analysis. Regarding samples with buttonhole channels, a mechanism similar to that of previous models was observed, i.e., crack hindering when the crack tip is around the pillar and fast propagation when it is below the channels. The introduction of channels locally modifies joint compliance as for the samples that have been described earlier. It should be noted that toughening associated with the fluctuations in the material stiffness was also reported in recent related works (Fratzl *et al.*, 2007; Kolednik *et al.*, 2014). A comparison between experimental and numerical snapshots allows us to observe there is a good match between the crack positions determined in experiments and simulations.

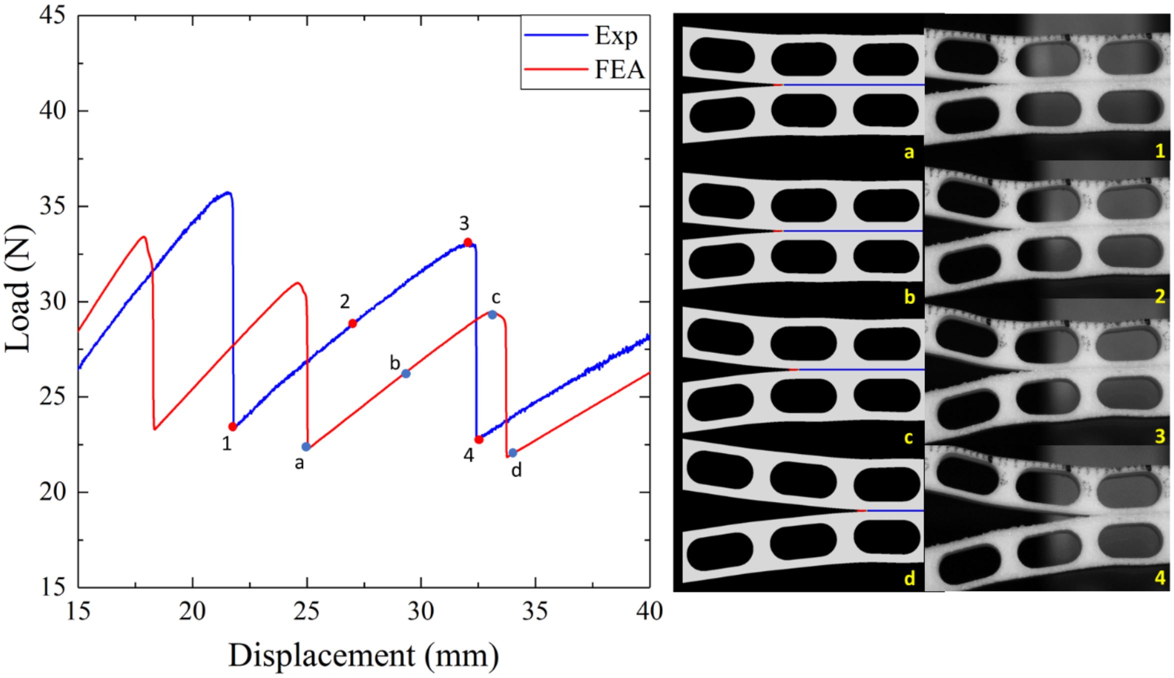

(a)

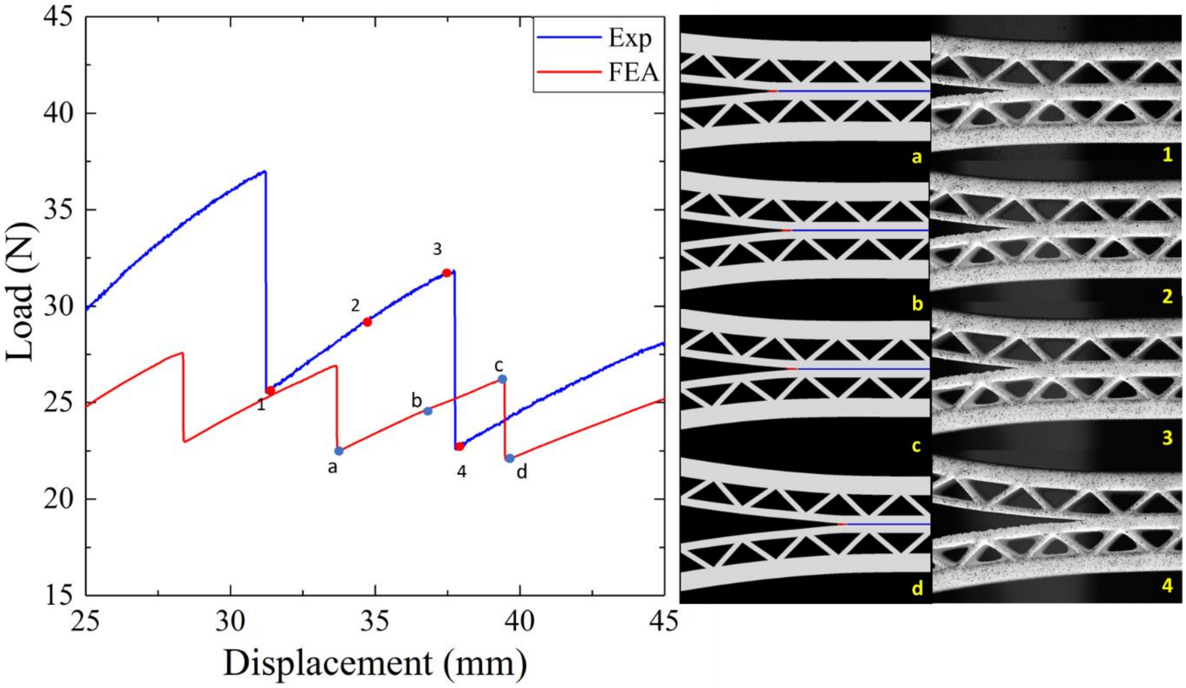

(b)

Fig. 5.10: Comparison between crack trapping mechanism observed numerically and experimentally for (a) buttonhole channels and (b) triangular channels

For triangular channels, even if it is not possible to identify a “bulk” zone, propagation follows the same mechanism observed for the other geometries.

5.3 Tuning energy dissipation using a parametric analysis

As explained before, the variation of each channel’s pattern dimension could influence joint fracture toughness. This aim could be obtained by using the dimensionless model. The dimensionless analysis is based on the Buckingham π theorem that provides a valid tool for the generation of dimensionless groups. Considering a generic equation, that could be written as Eq. 5.1:

$$f(x_1, x_2, \dots, x_i, \dots, x_n) = 0 \tag{5.1}$$

where x_i are n different physical variables, that could be express in terms of k independent fundamental physical units; the above equation can be reformulated as a function of "$p = n - k$" dimensionless parameters obtained from the original variables, Eq. 5.2:

$$F(\pi_1, \pi_2, \dots, \pi_i, \dots, \pi_p) = 0 \tag{5.2}$$

The dimensionless parameters π_i can be obtained as the following Eq. 5.3:

$$\pi_i = x_1^{n1}, x_2^{n2}, \dots, x_n^{nm} \tag{5.3}$$

where n_i is a rational number. The theory gives a strategy to build a dimensionless equation though the original equation form is unknown and without introducing any limitation on the dimensionless variable's selection. For this reason, the choice of parameters is not unique. The influence of geometrical parameters, as well as material characteristics, on the capability to improve the damage tolerance of DCB joints, could be studied as a function of mechanical and geometrical variables, considering the variation of effective fracture toughness, i.e., G_{eff}, calculated as the total energy dissipated during crack propagation divided by crack area. To understand how variables, i.e., input variables, are involved in the determination of the fracture toughness, i.e., output variable, it could be useful to divide the problem into three different groups: (a) Substrate (b) adhesive and (c) geometric properties.

5.3.1 Substrate properties

The material used for the realization of the substrate is a 3D printed nylon. To simplify the problem, it was considered to be isotropic, i.e., E_1=E_2=E and ν_{12}= ν_{21}= ν. The anisotropy, that could be introduced by 3D printing build direction, was excluded thanks to preliminary tests made on dogbone samples printed using different part orientation.

The effect of the plastic deformation observed during DCB experimental tests was considered by two other parameters: the yield stress, i.e., σ_y, and the strain-hardening exponent, i.e., n, assuming a stress-strain curve, for $\varepsilon \geq \frac{\sigma_y}{E}$, described by the following equation 5.4:

$$\sigma_y = k\ \varepsilon^n \tag{5.4}$$

The physical units for these variables are:

$$\begin{cases} E = [Nmm^{-2}] \\ \nu = [-] \\ \sigma_y = [Nmm^{-2}] \\ n = [-] \end{cases}$$

where both ν and n are already dimensionless.

5.3.2 Adhesive properties

The thickness of the adhesive layer, employed during experiments, was very small compared to the substrate thickness, therefore in FE analysis, it was modeled as an interface using cohesive elements. For that reason, the variables involved in the problem definition are the same chosen in the numerical model, i.e., cohesive strength σ_{max}, the cohesive energy, G_{IC} and the initial stiffness k_n. These variables are expressed in terms of:

$$\begin{cases} \sigma_{max} = [Nmm^{-2}] \\ G_{IC} = [Nmm^{-1}] \\ k_n = [Nmm^{-3}] \end{cases}$$

5.3.3 Geometry

The channels geometry play a fundamental role in the definition of G_{eff} equation. To identify all variables required for the definition of the problem, a geometric model was built as shown in Fig. 5.11. Overall, six different variables were chosen: (a) B, i.e., the channel height; (b) C, i.e., the channel width; (c) r, i.e., the fillet radius of the channel; (d) t, i.e., the distance between the channel center and the interface; (e) λ, i.e., the distance between two channels; (f) H, the substrates thickness. It is important to notice that the geometric model allows reproducing both geometries tested experimentally: the square channels are obtained with $r = 0$ and $B = C = 4\,mm$ while circular one is achieved with $r = \frac{B}{2} = \frac{C}{2} = 2\,mm$. The physical unit for these variables is the length, i.e., mm.

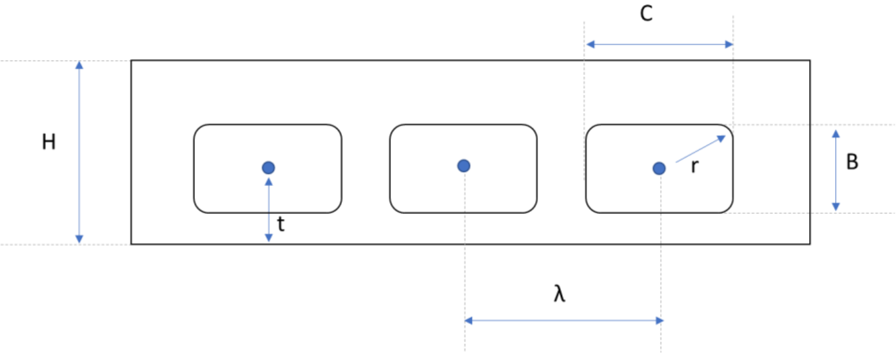

Fig. 5.11: Channels' geometric model used for dimensionless analysis

Overall, *n=14* different variables were identified, as summarized in Tab. 5.1, expressed in terms of *k=2* independent fundamental physical units, i.e., N and mm.

Tab. 5.1: Variables definition for dimensionless model

Input	**Output**
Substrate: $\boldsymbol{E, \nu, \sigma_y, n}$	G_{IC}
Adhesive: $\boldsymbol{\sigma_{max}, G_{IC}, k_n}$	
Geometry: $\boldsymbol{B, C, r, t, \lambda, H}$	

Based on Buckingham's π-theorem, it is possible to build a new dimensionless equation as a function of the *p=n-k=14-2=12* dimensionless group obtained as a combination of the abovementioned variables as following in Eq. 5.5:

$$\pi_i = (G_{eff}^{n_1} \cdot E^{n_2} \cdot \nu^{n_3} \cdot \sigma_y^{n_4} \cdot n^{n_5} \cdot \sigma_{max}^{n_6} G_{IC}^{n_7} \cdot k_n^{n_8} \cdot B^{n_9} \cdot C^{n_{10}} \cdot r^{n_{11}} \cdot t^{n_{12}} \cdot \lambda^{n_{13}} \cdot H^{n_{14}}) \tag{5.5}$$

By introducing the physical units for each variable, equation 5.5 could be rewritten as:

$$1 = \left(\frac{N}{mm}\right)^{n_1} \cdot \left(\frac{N}{mm^2}\right)^{n_2} \cdot (1)^{n_3} \cdot \left(\frac{N}{mm^2}\right)^{n_4} \cdot (1)^{n_5} \cdot \left(\frac{N}{mm^2}\right)^{n_6} \cdot \left(\frac{N}{mm}\right)^{n_7} \cdot \left(\frac{N}{mm^3}\right)^{n_8} \cdot (mm)^{n_9} \cdot (mm)^{n_{10}} \cdot (mm)^{n_{11}} \cdot (mm)^{n_{12}} \cdot (mm)^{n_{13}} \cdot (mm)^{n_{14}} \tag{5.6}$$

Consequently, a two-equation system could be obtained:

$$\begin{cases} n_1 + n_2 + n_4 + n_6 + n_7 + n_8 = 0 & for\ [N] \\ -n_1 - 2n_2 - 2n_4 - 2n_6 - n_7 - 3n_8 + n_9 + n_{10} + n_{11} + n_{12} + n_{13} + n_{14} = 0 & for\ [mm] \end{cases} \quad (5.7)$$

while n_3 and n_5 are not included in the equations, meaning that the Poisson's Ration and the strain-hardening exponent could be considered as an independent dimensionless variable. The objective is to find the 10 dimensionless groups that should satisfy equations 5.7. As said before, the system admits more than one solution and for this reason, the selection of the dimensionless group will depend more on the intuition than on the mathematical calculation. In the end, the Buckingham's π-theorem will be used to verify the suitability of the choice.

5.3.4 Dimensionless group

Considering the output variables, i.e., G_{eff}, the easiest choice is to normalize it with the cohesive energy. For this reason, the n_1 value was set equal to 1, the n_7 equal to -1 while all the other exponents were set equal to zero. In conclusion, the first vector that could satisfy the system of equation 5.7 is $[1\ 0\ 0\ 0\ 0\ 0 -1\ 0\ 0\ 0\ 0\ 0\ 0\ 0]$ and it leads to determine the first dimensionless group:

$$\pi_1 = \frac{G_{eff}}{G_{IC}}$$

The second dimensionless group involved the nylon Young's modulus and yield stress and it could be formulated using the following vector $[0 - 1\ 0\ 1\ 0\ 0\ 0\ 0\ 0\ 0\ 0\ 0\ 0\ 0]$:

$$\pi_2 = \frac{\sigma_y}{E}$$

Similarly, the third dimensionless group was obtained as normalization of the cohesive strength with Young's modulus. The vector $[0 - 1\ 0\ 0\ 0\ 1\ 0\ 0\ 0\ 0\ 0\ 0\ 0\ 0]$ allows to obtain the following equation:

$$\pi_3 = \frac{\sigma_{max}}{E}$$

The cohesive energy needs to be combined with more than one parameter to obtain a new dimensionless group and it is possible to make different choices. One option is to consider the equation for the calculation of fracture length scale, i.e., the dimension of the fracture process zone, $l_{cz} = \frac{E\,G_{IC}}{\sigma_{max}^2}$, and to normalize this value using a length. For this purpose, it was chosen the substrate thickness, i.e., H. The fourth dimensionless group was then obtained using the following vector $[0\ 1\ 0\ 0\ 0\ -2\ 1\ 0\ 0\ 0\ 0\ 0\ 0\ 1]$ as:

$$\pi_4 = \frac{E\ G_{IC}}{H\sigma_{max}^2}$$

Concerning the initial stiffness of the cohesive model, the best option is to normalize it with Young’s modulus and a geometric variable, i.e., substrates’ thickness. The vector that satisfies the system of equation (2) is $[0\ -1\ 0\ 0\ 0\ 0\ 0\ 1\ 0\ 0\ 0\ 0\ 0\ 0\ 1]$ and the dimensionless variable is:

$$\pi_5 = \frac{Hk_n}{E}$$

The next five dimensionless groups are related to the specimen’s geometry. The first one represents the effect of the channels’ height compared to substrates thickness. The vector utilized was $[0\ 0\ 0\ 0\ 0\ 0\ 0\ 0\ 0\ 0\ 1\ 0\ 0\ -1]$ while the dimensionless variable is:

$$\pi_6 = \frac{r}{C}$$

The second geometric dimensionless group was formulated in order to represent the channel aspect ratio. For this reason, the vector $[0\ 0\ 0\ 0\ 0\ 0\ 0\ 0\ 1\ 0\ 0\ 0\ 0\ -1]$ allow to identify the following variable:

$$\pi_7 = \frac{B}{H}$$

The influence of the position of the distance between the channel center and the bondline, it was chosen the vector $[0\ 0\ 0\ 0\ 0\ 0\ 0\ 0\ 0\ -1\ 0\ 0\ 1\ 0]$ and:

$$\pi_8 = \frac{\lambda}{C}$$

The distance between two channels was considered in relation to the channel width in order to take account of the ratio between bulk structure and empty space. The vector utilized was $[0\ 0\ 0\ 0\ 0\ 0\ 0\ 0\ -1\ 1\ 0\ 0\ 0\ 0]$ while the dimensionless variable is:

$$\pi_9 = \frac{C}{B}$$

The last geometric dimensionless group relate the fillet radius of the channels with the channels width as follows as $[0\ 0\ 0\ 0\ 0\ 0\ 0\ 0\ 0\ 0\ 0\ 1\ 0\ -1]$

$$\pi_{10} = \frac{t}{H}$$

For the last two dimensionless groups, we can consider the two a-dimensional variables, i.e., ν and n. For that, it's possible to consider all the n_i equal to zero, except n_3 for π_{11} and n_5 for π_{12}. Therefore:

$$\pi_{11} = \nu$$

$$\pi_{12} = n$$

As said before, the aim is to modify the geometry of the channels in order to improve the joint's damage tolerance capability. For this reason, the effect of the variation of the six geometrical dimensionless groups on the joint's behavior was studied: each group was modified individually, while the other dimensionless groups were kept constant. To simplify the problem, it was chosen to fix the substrate's thickness equal to 6 mm and 8 mm, i.e., the values employed during experimental tests, while for the other geometrical variable it was identified a variation range based on physical limits or design choices. The baseline value of each group was selected starting from the experimental dimensions of hollow channels with a square cross-section as a reference, *i.e.*, r_0/C_0=0, B_0/H_0=2/3, λ_0/C_0=3/2, C_0/B_0=1 for thinner substrates and r_0/C_0=0, B_0/H_0=2, λ_0/C_0=3/2, C_0/B_0=1 for thicker substrates. For the channels height, the lower limit was set equal to 2 mm to ensure the effect of the channel on the substrate (too small channels could not affect the crack propagation phenomena), while the upper limit set equal to 4 mm to guarantee that the minimum thickness in each substrate was at least 1 mm, i.e., $H - B = 2\ mm$. For the width of the channels as for the height, the lower limit was set equal to 2 mm. The upper limit was not influenced by physical limits at it was chosen in order to create a channel aspect ratio equal to 2, i.e., $C^{max} = 8\ mm$. The t value, in order to ensure that the minimum thickness in each substrate was at least 1 mm, cannot be changed when the substrate thickness is equal to 6 mm and it was fixed equal to 3 mm. For 8 mm thickness, the lower limit was 3 mm while the upper limit was chosen equal to 5 mm. The variation of channels period allows greater flexibility: there was not any upper limit and it was decided to fix as maximum value three times higher than the baseline channel width, i.e., $\lambda^{max} = 12\ mm$. The lower limit, instead, was influenced by the need to guarantee a thickness of 1 mm between two channels, i.e., $\lambda^{min} = 5\ mm$. The last geometric parameter, r, was strictly influenced by the channels dimension because it could be at least equal to $\frac{C}{2}$, i.e., circular channels, while the lower limit was fix equal to zero, i.e., square channels.

Based on these choices, two different experimental plans were built, the first one for $H = 6\ mm$ (Tab. 5.2), the second one for $H = 8\ mm$ (Tab. 5.3).

Tab. 5.2: Finite element simulations plan for H=6 mm

	B	**C**	**t**	**λ**	**r**	**π6**	**π7**	**π8**	**π9**	**π10**
Basic configuration	4	4	3	6	0	0.67	1	0.5	1.5	0
variation π6	2	2	3	3	0	0.33	1	0.5	1.5	0
	2.5	2.5		3.75		0.42				
	3	3		4.5		0.50				
	3.5	3.5		5.25		0.58				
	4	4		6		0.67				
variation π7	4	2	3	3	0	0.67	0.5	0.5	1.5	0
		3		4.5			0.75			
		4		6			1			
		5		7.5			1.25			
		6		9			1.5			
		8		12			2			
variation π9	4	4	3	5	0	0.67	1	0.5	1.25	0
				6					1.5	
				7					1.75	
				8					2	
				9					2.25	
				10					2.5	
				11					2.75	
				12					3	
variation π10	4	4	3	6	0	0.67	1	0.5	1.5	0
					0.2					0.05
					0.5					0.125
					1					0.25
					1.5					0.375

Tab. 5.3: Finite elements simulation plans for H=8 mm

	B	**C**	**t**	**λ**	**r**	**π6**	**π7**	**π8**	**π9**	**π10**
Basic configuration	4	4	3	6	0	0.5	1	0.375	1.5	0
variation π6	2	2	3	3	0	0.25	1	0.375	1.5	0
	2.5	2.5		3.75		0.3125				
	3	3		4.5		0.375				
	3.5	3.5		5.25		0.4375				
	4	4		6		0.5				
variation π7	4	2	3	3	0	0.5	0.5	0.375	1.5	0
		3		4.5			0.75			
		4		6			1			
		5		7.5			1.25			
		6		9			1.5			
		7		10.5			1.75			
		8		12			2			
		10		15			2.5			
		12		18			3			
variation π8	4	4	3	6	0	0.5	1	0.375	1.5	0
			3.5					0.4375		
			4					0.5		
			4.5					0.5625		
			5					0.625		
			5.5					0.6875		
variation π9	4	4	3	5	0	0.5	1	0.375	1.25	0
				6					1.5	
				7					1.75	
				8					2	
				9					2.25	
				10					2.5	
				12					3	
variation π10	4	4	3	6	0	0.5	1	0.375	1.5	0
					0.2					0.05
					0.5					0.125
					1					0.25
					1.5					0.375

5.4 Results of the parametric analysis

The dimensionless model, obtained as described earlier, allows us to shed light on the influence of most important geometrical variables on the joint behavior. In particular, the results have been compared in terms of G_{eff} normalized in function of fracture toughness, *i.e.*, G_{eff}/G_{IC}. In the following sections, the effects of variation each parameter on joint damage tolerance is analyzed.

5.4.1 Effect of fillet radius

The results obtained for varying fillet radius of the channel, *i.e.*, π_6, are reported in Fig. 5.12 (a) and (b) and allows us to assess the effect of the channel shape. Indeed, changing π_6 from 0 to 0.5, a shape transition occurs from a square to a circular one. Accordingly, a decrease of the effective fracture energy needed for crack propagation is observed, which agrees well with the experimental observations reported in previous chapters. The best result, *i.e.*, $G_{eff}/G_{IC} \cong 4$, which is obtained for $\pi_6 = 0$ for both H values. It should be noted that in this case, some plastic dissipation is included, because of the local yielding around the sharp edges of the channels. The amount of plastic dissipation was at least 17% of the total dissipated energy for H=6mm. On the other hand, for the circular channels, $\pi_6 = 0.5$, plastic deformations were negligible and the plastic dissipation was only 1% for H=6 mm and zero for H=8 mm. However, it is noted, that the effective work is at least twice the nominal toughness of the benchmark interface.

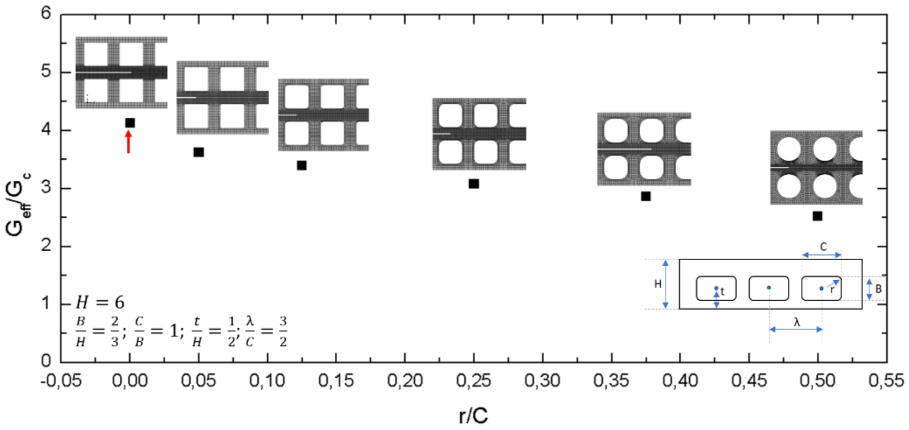

(a)

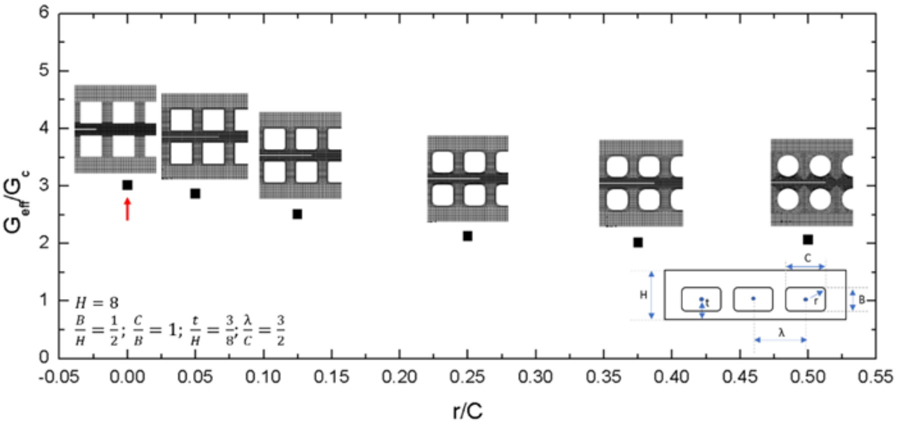

(b)

Fig. 5.12: Joint's fracture toughness variation as a function of $\pi10$, i.e., the fillet radius of the channel for (a) H= 6 mm and (b) H= 8 mm.

5.4.2 Effect of channel size

The results of the variation of channel dimensions, *i.e.*, π_7, are reported in Fig. 5.13 (a) and (b). As expected, increasing the channel dimension, when the thickness of the substrate is fixed, increases the total energy needed for crack propagation. In fact, it should be noted that increasing the area of the channels translates into higher flexibility and an increase in plastic deformations. When the channels are small, load fluctuation due to crack-trapping effect becomes negligible and the G_{eff} value is only slightly affected compared to the effective work of fracture obtained for bulk samples. The hollow channels get really important when $\pi_7 > 1/2$ for H=6mm and when $\pi_7 > 2/5$ for H=8mm. The best result, in both cases, is obtained with the geometry that corresponds to geometry employed for preliminary experimental tests. In particular, for H=6mm, $G_{eff}/G_{IC} \cong 4$ obtained when $\pi_7 = 2/3$. These results highlight once more that the dissipation is mostly sensitive to the thickness of the material adjacent to the interfacial region. For the larger value of π_7 that thickness is equal to the minimum value set in the experiments, as described earlier, and it is clear that it largely controls the degree of dissipation.

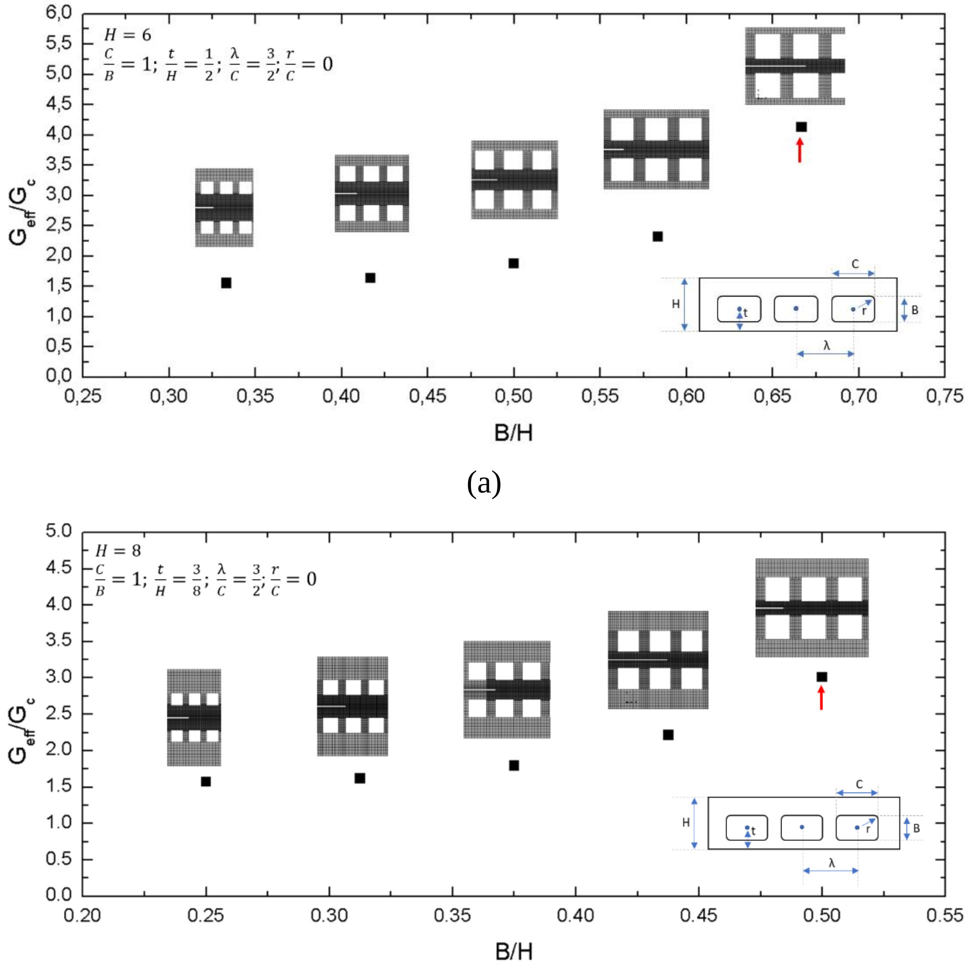

(a)

(b)

Fig. 5.13: Joint's fracture toughness variation as a function of π6, i.e., channel dimensions' alteration for (a) H= 6 mm and (b) H= 8 mm.

5.4.3 Effect of channel wavelength

Channels wavelength, *i.e.*, π_8, plays an important role in the joint behavior with H=6mm as is shown in Fig. 5.15 a). Overall, it was possible to reach a maximum value of the G_{eff}/G_{IC} ratio equal to 10 for $\pi_8 = 2$ that correspond to a 64% increase of effective work of fracture, compared to the value obtained with the baseline model where $\pi_8 = 3/2$. After that, the G_{eff}/G_{IC} ratio shows a slowly decrease even if the damage tolerance effect is still more efficient than that obtained with the baseline model. When the G_{eff}/G_{IC} ratio becomes high, *i.e.*, more than 8, two different phenomena were observed during FE analysis: buckling in a thin plate of the substrate upper part and the nucleation of a secondary crack behind primary crack tip as reported in Fig. 5.16. These two phenomena enhance the energy dissipated for crack propagation.

The buckling effect increases the energy needed for crack propagation thanks to plastic deformation. This effect is commonly observed in sandwich structure typically used in metamaterials building (Côté *et al.*, 2009; Qianqian Wu *et al.*, 2019) where, with a low relative density, the buckling effect became dominant. For structures under compression, like sandwiches, this condition could be very dangerous. In that case, the compression condition, that acts on the thin upper plate, do not allow reaching instability and buckling failure but enhances plastic energy dissipation improving damage tolerance effect. The second phenomenon observed is related to the formation of a secondary crack behind crack tip that contributes to the buckling effect of the thin upper plate by introducing a rigid rotation of the pillar between two channels. The secondary cracks appearing ahead of the main ones are due to the deformation process described above that, in turn, depends on the thickness of the wall.

It was also chosen to further analyze, as proposed in Fig. 5.14, the evolution of the load-displacement curve during one cycle and compared with corresponding deformed configurations of the sample for λ/C=2.0. As the load increases, primary and secondary crack extend simultaneously and damage nucleates ahead of this extended process zone (1→2). Once the load reaches a critical value, the two cracks coalesce and the main crack snaps through (2→3) leading to a new formation of a secondary crack. Therefore, while in previous cases the crack grows by continuous extension of the original crack, when λ/C>1.5 a secondary crack appears and grows simultaneously with the main one. It is interesting to note that the nucleation of the secondary crack front was also observed in related works (Ghatak *et al.*, 2004; Wang and Xia, 2017).

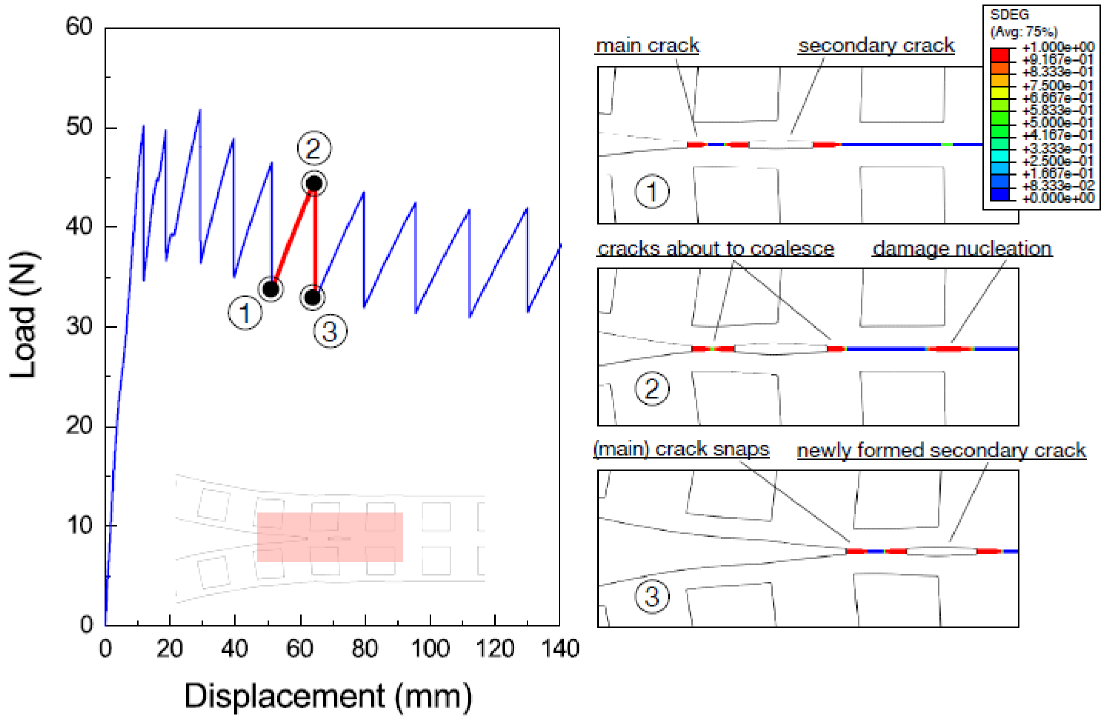

Fig. 5.14: Load-displacement curve for λ/C=2.0 and corresponding (selected) snapshots extracted from FEA which illustrate the mechanisms of crack propagation with nucleation of a secondary crack.

Wang and Xia (Wang and Xia, 2017) studied crack propagation on heterogeneous materials, i.e., materials obtained by the alternation of two different materials that exhibit a different value of Young modulus. They observed, both numerically and experimentally, the growth of a secondary crack induced by compliance variation. After that, the secondary crack propagates in the opposite direction to the main one until the two cracks coalesce, causing a slower crack propagation. Subsurface channels produce a compliance variation allowing us to observe the same phenomena. Ghatak et al (Ghatak *et al.*, 2004) observed a similar phenomenon analyzing the behavior of a cantilever flexible plate peeled-off from an incision-patterned thin adhesive elastic layer. They observed that, due to an adhesion induced instability, cavitation bubbles nucleated ahead of the main crack. Because of that, crack initiation occurred at a load higher than that required by the smooth interface. This mechanism was also artificially induced by Hill et al (Hill *et al.*, 2003). An internal crack was produced by inserting a fiber into the bondline. As the crack tip approaches the internal crack, its growth is retarded by the defect, producing an increase in the apparent fracture resistance.

For joints with H=8mm, no significant differences on G_{eff}/G_{IC} value has been obtained by π_8 variation, Fig. 5.15 (b). Moreover, for $\pi_8 = 2$, where it was observed a maximum for H=6mm, it was obtained a minimum. This result allows concluding that the substrate thickness plays a fundamental role in the crack propagation mechanism and it is important to study the interaction between channel dimensions and substrate thickness. To understand deeply the influence of channels shape, it could be interesting to use another joints geometry, i.e., TDCB or boundary layer.

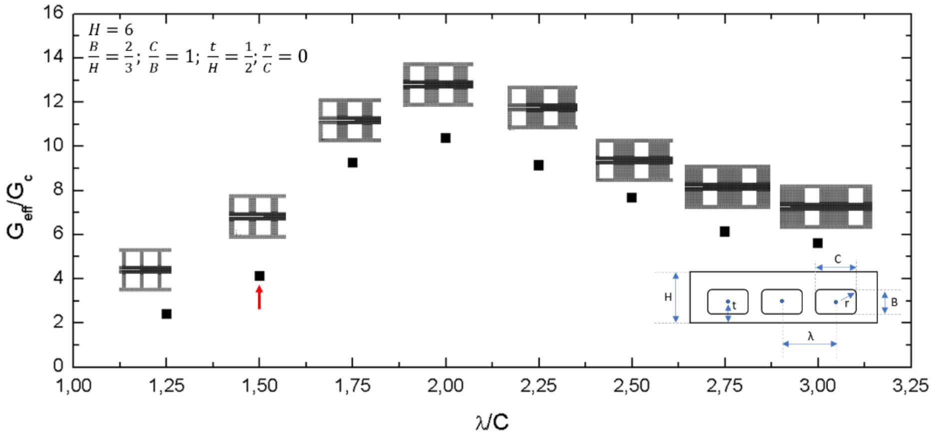

(a)

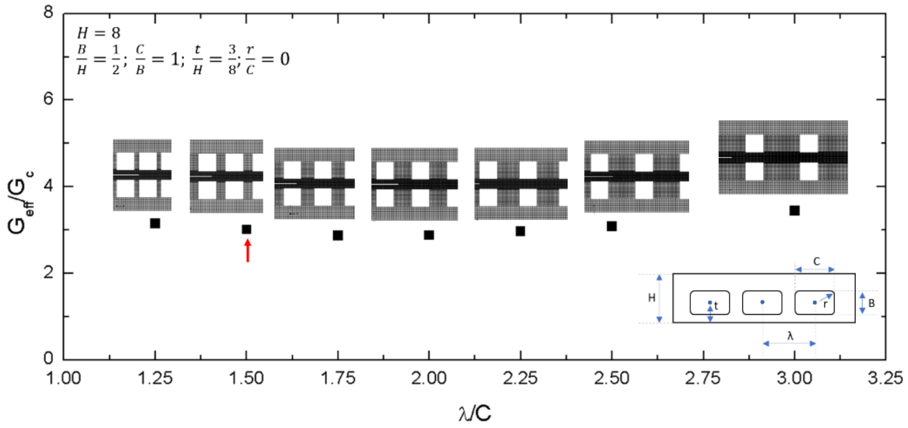

(b)

Fig. 5.15: Joint’s fracture toughness variation as a function of π9, i.e., the distance between two channels for (a) H= 6 mm and (b) H= 8 mm.

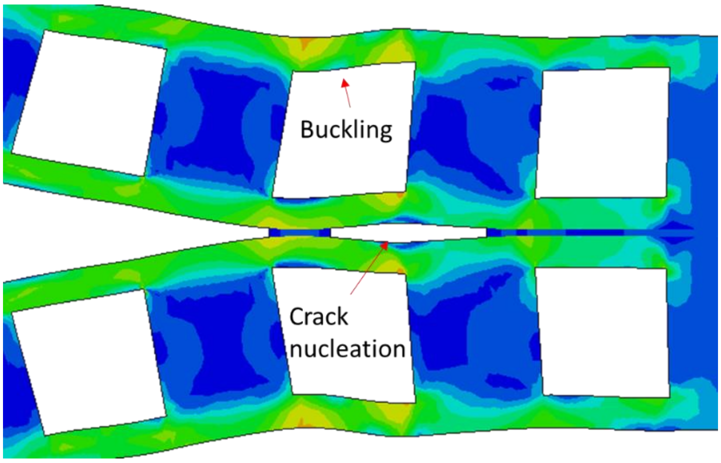

Fig. 5.16: FEM plastic deformation for π_9=2

5.4.4 Effect of channel aspect ratio

The channel aspect ratio, *i.e.*, π_9, plays an important role in joint behavior as is shown in Fig. 5.17 a) and b): increasing the width of the channels leads the enhancement in the G_{eff}/G_{IC} ratio, especially for H=6mm where it was obtained a meaningful improvement of the effective work of fracture. In particular, when $\pi_9 = 5/4$, it is possible to enhance joint damage tolerance, *i.e.*, G_{eff} increase by 55% compared to the value obtained with the baseline model where $\pi_9 = 1$. The buckling effect in the thin plate of the substrate and the secondary crack occurrence, similarly to geometry with wavelength variation, were observed for geometries that involve $\pi_9 > 1.3$. Moreover, the high level of plastic deformation by the thin plate in the upper part of the substrate reached during propagation, as shown in Fig. 5.18, introduce the possibility to reach buckling failure, do not allow to reach simulation convergence. This result highlights the fundamental role of the buckling effect during crack propagation. For joints with H=8 mm, the $\frac{G_{eff}}{G_{IC}}$ ratio reaches a maximum for $\frac{C}{B} = 1.75$ after which the value remain almost constant without achieving the values obtained with $H = 6\ mm$. That result suggests how the thin plate in the upper part of the substrate plays a fundamental role during crack propagation due to the buckling effect, as observed in the previous section.

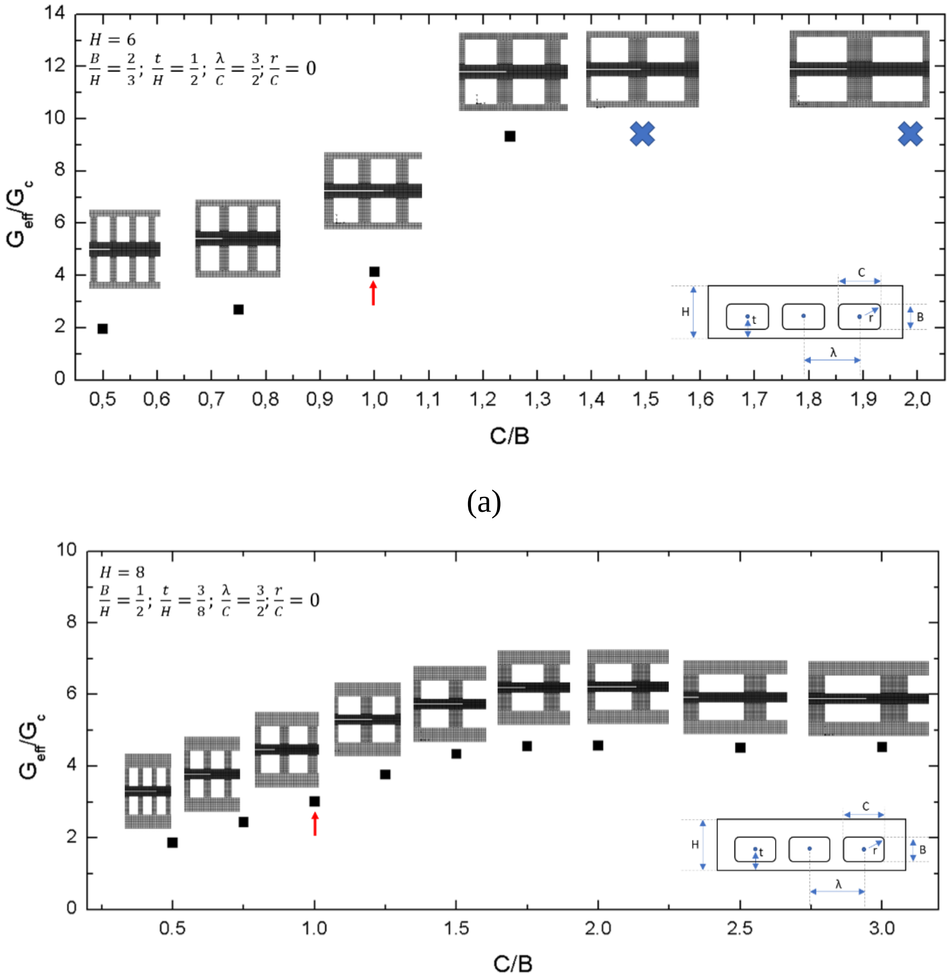

(a)

(b)

Fig. 5.17: Joint's fracture toughness variation as a function of π9, i.e., channels width alteration for (a) H= 6 mm and (b) H= 8 mm.

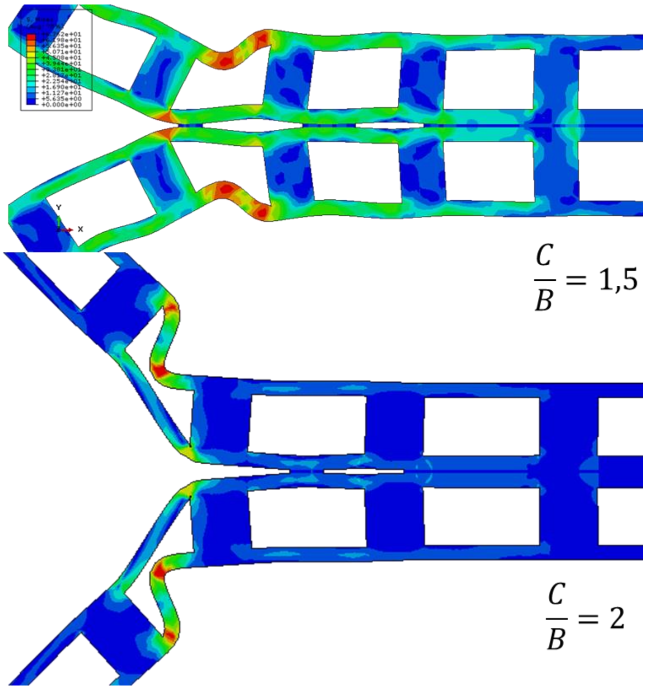

Fig. 5.18: High plasticity during crack propagation for H= 6 mm with different channel aspect ratio.

5.4.5 Effect of base plate thickness

As said before, the variation of π_8 dimensionless group it's possible only for substrate thickness equal to 8 mm and the results are reported in Fig. 5.19: increasing the distance between the channels and the bondline has little or no influence on the joint's damage tolerance even if it slightly decreases when such distance increases in the considered range.

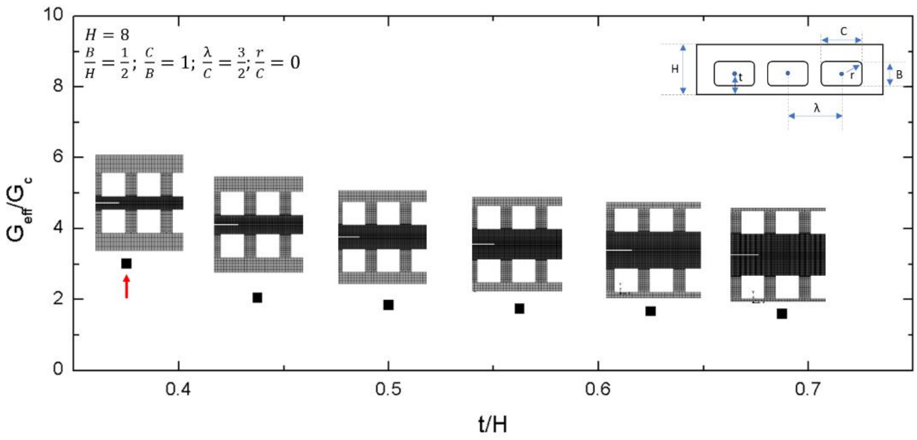

Fig. 5.19: Joint's fracture toughness variation as a function of π8, i.e., the distance between the channel center and the interface for H= 8 mm.

Results obtained by modifying channels geometry demonstrate the joint damage tolerance is mainly influenced by two dimensionless groups, i.e., λ/C and C/B. It could be interesting to analyze the effect of simultaneous variation of these two parameters by combining the full ranges of variation of both *C/B* and *λ/C*. As shown earlier, the variation of these parameters can lead to competing for failure modes, which include the formation of a secondary crack as well as the failure of the top plate under severe buckling. It was chosen to restrict the study to 6 millimeters thickness substrate and, considering the variation range described before, a new simulation plan was elaborated. The results are reported in the form of a failure map where the two non-dimensional variables are reported on two axes, as shown in Fig. 5.20.

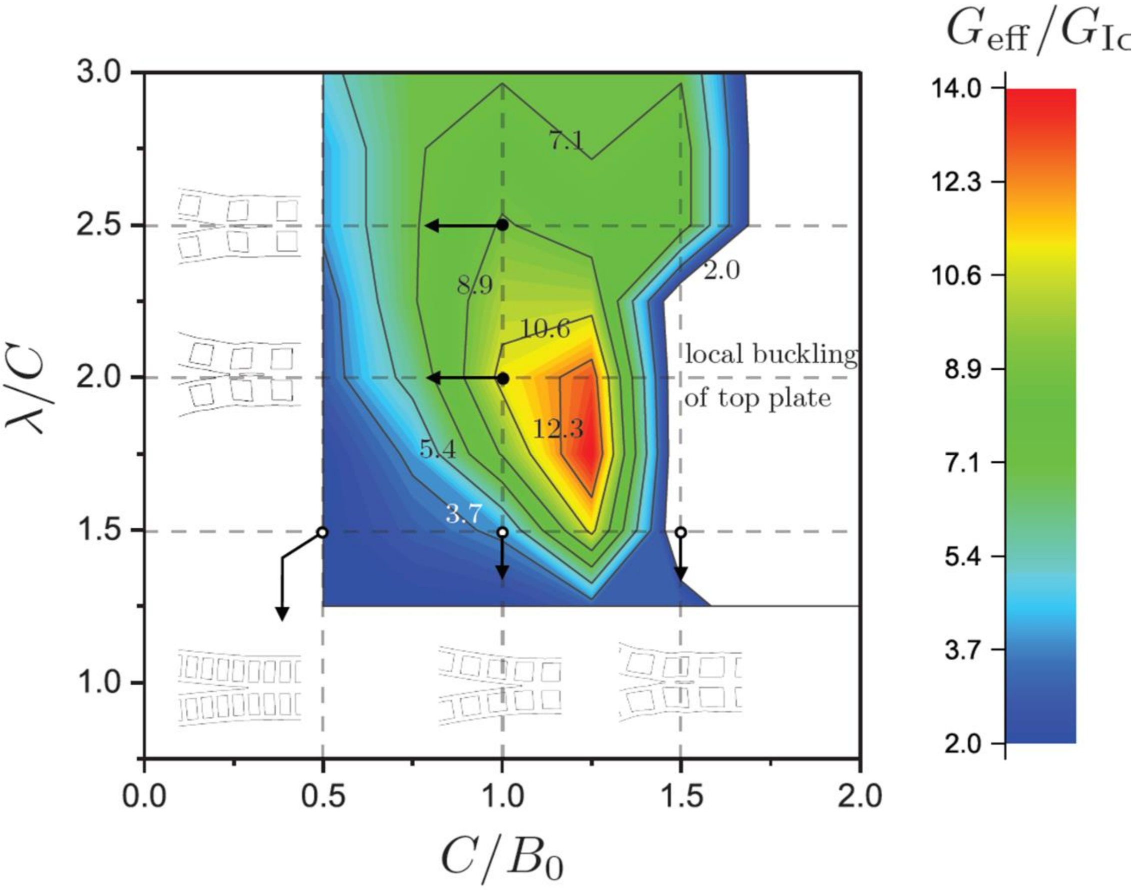

Fig. 5.20: New simulations map for the of the non-dimensional width and channels pattern period of the samples with the sub-surface channels.

The map shows that the choice of higher values for the C/B ratio can lead to large deformations inducing buckling of the top plate that could produce the failure of the sample. Moreover, the effect of λ/C is less critical, and whenever C/B is within allowable bounds (<1.3), it allows to tailor the energy dissipated through the fracture process. The red zone on the map indicate the channels geometric characteristic that allows obtaining the highest values of G_{eff}/G_{IC} ratio, while the blue is referred to geometries with lowest ratio values. Results have been analyzed in terms of energy values and are reported in Fig. 5.21. Energy values obtained on models with the occurrence of buckling have been excluded from the analysis.

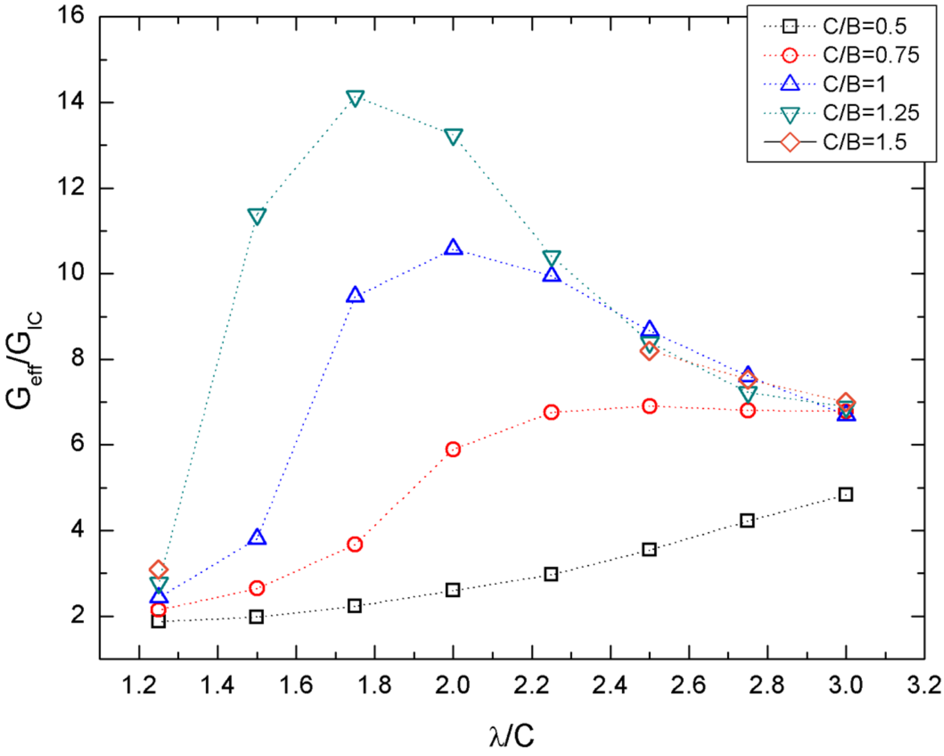

Fig. 5.21: Total energy requested for crack propagation for DCB samples with different sub-surface channel shape obtained with the non-dimensional model.

The best result was obtained for λ/C equal to 1.75 and C/B equal to 1.25 with a G_{eff} value 14 times higher than fracture toughness. The original model, i.e., square channels with λ/C equal to 1.5, is characterized by a ratio approximately equal to four that is greatly lower than maximum obtained by properly combining the two non-dimension parameters. These results still confirm what observed before, that it is possible to improve joints damage tolerance just modifying channels geometry. As for triangular channels, it was chosen to realize by 3D printing some models to validate with experimental results what observed numerically. In particular, three different models, in addition to the basic one, have been selected: the first is characterized by square channels, i.e., C/B=1 and λ/C equal to 2, the second has square channel with a λ/C ratio equal to 2.5 and the third shown a channels aspect ratio equal to 1.25 and a λ/C ratio equal to two. The results will be discussed in the next section.

5.5 Experimental validation

Numerical results demonstrate that the energy requested for crack propagation is strictly dependent on channel shape. Dimensionless analysis results demonstrate that it is possible to improve joint damage tolerance by combining the effect of single geometrical variables. In order to strongly validate these results, it was chosen to realize by 3D printing 3 different channels geometries from the dimensionless analysis. 3D printed DCB joints with bioinspired channels have been realized as described before. Tests have been conducted in the same condition in order to avoid the introduction of differences. Benchmark samples and target bioinspired joint with square cross-section channels have been added to the printing batch to verify the cohesive properties of the interface of the new batch. The results will be discussed below.

5.5.1 Dimensionless model

Load-displacement curves obtained on DCB joint with bioinspired channels designed with dimensionless analysis are reported in Fig. 5.22. Load–displacement curves get from simulation have been superimposed to experimental ones in order to compare the two behavior. Results show differences between numerical and experimental models. In particular, it seems that the numerical model overestimates joints behavior and curves move through higher load values.

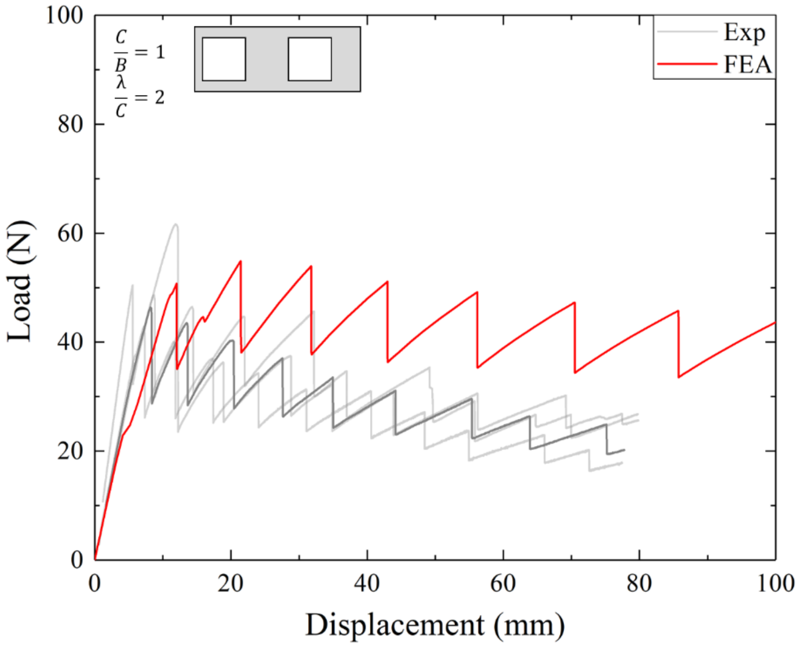

100
80
60
40
20
0
Load (N)
0
20
40
60
80
100
Displacement (mm)
$\frac{C}{B} = 1$
$\frac{\lambda}{C} = 2$
Exp
FEA

(a)

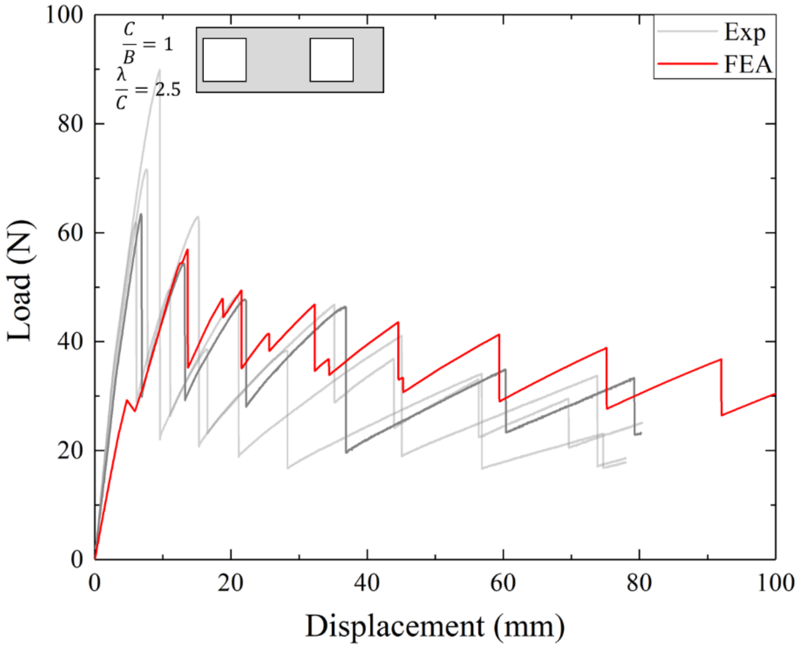

100
80
60
40
20
0
Load (N)
0
20
40
60
80
100
Displacement (mm)
$\frac{C}{B} = 1$
$\frac{\lambda}{C} = 2.5$
Exp
FEA

(b)

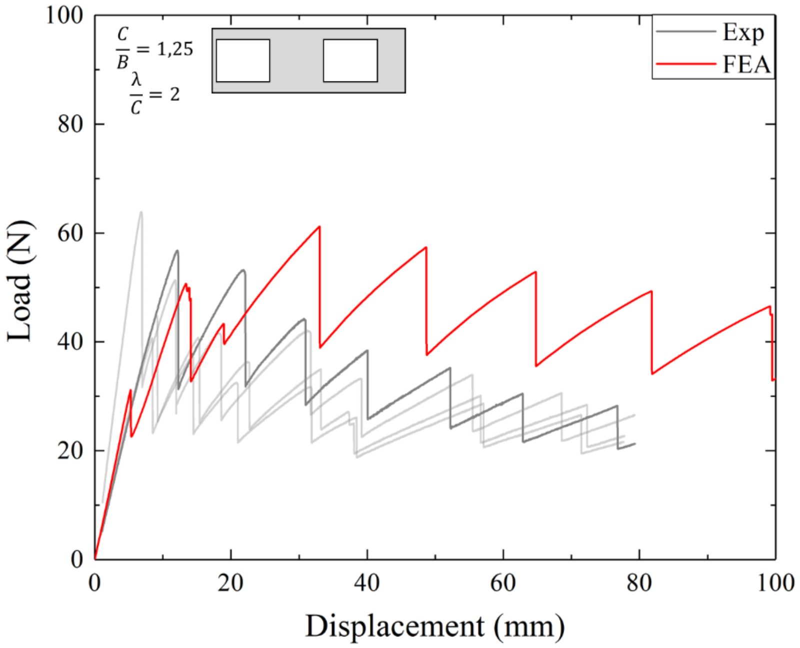

(c)

Fig. 5.22: Load-displacement curves obtained experimentally (grey) and numerically (red) on bioinspired DCB joints with subsurface channels obtained by the dimensionless model with (a) C/B=1 and λ/C=2 (b) C/B=1 and λ/C=2.5 and (c) C/B=1.25 and λ/C=2

Experimental results have been also compared with numerical one in function of G_{eff}/G_{IC} ratio and results are reported in Fig. 5.23. For simplicity it was chosen to indicate each geometry with a progressive code where: #1 is referred to target joint, i.e., C/B=1 and λ/C=1.5, #2 is model with C/B=1 and λ/C=2, model #3 is C/B=1 and λ/C=2.5 and #4 is the model with C/B=1.25 and λ/C=2. It is possible to notice that some difference between results have been obtained and that this dissimilarity became more evident with the increment of the plastic energy estimated for each geometry by numerical simulation

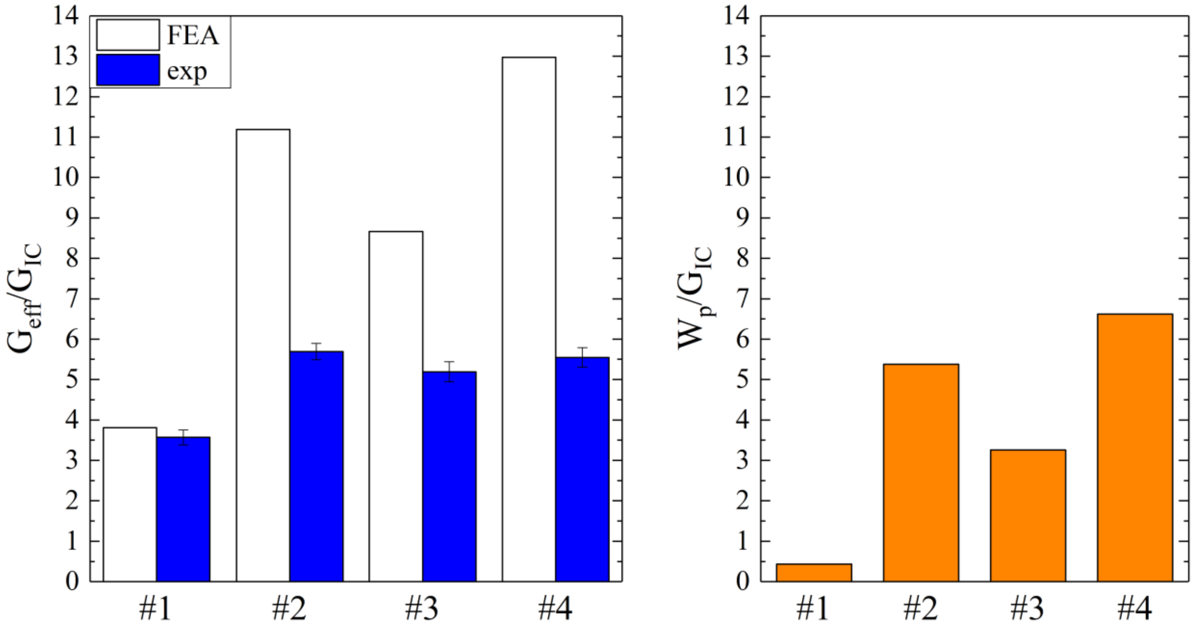

(a) (b)

Fig. 5.23: (a) Comparison between experimental results and numerical results obtained for bioinspired DCB joints with subsurface channels obtained by the dimensionless model and (b) amount of plastic energy evaluated numerically

Plastic deformation could be directly related to cohesive strength: higher cohesive strength values involves a higher stress field at the crack tip that implies growth of the amount of plastic deformation in substrates. Furthermore, as explained before, cohesive strength determination needs specific tests to be identified since the DCB test could not provide direct information about that and, for this reason, it is reasonable to attribute results differences to this parameter. To confirm that, numerical simulations have been conducted by keeping constant cohesive energy and modifying σ_{max} into the variation range identified with the calibration procedure. Results of the total energy requested for crack propagation are reported in Fig. 5.24.

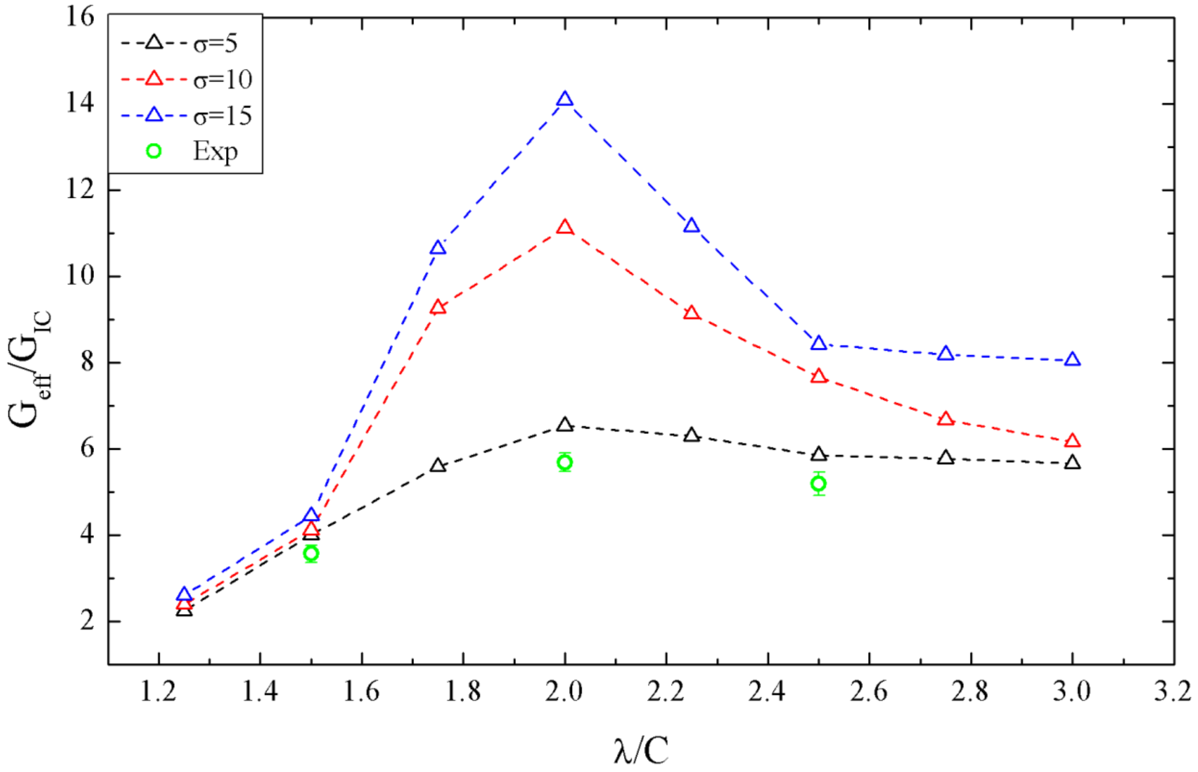

Fig. 5.24: Normalized energy requested for crack propagation obtained modifying cohesive strength compared with experimental results

Results clearly demonstrate that this parameter, which does not affect results on benchmark DCB, largely influences bioinspired joints behavior proportionally to the amount of plastic energy assessed by numerical simulations. Moreover, numerical results obtained with $\sigma_{max} = 5\,MPa$ are in good agreement with experimental results and could be also observed by comparing load-displacement curves (Fig. 5.25).

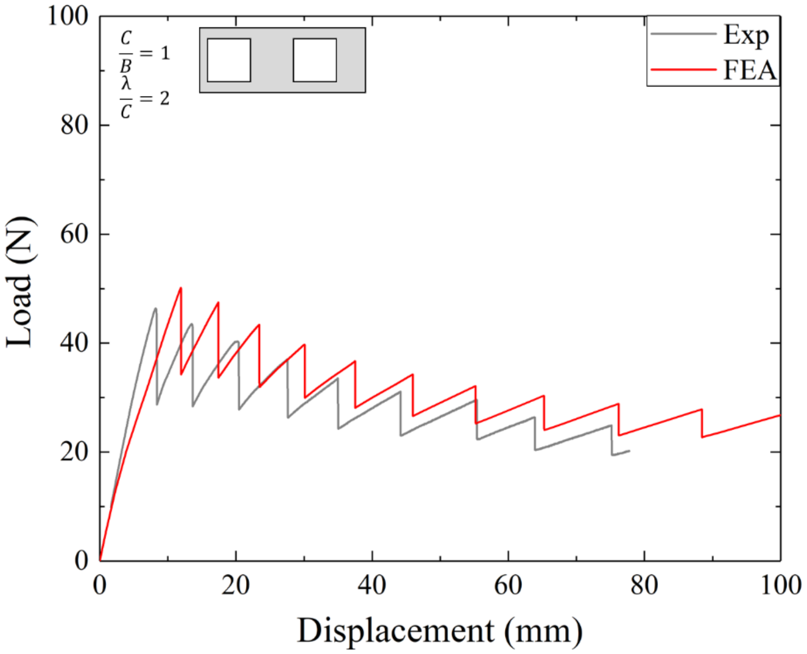
100
80
60
40
20
0
Load (N)
0
20
40
60
80
100
Displacement (mm)
$\frac{C}{B} = 1$
$\frac{\lambda}{C} = 2$
Exp
FEA

(a)

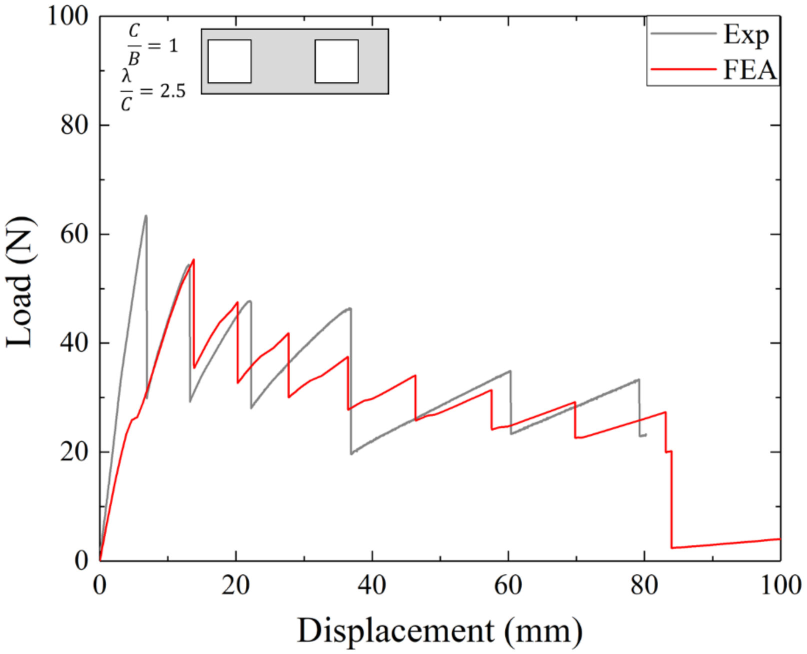
100
80
60
40
20
0
Load (N)
0
20
40
60
80
100
Displacement (mm)
$\frac{C}{B} = 1$
$\frac{\lambda}{C} = 2.5$
Exp
FEA

(b)

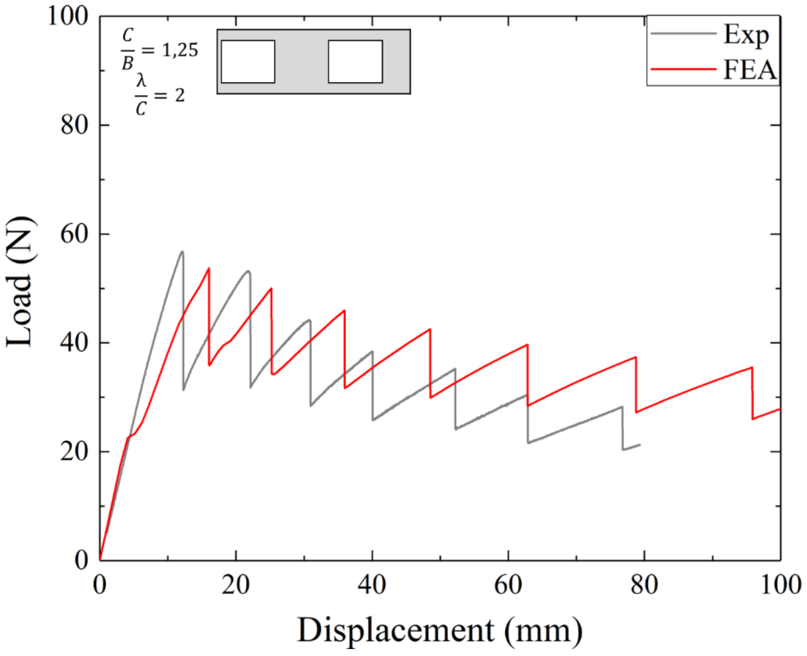

(c)

Fig. 5.25: Load-displacement curves obtained experimentally (grey) and numerically (red) by reducing cohesive strength value on bioinspired DCB joints with subsurface channels obtained by dimensionless model with (a) C/B=1 and λ/C=2 (b) C/B=1 and λ/C=2.5 and (c) C/B=1.25 and λ/C=2

Analyzing crack propagation mechanism by high-resolution images, it was possible to observe experimentally the development and growth of the secondary crack into two different channels geometry: the model with C/B=1 and λ/C=2 (Fig. 5.26) and model with C/B=1.25 and λ/C=2 (Fig. 5.27). When the primary crack tip is located below the pillar, secondary crack nucleation under channel edge and starts to propagate in the opposite direction of the main one following the same mechanism observed numerically. Overall, experimental results allow confirming what observed numerically even if it seems necessary to use a new experimental test to identify the correct value of the σ_{max} with a good accuracy.

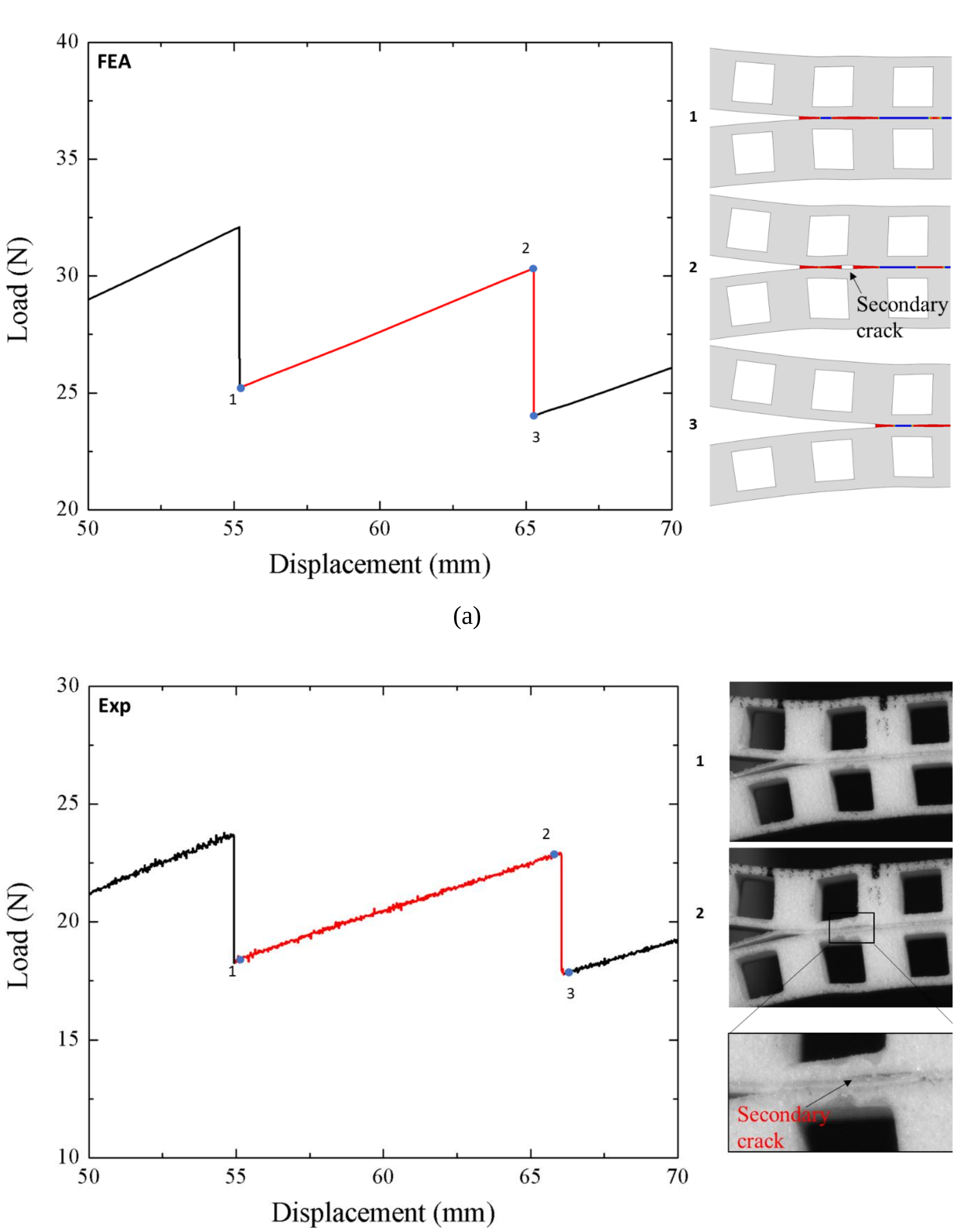

(a)

(b)

Fig. 5.26: Development of secondary crack observed (a) numerically and (b) experimentally for bioinspired DCB joints with subsurface channels obtained by the dimensionless model with C/B=1 and λ/C=2

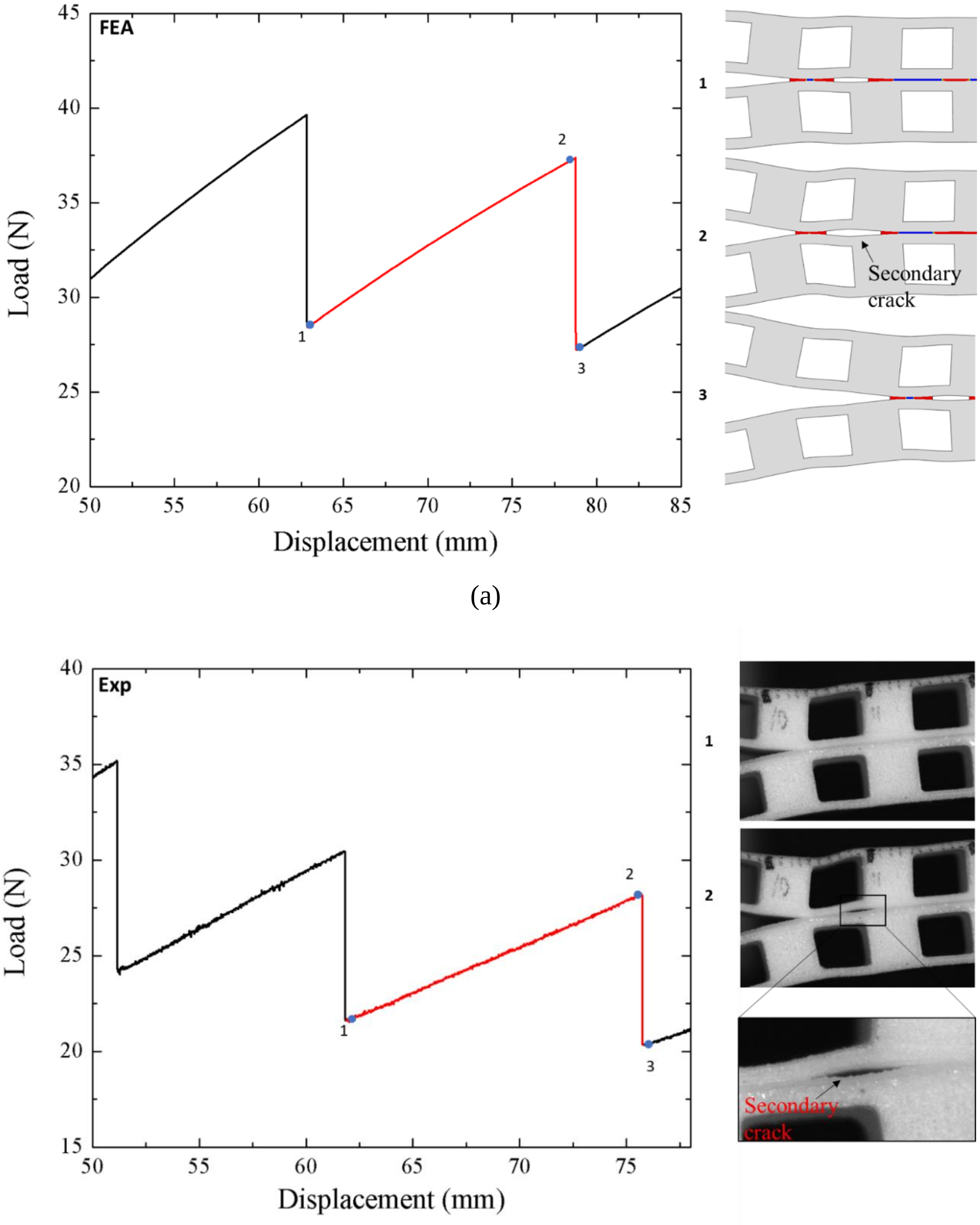

(a)

(b)

Fig. 5.27: Development of secondary crack observed (a) numerically and (b) experimentally for bioinspired DCB joints with subsurface channels obtained by the dimensionless model with C/B=1.25 and λ/C=2

Chapter 6: Conclusions and future works

The present work proposed novel strategies to enable toughening and damage tolerance in adhesively bonded joints. In particular, bio-inspired strategies were deployed in 3D printed DCB adhesive joints comprising adhesive bonded thermoplastics substrates. The attention has been focused on bio-inspired architectures resembling those observed in sutures joints, and subsurface channels such as those reported in the attachment base plate of the barnacles. DCB joints have been analyzed in detail through experiments and the results have been compared in terms of load-displacement curves and energy requested for crack propagation. *In situ* high-resolution imaging of the fracture process was also accomplished to complement the experimental work. Numerical simulations, carried using finite element models embedding interface elements, were carried out to gain a deep understanding of all mechanisms observed experimentally and to explain the key differences observed in the crack propagation and dissipated energy between the benchmark and bioinspired DCB samples. In particular, a cohesive zone model was employed to analyze crack propagation and a bilinear model was used, while the cohesive properties were determined iteratively by comparing experiments and simulations. A good agreement was achieved between experiments and numerical results, and the cohesive parameters were then successfully deployed to predict the response of bio-inspired samples. This step served to create a physically validated numerical model that was subsequently used to predict interfacial response for additional samples architecture. Special attention was paid to the effect of subsurface channels on toughening and damage tolerance since it was found that this strategy combines enhanced energy dissipation and weight reduction that is a key factor in view of increasing requirement for structural lightweighting in the field of transportation. A parametric investigation was carried out to build a model where the effective work of fracture could be given as a function of the most relevant geometrical properties of the channel geometry. The mechanical response was assessed by combining the analysis of load-displacement curves, energy dissipation and *in situ* high-resolution imaging of a region of interest around the current crack tip. The following conclusion could be drawn. The use of bioinspired structure, either in the form of sub-surface channels or sinusoidal interfaces, allows to improve the performances of adhesive joints, by providing damage tolerance and, in the case of stiffness modulation through subsurface channels, also a significant weight reduction.

A crack trapping mechanism effectively delayed the crack propagation process and its intensity depended on the interface architecture (i.e., channel shape or wavelength of the sinusoidal interface). Sinusoidal interfaces provided a four-fold increase in the energy requested for crack propagation if compared to benchmark samples. This improvement is related to both an increase in the bonding area and a change in crack propagation mechanism, i.e., mixed-mode.

The results of DCB fracture tests have shown that also bio-inspired subsurface channels induce a large increase in the total dissipated energy with respect to the benchmark samples, i.e., no channels. High-resolution imaging of the fracture process zone indicated that the observed fluctuations in the global response are related to the sequential storage and sudden release of elastic energy. Indeed, it is the spatial modulation of the stiffness around the interfacial region that affects the available driving force for crack growth. Regarding channel shape, the best results were obtained with slot channels and triangular ones. The enhancement in the energy needed for crack propagation was up to 330% for slot channels and up to 270% for the triangular ones. These results are accompanied by a relevant weight reduction, i.e., 28% (triangular channels) and 39% (slot channels). These results have been validated by experiments demonstrating the validity and reproducibility of the mechanisms observed in the finite element simulations. A parametric investigation revealed the most significant geometrical variables that control crack propagation in architected interfaces with subsurface channels, i.e. the period and width of the channels. In particular, by properly combining these two parameters it was possible to obtain effective fracture energy fourteen times higher than the fracture toughness of the baseline interfaces. The increase of energy dissipation needed for crack propagation was shown to be related to the following phenomena: buckling of the top plate and nucleation/propagation of a secondary crack.

The overall results reported in this work demonstrate that is possible to improve joints effective fracture toughness by modifying joints architecture without any action on adhesive and/or interface properties (e.g., surface energy). This study further confirms that additive manufacturing represents a powerful platform for the experimental study of bio-inspired materials. Future developments will focus on the analysis of alternative channel geometries or the combination of both surface macro roughness and subsurface channels. Moreover, the extension to different material systems is also an important point that needs to be addressed. For instance, it would be interesting to assess whether the proposed strategy can be extended to metallic structures. It is surmised that in this case, it will be necessary to consider joining techniques alternative to adhesive bonding, e.g., diffusion bonding.

Acknowledgments

This thesis was carried out at the Department of Mechanical, Energetic and Management with the financial support of the University of Calabria.

First of all, I would like to thank my Ph.D. supervisor, Professor Marco Alfano, for his endless support, for his motivation, his great knowledge and the encouragement he gave me. His guidance and constant feedback helped me through these years. I cannot imagine a better advisor and mentor for my Ph.D. study.

Besides my supervisor, special thanks have to be given to all professors of my research group, in particular professor Franco Furgiuele, as Ph.D. course coordinator, always helpful and available for any doubt or clarification, the professor Luigi Bruno for his teachings and his support, the professors Leonardo Pagnotta and Carmine Maletta and last but not least, professor Emanuele Sgambitterra for his help and his friendship. I would like also to thank all the other research team members, Fabio, Danilo, Edoardo, Valentina, Carlo and, above all, my friend Giovanna for her constant support and for our time together. A special thanks have to be given to Giulia for her always good humor and her friendship.

I greatly appreciate the support received during the six months that I spent at Purdue University by Professor Pablo Zavattieri who was helpful and provided me with his assistance and his valuable advice.

A special mention is necessary for the MechLab staff, Renato Bentrovato, Diego Pulice and Ernesto Ramundo, for its helpful assistance with experimental set-ups, practical advice, and sample preparation.

I would like to thank the MaTeRiA laboratory at the University of Calabria for making it available the necessary equipment for 3D printing and full-field measurements through digital correlation of images and the MechLab laboratory for all the equipment necessary for my research.

I am indebted to all my friends in the United States that opened for me their homes during my time at Purdue University and that were as a family for me. Special thanks to Jorge, Narda, Camilo, Lina, and Liliana that provided me with some of my happiest memories and taught me the true meaning of friendship.

I would like to thank my parents, Francesco and Sara, who have never stopped believing in me and encouraging me to follow my dreams allowing me to reach this important milestone, with all the affection and support possible. I would like to thanks my sisters, Elisa and Francesca, my best friends, for their endless support and their unconditional love. They were always being able to give me the courage to overcome all the difficulties and I love them deeply for that. My older sister, Elisa was as a guide since I was a child, helping me to become who I am today, and my younger sister, Francesca, was my playmate and always encouraging me to follow my dreams. I have been lucky for such a loving and supportive family.

Last but not least, I want to thank Pietro, who was always on my side throughout this Ph.D. It is very difficult to say how grateful I am and how much I love him. He taught me to believe in myself and gave me the right strength and motivation in all the hardest situations. Pietro was a great supporter and he unconditionally loved me during my good and, especially, my bad times.

Appendix A: Boundary layer model

In this work, finite element simulations were carried out to extract the energy release rate using a *boundary layer* approach (Kalamkarov, Kudriavtsev and Parton, 1990; Zavattieri, Hector and Bower, 2008). A circular model that contains a crack, as illustrated in Fig. A.1, was prepared and the in-plane displacement field stemming from linear elastic fracture mechanics was applied on the outer boundary. This configuration simulates the near-tip conditions in an arbitrary geometry featuring a crack between two identical semi-infinite elastic materials. The crack tip is at the center of the global coordinate system that is located in the center of the domain.

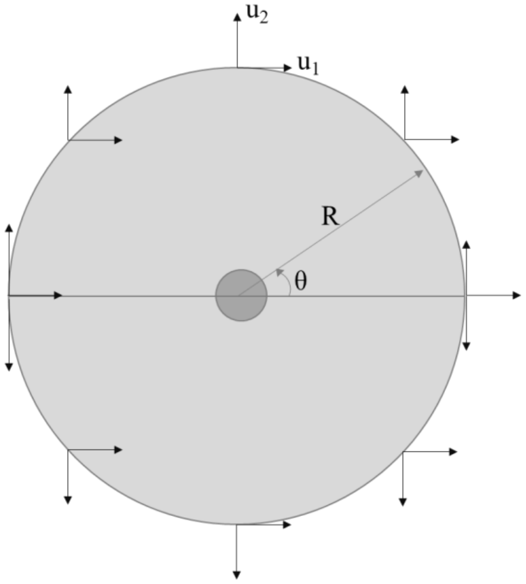

Fig. A.1: Schematic depiction of the boundary layer model used to study the driving force.

The problem was modeled in plane strain condition and the material was assumed to be linear elastic. The radius of the domain, i.e., R, was chosen such that it was much greater than any characteristic length scale of the channels. The displacement field on at the boundary of the circular domain was given as (Anderson, 2005):

$$u_1 = \frac{K_I(1+\nu)}{E}\sqrt{\frac{R}{2\pi}}(3-4\nu-\cos\theta)\cos\frac{\theta}{2} \tag{A.1}$$

$$u_2 = \frac{K_I(1+\nu)}{E}\sqrt{\frac{R}{2\pi}}(3-4\nu-\cos\theta)\sin\frac{\theta}{2} \tag{A.2}$$

where:

- K_I is the stress intensity factor;
- ν is the Poisson's ratio;
- E is the substrate Young modulus;
- R is the radius of the circular domain;
- θ is the angle defined by the x-axis and the straight line passing through the origin of the reference system and the application displacement point (Fig. A.1);

The crack tip was located in the middle of the circular domain, i.e., the interface is open for x<0 and connected for x≥0. Crack was moved along the interface manually and the driving force was evaluated for each crack tip position along with the interface. As explained before, the introduction of subsurface channels does not modify the interface that will be still flat. For this reason, the model is still symmetric, then it was chosen to analyze only half of the domain.

The problem was studied by using Abaqus Standard 14.1 (Simulia Corporation), where a 2D model was created (Fig. A.2). The model was discretized by using eight-noded two-dimensional plane strain elements, i.e., CPE8. The displacement field was prescribed at the outer nodes of the outmost layer of elements, while the *y*-displacement was constrained for all nodes along the axis of symmetry. The value of *J*-integral was obtained directly as Abaqus output. The software offers the evaluation of several parameters from fracture mechanics based on the finite element method, such as the *J*-integral, which is widely accepted as a quasi-static fracture mechanics parameter for a linear material response. The crack front and the virtual the crack extension direction must be defined. It is possible to evaluate the *J*-integral using different contours. Each contour is a ring of elements surrounding the crack tip. These rings of elements are defined recursively to surround all previous contours. The number of evaluations is equal to the number of such rings of elements. The *J*-integral could be used in quasi-static fracture analysis to obtain the energy release associated with crack advance. For a virtual crack growth, i.e., *λ(s)*, the energy release rate could be obtained as:

$$J = \int_A \lambda(s) n \cdot H \cdot q \, dA \tag{A.3}$$

Where *dA* is a surface element along a small cylindrical surface enclosing the crack tip, *n* is the outward normal to *dA*, and *q* is the direction of the virtual crack extension. *H* is given by:

$$H = \left(WI - \sigma \frac{\delta u}{\delta v} \right) \tag{A.4}$$

For elastic-plastic or elasto-viscoplastic material behavior, *W* is defined as the elastic strain energy density plus the plastic dissipation. The *J*-integral should be independent of the domain used. However, the *J*-integral estimates from different rings may vary due to the approximate nature of the finite element solution. Variation in *J* value typically may indicate that a finer mesh is needed or, for an elasto-plastic model, that the contour integral domain does not totally include the plastic zone. To check the accuracy of contours, it is necessary to request more contours and evaluate the value of the contour integral that appears approximately constant from one contour to the next: typically the first and second contours should be ignored as inaccurate. It was chosen to evaluate the *J* value on 10 contours.

This parameter was evaluated for different crack tip position respect channels geometry by removing the symmetry constrain along with the interface. Mesh size was reduced at the crack tip to ensure a robust determination of the *energy release rate* (Fig A.2).

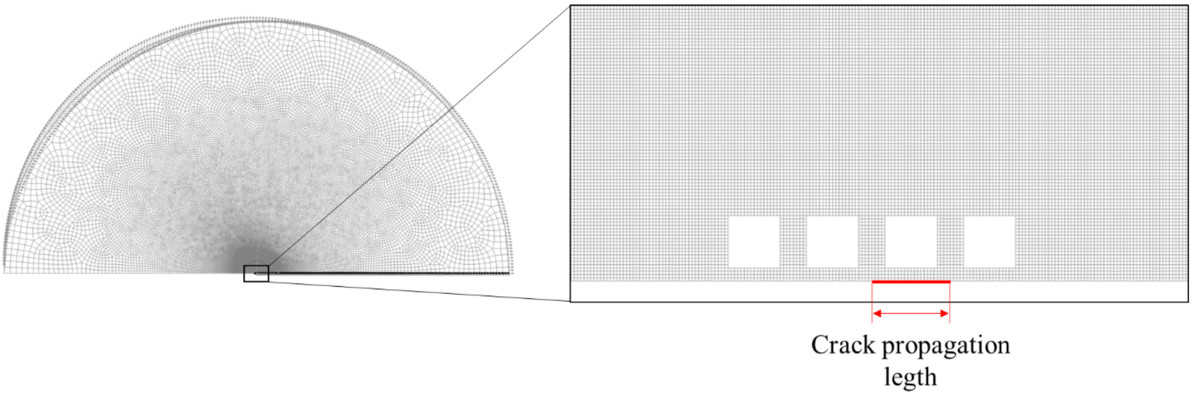

Fig. A.2: Finite element model with details of the mesh around the crack tip.

The same model was created to study the effect of sinusoidal interfaces. As explained before, The crack tip is located in the center of the global coordinate system that is located in the center of the domain and the crack propagation is due to remote Mode-I loading, applied at the boundary of the circular domain. As before, the material was assumed to be linearly elastic and the problem was modeled in plane strain condition. In that case, the radius of the domain was chosen to guarantee that R>>(*A*, *λ*), i.e., Mode-I singular field far from the crack tip. The displacement field was applied at the boundary of the circular domain. Displacement components, according to LEFM, could be written as Eqs. A.1- A.2 as explained before.

The crack tip was located in the middle of the circular domain, i.e., the interface is open for x<0 and connected for x≥0. Crack was displaced along the sinusoidal interface manually and the value of J-integral was evaluated for each crack tip position along the sinusoidal interface. A 2D plane strain model, realized by using Abaqus Standard 14.1 (Simulia Corporation), is shown in Fig. A.3. The problem was formulated by using eight-node two-dimensional plane strain elements, i.e., CPE8. Mesh dimension was reduced in the crack tip to ensure a good reproduction of the *energy release rate* fluctuation as a function of crack tip position on the sinusoid. The displacement field was prescribed at the nodes of the elements pertaining to the model outer boundary. The value of *J*-integral given by the software was evaluated for different crack tip position respect channels geometry. Mesh size was reduced around the crack tip to ensure accurate results. The FE analysis was conducted for the three different sinusoids chosen in the previous section.

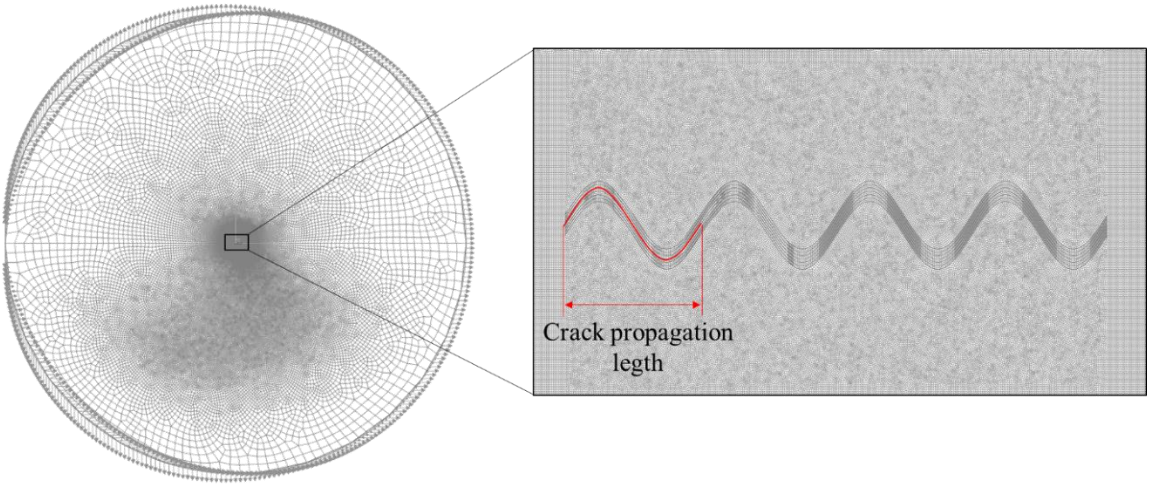

Fig. A.3: Finite element mesh with a detail of the mesh of the sinusoidal interface at the crack tip.

References

Acorn Barnacle (no date). Available at: https://oceana.org/marine-life/cephalopods-crustaceans-other-shellfish/acorn-barnacle (Accessed: 15 November 2019).

Afferrante, L., Carbone, G. and Demelio, G. (2012) 'PROGETTAZIONE DI SUPERFICI ADESIVE ISPIRATE ALLA NATURA : CONTROLLO DEL MECCANISMO DI DISTACCO'.

Akpinar, I. A. *et al.* (2017) 'Research on strength of nanocomposite adhesively bonded composite joints', *Composites Part B: Engineering*, 126, pp. 143–152. doi: 10.1016/j.compositesb.2017.06.016.

Alfano, M. *et al.* (2009) 'Mode I fracture of adhesive joints using tailored cohesive zone models', *International Journal of Fracture*, 157(1–2), pp. 193–204. doi: 10.1007/s10704-008-9293-4.

Alfano, M. *et al.* (2011) 'On the enhancement of bond toughness for Al/epoxy T-peel joints with laser treated substrates', *International Journal of Fracture*, 171(2), pp. 139–150. doi: 10.1007/s10704-011-9636-4.

Alfano, M., Lubineau, G. and Paulino, G. H. (2015) 'Global sensitivity analysis in the identification of cohesive models using full-field kinematic data', *International Journal of Solids and Structures*. Elsevier Ltd, 55, pp. 66–78. doi: 10.1016/j.ijsolstr.2014.06.006.

Anderson, T. L. (2005) *Fracture Mechanics-Fundamentals and Applications*, *Taylor & Francis*. doi: 10.1017/CBO9781107415324.004.

Aradhana, R., Mohanty, S. and Nayak, S. K. (2018) 'High performance epoxy nanocomposite adhesive: Effect of nanofillers on adhesive strength, curing and degradation kinetics', *International Journal of Adhesion and Adhesives*, 84, pp. 238–249. doi:

10.1016/j.ijadhadh.2018.03.013.

Arul, E. P. and Ghatak, A. (2012) 'Control of adhesion via internally pressurized subsurface microchannels', *Langmuir*, 28(9), pp. 4339–4345. doi: 10.1021/la204618u.

ASTM Standard D3433-99 (2012) '"Standard Test Method for Fracture Strength in Cleavage of Adhesives in Bonded Metal Joints"', *ASTM International*, 99(Reapproved), pp. 1–8. doi: 10.1520/D3433-99R12.2.

ASTM Standard D638-14 (2004) 'Standard Test Method for Tensile Properties of Plastics', *ASTM International*, 12(Reapproved), pp. 1–8. Available at: www.radford.edu/~biol-web/stats/standarderrorcalc.pdf%5Cnhttps://books.google.com/books?id=6J6Vv3l6GvQC&pgis=1.

Avalle, M. *et al.* (2010) 'Bi-material joining for car body structures: Experimental and numerical analysis', *Journal of Adhesion*, 86(5–6), pp. 539–560. doi: 10.1080/00218464.2010.484308.

Baburaj, E. G. *et al.* (2007) 'Enhancement of adhesive joint strength by laser surface modification', 27(4), pp. 268–276. doi: 10.1016/j.ijadhadh.2006.05.004.

Barnes, T. A. and Pashby, I. R. (2000) 'Joining techniques for aluminum spaceframes used in automobiles. Part II - adhesive bonding and mechanical fasteners', *Journal of Materials Processing Technology*, 99(1), pp. 72–79. doi: 10.1016/S0924-0136(99)00361-1.

Beese, A. M. *et al.* (2014) 'Defect-tolerant nanocomposites through bio-inspired stiffness modulation', *Advanced Functional Materials*, 24(19), pp. 2883–2891. doi: 10.1002/adfm.201303503.

Borsellino, C., Di Bella, G. and Ruisi, V. F. (2009) 'Adhesive joining of aluminium AA6082: The effects of resin and surface treatment', *International Journal of Adhesion and Adhesives*, 29(1), pp. 36–44. doi: 10.1016/j.ijadhadh.2008.01.002.

Boutar, Y. *et al.* (2016) 'Effect of surface treatment on the shear strength of aluminium adhesive single-lap joints for automotive applications', *International Journal of Adhesion and Adhesives*. Elsevier, 67, pp. 38–43. doi: 10.1016/j.ijadhadh.2015.12.023.

Brugo, T. M. *et al.* (2019) 'Development and fracture toughness characterization of a nylon nanomat epoxy adhesive reinforcement', *Proceedings of the Institution of Mechanical Engineers, Part L: Journal of Materials: Design and Applications*, 233(3), pp. 465–474. doi: 10.1177/1464420718807733.

Buchanan, C. and Gardner, L. (2019) 'Metal 3D printing in construction: A review of methods, research, applications, opportunities and challenges', *Engineering Structures*. Elsevier, 180(November 2018), pp. 332–348. doi: 10.1016/j.engstruct.2018.11.045.

Budzik, M. K., Jumel, J. and Shanahan, M. E. R. (2012) 'Antagonist adhesion effects due to variable substrate surface', *Soft Matter*, 8(32), pp. 8321–8326. doi: 10.1039/c2sm25180a.

Burden, D. K. *et al.* (2012) 'Barnacle Balanus amphitrite adheres by a stepwise cementing process', *Langmuir*, 28(37), pp. 13364–13372. doi: 10.1021/la301695m.

Chan, E. P., Ahn, D. and Crosby, A. J. (2007) 'Adhesion of patterned reactive interfaces', *Journal of Adhesion*, 83(5), pp. 473–489. doi: 10.1080/00218460701377628.

Chiodo, G. *et al.* (2015) 'On the effect of pulsed laser ablation on shear strength and mode I fracture toughness of Al/epoxy adhesive joints', *Journal of Adhesion Science and Technology*. Taylor & Francis, 29(17), pp. 1820–1830. doi: 10.1080/01694243.2015.1049325.

Cordisco, F. A. *et al.* (2016) 'Mode I fracture along adhesively bonded sinusoidal interfaces', *International Journal of Solids and Structures*. Elsevier Ltd, 83, pp. 45–64. doi: 10.1016/j.ijsolstr.2015.12.028.

Côté, F. *et al.* (2009) 'The through-thickness compressive strength of a composite sandwich panel with a hierarchical square honeycomb sandwich core', *Journal of Applied Mechanics, Transactions ASME*, 76(6), pp. 1–8. doi: 10.1115/1.3086436.

Dally, J. W. (1987) 'Statistical Analysis of Experimental Data', in *Handbook of Experimental Solid Mechanics*. 1st edition. New Jersey: Springer, Boston, MA, pp. 971–972.

Dávila, C. G., Camanho, P. P. and Turon, A. (2008) 'Effective simulation of delamination in aeronautical structures using shells and cohesive elements', *Journal of Aircraft*, 45(2), pp. 663–672. doi: 10.2514/1.32832.

Dunlop, J. W. C. and Fratzl, P. (2010) 'Biological Composites.', *Annual Review of Materials Research*, 40, pp. 1–24. doi: 10.1146/annurev-matsci-070909-104421.

Dunlop, J. W. C. and Fratzl, P. (2013) 'Multilevel architectures in natural materials', *Scripta Materialia*. Acta Materialia Inc., 68(1), pp. 8–12. doi: 10.1016/j.scriptamat.2012.05.045.

EOS GmbH (no date) 'Product Information EOSINT P / PA2200-Pulver'.

Evans, A. G. *et al.* (2001) 'Model for the robust mechanical behavior of nacre', *Journal of Materials Research*, 16(9), pp. 2475–2484. doi: 10.1557/jmr.2001.0339.

Fratzl, P. *et al.* (2007) 'Hindered crack propagation in materials with periodically varying young's modulus - Lessons from biological materials', *Advanced Materials*, 19(18), pp. 2657–2661. doi: 10.1002/adma.200602394.

Ghatak, A. *et al.* (2004) ‘Peeling from a biomimetically’, *The royal society*, 460, pp. 2725–2735.

Ghazlan, A., Ngo, T. D. and Tran, P. (2015) ‘Influence of interfacial geometry on the energy absorption capacity and load sharing mechanisms of nacreous composite shells’, *Composite Structures*. Elsevier Ltd, 132, pp. 299–309. doi: 10.1016/j.compstruct.2015.05.045.

Glassmaker, N. J. *et al.* (2007) ‘Biologically inspired crack trapping for enhanced adhesion’, *Proceedings of the National Academy of Sciences of the United States of America*, 104(26), pp. 10786–10791. doi: 10.1073/pnas.0703762104.

Goglio, L. and Rezaei, M. (2013) ‘Effect of different substrate pre-treatments on the resistance of aluminum joints to moist environments’, *Journal of Adhesion*, 89(10), pp. 769–784. doi: 10.1080/00218464.2012.759883.

Harris, A. and Beevers, A. (1999) ‘The effects of grit-blasting on surface properties for adhesion’, *International Journal of Adhesion &Adhesives*, 19(November 1998), pp. 445–452.

Harris, A. F. and Beevers, A. (1999) ‘Effects of grit-blasting on surface properties for adhesion’, *International Journal of Adhesion and Adhesives*, 19(6), pp. 445–452. doi: 10.1016/S0143-7496(98)00061-X.

He, X. (2011) ‘A review of finite element analysis of adhesively bonded joints’, *International Journal of Adhesion and Adhesives*. Elsevier, 31(4), pp. 248–264. doi: 10.1016/j.ijadhadh.2011.01.006.

Heide-Jørgensen, S. and Budzik, M. K. (2018) ‘Effects of bondline discontinuity during growth of interface cracks including stability and kinetic considerations’, *Journal of the Mechanics and Physics of Solids*, 117, pp. 1–21. doi: 10.1016/j.jmps.2018.04.002.

Heide-Jørgensen, S., Teixeira de Freitas, S. and Budzik, M. K. (2018) ‘On the fracture behaviour of CFRP bonded joints under mode I loading: Effect of supporting carrier and interface contamination’, *Composites Science and Technology*, 160, pp. 97–110. doi: 10.1016/j.compscitech.2018.03.024.

Hernandez, E. *et al.* (2017) ‘Toughness amplification in copper/epoxy joints through pulsed laser micro-machined interface heterogeneities’, *Scientific Reports*, 7(1), pp. 1–12. doi: 10.1038/s41598-017-16471-6.

Hill, J. C. *et al.* (2003) ‘Co-planar crack interaction in cleaved mica’, *International Journal of Fracture*, 120(1–2), pp. 365–386. doi: 10.1023/a:1024975728664.

Hillerborg, A., Modéer, M. and Petersson, P. E. (1976) ‘Analysis of crack formation and crack growth in concrete by means of fracture mechanics and finite elements', *Cement and Concrete Research*, 6(6), pp. 773–781. doi: 10.1016/0008-8846(76)90007-7.

Högberg, J. L. (2006) 'Mixed mode cohesive law', *International Journal of Fracture*, 141(3–4), pp. 549–559. doi: 10.1007/s10704-006-9014-9.

Van Hooreweder, B. *et al.* (2010) 'Microstructural characterization of SLS-PA12 specimens under dynamic tension/compression excitation', *Polymer Testing*, 29, pp. 319–326. doi: 10.1016/j.polymertesting.2009.12.006.

Hornung, M. and Hajj, M. (2009) 'Structural bonding for lightweight construction', *Materials Science Forum*, 618 619, pp. 49–56. doi: 10.4028/www.scientific.net/MSF.618-619.49.

Hui, C. Y. *et al.* (2011) 'Barnacles resist removal by crack trapping', *Journal of the Royal Society Interface*, 8(59), pp. 868–879. doi: 10.1098/rsif.2010.0567.

Jagota, A. and Hui, C. Y. (2011) 'Adhesion, friction, and compliance of bio-mimetic and bio-inspired structured interfaces', *Materials Science and Engineering R: Reports*. Elsevier B.V., 72(12), pp. 253–292. doi: 10.1016/j.mser.2011.08.001.

Jain, S., Liechti, K. M. and Bonnecaze, R. T. (2019) 'Cohesive zone models to understand the interface mechanics of thin film transfer printing', *Journal of Applied Physics*, 125(7). doi: 10.1063/1.5049804.

Jakubinek, M. B. *et al.* (2018) 'Nanoreinforced epoxy and adhesive joints incorporating boron nitride nanotubes', *International Journal of Adhesion and Adhesives*, 84(March), pp. 194–201. doi: 10.1016/j.ijadhadh.2018.03.008.

Jaslow, C. R. (2000) 'Of cranial sutures 1025', *Biomechanics*.

Jia, Z., Feng, X. and Zou, Y. (2018a) 'An investigation on mode II fracture toughness enhancement of epoxy adhesive using graphene nanoplatelets', *Composites Part B: Engineering*. Elsevier, 155(August), pp. 452–456. doi: 10.1016/j.compositesb.2018.09.094.

Jia, Z., Feng, X. and Zou, Y. (2018b) 'Graphene Reinforced Epoxy Adhesive For Fracture Resistance', *Composites Part B: Engineering*. Elsevier, 155(August), pp. 457–462. doi: 10.1016/j.compositesb.2018.09.093.

Jin, Z. H., Paulino, G. H. and Dodds, R. H. (2003) 'Cohesive fracture modeling of elastic-plastic crack growth in functionally graded materials', *Engineering Fracture Mechanics*, 70(14), pp. 1885–1912. doi: 10.1016/S0013-7944(03)00130-9.

Jojibabu, P. *et al.* (2017) 'Effect of carbon nano-filler addition on the degradation of epoxy adhesive joints subjected to hygrothermal aging', *Polymer Degradation and Stability*. Elsevier

Ltd, 140, pp. 84–94. doi: 10.1016/j.polymdegradstab.2017.04.017.

Kalamkarov, A. L., Kudriavtsev, B. A. and Parton, V. Z. (1990) 'The boundary-layer method in the fracture mechanics of composites of periodic structure', 54(2), pp. 266–271.

Kamino, K. (2013) 'Mini-review: Barnacle adhesives and adhesion', *Biofouling*, 29(6), pp. 735–749. doi: 10.1080/08927014.2013.800863.

Katsiropoulos, C. V. *et al.* (2012) 'Fracture toughness and shear behavior of composite bonded joints based on a novel aerospace adhesive', *Composites Part B: Engineering*. Elsevier Ltd, 43(2), pp. 240–248. doi: 10.1016/j.compositesb.2011.07.010.

Khoramishad, H. and Zarifpour, D. (2018) 'Fracture response of adhesive joints reinforced with aligned multi-walled carbon nanotubes using an external electric field', *Theoretical and Applied Fracture Mechanics*. Elsevier, 98(September), pp. 220–229. doi: 10.1016/j.tafmec.2018.10.007.

Khoshhesab, M. M. and Li, Y. (2018) 'Mechanical behavior of 3D printed biomimetic Koch fractal contact and interlocking', *Extreme Mechanics Letters*. Elsevier Ltd, 24, pp. 58–65. doi: 10.1016/j.eml.2018.09.003.

Kim, W. S. *et al.* (2010) 'Evaluation of mechanical interlock effect on adhesion strength of polymermetal interfaces using micro-patterned surface topography', *International Journal of Adhesion and Adhesives*. Elsevier, 30(6), pp. 408–417. doi: 10.1016/j.ijadhadh.2010.05.004.

Kinloch, A. J. (1987) *Adhesion and Adhesives- SCIENCE AND TECHNOLOGY*. 1st edition. Chapman & Hall.

Kolednik, O. *et al.* (2011) 'Bioinspired design criteria for damage-resistant materials with periodically varying microstructure', *Advanced Functional Materials*, 21(19), pp. 3634–3641. doi: 10.1002/adfm.201100443.

Kolednik, O. *et al.* (2014) 'Improvements of strength and fracture resistance by spatial material property variations', *Acta Materialia*. Acta Materialia Inc., 68, pp. 279–294. doi: 10.1016/j.actamat.2014.01.034.

Korayem, A. H. *et al.* (2015) 'Effect of carbon nanotube modified epoxy adhesive on CFRP-to-steel interface', *Composites Part B: Engineering*. Elsevier Ltd, 79, pp. 95–104. doi: 10.1016/j.compositesb.2015.03.063.

Langer, M. *et al.* (2012) 'Surface analytical characterization of Nd:YAG-laser pre-treated Al Mg3 as a preparation for bonding', *Solid State Sciences*. Elsevier Masson SAS, 14(7), pp. 926–935. doi: 10.1016/j.solidstatesciences.2012.04.029.

Launey, M. E. and Ritchie, R. O. (2009) ‘On the fracture toughness of advanced materials’, *Advanced Materials*, 21(20), pp. 2103–2110. doi: 10.1002/adma.200803322.

Lee, H. Y. and Qu, J. (2003) ‘Microstructure, adhesion strength and failure path at a polymer/roughened metal interface’, *Journal of Adhesion Science and Technology*, 17(2), pp. 195–215. doi: 10.1163/156856103762302005.

Li, S. *et al.* (2005) ‘Use of mode-I cohesive-zone models to describe the fracture of an adhesively-bonded polymer-matrix composite’, *Composites Science and Technology*, 65(2), pp. 281–293. doi: 10.1016/j.compscitech.2004.07.009.

Li, Y., Ortiz, C. and Boyce, M. C. (2011) ‘Stiffness and strength of suture joints in nature’, *Physical Review E - Statistical, Nonlinear, and Soft Matter Physics*, 84(6), pp. 1–5. doi: 10.1103/PhysRevE.84.062904.

Libonati, F. *et al.* (2016) ‘Bone-Inspired Materials by Design: Toughness Amplification Observed Using 3D Printing and Testing’, *Advanced Engineering Materials*, 18(8), pp. 1354–1363. doi: 10.1002/adem.201600143.

Lin, E *et al.* (2014) ‘Tunability and enhancement of mechanical behavior with additively manufactured bio-inspired hierarchical suture interfaces’, *Journal of Materials Research*, 29(17), pp. 1867–1875. doi: 10.1557/jmr.2014.175.

Lin, Erica *et al.* (2014) ‘Tunability and enhancement of mechanical behavior with additively manufactured bio-inspired hierarchical suture interfaces’, *Journal of Materials Research*, 29(17), pp. 1867–1875. doi: 10.1557/jmr.2014.175.

Liu, L. *et al.* (2017) ‘The effects of morphological irregularity on the mechanical behavior of interdigitated biological sutures under tension’, *Journal of Biomechanics*. Elsevier Ltd, 58, pp. 71–78. doi: 10.1016/j.jbiomech.2017.04.017.

Loctite-Henkel (2014) ‘LOCTITE ® EA 9466^{TM}-Technical datasheet’. Available at: www.henkel.com/industrial.

Loureiro, A. L. *et al.* (2010) ‘Comparison of the mechanical behaviour between stiff and flexible adhesive joints for the automotive industry’, *Journal of Adhesion*, 86(7), pp. 765–787. doi: 10.1080/00218464.2010.482440.

Lunder, O. *et al.* (2004) ‘Effect of pre-treatment on the durability of epoxy-bonded AA6060 aluminium joints’, *International Journal of Adhesion and Adhesives*, 24, pp. 107–117. doi: 10.1016/j.ijadhadh.2003.07.002.

Majumder, A., Ghatak, A. and Sharma, A. (2007) ‘Microfluidic adhesion induced by subsurface microstructures', *Science*, 318(5848), pp. 258–261. doi: 10.1126/science.1145839.

Malik, I. A., Mirkhalaf, M. and Barthelat, F. (2017) 'Bio-inspired "jigsaw"-like interlocking sutures: Modeling, optimization, 3D printing and testing', *Journal of the Mechanics and Physics of Solids*. Elsevier Ltd, 102, pp. 224–238. doi: 10.1016/j.jmps.2017.03.003.

Malkin, R., Trask, R. S. and Bond, I. P. (2013) 'Control of unstable crack propagation through bio-inspired interface modification', *Composites Part A: Applied Science and Manufacturing*. Elsevier Ltd, 46(1), pp. 122–130. doi: 10.1016/j.compositesa.2012.11.001.

Maloney, K. and Fleck, N. (2018) 'Damage tolerance of an architected adhesive joint', *International Journal of Solids and Structures*. Elsevier Ltd, 132–133, pp. 9–19. doi: 10.1016/j.ijsolstr.2017.06.010.

Maloney, K. and Fleck, N. (2019a) 'Toughening strategies in adhesive joints', *International Journal of Solids and Structures*. Elsevier Ltd, 158, pp. 66–75. doi: 10.1016/j.ijsolstr.2018.08.028.

Maloney, K. and Fleck, N. (2019b) 'Toughening strategies in adhesive joints', *International Journal of Solids and Structures*. Elsevier Ltd, 158, pp. 66–75. doi: 10.1016/j.ijsolstr.2018.08.028.

Mancini, S. D. *et al.* (2017) 'Replacement of metallic parts for polymer composite materials in motorcycle oil pumps', *Journal of Reinforced Plastics and Composites*, 36(2), pp. 149–160. doi: 10.1177/0731684416673727.

Matsuzaki, R., Tsukamoto, N. and Taniguchi, J. (2016) 'Mechanical interlocking by imprinting of undercut micropatterns for improving adhesive strength of polypropylene', *International Journal of Adhesion and Adhesives*. Elsevier, 68, pp. 124–132. doi: 10.1016/j.ijadhadh.2016.03.002.

Moroni, F. *et al.* (2018) 'Influence of laser treatment parameters on the mode I strain energy release rate of aluminum double cantilever beam joints', *International Journal of Adhesion and Adhesives*. Elsevier Ltd, 83(March), pp. 31–40. doi: 10.1016/j.ijadhadh.2018.02.023.

Musiari, F. *et al.* (2018) 'Experimental investigation on the enhancement of Mode I fracture toughness of adhesive bonded joints by electrospun nanofibers', *Journal of Adhesion*. Taylor & Francis, 94(11), pp. 974–990. doi: 10.1080/00218464.2017.1402301.

Musiari, F. *et al.* (2019) 'Durability assessment of laser treated aluminium bonded joints', *International Journal of Adhesion and Adhesives*. Elsevier Ltd, 93(January), p. 102323. doi: 10.1016/j.ijadhadh.2019.01.017.

Ocaña, R. *et al.* (2015) 'Evaluation of Degradation of Structural Adhesive Joints in Functional Automotive Applications', *Procedia Engineering*. Elsevier B.V., 132, pp. 716–723. doi: 10.1016/j.proeng.2015.12.552.

Okumura, K. (2005) 'Fracture strength of biomimetic composites: Scaling views on nacre', *Journal of Physics Condensed Matter*, 17(31). doi: 10.1088/0953-8984/17/31/015.

Packham, D. E. (2010) 'Discontinuities at the interface and adhesion', *Journal of Adhesion*, 86(12), pp. 1231–1243. doi: 10.1080/00218464.2010.529398.

Park, K. and Paulino, G. H. (2011) 'Cohesive zone models: A critical review of traction-separation relationships across fracture surfaces', *Applied Mechanics Reviews*, 64(6). doi: 10.1115/1.4023110.

Paul, C. R. C. (2015) 'Sutural asymmetry in the ammonites Bifericeras and Leptonotoceras from the Lower Jurassic of Bishop's Cleeve, Gloucestershire, England and its significance for ammonite life orientation', *Palaeogeography, Palaeoclimatology, Palaeoecology*. Elsevier B.V., 418, pp. 160–175. doi: 10.1016/j.palaeo.2014.11.005.

Porter, M. M. *et al.* (2017) '3D-printing and mechanics of bio-inspired articulated and multi-material structures', *Journal of the Mechanical Behavior of Biomedical Materials*. Elsevier Ltd, 73(June 2016), pp. 114–126. doi: 10.1016/j.jmbbm.2016.12.016.

Raman, S. and Kumar, R. (2011) 'Construction and nanomechanical properties of the exoskeleton of the barnacle, Amphibalanus reticulatus', *Journal of Structural Biology*. Elsevier Inc., 176(3), pp. 360–369. doi: 10.1016/j.jsb.2011.08.015.

Ranade, S. R. *et al.* (2018) 'Characterizing fracture performance and the interaction of propagating cracks with locally weakened interfaces in adhesive joints', *International Journal of Adhesion and Adhesives*. doi: 10.1016/j.ijadhadh.2017.12.006.

Ranatunga, V. (2011) 'WCE2011_pp2604-2609.pdf', III, pp. 6–11.

Reddy, S., Arzt, E. and Del Campo, A. (2007) 'Bioinspired surfaces with switchable adhesion', *Advanced Materials*, 19(22), pp. 3833–3837. doi: 10.1002/adma.200700733.

Rotella, G. *et al.* (2015) 'Enhancement of static strength and long term durability of steel/epoxy joints through a fiber laser surface pre-treatment', *International Journal of Adhesion and Adhesives*, 63, pp. 87–95. doi: 10.1016/j.ijadhadh.2015.08.009.

Rotella, G. *et al.* (2016) 'Evaluation of mechanical and laser surface pre-treatments on the strength of adhesive bonded steel joints for the automotive industry', *Journal of Adhesion Science and Technology*, 30(7), pp. 747–758. doi: 10.1080/01694243.2015.1123559.

Rotella, G., Alfano, M. and Candamano, S. (2015) ‘Surface modification of Ti6Al4V alloy by pulsed Yb-laser irradiation for enhanced adhesive bonding’, *CIRP Annals - Manufacturing Technology*, 64(1), pp. 527–530. doi: 10.1016/j.cirp.2015.04.042.

Rudawska, A. (2014) ‘Selected aspects of the effect of mechanical treatment on surface roughness and adhesive joint strength of steel sheets’, *International Journal of Adhesion and Adhesives*. Elsevier, 50, pp. 235–243. doi: 10.1016/j.ijadhadh.2014.01.032.

Sadigh, M. A. S. and Marami, G. (2018) ‘Enhancing fatigue life in adhesively bonded joints using reduced graphene oxide additive: Experimental and numerical evaluation’, *International Journal of Adhesion and Adhesives*, 84, pp. 283–290. doi: 10.1016/j.ijadhadh.2018.04.001.

Sancaktar, E. and Gomatam, R. (2001) ‘A study on the effects of surface roughness on the strength of single lap joints’, *Journal of Adhesion Science and Technology*, 15(1), pp. 97–117. doi: 10.1163/156856101743346.

Sánchez-Romate, X. F. *et al.* (2018) ‘Development of bonded joints using novel CNT doped adhesive films: Mechanical and electrical properties’, *International Journal of Adhesion and Adhesives*. Elsevier Ltd, 86(September), pp. 98–104. doi: 10.1016/j.ijadhadh.2018.09.001.

Saunders, W. B., Work, D. M. and Nikolaeva, S. V. (1999) ‘Evolution of complexity in paleozoic ammonoid sutures’, *Science*, 286(5440), pp. 760–763. doi: 10.1126/science.286.5440.760.

Shahar, R. *et al.* (2009) ‘Mechanical function of a complex three-dimensional suture joining the bony elements in the shell of the red-eared slider turtle’, *Materials Research Society Symposium Proceedings*, 1187, pp. 9–15. doi: 10.1002/adma.200801256.

Shen, L., Hui, C. Y. and Jagota, A. (2008) ‘A two-dimensional model for enhanced adhesion of film-terminated fibrillar interfaces by crack trapping’, *Journal of Applied Physics*, 104(12). doi: 10.1063/1.3035908.

Sills, R. B. and Thouless, M. D. (2015) ‘Cohesive-length scales for damage and toughening mechanisms’, *International Journal of Solids and Structures*. doi: 10.1016/j.ijsolstr.2014.06.010.

Sitti, M. and Fearing, R. S. (2003) ‘Synthetic gecko foot-hair micro/nano-structures as dry adhesives’, *Journal of Adhesion Science and Technology*, 17(8), pp. 1055–1073. doi: 10.1163/156856103322113788.

Smith, B. L. *et al.* (1999) ‘Molecular mechanistic origin of the toughness of natural adhesives, fibres and composites’, *Nature*, 399(6738), pp. 761–763. doi: 10.1038/21607.

Suzuki, T. *et al.* (2013) 'Crack growth analysis of a composite/adhesive interface toughened by in-mold surface preparation', *International Journal of Adhesion and Adhesives*. Elsevier, 42, pp. 36–43. doi: 10.1016/j.ijadhadh.2013.01.008.

Tao, R., Alfano, M. and Lubineau, G. (2018) 'Laser-based surface patterning of composite plates for improved secondary adhesive bonding', *Composites Part A: Applied Science and Manufacturing*, 109, pp. 84–94. doi: 10.1016/j.compositesa.2018.02.041.

Tao, R., Alfano, M. and Lubineau, G. (2019) 'In situ analysis of interfacial damage in adhesively bonded composite joints subjected to various surface pretreatments', *Composites Part A: Applied Science and Manufacturing*, 116, pp. 216–223. doi: 10.1016/j.compositesa.2018.10.033.

Vajpayee, S. *et al.* (2009) 'Effect of rate on adhesion and static friction of a film-terminated fibrillar interface', *Langmuir*, 25(5), pp. 2765–2771. doi: 10.1021/la8033885.

Wang, N. and Xia, S. (2017) 'Cohesive fracture of elastically heterogeneous materials: An integrative modeling and experimental study', *Journal of the Mechanics and Physics of Solids*. Elsevier, 98, pp. 87–105. doi: 10.1016/j.jmps.2016.09.004.

Wang, Q. *et al.* (2015) 'Bio-inspired direct patterning functional nanothin microlines: Controllable liquid transfer', *ACS Nano*, 9(4), pp. 4362–4370. doi: 10.1021/acsnano.5b00861.

Wang, X. *et al.* (2017) 'Hierarchical interfacial structuring of the calcareous base of the barnacle Balanus albicostatus over different length scales', *Materials Chemistry and Physics*. Elsevier B.V, 192, pp. 48–57. doi: 10.1016/j.matchemphys.2017.01.053.

Wegst, U. G. K. *et al.* (2015) 'Bioinspired structural materials', *Nature Materials*, 14(1), pp. 23–36. doi: 10.1038/nmat4089.

Wu, Qianqian *et al.* (2019) 'Lattice materials with pyramidal hierarchy: Systematic analysis and three dimensional failure mechanism maps', *Journal of the Mechanics and Physics of Solids*, 125, pp. 112–144. doi: 10.1016/j.jmps.2018.12.006.

Wu, Qianru *et al.* (2019) 'Residual stresses and distortion in the patterned printing of titanium and nickel alloys', *Additive Manufacturing*. Elsevier, 29(August), p. 100808. doi: 10.1016/j.addma.2019.100808.

Xia, S. M. *et al.* (2013) 'Adhesion of heterogeneous thin films - I: Elastic heterogeneity', *Journal of the Mechanics and Physics of Solids*. Elsevier, 61(3), pp. 838–851. doi: 10.1016/j.jmps.2012.10.014.

Xu, X. P. and Needleman, A. (1994) 'Numerical simulations of fast crack growth in brittle solids', *Journal of the Mechanics and Physics of Solids*, 42(9), pp. 1397–1434. doi: 10.1016/0022-5096(94)90003-5.

Yang, Q. D., Thouless, M. D. and Ward, S. M. (1999) 'Numerical simulations of adhesively-bonded beams failing with extensive plastic deformation', *Journal of the Mechanics and Physics of Solids*, 47(6), pp. 1337–1353. doi: 10.1016/S0022-5096(98)00101-X.

Yukimoto, Y., Matsuzaki, R. and Todoroki, A. (2015) 'Effects of mixed-mode ratio and step-shaped micro pattern surface on crack-propagation resistance of carbon-fiber-reinforced plastic/adhesive interface', *Composites Part A: Applied Science and Manufacturing*. Elsevier Ltd, 69, pp. 139–149. doi: 10.1016/j.compositesa.2014.11.014.

Zavattieri, P. D., Hector, L. G. and Bower, A. F. (2008) 'Cohesive zone simulations of crack growth along a rough interface between two elastic-plastic solids', *Engineering Fracture Mechanics*, 75(15), pp. 4309–4332. doi: 10.1016/j.engfracmech.2007.11.007.

Zhang, P., Heyne, M. A. and To, A. C. (2015) 'Biomimetic staggered composites with highly enhanced energy dissipation: Modeling, 3D printing, and testing', *Journal of the Mechanics and Physics of Solids*. Elsevier, 83, pp. 285–300. doi: 10.1016/j.jmps.2015.06.015.

Zhu, X. B. *et al.* (2016) 'Reinforcing cross-tension strength of adhesively bonded joints using metallic solder balls', *International Journal of Adhesion and Adhesives*. Elsevier, 68, pp. 263–272. doi: 10.1016/j.ijadhadh.2016.04.009.